

PACIFIC EARTHQUAKE ENGINEERING RESEARCH CENTER

A Probabilistic Framework to Include the Effects of Near-Fault Directivity in Seismic Hazard Assessment

Shrey Kumar Shahi

Jack W. Baker

Department of Civil and Environmental Engineering
Stanford University

Disclaimer

The opinions, findings, and conclusions or recommendations expressed in this publication are those of the author(s) and do not necessarily reflect the views of the study sponsor(s) or the Pacific Earthquake Engineering Research Center.

A Probabilistic Framework to Include the Effects of Near-Fault Directivity in Seismic Hazard Assessment

Shrey Kumar Shahi

Jack W. Baker

Department of Civil and Environmental Engineering
Stanford University

PEER Report 2013/15
Pacific Earthquake Engineering Research Center
Headquarters at the University of California, Berkeley

October 2013

ABSTRACT

Growth of major population centers near seismically active faults has significantly increased the probability of a large earthquake striking close to a big city in the near future. This, coupled with the fact that near-fault ground motions are known to impose larger demands on structures than ground motions far from the fault, makes the quantitative study of near-fault seismic hazard and risk important.

Directivity effects cause pulse-like ground motions that are known to increase the seismic hazard and risk in near-fault region. These effects depend on the source-to-site geometry parameters, which are not included in most ground-motion models used for probabilistic seismic hazard assessment computation. In this study, we develop a comprehensive framework to study near-fault ground motions, and account for their effects in seismic hazard assessment. The proposed framework is designed to be modular, with separate models to predict the probability of observing a pulse at a site, the probability distribution of the period of the observed pulse, and a narrow band amplification of the spectral ordinate conditioned on the period of the pulse. The framework also allows deaggregation of hazard with respect to probability of observing the pulse at the site and the period of the pulse. This deaggregation information can be used to aid in ground-motion selection at near fault sites.

A database of recorded ground motions with each record classified as pulse-like or non-pulse-like is needed for an empirical study of directivity effects. Early studies of directivity effects used manually classified pulses. Manual classification of ground motions as pulse-like is labor intensive, slow, and has the possibility to introduce subjectivity into the classifications. To address these problems we propose an efficient algorithm to classify multi-component ground motions as pulse-like and non-pulse-like. The proposed algorithm uses the continuous wavelet transform of two orthogonal components of the ground motion to identify pulses in arbitrary orientations. The proposed algorithm was used to classify each record in the NGA-West2 database, which created the largest set of pulse-like motions ever used to study directivity effects.

The framework to include directivity effects in seismic hazard assessment, as proposed in this study, requires a ground-motion model that accounts for directivity effects in its prediction. Most of

the current directivity models were developed as a correction for already existing ground-motion models, and were fitted using ground-motion model residuals. Directivity effects are dependent on magnitude, distance, and the spectral acceleration period. This interaction of directivity effects with magnitude and distance makes separation of distance and magnitude scaling from directivity effects challenging. To properly account for directivity effects in a ground-motion model they need to be fitted as a part of the original model and not as a correction. We propose a method to include the effects of directivity in a ground-motion model and also develop models to make unbiased prediction of ground-motion intensity, even when the directivity parameters are not available.

Finally, following the approach used to model directivity effects, we developed a modular framework to characterize ground-motion directionality, which causes the ground-motion intensity to vary with orientation. Using the expanded NGA-West2 database we developed new models to predict the ratio between maximum and median ground-motion intensity over all orientations. Other models to predict distribution of orientations of the maximum intensity relative to the fault and the relationship between this orientation at different periods are also presented. The models developed in this dissertation allow us to compute response spectra that are expected to be observed in a single orientation (e.g., fault normal, orientation of maximum intensity at a period). It is expected that the proposed spectra can be a more realistic representation of single orientation ground motion compared to the median or maximum spectra over all orientations that is currently used.

ACKNOWLEDGMENTS

This work was supported in part by the Earthquake Engineering Research Centers Program of the National Science Foundation under award number EEC-9701568 through the Pacific Earthquake Engineering Research Center (PEER).

Any opinions, findings, and conclusions or recommendations expressed in this material are those of the authors and do not necessarily reflect those of the National Science Foundation.

This report was originally published as the PhD. dissertation of the first author. The authors would like to thank Professor Eduardo Miranda and Professor Greg Deierlein for their invaluable suggestions that improved this document significantly.

CONTENTS

ABSTRACT	iii
ACKNOWLEDGMENTS	v
1 Introduction	1
1.1 Motivation	1
1.1.1 PEER Seismic Risk Assessment Framework	3
1.1.2 Near-Fault Effects	4
1.2 Areas of Contribution	8
1.2.1 Comprehensive Framework to Account for Directivity Effects in Hazard Assessment and Ground-Motion Selection	8
1.2.2 Efficient Identification of Pulses in Multi-Component Ground Motions	9
1.2.3 Explicit Inclusion of Directivity Effects in a Ground-Motion Model	10
1.2.4 Comprehensive Study of Ground-Motion Directionality	10
1.3 Organization	11
2 An Empirically Calibrated Framework for Including the Effects of Near-Fault Direc- tivity in Probabilistic Seismic Hazard Analysis	13
2.1 Introduction	13
2.2 Identification of Pulse-Like Ground Motions	14
2.3 Development of Input Models for Modified PSHA	17
2.3.1 Probability of Observing a Pulse	19
2.3.2 Pulse Orientation	20
2.3.3 Period of the Pulse	26
2.3.4 Amplification of Spectral Acceleration due to the Presence of Pulse	26

2.3.5	Modification of Ground-Motion Model to Predict Non-Pulse-Like Ground Motion	31
2.4	Algorithm to Include the Effects of Pulse-Like Ground Motion in PSHA	32
2.5	Example Calculations	35
2.5.1	PSHA for a Single Site	35
2.5.2	Spatial Pattern of PSHA Amplification due to Pulse-Like Ground Motion	36
2.5.3	Deaggregation to Aid in Ground Motion Selection	38
2.6	Conclusion	38
3	Regression Models for Predicting the Probability of Near-Fault Earthquake Ground Motion Pulses, and Their Period	43
3.1	Introduction	43
3.2	Dataset Used to Build the Models	45
3.3	Probability of Pulse	45
3.3.1	Logistic Regression	45
3.3.2	Fitting of the Model	46
3.4	Pulse Period	52
3.4.1	Mixed-effects Regression	54
3.4.2	Search for Predictors	54
3.4.3	Fitting of the Model	55
3.4.4	Statistical versus Practical Significance	56
3.5	Conclusion	57
4	An Efficient Algorithm to Identify Strong Velocity Pulses in Multi-Component Ground Motions	59
4.1	Introduction	59
4.2	Wavelet Transform for Multi-Component Ground Motion	61
4.2.1	Efficient Wavelet Transform in Multiple Orientations	64
4.3	Classification Algorithm	65
4.3.1	Late Pulses	70
4.3.2	Pulse Period	70
4.3.3	Software Implementation	70
4.4	Comparison with Previously Developed Algorithms	71
4.5	Directivity Models	73
4.5.1	Model for Pulse Period	73

4.5.2	Model for Probability of Directivity Pulse	74
4.6	Pulse Models	75
4.7	Conclusion	77
5	Explicit Inclusion of Directivity Effects in Ground-Motion Models	79
5.1	Introduction	79
5.2	Ground-Motion Models	81
5.2.1	Base Ground-Motion Model	81
5.3	Fitting the Ground-Motion Models	83
5.3.1	Fitting CBR	84
5.3.2	Fitting the CBSB Model	89
5.4	Average Directivity Amplification	95
5.4.1	Average Directivity Computation	96
5.4.2	Fitting Functional Forms to Average Directivity Amplification	99
5.5	Comparison of Ground-Motion Predictions	104
5.5.1	Median Predictions from CBR and CBSB with Average Directivity	104
5.5.2	Comparison of CBSB Predictions under Different Levels of Information	105
5.5.3	Standard Deviations from the Ground-Motion Models	105
5.6	Conclusion	110
6	Approximate Deaggregation Results for Hazard Consistent Ground Motion Selection in Near-Fault Regions	111
6.1	Introduction	111
6.2	Probability of Directivity Pulse causing Exceedance of a Given S_a Level	112
6.3	Periods of Pulse-Like Ground Motions Conditioned at a Given S_a Level	119
6.4	Number of Ground Motions Needed	121
6.5	Conclusion	121
7	NGA-West2 Models for Ground-Motion Directionality	125
7.1	Introduction	125
7.2	Ground-Motion Intensity and Directionality	126
7.3	Ratio of $S_{a_{RotD100}}$ to $S_{a_{RotD50}}$	128
7.3.1	Comparison with Other Models	130
7.3.2	Dependence of $S_{a_{RotD100}}/S_{a_{RotD50}}$ on Other Parameters	133
7.4	Orientation of $S_{a_{RotD100}}$	135

7.4.1	Relationship between $Sa_{RotD100}$ Orientations at Different Periods	139
7.5	Sa at Arbitrary Orientations	140
7.6	Example Target Spectra	143
7.6.1	Spectra Conditioned on Orientation	143
7.6.2	Spectra Conditioned on the Orientation of $Sa_{RotD100}$ at a Given Period	144
7.7	Conclusion	146
8	Conclusion	149
8.1	Practical Implications and Contributions	149
8.1.1	Framework to Include Directivity Effects in Seismic Hazard Assessment	149
8.1.2	Models to Predict Probability of Pulse Occurrence and its Period	150
8.1.3	Algorithm to Identify Pulse-Like Ground Motions	150
8.1.4	Including Directivity Effects in Ground-Motion Models	151
8.1.5	Study of Hazard Deaggregation Accounting for Directivity Effects	152
8.1.6	Ratio of $Sa_{RotD100}$ to Sa_{RotD50}	152
8.1.7	Orientation of $Sa_{RotD100}$ and Single Orientation Conditional Spectra	153
8.2	Limitations and Future Work	153
8.2.1	Data Limitations	153
8.2.2	Classification of Directivity Pulses	154
8.2.3	Ground-Motion Model with Directivity Effects	155
8.2.4	Ground Motion Selection	156
8.3	Concluding Remarks	156
APPENDIX A	Pulse-Like Ground Motions Classified using Method Describe in Chapter	
2		159
APPENDIX B	Pulse-Like Ground Motions Classified using Method Described in Chap-	
ter 4		165
APPENDIX C	Expected Value of $\ln Amp$ Given M	171
APPENDIX D	Approximations Made in Chapter 6	175
References		177

LIST OF TABLES

3.1	AIC for strike-slip models with different predictors.	49
3.2	Result of mixed-effects regression, for both strike-slip and non-strike-slip faults.	56
4.1	Details of logistic regression models tested to predict the probability of directivity pulse at a site.	76
5.1	Coefficients for the CBR ground-motion model.	85
5.2	Coefficients for the CBSB ground-motion model.	91
5.3	Period-independent coefficients of the directivity terms.	91
5.4	Coefficients for the average directivity amplification model.	100
5.5	Standard deviation of total error (σ) for different models considered in the study.	109
6.1	$P(\text{directivity})$ conditioned on 2% for a 50-year hazard at different periods and site locations.	118
6.2	$P(\text{directivity})$ conditioned on 10% for a 50-year hazard at different periods and site locations.	118
7.1	Fitted values of $\ln(Sa_{RotD100}/Sa_{RotD50})$ with the within-event standard deviation (ϕ), between-event standard deviation (τ), and total standard deviation (σ), estimated by mixed-effects regression. Note that the estimates are for mean of $\ln(Sa_{RotD100}/Sa_{RotD50})$ and geometric mean of $Sa_{RotD100}/Sa_{RotD50}$ and the reported standard deviations are for $\ln(Sa_{RotD100}/Sa_{RotD50})$ estimates.	131
7.2	Probability density of α for $R_{rup} < 5km$ and $T \geq 1$ sec.	138
7.3	Estimated values of the parameter λ for the truncated exponential model.	141
7.4	Geometric mean of $\frac{Sa_\phi}{Sa_{RotD50}}$ at various values of ϕ and T	142
A.1	List of pulse-like ground motions.	159
B.1	List of pulse-like ground motions.	165

LIST OF FIGURES

1.1	Map of Imperial Valley earthquake rupture with the location of sites where ground motion was recorded. Site (c) was close to the epicenter is the Bonds Corner station (NGA # 160) and no directivity pulse was observed here; however, a directivity pulse was observed at site (b) El Centro Array # 4 station (NGA # 179), which is located down the rupture at a similar distance as site (c) from the fault. The fault-normal component of the two ground motions is shown here.	3
1.2	Some examples of ground-motion recordings with directivity pulse. (a) Brawley Airport station from the 1979 Imperial Valley earthquake (NGA # 161), (b) Lucerne station from the 1992 Landers earthquake (NGA # 879), and (c) Rinaldi station from 1994 Northridge earthquake (NGA # 1063).	5
2.1	Illustration of the procedure used by Baker (2007)'s algorithm to extract the largest pulse from a velocity time history (1979 Imperial Valley, EC Meloland Overpass recording). Here, the pulse is large and the ground motion is classified as pulse-like.	15
2.2	Pulse indicator values as a function of orientation for the 1979 Imperial Valley, EC County Center recording. Shaded orientations indicate orientations in which a strong pulse is apparent. See Baker (2007) for more information on how the pulse indicator is calculated.	16
2.3	Response spectra (5% damped) of 1979 Imperial Valley, El Centro Array # 5 ground motion in the fault-normal orientation. The Boore and Atkinson (2007) median prediction and the response spectra from residual ground motion are also shown.	21
2.4	Plot explaining the parameters needed to fit the logistic regression for (a) strike-slip and (b) non-strike-slip faults. The parameter α , the angle between orientation of interest and the strike of the fault, is also shown (after Somerville et al., 1997).	22

2.5	Map of 1979 Imperial Valley earthquake ($M = 6.53$) showing (a) contours of probability of pulse occurrence for the given rupture, and (b) sites where pulse-like ground motion was observed. The site within the shaded circle is the one for which example hazard analysis is done.	23
2.6	Map of 1994 Northridge earthquake ($M = 6.69$) showing (a) contours of probability of pulse occurrence for the given rupture, and (b) sites where pulse-like ground motion was observed.	24
2.7	Plot of probability of pulse at α given pulse at site for both strike-slip and non-strike-slip faults.	25
2.8	Pulse period versus earthquake magnitude for observed pulse-like ground motions.	27
2.9	Observed ϵ values of residual ground motions.	28
2.10	Amplification factor for S_a due to the presence of pulse-like features in ground motions. (a) Plot of predictive equation along with the observed data, and (b) mean amplification due to pulses oriented in different directions.	29
2.11	Ratio of standard deviation of residuals from predictions of pulse-like spectra ($\sigma_{\ln S_{a,pulse}}$) to the BA2008 ground-motion model standard deviation ($\sigma_{\ln S_{a,gmm}}$).	30
2.12	Median $S_a(2 \text{ sec})$ prediction from Boore-Atkinson 2008 model with and without the de-amplification along with the actual observations from Northridge earthquake. The Boore-Atkinson model prediction includes the inter-event residual of the Northridge earthquake.	33
2.13	Two percent for a 50-year uniform hazard spectra from ordinary PSHA, PSHA with pulse modification suggested in this paper and PSHA with modification suggested by the Somerville-Abrahamson model for comparison. The PSHA is performed for the strike-normal orientation.	37
2.14	Map showing contours of amplification in 2% in 50 years $S_a(5 \text{ sec})$ by using (a) modified PSHA described in this paper, (b) using the Somerville-Abrahamson model.	37
2.15	Deaggregation result showing $P(\text{pulse} S_a(5 \text{ sec}) > x)$	39
2.16	Deaggregation results showing % contribution to hazard by T_p given $S_a(5 \text{ sec}) > 0.3g$	40
3.1	A diagram explaining the source-to-site parameters used to predict probability of pulse for (a) strike-slip fault and (b) non-strike-slip fault.(after Somerville et al., 1997).	48

3.2	A diagram showing regions where r and s completely defines the source-to-site geometry and θ is redundant, and the region where θ is needed along with r and s to completely define the source-to-site geometry. The figure shows two sites (A and B) that have same r and s but different θ to show the importance of θ in the shaded region.	49
3.3	Histogram of $\frac{R_{epi} \cdot \cos(\theta)}{s}$	50
3.4	Contours of predicted probability of pulse due to an earthquake from a strike-slip fault at different r and s values.	51
3.5	Map of Imperial Valley earthquake showing (a) contours of probability of pulse occurrence for the given rupture, and (b) sites where pulse-like ground motion was observed (from Chapter 2).	52
3.6	Map of Northridge earthquake showing (a) contours of probability of pulse occurrence for the given rupture, and (b) sites where pulse-like ground motion was observed (from Chapter 2).	53
3.7	Comparison of predictions from models for non-strike-slip faults using M and r^2 as predictors and only M as predictor at different r values.	58
4.1	Different types of ground motions (a) clear pulse (El Centro Array # 4 recording, from the 1979 Imperial Valley earthquake), (b) clear non-pulse (Pasadena-CIT recording, from the 1971 San Fernando earthquake), and (c) an ambiguous pulse (Salton Sea Wildlife Refuge recording, from the 1987 Superstition Hills earthquake).	60
4.2	The Pasadena - CIT Athenaeum recording from 1971 San Fernando earthquake (original ground motion) is broken down into 50 wavelets using the continuous wavelet transform. The wavelets are summed together to get the reconstructed ground motion, which is an approximation of the original ground motion. The quality of approximation improves as the number of wavelets used is increased.	62
4.3	The El Centro Array #4 recording from 1979 Imperial Valley earthquake (original ground motion) is broken down into 30 wavelets using the continuous wavelet transform. The wavelets are summed together to get the reconstructed ground motion, which is an approximation of the original ground motion. Note that pulse-like ground motions are dominated by a few strong wavelets.	63

4.4	Two orthogonal components of a ground motion, labeled X_0 and X_{90} , are shown along with the absolute value of their wavelet transform coefficients, labeled $ c_0 $ and $ c_{90} $. The wavelet coefficients c_0 and c_{90} are combined to get an estimate of $c_{44.3}$ (coefficients for ground motion in an orientation 44.3 degrees away from X_0). The wavelet coefficients computed directly using the rotated time histories are shown for comparison.	65
4.5	The orientation of principal component along with the energy ratio and PGV ratio from individual ground motions is shown (only the ratios from from pulse with largest wavelet coefficient is shown). Note that sometimes the PGV ratio of residual to original ground motion can be greater than 1. The points with PGV ratio equal to 1 represent those ground-motions where the extracted pulse did not cause the PGV. 68	68
4.6	Classification boundary of Equation 4.12 shown with individual ground motions. The non-pulse-like ground motions on the positive pulse indicator side of the figure were rejected by the late arrival criteria.	69
4.7	Comparison on the classification rule for the proposed algorithm and Baker (2007) algorithm. Note that the two vertical lines for Baker (2007) show the maximum and minimum values PC can take when the pulse indicator is equal to 0.85.	72
4.8	(a) A pulse-like ground motion with low PGV (SMART1 M01 recording from 1986 Taiwan earthquake), and (b) a non-pulse classified as pulse-like in a few orientations by the Chapter 2 algorithm (Agnews State Hospital recording from the 1994 Morgan Hill earthquake). For both ground motions the orientation with highest wavelet coefficient is shown.	72
4.9	Parameters used to fit the logistic regressions for (a) strike-slip and (b) non-strike-slip faults.	75
4.10	Probability of directivity pulse contours. Predictions from Equation 4.17 for rupture of length (a) 50 km and (b) 200 km. Prediction from Equation 4.18 for rupture of length (c) 50 km and (d) 200 km.	76
5.1	Comparison of magnitude scaling of the Campbell and Bozorgnia (2008) and CBR model fitted in this study, for $R_{rup} = 30$ km, $V_{s30} = 760$ m/sec and periods (a) 0.1 sec, (b) 0.2 sec, (c) 1 sec, and (d) 3 sec.	86
5.2	Comparison of distance scaling of the Campbell and Bozorgnia (2008) and CBR model fitted in this study for $M = 7$, $V_{s30} = 760$ m/sec and periods (a) 0.1 sec, (b) 0.2 sec, (c) 1 sec and (d) 3 sec.	87

5.3	Comparison of V_{s30} scaling of the Campbell and Bozorgnia (2008) and CBR model fitted in this study for $M = 7$, $R_{rup} = 30$ km and periods (a) 0.1 sec, (b) 0.2 sec, (c) 1 sec, and (d) 3 sec.	88
5.4	Comparison of the median response spectra predicted by Campbell and Bozorgnia (2008) and CBR model for (a) $M = 5$, (b) $M = 6$, (c) $M = 6.5$, and (d) $M = 7.5$. . .	89
5.5	Comparison of the median response spectra predicted by CBSB and CBR models when a directivity pulse of period 2.2 sec is assumed to have occurred.	92
5.6	Comparison of the median response spectra predicted by CBR model and the CBSB model when a directivity pulse of period 2.2 sec is assumed to have occurred and when pulse occurrence is considered uncertain. For the uncertain pulse, case P(directivity) is assumed to be 0.6 and the T_p follows the log-normal distribution described by Equations 5.17 and 5.18.	94
5.7	Comparison of the median response spectra predicted by CBR model and the CBSB model when $I_{directivity}$ is set to 0. The comparisons are for $R_{rup} = 1$ km and $R_{rup} = 20$ km.	95
5.8	Diagram showing location of sites at a distance R from a vertical strike-slip rupture. Note in this case R is both the R_{jb} and R_{rup}	98
5.9	Diagram showing difference in the value of parameter d for sites at same closest distance on hanging wall (d_1) and foot wall (d_2).	99
5.10	Comparison of average directivity computed using Equation 5.22 (solid lines) and predictions from Equation 5.27 (dashed lines). The comparison is shown as a function of M at various R values. The period is 1 sec in (a) and 7.5 sec in (b).	101
5.11	Comparison of average directivity computed using Equation 5.22 (solid lines) and predictions from Equation 5.27 (dashed lines). The comparison is shown as a function of T at various R values. The magnitude (M) is 6.5 in (a) and 7.5 in (b).	102
5.12	Comparison of average directivity computed using Equation 5.22 (solid lines) and predictions from Equation 5.27 (dashed lines). The comparison is shown as a function of R at various M values. The period is 1 sec in (a) and 7.5 sec in (b).	103
5.13	Comparison of prediction from CBR and CBSB model when directivity parameters are unknown. The comparison is shown for a vertical strike-slip rupture of magnitude 6.5. The site is 1 km away from the rupture and the site has $V_{s30} = 760$ m/sec and $Z_{2.5} = 2$ km.	104
5.14	The three sites and fault rupture used for comparison of the CBSB model prediction.	106

5.15	Comparison of median prediction from the CBSB model when the epicenter location is unknown for the three sites shown in Figure 5.14 . Median spectra prediction from the CBR model is also shown for comparison.	107
5.16	Comparison of median prediction from the CBSB model when the epicenter location is known for the three sites shown in Figure 5.14. The epicenter is assumed to be located at the location of site C. Median spectra prediction from the CBR model is also shown for comparison.	108
5.17	Comparison of σ of residuals from the CBR, CBSB, and CBSB models with random/unknown T_p and $I_{directivity}$ as a function of R_{rup} for (a) $T = 0.2$ sec and (b) $T = 2$ sec. Published values of σ from Campbell and Bozorgnia (2008) are also shown for comparison.	110
6.1	Location of the eight sites where PSHA was performed. Sites 1 and 5 are 0 km away from the fault, 2 and 6 are 5 km away, 3 and 7 are 10 km away and sites 4 and 8 are 20 km away. The fault is 60 km long and 12 km wide vertical strike-slip fault. With earthquakes assumed to occur at a rate of 0.09 per year. Magnitudes from 5 to 7 were considered for the study and Gutenberg-Richter b parameter was assumed to be 0.91. Note that the source parameters were selected to represent Imperial fault as in Chapter 2.	114
6.2	$P(directivity Sa > x)$ conditioned on different $Sa(3s)$ levels for sites 1 to 4. The 2% in 50 years hazard is highlighted at each site by a circle and the 10% in 50 years hazard level is highlighted by a cross.	115
6.3	$P(directivity Sa > x)$ conditioned on different $Sa(3s)$ levels for sites 5 to 8. The 2% in 50 years hazard is highlighted at each site by a circle and the 10% in 50 years hazard level is highlighted by a cross.	116
6.4	The deaggregated probability that a directivity pulse caused exceedance of hazard is plotted as a function of period. Estimates of the deaggregated pulse probability from a full directivity PSHA and Equation 6.5 are compared for different hazard levels at (a) site 1, (b) site 2, (c) site 3, and (d) site 4.	119
6.5	T_p deaggregation at site 1, for Sa with 2% in 50 years exceedance probability. Results are for spectral acceleration periods (a) 3 sec and (b) 5 sec.	120

6.6	The deaggregated T_p distribution computed through deaggregation of a full directivity PSHA is shown for Sa with (a) 2% in 50 years exceedance probability and (c) 10% in 50 years exceedance probability. This can be compared with the approximate distribution computed using Equation 6.12 for Sa with (b) 2% in 50 years exceedance probability and (d) 10% in 50 years exceedance probability. This figure shows results for site 1 and spectral acceleration period (T) of 3 sec.	122
7.1	Displacement response trace ($T = 1$ sec) and spectral acceleration in all orientations (a) when ground motion is almost unpolarized (HWA031 recording from 1999 Chi-Chi-04 earthquake) and (b) when the ground motion is almost completely polarized (Gilroy Array#6 recording from 1984 Morgan Hill earthquake).	128
7.2	Histogram of observed ratios of $Sa_{RotD100}$ and Sa_{RotD50} in the NGA-West2 database for (a) $T = 0.2$ sec and (b) $T = 1$ sec.	129
7.3	Geometric mean of the observed ratio of $Sa_{RotD100}$ to Sa_{RotD50} estimated by mixed-effects regression using NGA-West2 database.	132
7.4	Comparison of various models for geometric mean $Sa_{RotD100}/Sa_{GMRot150}$ ratios.	134
7.5	Comparison of the geometric means of $Sa_{RotD100}/Sa_{RotD50}$ estimated using datasets with and without the 1999 M=7.6 Chi-Chi ground motions.	134
7.6	Prediction of $Sa_{RotD100}/Sa_{RotD50}$ by the distance dependent model in Equation 7.4 for $R = 5$ km, compared with the non-distance dependent estimates of $Sa_{RotD100}/Sa_{RotD50}$ given in Table 7.1 and the empirical geometric mean of $Sa_{RotD100}/Sa_{RotD50}$ ratio using only the data with closest distance between 2.5 to 7.5 km.	136
7.7	Probability density of α ($Sa_{RotD100}$ orientations) in different M , R_{rup} bins.	137
7.8	Probability density of α for sites with $R_{rup} < 5$ km, binned by period (sec).	138
7.9	Displacement response trace to the El Centro differential array recording from the 1979 Imperial Valley earthquake. The period of the SDOF oscillator is (a) $T^* = 1.5$ sec and (b) $T' = 3$ sec. The orientations of $Sa_{RotD100}$ along with the difference between these orientations at the two periods ($ \alpha^* - \alpha' $) is also shown.	139
7.10	Distribution of $ \alpha^* - \alpha' $ as predicted by the truncated exponential model is compared with the normalized histogram for (a) $T^* = 2$ sec and $T' = 0.1$ sec and (b) $T^* = 2$ sec and $T' = 1$ sec.	140
7.11	The geometric mean of $\frac{Sa_\phi}{Sa_{RotD50}}$ as a function of ϕ for different periods.	143
7.12	Comparison of the median predicted $Sa_{RotD100}$ and Sa_{RotD50} spectra with spectra conditioned in strike-normal and strike-parallel orientations. All results are for an earthquake with magnitude 7, at distance of 2.5 km and $V_{s30} = 760$ m/sec.	145

7.13 Comparison of the $Sa_{RotD100}$ and Sa_{RotD50} spectra with spectra conditioned on $Sa_{RotD100}$ orientation at $T^* = 1$ sec and $T^* = 3$ sec. All results are for an earthquake with magnitude 7, at distance of 2.5 km and $V_{s30} = 760$ m/sec. 146

1 Introduction

1.1 MOTIVATION

Growth of major population centers near seismically active faults (e.g., major cities in California like Los Angeles and San Francisco, Japanese cities like Tokyo and Osaka) has significantly increased the probability of a large earthquake striking close to a big city in the near future. The statement by Hall et al. (1995) that, “Occurrence of large earthquakes close to cities in California is inevitable,” is true for many large cities around the world. This along with the fact that near-fault ground motions are known to impose larger demands on structures than ground motion far from the fault and have caused extensive damage in past earthquakes (e.g., Bertero et al., 1978; Anderson and Bertero, 1987; Hall et al., 1995; Iwan, 1997; Alavi and Krawinkler, 2001; Menun and Fu, 2002; Makris and Black, 2004; Mavroeidis et al., 2004; Akkar et al., 2005; Luco and Cornell, 2007), makes the quantitative study of near-fault seismic hazard and risk important.

Quantitative seismic risk assessment is a complex, multidisciplinary problem that involves knowledge about fault-rupture process and propagation of seismic waves through earth (seismology), the effect of soil on seismic waves (geotechnical engineering), response of structures to earthquake ground motion excitation (structural engineering), evaluation of monetary losses from structural damage and business interruption (finance and economics), and properly accounting for uncertainty, which is present in almost all aspects of the computation (statistics). A formal process to compute the probability distribution of losses due to seismic events has been proposed by the Pacific Earthquake Engineering Research (PEER) Center (e.g., Cornell and Krawinkler, 2000; Deierlein, 2004). The PEER seismic risk assessment framework, described in detail below, simplifies the seismic risk computation by splitting the task into several modular stages. Probabilistic seismic hazard assessment (PSHA), is the first stage of the PEER framework.

Probabilistic seismic hazard assessment (e.g., Cornell, 1968; Kramer, 1996; McGuire, 2004) is used to compute the probability distribution of ground-motion intensity at the site of interest from a future earthquake. A PSHA computation uses a ground-motion model (e.g., Power et al., 2008; Bommer et al., 2009; Travararou et al., 2003) that predicts the conditional distribution of

ground-motion intensity at a site, given earthquake parameters such as magnitude, distance, soil condition, etc. To compute the marginal distribution of ground-motion intensity at the site, the ground-motion model prediction and the joint probability distribution of the earthquake parameters are combined using the law of total probability (e.g., Benjamin and Cornell, 1970). This calculation can be summarized by Equation 1.1 below.

$$P(IM > x) = \int_{M,R,\Theta} P(IM > x|M, R, \Theta)P(M, R, \Theta)dM \cdot dR \cdot d\Theta \quad (1.1)$$

where IM is the intensity measure, M represents the magnitude of the earthquake, R represents the distance between the site and the fault rupture, and Θ represents all other parameters used by the ground-motion model. $P(IM > x)$ is the probability that the intensity measure exceeds a value x in a future earthquake. Generally, hazard is described in terms of return periods or rate of exceedance (Cornell, 1968). The rate of exceedance of intensity measure (referred as λ_{IM}) can be computed by multiplying the probability of exceedance from an earthquake, given by Equation 1.1, with the rate of earthquakes in the region. The probability distribution of common intensity measures, like spectral acceleration (S_a), given M, R , etc., is generally assumed to be log-normal (Abrahamson, 1988; Jayaram and Baker, 2008). Thus, the $P(IM > x|M, R, \Theta)$ can be computed using the median and standard deviation of the intensity measure, which is predicted by the ground-motion model.

Ground-motion models use common predictor variables like magnitude, distance, fault-type, soil conditions, etc., to predict the distribution of ground-motion intensity. However, ground-motion intensity in near-fault regions depends on source-to-site geometry parameters (e.g., Somerville et al., 1997; Spudich and Chiou, 2008) which are not used in ground-motion models. For example, Figure 1.1 shows that the two highlighted sites have similar distance from the rupture (a parameter used in ground-motion model), while the length of rupture between the epicenter and the closest point on the rupture to the site (a parameter important for predicting directivity but not present in most ground-motion models) is much larger at the site where a directivity pulse is observed. Thus, most current ground-motion models fail to account for some near-fault effects. In this study, we developed a comprehensive framework to study near-fault ground motions and account for their effects in seismic hazard assessment and ground motion selection. We begin with a brief review of the PEER framework for seismic risk assessment and near-fault effects.

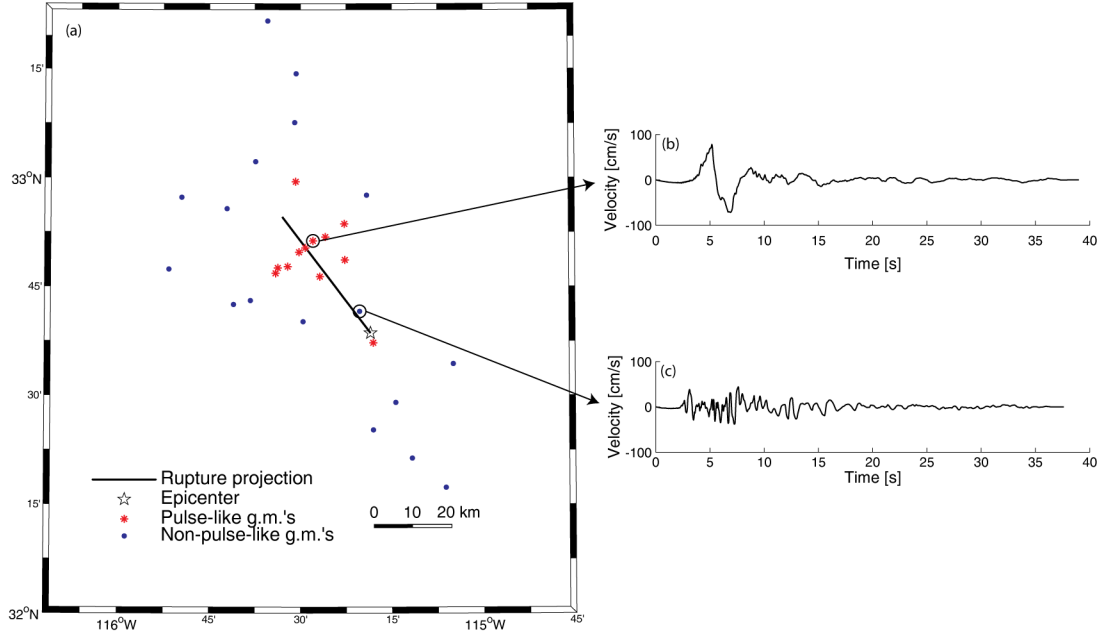


Figure 1.1 Map of Imperial Valley earthquake rupture with the location of sites where ground motion was recorded. Site (c) was close to the epicenter is the Bonds Corner station (NGA # 160) and no directivity pulse was observed here; however, a directivity pulse was observed at site (b) El Centro Array # 4 station (NGA # 179), which is located down the rupture at a similar distance as site (c) from the fault. The fault-normal component of the two ground motions is shown here.

1.1.1 PEER Seismic Risk Assessment Framework

Quantitative assessment of seismic risk involves accounting for various uncertainties, some of which are aleatoric or inherent to the earthquake process (e.g., time and location of rupture), and others are epistemic or present due to lack of knowledge (e.g., response of an existing structure from seismic excitation). Modeling the interaction between several random variables makes seismic risk assessment challenging. A formal process for quantitative seismic risk assessment was proposed by PEER (Cornell and Krawinkler, 2000; Moehle and Deierlein, 2004). The PEER framework computes the seismic risk at a site by evaluating the risk integral as shown in Equation 1.2 below:

$$\lambda_{DV} = \int \int \int G(DV|DM)dG(DM|EDP)dG(EDP|IM)d\lambda_{IM}. \quad (1.2)$$

where $G(\cdot)$ represents the inverse cumulative distribution (or probability of exceedance). The term DV is the decision variable under consideration (e.g., number of fatalities, direct monetary losses, indirect business losses due to downtime, etc.), and the integration shown in Equation 1.2 aims to compute the rate of exceedance of various levels of the chosen DV (λ_{DV}). A one-step Markovian assumption is made to make the computation tractable. It is assumed that the distribution of DV

depends only on the damage measure (DM), the distribution of DM depends only on the engineering demand parameter (EDP) and the distribution of the EDP depends only on the intensity measure (IM). Although the Markovian assumption may seem to limit the ability of models to incorporate more information, distributions can be conditioned on vector of values computed in previous steps to incorporate more information when needed. Vector valued intensity measures have been previously used in PSHA computations (e.g., Bazzurro and Cornell, 2002; Somerville and Thio, 2005), and vector intensity measures like S_a and ϵ (epsilon) are commonly used to improve the prediction of an EDP -given IM (Baker and Cornell, 2005, 2008b).

Along with making the computation tractable, the Markovian assumption in the PEER integral makes the computation modular. The computation is performed by chaining together different tasks, which are generally performed by different groups of experts. The first step is the seismic hazard assessment, which produces the distribution of an intensity measure expected in future at a site. The second step is to compute the distribution of an EDP for a given intensity (IM) level. The distribution of an EDP conditioned on an intensity is often computed by nonlinear dynamic analysis (e.g., Vamvatsikos and Cornell, 2002, 2004), using a set of ground motions representative of the hazard computed in the first step. Ground motion selection is the process of selecting this hazard consistent set of ground motions, and it is the intermediate step that links PSHA and structural analysis. Fragility functions are then used to compute the probability-distribution-of-being in different damage states (DM) for a given value of the EDP . Finally, loss functions are used to compute the distribution of the decision variable of choice for each damage state.

Near-fault effects change the properties of the earthquake ground motion and affect the intensity measure. Due to the common Markovian assumption as typically implemented, the computation of DM and DV distributions do not depend on the intensity measure. Thus, to compute the seismic risk at near-fault sites, one needs to account for the near-fault effects only during the computation of the distribution of the intensity measure and EDP . This report will focus on accounting for the effect of near-fault ground motions on seismic hazard assessment and ground motion selection.

1.1.2 Near-Fault Effects

Some of the important factors influencing the ground motion in near-fault region are directivity, directionality/polarization, and fling effects. This report focuses on directivity and directionality effects. Fling is a near-fault effect that results in large permanent ground displacement, mostly in the direction parallel to the fault. Fling effects are not studied herein, but are mentioned here for completeness.

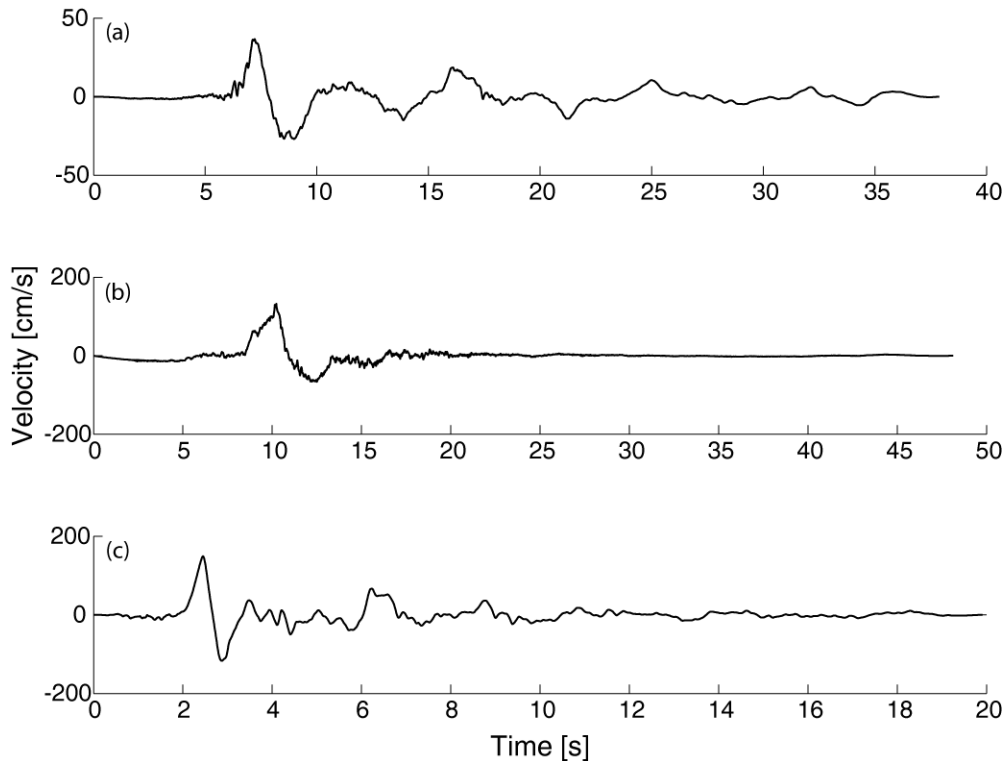


Figure 1.2 Some examples of ground-motion recordings with directivity pulse. (a) Brawley Airport station from the 1979 Imperial Valley earthquake (NGA # 161), (b) Lucerne station from the 1992 Landers earthquake (NGA # 879), and (c) Rinaldi station from 1994 Northridge earthquake (NGA # 1063).

Directivity Effects

Directivity effects are observed at a site when the fault ruptures towards the site at a speed close to the propagation velocity of the shear waves. When this condition is satisfied, a large portion of the energy from the rupture arrives at the site in a small time interval (Somerville et al., 1997). A large amount of energy arriving in a short time window can cause a distinct pulse in the velocity time history of the ground motion, as can be seen in Figures 1.1 and 1.2. These ground motions with a distinct velocity pulse are also known as pulse-like ground motions (e.g., Baker, 2007). The presence of the pulse amplifies traditional intensity measures like spectral acceleration (S_a) at periods close to the period of the pulse. Along with amplifying the ground-motion intensity, a pulse-like ground motion can cause larger or smaller inelastic response in structures when compared to non-pulse-like ground motions, depending on the period of the pulse (e.g., MacRae et al., 2001; Alavi and Krawinkler, 2004). Thus, presence of a directivity pulse changes the distribution of the intensity measure and that of the *EDP*-given *IM*.

Occurrence of directivity effects depends on source-to-site geometry parameters. e.g., the amount of rupture between the epicenter and the site. Many source-to-site geometry parameters,

which are important predictors of directivity effects, are not used by ground-motion models. Thus, the ground-motion models do not account for directivity effects in their intensity prediction. Several researchers have proposed modifications to ground-motion models to account for the potential presence of directivity effects (e.g., Somerville et al., 1997; Abrahamson, 2000; Spudich and Chiou, 2008). These models generally use source-to-site geometry parameters that are important in predicting directivity effects but are not used in conventional ground-motion models. The directivity model is then fitted using residuals from a ground-motion model to predict the amplification/de-amplification due to directivity effects relative to the original ground-motion model prediction. Somerville (2003) classified the directivity correction models into narrowband models and broadband models. Narrowband models amplify the response spectra predicted by the ground-motion model in a small range of periods around the period of the pulse, which is a function of magnitude of the earthquake (e.g., Somerville, 2003; Mavroeidis and Papageorgiou, 2003; Bray and Rodriguez-Marek, 2004; Baker, 2007), while the broadband models (e.g., Somerville et al., 1997; Abrahamson, 2000; Spudich and Chiou, 2008) amplify a larger range of periods. Somerville (2003) reports, however, that recorded ground motions with directivity pulses show narrowband amplification of response spectra. Also, the process of fitting directivity models using residuals from a ground-motion model has some flaws. As directivity effects are primarily observed close to the fault, the directivity amplification and the distance scaling term of the ground-motion model are closely coupled. The directivity models fitted using residuals from ground-motion models cannot separate the effect of distance and directivity properly.

In this study, we have developed a narrowband model for directivity amplification, along with other models needed to include directivity effects in seismic hazard computation. A method to include directivity effects explicitly in ground-motion models is also proposed, which results in more consistent ground-motion models than correcting for directivity effects after the fact.

Directionality of Ground-Motion Intensity

Structures designed to resist seismic loads are generally designed considering the ground motion in horizontal plane. The intensity measure commonly used for design, however, is pseudo spectral acceleration, which for lightly damped single-degree-of-freedom (SDOF) systems are approximately the same as the peak response of the SDOF system when excited by a single component of ground motion. Several intensity measures have been proposed to represent the two-dimensional intensity of ground motion in the horizontal plane. An early example of such an intensity measure is Sa_{GM} , the geometric mean of spectral acceleration (with a specified period and damping) from two orthogonal components of the ground motion. Generally, the two as-recorded components of

the ground motion, or ground motion in fault-normal and fault-parallel orientations, are used for computation. The Sa_{GM} intensity depends on the orientations used for computation, which are often arbitrarily chosen. To remove the dependence on arbitrarily chosen orientations, orientation independent intensity measures like $Sa_{GMRotInn}$, $Sa_{GMRotDnn}$, Sa_{RotInn} and Sa_{RotDnn} have been proposed (Boore et al., 2006; Boore, 2010). These intensity measures will be defined and discussed in more detail in Chapter 7.

In general, a one-dimensional intensity measure will only be able to capture a part of the two-dimensional nature of ground-motion intensity. Thus, different definitions of the intensity measure may capture different aspects of the ground motion and may be appropriate for different tasks. For example, some structural engineers prefer using the maximum intensity in any orientation ($Sa_{RotD100}$) for design (e.g., NEHRP, 2009), while the ground-motion modelers prefer to use the median intensity over all orientations (Sa_{RotD50}) (Bozorgnia et al., 2012). Hence, the hazard analysis stage will use Sa_{RotD50} as the intensity measure and the structural analysis stage (computation of $G(EDP|IM)$) will use $Sa_{RotD100}$ as the intensity measure. Equation 1.2 is mathematically valid only when a consistent definition of intensity measure is used throughout (Baker and Cornell, 2006; Beyer and Bommer, 2006). Thus, models are needed to convert one intensity measure to another to allow correct computation of the integration in Equation 1.2, while allowing the ground-motion modelers and structural engineers to use their preferred intensity measure.

Polarization or directionality of ground-motions have long been known (e.g., Kubo and Penzien, 1979), and several past studies have proposed models for ratios of different intensity measures, which can be used as multiplicative factors to convert between them (e.g., Beyer and Bommer, 2006; Watson-Lamprey and Boore, 2007; Huang et al., 2008, 2010). But these studies focused on ratios involving $Sa_{GmRotI50}$ intensity, which was used to develop the older Next Generation Attenuation (NGA) ground-motion models (Abrahamson et al., 2008). This study used the NGA-West2 database (Ancheta et al., 2012) to study the ratio of $Sa_{RotD100}$ with Sa_{RotD50} , and propose models to convert between the two. The NGA-West2 database has more ground-motion records than previous databases used for similar studies, which allows for careful study of orientations in which $Sa_{RotD100}$ are observed. The models developed herein allow us to compute response spectra that are expected to be observed in a single orientation (e.g., fault-normal orientation of $Sa_{RotD100}$ at a period), which can be more realistic target spectra than assuming occurrence of $Sa_{RotD100}$ in a single orientation at all periods.

1.2 AREAS OF CONTRIBUTION

This study highlights several challenges associated with accounting for the near-fault effects in seismic risk assessment. The major contributions of this study are summarized below.

1.2.1 Comprehensive Framework to Account for Directivity Effects in Hazard Assessment and Ground-Motion Selection

As explained above, most ground-motion models used in PSHA computations do not account for directivity effects. Previous studies have proposed methods to account for directivity effects in PSHA computations (e.g., Abrahamson, 2000), but they use broadband directivity models. Development of a narrow band directivity model is challenging as pulses are not observed at all sites satisfying source-to-site geometry conditions favorable for directivity effects, and the period of the pulse around which Sa is amplified is different at different sites. Due to these uncertainties, the narrow band amplification is “smeared out” when pulses with different periods and both pulse-like and non-pulse-like ground motions are pooled together to fit directivity models (Tothong et al., 2007).

The framework proposed herein accounts for the uncertainty in pulse observation and in the period of the pulse. The framework has been designed to be modular, with separate models to predict the probability of observing a pulse at a site, the probability distribution of the period of the observed pulse, and a narrow band correction for ground-motion models conditioned on the period of the pulse. An algorithm to use these models to compute the seismic hazard at the site is also proposed. The proposed framework extends the approach proposed by Tothong et al. (2007) and uses data-constrained models for all calculations rather than hypothetical models. The modular design of the framework allows hazard deaggregation conditioned on several important directivity parameters, e.g., the period of the pulse and the probability of pulse observation. This deaggregation information with respect to pulse period and probability of occurrence can be used to select sets of ground motions that have appropriate fractions of pulse-like ground motions and that represent the deaggregated distribution of pulse periods. A hazard consistent ground motion set can then be used to compute the distribution of the EDP at different intensity levels by using nonlinear dynamic analysis. Thus, the framework and models presented herein allow a consistent method to account for near-fault directivity effects while using the PEER risk assessment framework.

1.2.2 Efficient Identification of Pulses in Multi-Component Ground Motions

An empirical study of pulse-like ground motions needs a database of recorded ground motions with each record classified as pulse-like or non-pulse-like. Early researchers used small databases of ground motions with individual ground motions manually classified as pulse or non-pulse (e.g., Mavroeidis and Papageorgiou, 2003; Fu and Menun, 2004; Akkar et al., 2005). Manual classification of ground motions as pulse-like is labor intensive, slow, and has the possibility to introduce subjectivity into the classifications. To address these problems, Baker (2007) proposed an automated algorithm to identify pulse-like ground motions using wavelet transforms. The Baker (2007) algorithm uses the fault-normal component of ground motion for classification. Though directivity effects are expected to produce a pulse in the fault-normal orientation, pulses are often found in other orientations too (e.g., Howard et al., 2005). Also, due to complex geometry of a real fault, the computed fault-normal orientation is generally an approximation of the real fault-normal orientation. Thus, the velocity pulse can be present in orientations other than the computed fault-normal orientation. In some cases—due to the absence of finite-fault models—identification of fault-normal orientation is not possible. The major challenge in this field is to find an efficient algorithm to classify pulses in arbitrary orientations.

Chapter 2 uses the Baker (2007) algorithm to classify the ground motions in 180 horizontal orientations. This overcomes the aforementioned problems but adds considerable computational cost. Continuous wavelet transforms are computationally expensive, and the method described in Chapter 2 repeats this computation many times, making it significantly slower than the Baker (2007) algorithm. With rapidly increasing size of ground-motion datasets, the main challenge is to develop computationally efficient classification methods that scale well with larger databases.

Chapter 4 proposes an efficient algorithm to classify multicomponent ground motions as pulse-like and non-pulse-like. The proposed algorithm uses the continuous wavelet transform of two orthogonal components of the ground motion to compute the maximum possible wavelet coefficient at each scale and location over all possible orientations. The orientations in which this maximum is attained at each scale and location are also computed. This information is used to identify potential pulses, which may lie in arbitrary orientations. These potential pulses are then examined to classify the ground motion as pulse-like and non-pulse-like. The algorithm proposed in Chapter 4 was used to classify 8611 ground motions in the NGA-West2 database and found 244 pulse-like ground motions.

1.2.3 Explicit Inclusion of Directivity Effects in a Ground-Motion Model

Directivity effects are observed at near-fault sites, and it is known that the probability of observing a directivity pulse depends on the distance between the rupture and the site (e.g., Iervolino and Cornell, 2008). Along with dependence on distance, the amplification in S_a due to directivity effects occurs in a band of periods close to the period of the pulse, which depends on earthquake magnitude (e.g., Somerville, 2003). The interaction between directivity amplification, distance, and magnitude may affect the magnitude and distance scaling terms in ground-motion models if directivity terms are included explicitly. Thus, inclusion of directivity effects may lead to changes in non-directivity predictions as well. This cannot be captured by the directivity models fitted using ground-motion model residuals. To properly isolate directivity amplification, the original ground-motion model needs to be fitted with directivity terms in the functional form.

A method is proposed to include directivity parameters in ground-motion models. As directivity effects are modeled by parameters that are not commonly used in practice, these parameters may not be available for some studies (e.g., legacy software may not allow the use of new parameters). We propose to use the conditional expectation given the values of the known parameters as a prediction of ground-motion intensity. This method allows making unbiased prediction of ground-motion intensity, even when the directivity parameters are unknown. We computed the average directivity amplification conditioned on a smaller set of parameters, e.g., magnitude, distance, and spectral acceleration period. This information was used to predict the expected value of directivity amplification conditioned on different levels of information. Predictive models are also proposed to predict the average directivity without any integration. An example ground-motion model with directivity terms was fitted, and several examples showing computation of ground-motion intensity when different directivity parameters were unknown are presented.

1.2.4 Comprehensive Study of Ground-Motion Directionality

The NEHRP (2009) provisions recommend using $S_{a_{RotD100}}$ response spectra for seismic design. The $S_{a_{RotD100}}$ intensity at each period may occur in different orientations, but the NEHRP provisions treat the $S_{a_{RotD100}}$ response spectrum as if it is associated with a ground motion in a single orientation. Thus, using $S_{a_{RotD100}}$ response spectrum to predict $EDPs$ dependent on multiple periods may lead to conservative estimates (Stewart et al., 2011).

Conditional spectra can be used to compute more realistic target spectra (e.g., Abrahamson and Al Atik, 2010; Baker, 2011; Lin et al., 2012a,b). Following the approach used to develop the directivity models proposed herein, we developed a modular framework to characterize ground motion

directionality. Different models are proposed to predict the ratios of $Sa_{RotD100}$ and Sa_{RotD50} , predict the probability distribution of orientations in which the $Sa_{RotD100}$ are observed, and model the relationship between the $Sa_{RotD100}$ orientations at different periods. These models are then combined to compute several types of target spectra conditioned on different parameters.

1.3 ORGANIZATION

Several issues related to accounting for near-fault effects, mainly directivity and directionality, in seismic risk assessment are presented. Chapters 2 to 6 focuses on directivity effects, while Chapter 7 studies directionality in ground motions. Chapter 2 introduces the probabilistic framework to account for the effects of directivity pulses in seismic hazard assessment. Chapter 3 describes statistical models for calibrating inputs to the proposed framework of Chapter 2. Chapter 4 introduces an efficient algorithm to classify ground motions as pulse-like and non-pulse-like. The classified pulses from Chapter 4 are used in Chapter 5 to fit a ground-motion model with explicit directivity terms. Chapter 6 explores hazard deaggregation at multiple example sites and proposes some guidelines for ground motion selection in near-fault regions.

Chapter 2 proposes a probabilistic framework to account for the effects of near-fault directivity in PSHA. A brute force method to classify pulse-like ground motions in arbitrary orientations is discussed and used to classify each ground motion in the NGA database (Chiou et al., 2008) as pulse-like or non-pulse-like. These classifications are used to develop initial models to predict the probability of pulse occurrence at a site, probability distribution of the orientations relative to the strike of the fault in which the pulses are observed, and the probability distribution of the period of the pulse. An algorithm to combine these models to account for directivity effects in PSHA is also presented.

Chapter 3 discusses the models to predict the probability of a pulse occurrence and the period of the pulse used in the framework proposed in Chapter 2. The considerations behind the choice of the functional forms and model parameters for these models are explained in detail. Several mixed-effects models for predicting the period of the pulse are explored, and the statistical and practical significance of the selected model parameters are discussed.

Chapter 4 proposes an efficient algorithm to classify multi-component ground motions as pulse-like or non-pulse-like. The proposed algorithm is orientation independent and significantly speeds up the initial method used in Chapter 2 to identify ground motions with pulses in arbitrary orientations. Coefficients from continuous wavelet transform are used to develop a classification criterion using support vector machines. The algorithm is then used to classify each ground motion in the NGA-West2 database as pulse-like or non-pulse-like.

Chapter 5 presents a method to fit a ground-motion model with explicit directivity terms. A simplified form of the amplification model developed in Chapter 2, along with the functional form of Campbell and Bozorgnia (2008) is used as the functional form for the ground-motion model with directivity effects. Mixed effects regression is used to fit this model using the NGA-West2 database. The differences between ground-motion models with and without directivity effects are studied in detail, and a method to compute unbiased ground-motion intensity prediction when directivity parameters are unknown is also presented.

Chapter 6 focuses on deaggregation of PSHA results to compute the on probability of pulse occurrence and period of the pulse given occurrence of a ground motion with a specified Sa value. Change in the deaggregation results with change in source-to-site geometry is studied, and guidelines for selection of ground motion in near-fault regions are discussed.

Chapter 7 studies ground motion directionality in detail. Models for the ratio of $Sa_{RotD100}$ to Sa_{RotD50} are presented. These models can be coupled with NGA-West2 ground-motion models that predict Sa_{RotD50} (median Sa over all orientations), to get predictions for $Sa_{RotD100}$ intensity (maximum Sa over all orientations). The orientation of $Sa_{RotD100}$ is studied, and some alternate target spectra for engineering analysis are proposed.

Finally, **Chapter 8** summarizes the important contributions of this report and discusses potential future extensions of this research.

2 An Empirically Calibrated Framework for Including the Effects of Near-Fault Directivity in Probabilistic Seismic Hazard Analysis

2.1 INTRODUCTION

Ground motions with a pulse at the beginning of the velocity time history belong to a special class of ground motion that causes severe damage in structures. This type of ground motion, referred herein as a “pulse-like” ground motion, is typically observed at sites located near the fault and is believed to be caused primarily by forward directivity effects (Somerville et al., 1997; Somerville, 2003, 2005; Spudich and Chiou, 2008). Pulse-like ground motions place extreme demands on structures and are known to have caused extensive damage in previous earthquakes (e.g., Housner and Hudson, 1958; Bertero et al., 1978; Anderson and Bertero, 1987; Hall et al., 1995; Iwan, 1997; Alavi and Krawinkler, 2001; Menun and Fu, 2002; Makris and Black, 2004; Mavroeidis et al., 2004; Akkar et al., 2005; Luco and Cornell, 2007). Traditional ground-motion models used in PSHA (e.g., Kramer, 1996; McGuire, 2004) do not account for the effects of pulse-like ground motions and may therefore under-predict the seismic hazard at near-fault sites where pulse-like ground motions are expected. In order to correctly assess the seismic hazard at near-fault sites, it is important to model the effects of pulse-like ground motion and incorporate these effects in hazard calculations. Another near-fault effect called the “fling step” causes permanent ground displacement; it is mentioned for completeness but is not considered herein.

Few attempts have been made in the past to incorporate the effect of near-fault pulses in seismic hazard assessment. These past efforts have tried to model the amplification of response spectra due to pulse-like motion either by monotonically increasing or decreasing the spectral ordinates over a range of periods (e.g., Somerville et al., 1997; Abrahamson, 2000) or by amplifying the response spectra in a narrow range of periods close to the period of pulse (T_p) (e.g., Somerville, 2005; Tothong et al., 2007). The former models are sometimes referred to as “broad-band” models, the latter as “narrow-band” models. The framework proposed here extends the approach proposed by

Tothong et al. (2007) and uses data-constrained models for all calculations rather than the hypothetical models used in some cases. The proposed framework also allows for computation of PSHA results for arbitrary orientations relative to surrounding faults. The model proposed here can be categorized as a narrow-band model, as the spectral acceleration is amplified in a narrow range of periods centered about the period of the pulse, but no assumptions about the level of amplification or the range of periods to be amplified were made beforehand. Instead the model was calibrated purely empirically. A modified version of the algorithm suggested by Baker (2007) is used here to classify pulse-like ground motions. The modified algorithm rotates the ground motion and identifies pulses in all orientations rather than only in the fault-normal direction. This modification allows identification of velocity pulses in arbitrary orientations, which are then used to calibrate the needed predictive models.

The complete framework includes models for predicting the probability of pulse occurrence for a given source-site geometry, the probability of observing a pulse in a particular orientation given a pulse is observed at the site, the distribution of period of the pulse, the amplification of the response spectra due to the presence of the pulse, and the deamplification of response spectra due to absence of pulse in near-fault ground motion. Example calculations are included, which suggest some of the ways in which the framework proposed here can be used.

2.2 IDENTIFICATION OF PULSE-LIKE GROUND MOTIONS

In order to complete a probabilistic study of pulse-like ground motions, a library of ground motions is needed, with each ground motion classified as pulse-like or non-pulse-like. Many researchers have developed libraries of pulse-like ground motions by classifying ground motions using visual or quantitative techniques (e.g., Mavroeidis and Papageorgiou, 2003; Somerville, 2003; Fu and Menun, 2004; Akkar et al., 2005). These documents do not provide non-pulse-like ground motions, preventing analysts from determining the likelihood of pulse occurrence.

We prefer to use the pulse classification algorithm suggested in Baker (2007); it is a completely quantitative method and allows classification of a large dataset like the NGA database (Chiou et al., 2008) without human intervention. The Baker (2007) algorithm uses wavelet analysis to extract the pulse-like feature from the velocity time history of the fault-normal component of the ground motion. The extracted pulse-like feature is then analyzed and is used to classify the ground motion as pulse-like or non-pulse-like. Although classification of some records into binary criteria of pulse-like and non-pulse-like is difficult, this algorithm is generally effective at providing defensible classifications. Figure 2.1 graphically illustrates the algorithm results.

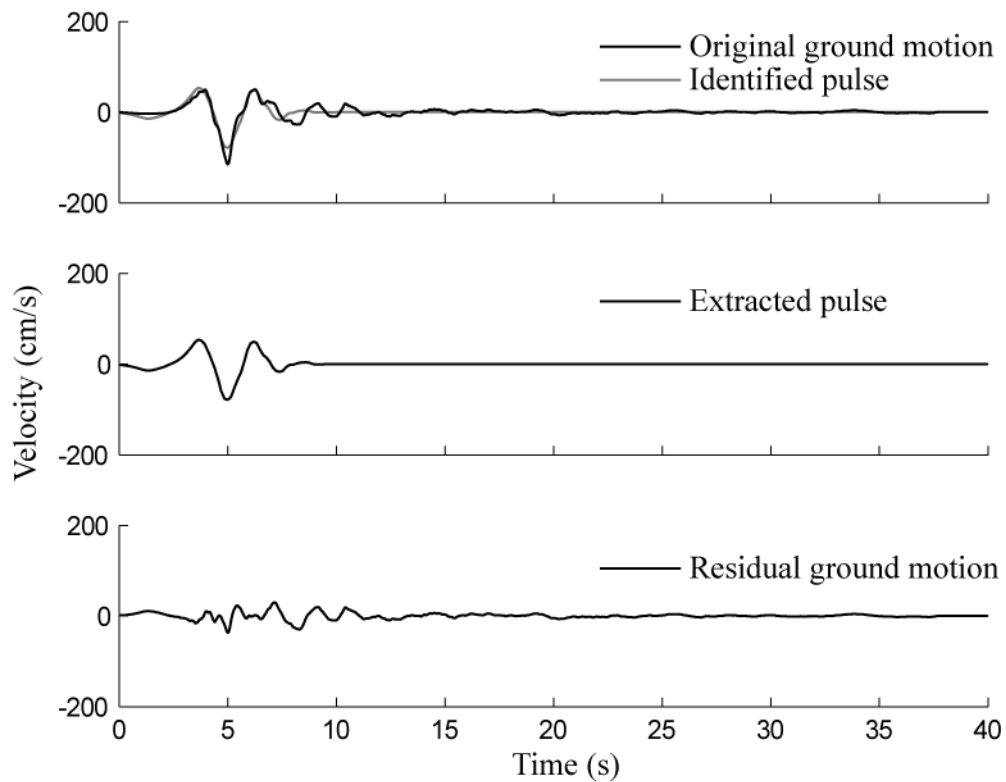


Figure 2.1 Illustration of the procedure used by Baker (2007)'s algorithm to extract the largest pulse from a velocity time history (1979 Imperial Valley, EC Meloland Overpass recording). Here, the pulse is large and the ground motion is classified as pulse-like.

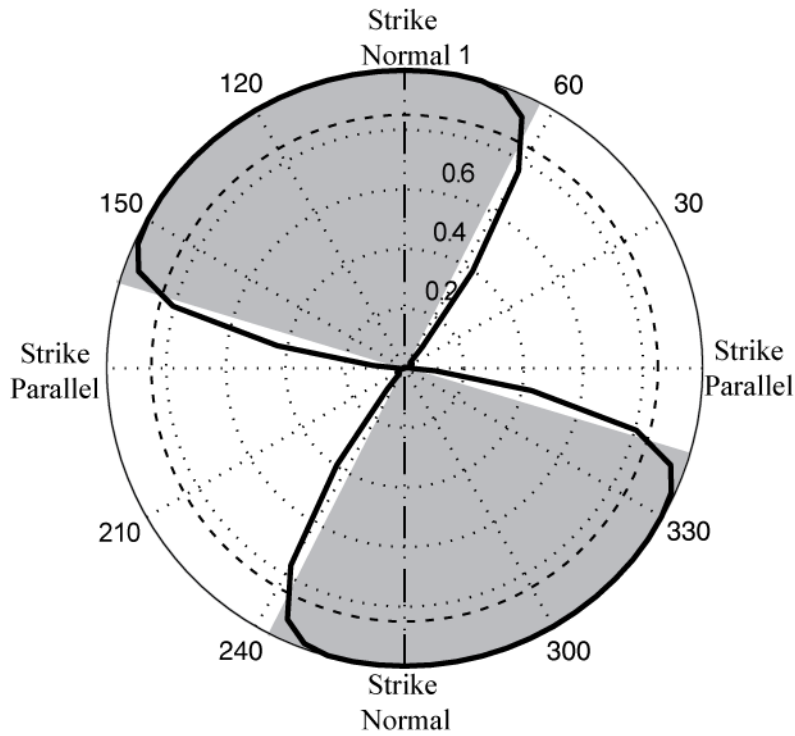


Figure 2.2 Pulse indicator values as a function of orientation for the 1979 Imperial Valley, EC County Center recording. Shaded orientations indicate orientations in which a strong pulse is apparent. See Baker (2007) for more information on how the pulse indicator is calculated.

Although velocity pulses caused by directivity effects are expected to be found in the fault-normal component of the ground motion (Somerville et al., 1997), many fault ruptures have irregular geometry, which makes determination of exact fault-normal direction difficult. Pulse-like ground motions are also observed in a range of orientations (e.g., Howard et al., 2005). To illustrate, Figure 2.2 shows the pulse indicator score as computed by the Baker (2007) algorithm at a site in different orientations (pulse-like ground motions have high pulse indicator values). The pulse indicator scores in Figure 2.2 show that pulse-like ground motions occurred in a range of orientations. The case illustrated in Figure 2.2 is a simple case where pulses are observed around the strike-normal orientation. More complex cases exist where the strike normal orientation does not lie in the range of orientation in which pulses were observed, but these cases are small in number.

In order to study the orientations in which pulse-like ground motions are observed, the ground motions were rotated in all possible orientations, and the ground motion in each orientation was classified as pulse-like or non-pulse-like. A site was then deemed to have experienced a pulse-like ground motion if the ground motion in any orientation at the site was classified as pulse-like. This scheme of rotating and classifying ground motions in every orientation led to the identification of

179 recordings in the NGA database that experienced pulse-like ground motion. For a list of these 179 recordings, see Table A.1 in Appendix A. This classification scheme identifies pulses in the horizontal directions only and may not classify some pulse-like ground motions when the pulse lies out of the horizontal plane. The fault-normal orientation may not lie in the horizontal plane for some non-strike-slip faults, and thus the non-strike-slip models developed herein should only be used when out of horizontal plane pulses are not important.

The previous study by Baker (2007), which studied only fault-normal ground motions, identified 91 pulse-like ground motions from the same database used here. Most of the additional pulse-like ground motions identified here were found to have a visual pulse-like feature in the strike-normal direction. These were not classified as pulse-like in the previous study by Baker (2007) because the pulse-like feature in strike-normal direction narrowly missed the thresholds used for classification. The presence of a visual pulse in the velocity time history of the strike-normal direction of most of the ground motions we classified as pulse-like suggests that directivity effects may be the chief cause of the pulse-like feature in these ground motions.

2.3 DEVELOPMENT OF INPUT MODELS FOR MODIFIED PSHA

The conventional PSHA equation shown in Equation 2.1

$$\nu_{S_a}(x) = \sum_{i=1}^{\#faults} \nu_i \iint P(S_a > x|m, r) \cdot f_i(m, r) \cdot dm \cdot dr \quad (2.1)$$

is used to find the annual rate by which S_a (the associated period T is omitted from the notation here for brevity) at the site exceeds a value x (for more details see, e.g., Kramer, 1996; McGuire, 2004). The term $P(S_a > x|m, r)$ provides the probability that S_a at a given period exceeds a value of x given the occurrence of an earthquake of magnitude m at distance r , which can be calculated using any ground-motion model. This probability, when multiplied by $f_i(m, r)$, the probability density of occurrence of such an earthquake (of magnitude m and distance r) on a particular fault i , and integrated over all possible m and r values, gives the probability of exceedance given an earthquake on a single fault. The total exceedance rate at a site can then be found by multiplying this probability by the rate of occurrence of earthquakes on the fault, ν_i , and summing over each fault in the vicinity of the site. Note that the probability $P(S_a > x|m, r)$ is obtained using a ground-motion model that is generally also a function of parameters such as rupture mechanism, site conditions, etc., other than magnitude and distance, but those parameters are omitted from the notation here for brevity.

The effects of pulse-like ground motion can be included in hazard analysis by using a modified ground-motion model that accounts for the amplification effect of directivity pulses on S_a values. Since directivity effects depend mainly on source-site geometry (Somerville et al., 1997), the ground-motion model accounting for pulses needs to be a function of source-site geometry along with magnitude and distance. So a modified ground-motion model that accounts for pulse-like ground motions can be used to calculate the probability of exceedance, $P^*(S_a > x|m, r, z)$ (where z represents the source-to-site geometry information in addition to r). This new probability of exceedance, $P^*(S_a > x|m, r, z)$, when used in the PSHA equation, can give the rate of exceedance of S_a at the site after accounting for effects of pulse-like ground motions.

Equation 2.2 shows how directivity effects can be accounted for in a PSHA calculation :

$$\nu_{S_a}(x) = \sum_{i=1}^{\#faults} \nu_i \iiint P^*(S_a > x|m, r, z) \cdot f_i(m, r, z) \cdot dm \cdot dr \cdot dz. \quad (2.2)$$

Note that this equation is derived from the equation proposed by Tothong et al. (2007) and additional details can be found there.

The presence of a pulse-like feature in the ground motion amplifies the response spectrum for a range of periods, as can be seen in Figure 2.3. This amplification of response significantly raises the probability of exceeding a particular S_a level when pulse-like ground motion occurs at a site. Therefore, the PSHA equation proposed here (Equation 2.2) can be practically evaluated by splitting $P^*(S_a > x|m, r, z)$ into two cases, depending on whether or not pulse-like ground motion is observed. These two cases can then be combined to calculate the overall exceedance rate, as explained below.

The current ground-motion models are fitted empirically using both pulse-like and non-pulse-like ground motions from a ground-motion database. In the near-fault region, where pulses are mostly observed, the ground-motion models may under-predict the pulse-like ground motion and over-predict the non-pulse-like ground motion. When a pulse is observed a prediction of S_a exceedance can be obtained from Equation 2.3

$$P(S_a > x|m, r, z, \text{pulse}) = 1 - \Phi\left(\frac{\ln(x) - \mu_{\ln S_a, \text{pulse}}}{\sigma_{\ln S_a, \text{pulse}}}\right), \quad (2.3)$$

where the pulse-like ground motions have mean $\mu_{\ln S_a, \text{pulse}}$ and standard deviation $\sigma_{\ln S_a, \text{pulse}}$. Note that $\mu_{\ln S_a, \text{pulse}}$ and $\sigma_{\ln S_a, \text{pulse}}$ are functions of m , r , and T_p , etc., but that dependence has again been omitted for brevity.

In the second case, when no pulse is observed, a modified ground-motion model after correcting for the over-prediction can be used to compute the probability of S_a exceeding x :

$$P(S_a > x|m, r, \text{no pulse}) = 1 - \Phi\left(\frac{\ln(x) - \mu_{\ln S_a, \text{no pulse}}}{\sigma_{\ln S_a, \text{no pulse}}}\right), \quad (2.4)$$

where the mean value $\mu_{\ln S_a, \text{no pulse}}$ and standard deviation $\sigma_{\ln S_a, \text{no pulse}}$ can be estimated using a modified ground-motion model for non-pulse-like ground motions. In both equations 2.3 and 2.4 $\Phi()$ represents the standard normal cumulative distribution function. A normal distribution of residuals was assumed, and histograms of the residuals from the model presented in this paper are consistent with that assumption.

These two cases (i.e., Equations 2.3 and 2.4) can be combined using the total probability theorem (e.g., Benjamin and Cornell, 1970) to get the overall probability of S_a exceeding x at a site:

$$\begin{aligned} P^*(S_a > x|m, r, z) &= P(\text{pulse}|m, r, z) \cdot P(S_a > x|m, r, z, \text{pulse}) \\ &+ (1 - P(\text{pulse}|m, r, z)) \cdot P(S_a > x|m, r, \text{no pulse}). \end{aligned} \quad (2.5)$$

The following sections will now present empirically calibrated models for the terms required in Equations 2.2 to 2.5.

2.3.1 Probability of Observing a Pulse

As seen in Equation 2.5, the probability of observing a pulse-like ground motion at a site is needed for the proposed PSHA calculation. We used a logistic regression model for predicting the probability of pulse occurrence given the source-site geometry. Logistic regression is a generalized linear model used for fitting binomial data (e.g., Kutner et al., 2004).

It has been well established that the forward directivity effect, which is believed to be a cause of pulse-like ground motions, depends on the source-to-site geometry (Somerville et al., 1997). Iervolino and Cornell (2008) showed that the parameters r , s , θ for strike-slip faults and r , d , and ϕ for non-strike-slip faults have better predictive power than other parameters when used in logistic regression to compute the probability of pulse occurrence. Where r represents the closest distance between the site and the rupture, s (d) represents the length of rupture between epicenter (hypocenter) and the point on the rupture closest to the site, and θ (ϕ) represents the angle between the strike (dip) of the fault and the line joining the epicenter (hypocenter) and the site, as shown graphically in Figure 2.4. We used the same parameters selected by Iervolino and Cornell (2008) to fit the logistic regression using information from all the sites in the NGA database. Refitting of the model was required since the Iervolino and Cornell (2008) model only predicts the probability of observing pulses in the fault-normal direction, and we needed a model to predict pulses in any

orientation. We found that only r and s were statistically significant predictors in the case of strike-slip earthquakes, whereas r , d , and ϕ were statistically significant in the non-strike-slip case. The result of the logistic regression is summarized by Equations 2.6 and 2.7

$$P(\text{pulse}|r, s) = \frac{1}{1 + e^{(0.642+0.167 \cdot r - 0.075 \cdot s)}} \quad \text{for strike-slip} \quad (2.6)$$

$$P(\text{pulse}|r, d, \phi) = \frac{1}{1 + e^{(0.128+0.055 \cdot r - 0.061 \cdot d + 0.036 \cdot \phi)}} \quad \text{for non-strike-slip.} \quad (2.7)$$

Here the units of r , d , and s are kilometers and ϕ is degrees. The dataset used for fitting contained r ranges from 0.3 km to 255 km in the case of non-strike-slip ruptures and 0.07 km to 472 km in the case of strike-slip ruptures, d ranges from 0 km to 70 km, ϕ ranges from 0 to 90 degrees, and s ranges from 0.3 km to 143 km.

A contour map of these predicted probabilities for a strike-slip fault is shown in Figure 2.5a and for a non-strike-slip fault in Figure 2.6a. Contours in the maps show the probability of pulse occurrence as predicted around the rupture geometries associated with the Imperial Valley earthquake and Northridge earthquake. These maps can be compared with the actual maps of sites where pulse-like ground motions were observed during the Imperial Valley earthquake, shown in Figure 2.5b and the Northridge earthquake, shown in Figure 2.6b. The model predicts high probability of pulses in regions where directivity effects were observed, and the shape of the contours also appears to be consistent with actual observations.

2.3.2 Pulse Orientation

Rotating and classifying ground motions led to identification of pulse-like ground motions in a range of orientations. To calculate hazard for a site with nearby faults at multiple orientations, one must know the probability of observing a pulse-like ground motion in an arbitrary direction. The data from rotated pulse classifications was used to determine the probability of finding a pulse in a direction (α) given that a pulse is observed at the site, i.e., $P(\text{pulse at } \alpha | \text{pulse})$. The angle α represents the smallest angle measured with respect to strike of the fault (strike values were taken from the NGA database). Figure 2.4a shows a schematic diagram illustrating α . We found that $P(\text{pulse at } \alpha | \text{pulse})$ was different for strike-slip and non-strike-slip faults.

Figure 2.7 shows the fraction of pulse-like motions containing a pulse in orientation α for strike-slip and non-strike-slip faults. The figure also shows the model that was fitted by minimizing squared errors between observation and prediction. The model is given in Equations 2.8 and 2.9 for strike-slip and non-strike-slip faults, respectively:

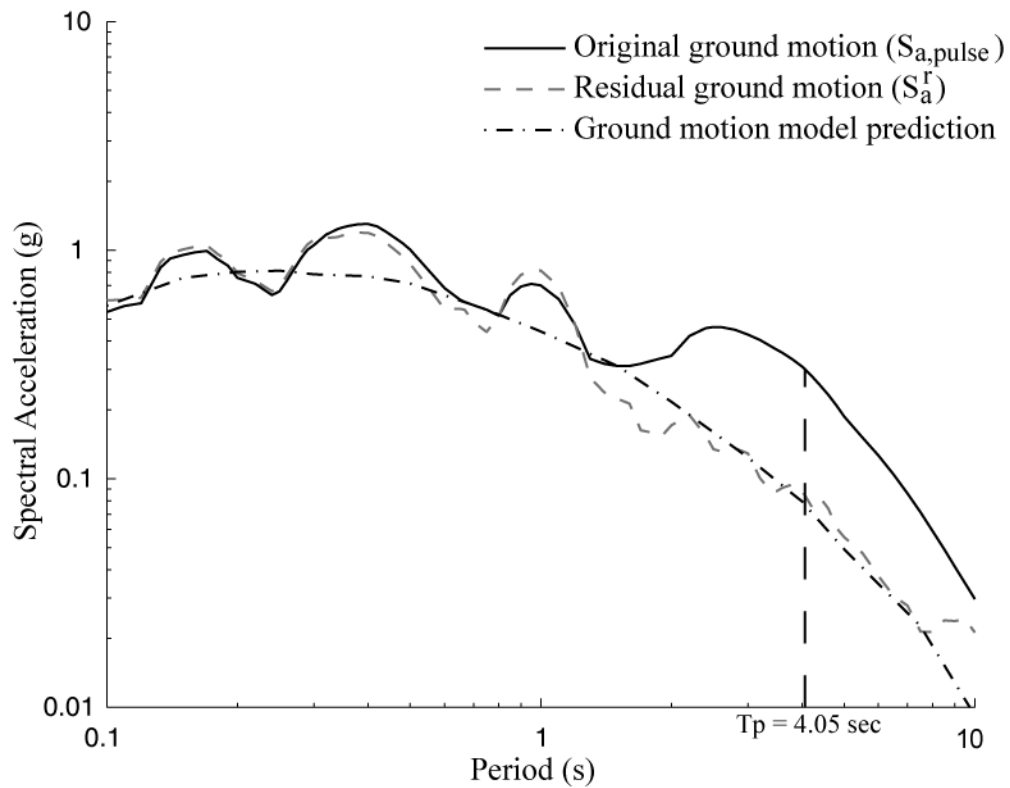


Figure 2.3 Response spectra (5% damped) of 1979 Imperial Valley, El Centro Array # 5 ground motion in the fault-normal orientation. The Boore and Atkinson (2007) median prediction and the response spectra from residual ground motion are also shown.

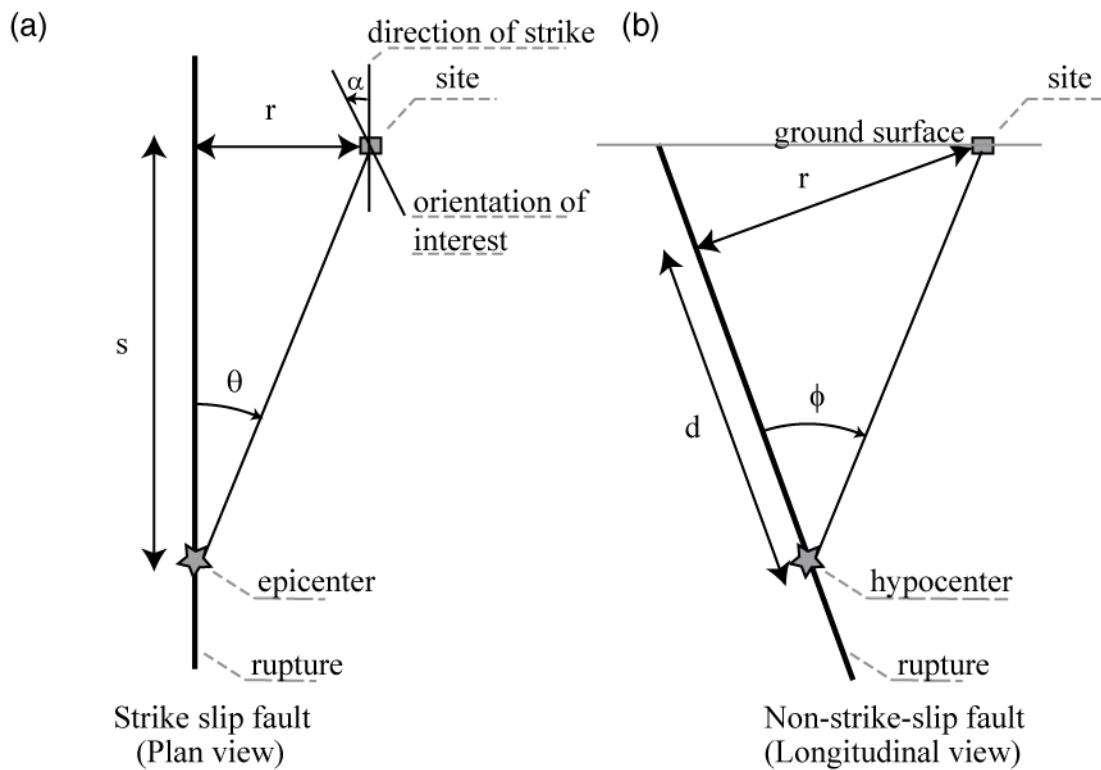


Figure 2.4 Plot explaining the parameters needed to fit the logistic regression for (a) strike-slip and (b) non-strike-slip faults. The parameter α , the angle between orientation of interest and the strike of the fault, is also shown (after Somerville et al., 1997).

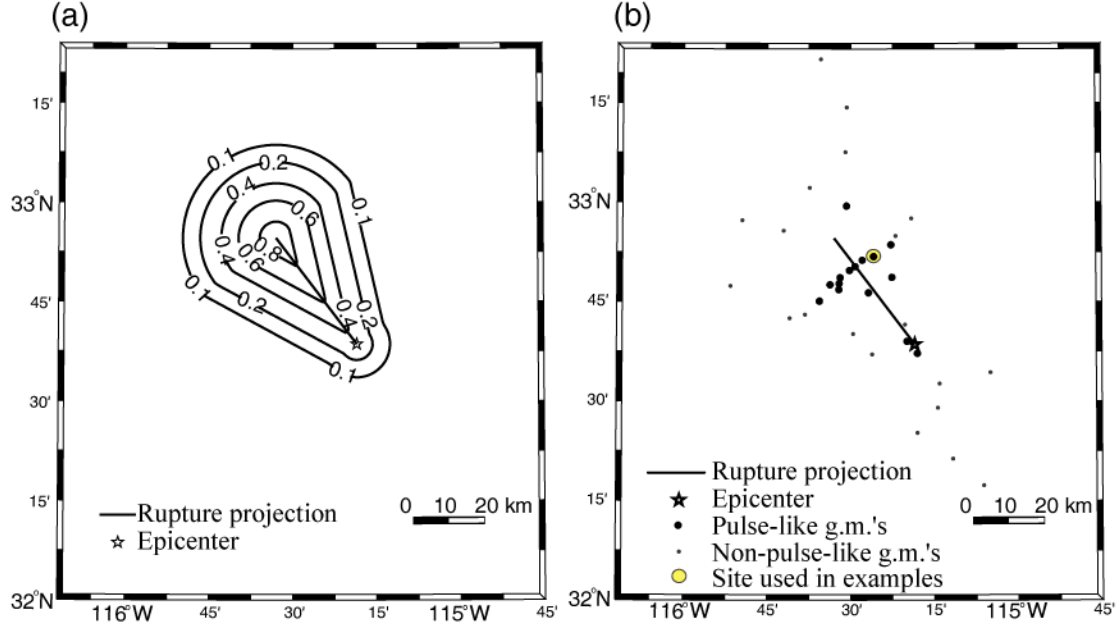


Figure 2.5 Map of 1979 Imperial Valley earthquake ($M = 6.53$) showing (a) contours of probability of pulse occurrence for the given rupture, and (b) sites where pulse-like ground motion was observed. The site within the shaded circle is the one for which example hazard analysis is done.

$$P(\text{pulse at } \alpha | \text{pulse}) = \min[0.67, 0.67 - 0.0041 \cdot (77.5 - \alpha)] \text{ for strike-slip} \quad (2.8)$$

$$P(\text{pulse at } \alpha | \text{pulse}) = \min[0.53, 0.53 - 0.0041 \cdot (70.2 - \alpha)] \text{ for non-strike-slip.} \quad (2.9)$$

Since the directivity effect is strongest in the fault-normal orientation and the strike-normal orientation is generally close to projection of fault-normal orientation in horizontal plane, it is expected to have higher probability of observing a pulse compared to other orientations. As expected, these results show that the most likely orientation to find a pulse-like ground motion is normal to the strike ($\alpha = 90$) while the least likely orientation is parallel to the strike ($\alpha = 0$) for both strike-slip and non-strike-slip faults.

The probability of observing a pulse-like ground motion at a site in a direction α degrees from the strike of fault segment can be expressed by Equation 2.10

$$P(\text{pulse at } \alpha) = P(\text{pulse at } \alpha | \text{pulse}) \cdot P(\text{pulse}), \quad (2.10)$$

where terms on the right-hand side of the equation are defined by Equations 2.6 through 2.9.

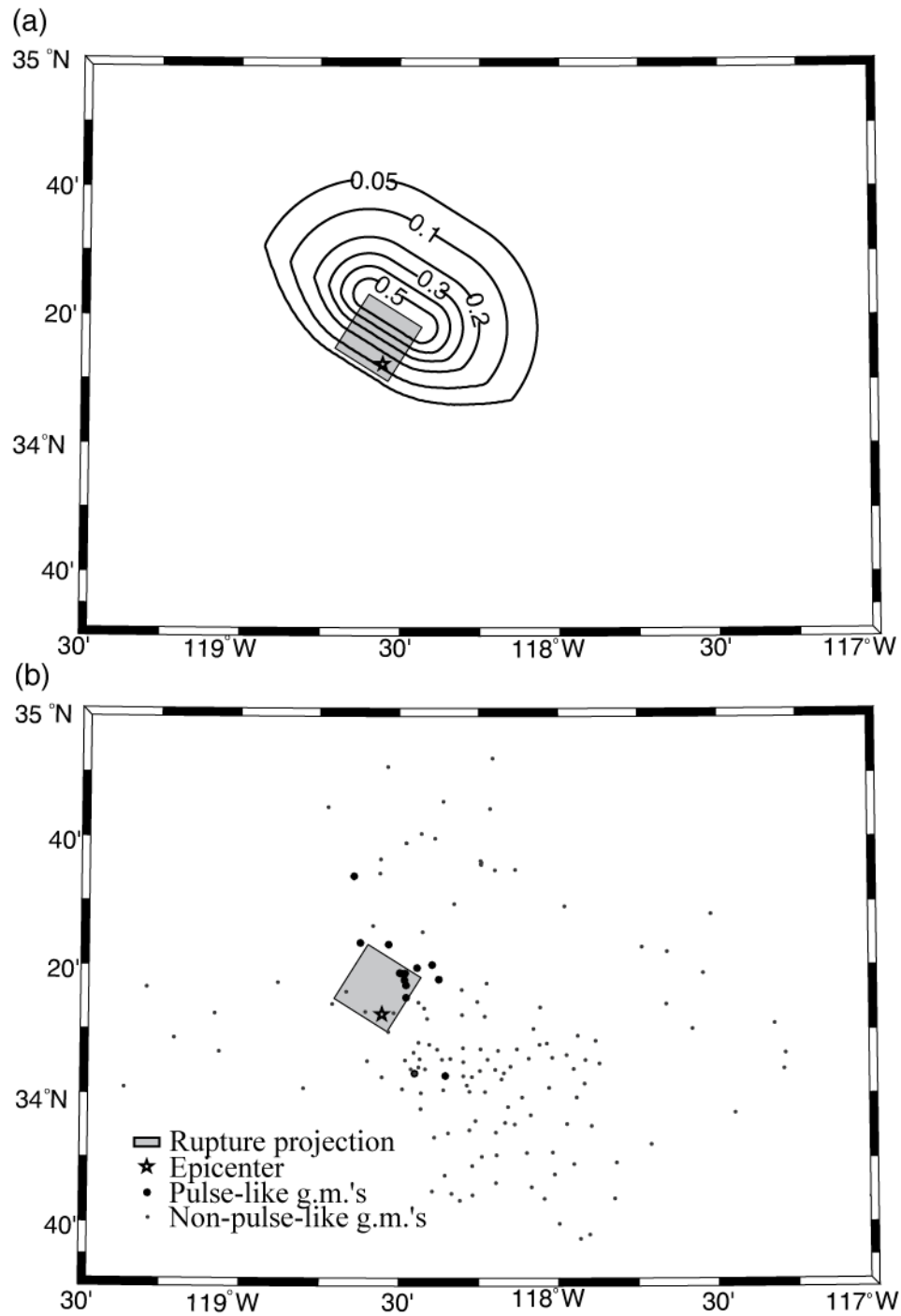


Figure 2.6 Map of 1994 Northridge earthquake ($M = 6.69$) showing (a) contours of probability of pulse occurrence for the given rupture, and (b) sites where pulse-like ground motion was observed.

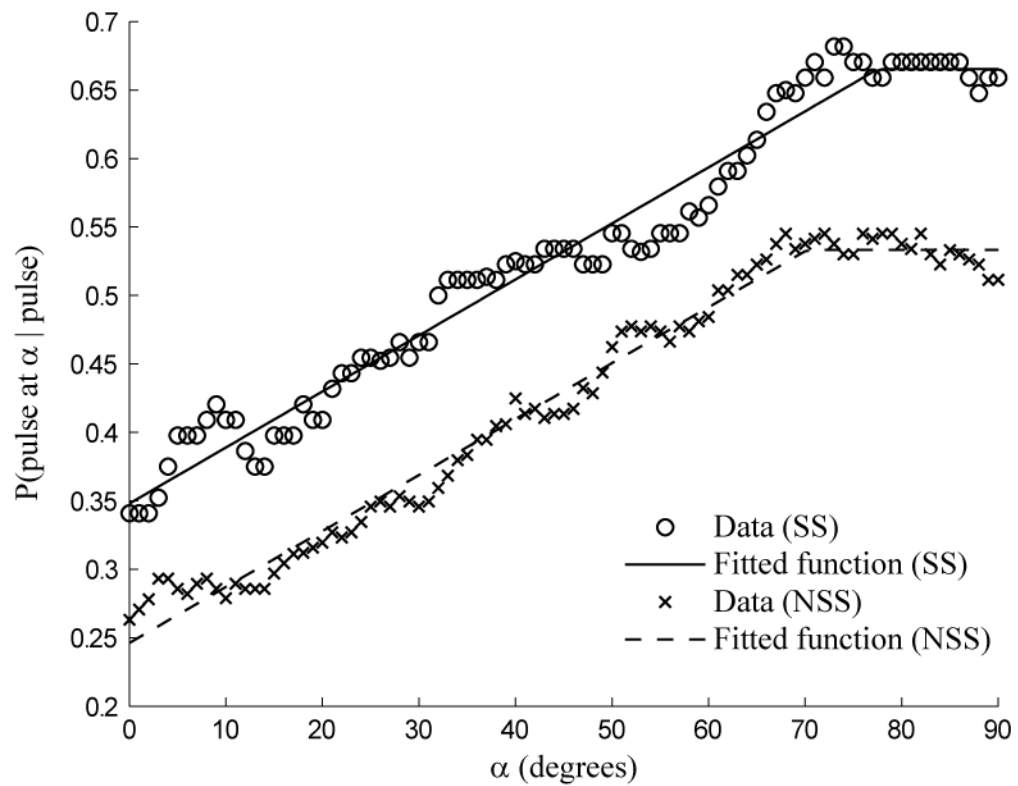


Figure 2.7 Plot of probability of pulse at α given pulse at site for both strike-slip and non-strike-slip faults.

2.3.3 Period of the Pulse

The amplification of spectral acceleration (S_a) due to the presence of a pulse-like feature in a ground motion depends on the period of the pulse. Previous research has demonstrated that the pulse period depends on the magnitude of the earthquake and have modeled this relationship (Mavroeidis and Papageorgiou, 2003; Somerville, 2003; Alavi and Krawinkler, 2004; Fu and Menun, 2004; Bray and Rodriguez-Marek, 2004; Baker, 2007). Since by using the modified classification algorithm we identified many ground motions with pulses that had not been used in previous studies, we modeled the relationship between pulse period and magnitude using all the pulses classified in this study.

In order to determine the relationship between pulse period and magnitude of the earthquake, the periods of all of the identified pulses were computed. For this study, the period associated with the maximum Fourier amplitude of the extracted pulse was used as a measure of the period of the pulse after Baker (2007). For ground-motions with pulses in multiple orientations, the average period of all identified pulses was used as the T_p for the record. Linear regression between $\ln T_p$ and magnitude gave the relationship shown in Equations 2.11 and 2.12

$$\mu_{\ln T_p} = -5.73 + 0.99M \quad (2.11)$$

$$\sigma_{\ln T_p} = 0.56 . \quad (2.12)$$

Figure 2.8 shows the average T_p and M values along with the relationship given in Equation 2.11. The residuals from this model fit a normal distribution well, so $\ln T_p$ can be assumed to be normally distributed (or T_p log-normally distributed) with the mean ($\mu_{\ln T_p}$) given by the prediction from Equation 2.11 and standard deviation ($\sigma_{\ln T_p}$) given by Equation 2.12.

Figure 2.8 shows that the number of pulse-like ground motions identified by the proposed method with low T_p are small. Values of $T_p < 0.6$ sec are rare and directivity pulses with these low periods are not expected to contribute significantly to seismic hazard. Thus $T_p < 0.6$ sec observations are ignored in these models and later calculations.

2.3.4 Amplification of Spectral Acceleration due to the Presence of Pulse

The proposed framework requires a ground-motion model that accounts for pulse-like features. The ground-motion model for the case when pulse is observed needs to predict mean and standard deviation of $\ln S_{a,\text{pulse}}$ at the site. In order to simplify the model, $\ln S_{a,\text{pulse}}$ can be broken down into

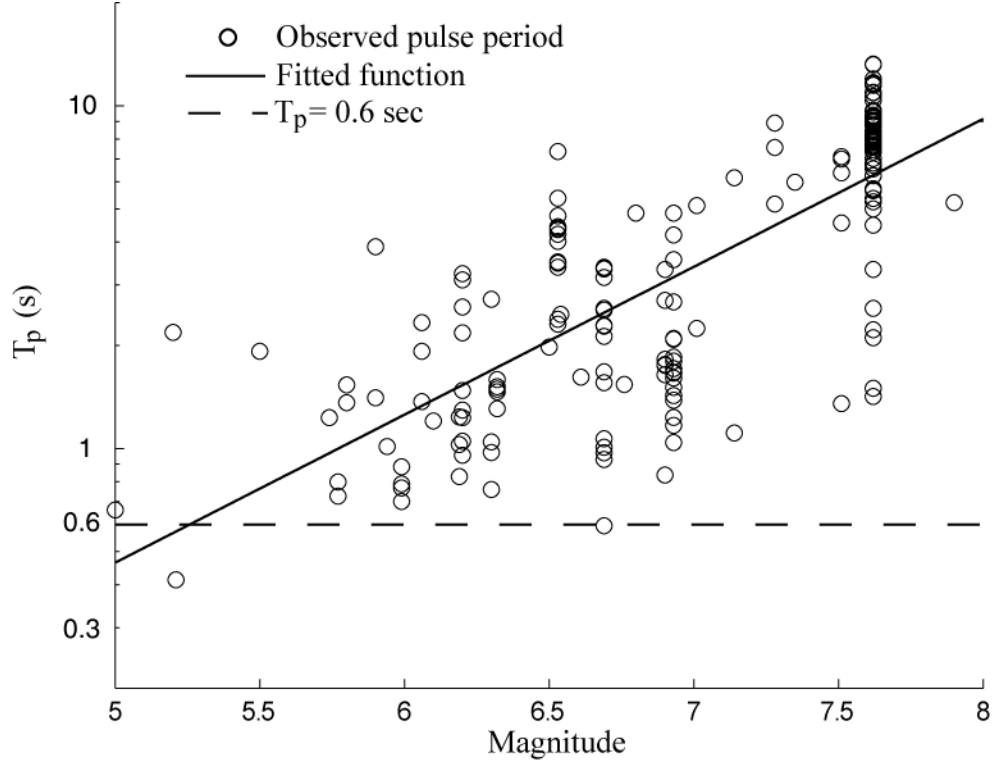


Figure 2.8 Pulse period versus earthquake magnitude for observed pulse-like ground motions.

two parts:

$$\ln S_{a,\text{pulse}} = \ln \left(\frac{S_{a,\text{pulse}}}{S_a^r} \cdot S_a^r \right) \quad (2.13)$$

$$= \ln(Af \cdot S_a^r) \quad (2.14)$$

$$= \ln Af + \ln S_a^r. \quad (2.15)$$

As discussed earlier, the S_a^r term in Equation 2.15 is the spectral acceleration of the residual ground motion (i.e., the ground motion after the observed pulse is removed), and Af is the amplification factor due to the presence of a pulse (i.e., $Af = S_{a,\text{pulse}}/S_a^r$). This representation of the ground-motion model allows us to model the amplification due to the pulse-like feature and the residual ground motion at a site separately. Figure 2.3 shows $S_{a,\text{pulse}}$ and S_a^r for a pulse-like ground motion.

Figure 2.9 shows the epsilons (ϵ) of the residual ground motion with respect to the Boore and Atkinson (2008) model (referred as BA2008 hereafter). The ϵ is the standardized residual of the BA2008 model prediction and will be discussed in more detail later. The figure shows that the mean ϵ is close to zero, suggesting that the ground-motion model is good at predicting S_a^r on average, and thus may be used to model the residual ground motions. Chioccarelli and Iervolino (2010) found

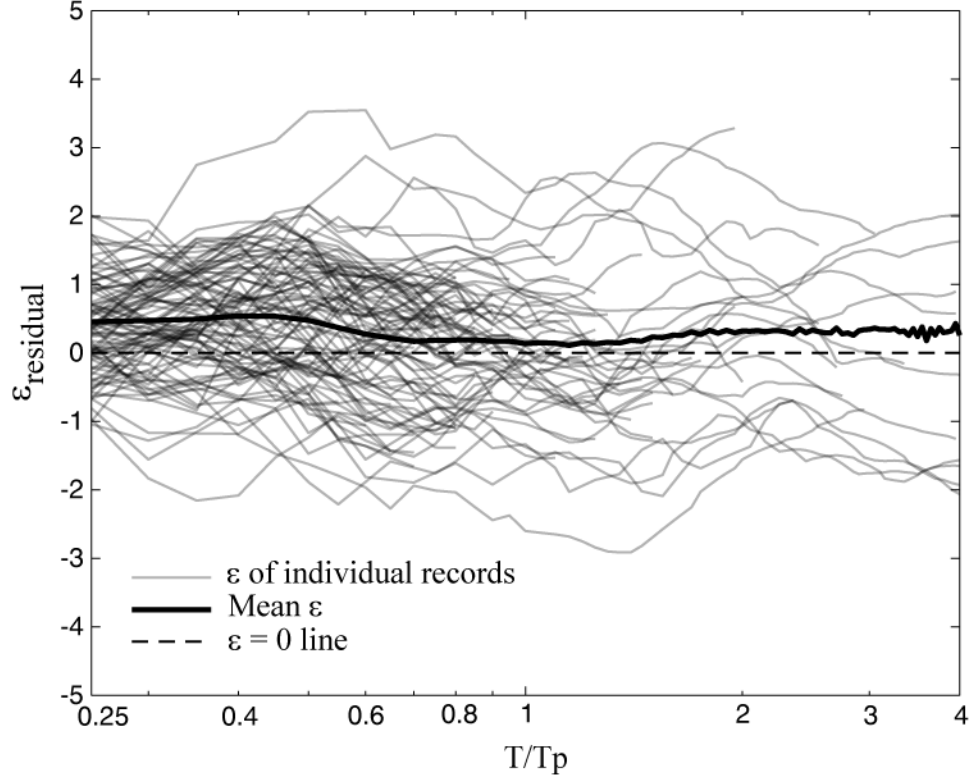


Figure 2.9 Observed ϵ values of residual ground motions.

that the fault-normal component is sometimes stronger than the fault-parallel component even after removal of the pulse. The result shown in Figure 2.9 is consistent with this finding as the ϵ from residual ground motion are positive (i.e., the residual ground motion is stronger than the prediction on average) but the ϵ are close enough to zero that we can assume that traditional ground-motion models can be used to predict the residual ground motion. Therefore, Equation 2.15 can be rewritten, replacing the $\ln S_a^r$ by prediction from traditional ground-motion models ($\ln S_{a,\text{gmm}}$):

$$\ln S_{a,\text{pulse}} = \ln A f + \ln S_{a,\text{gmm}}. \quad (2.16)$$

We computed amplification factors as the ratio of the S_a from original ground motion to the S_a from residual ground motions. Figure 2.10a shows the amplification factors plotted against the ratio of the period of interest (T) and period of pulse (T_p). The average amplification forms a bell-shaped pattern centered near to $T/T_p = 1$.

We tested several functional forms and fitted the best among them to data using minimization of the squared errors, to obtain the following mean amplification function:

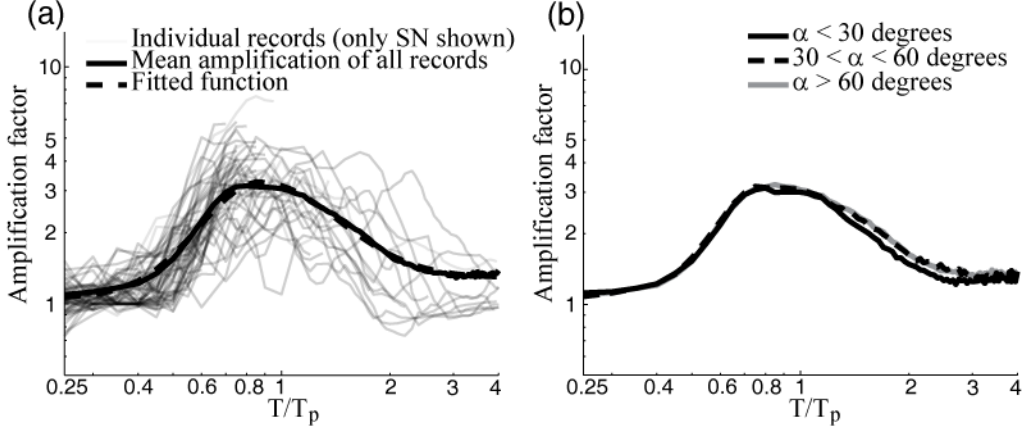


Figure 2.10 Amplification factor for S_a due to the presence of pulse-like features in ground motions. (a) Plot of predictive equation along with the observed data, and (b) mean amplification due to pulses oriented in different directions.

$$\mu_{\ln Af} = \begin{cases} 1.131 \cdot \exp(-3.11 \cdot (\ln(T/T_p) + 0.127)^2) + 0.058 & \text{if } T \leq 0.88 \cdot T_p \\ 0.924 \cdot \exp(-2.11 \cdot (\ln(T/T_p) + 0.127)^2) + 0.255 & \text{if } T > 0.88 \cdot T_p \end{cases} \quad (2.17)$$

Figure 2.10a also shows this fitted model along with the observed amplifications. Amplifications for pulses found in different orientations are plotted in Figure 2.10b, which shows that the model is stable with respect to change in orientation. Similar tests showed that the amplification due to the presence of a pulse is stable with respect to change in earthquake magnitudes and type of faulting as well. We can take expectations of Equation 2.16 to get:

$$\mu_{\ln S_{a,pulse}} = \mu_{\ln Af} + \mu_{\ln S_{a,gmm}} \quad (2.18)$$

Since the modified ground-motion model presented here is only for pulse-like ground motions, we expected the standard deviation within this subset to be lower than the standard deviation of the entire ground-motion library (which contains both pulse-like and non-pulse-like ground motions). Also, since the modified ground-motion model presented here accounts for the amplification by directivity pulses, this refinement leads to a reduction in standard deviation of the residuals. The observed reduction in standard deviation depends on T/T_p , and is modeled by Equation 2.19

$$\sigma_{\ln S_{a,pulse}} = Rf \cdot \sigma_{\ln S_{a,gmm}}, \quad (2.19)$$

where Rf , the reduction factor, is modeled as :

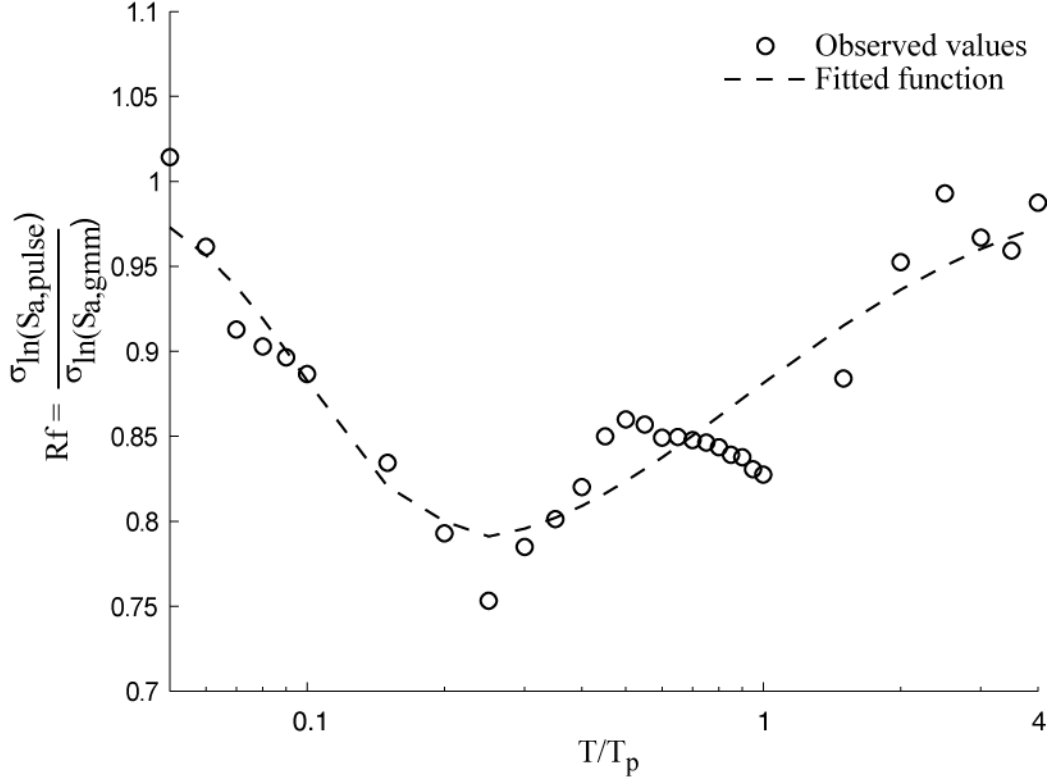


Figure 2.11 Ratio of standard deviation of residuals from predictions of pulse-like spectra ($\sigma_{\ln S_{a, \text{pulse}}}$) to the BA2008 ground-motion model standard deviation ($\sigma_{\ln S_{a, \text{gmm}}}$).

$$Rf = \begin{cases} 1 - 0.2 \cdot \exp(-0.96 \cdot (\ln(T/T_p) + 1.56)^2) & \text{if } T \leq 0.21 \cdot T_p \\ 1 - 0.21 \cdot \exp(-0.24 \cdot (\ln(T/T_p) + 1.56)^2) & \text{if } T > 0.21 \cdot T_p \end{cases} \quad (2.20)$$

Figure 2.11 shows the ratio of standard deviation of residuals from the modified model to that from the BA2008 model. Note that Equations 2.17 and 2.20 are strictly empirical fits to observed data. While these equations effectively reproduce the data, physical explanations for these functional forms are not yet available. The results from Equations 2.18 to 2.20 can be used to evaluate Equation 2.3.

All the results presented in this section are statistically fitted to data and depend on the period of the pulse (T_p). As discussed earlier, observation of $T_p < 0.6$ sec is rare and extrapolating the model for cases when $T_p < 0.6$ sec will result in amplification at low periods, so we recommend using these results to modify the conventional ground-motion models only for cases when $T_p > 0.6$ sec. Note that this limit restricts amplification of S_a at small periods, which is consistent with limits used in some other models (e.g., Somerville et al., 1997; Abrahamson, 2000).

2.3.5 Modification of Ground-Motion Model to Predict Non-Pulse-Like Ground Motion

The proposed framework requires a ground-motion model to predict the probability of $S_a > x$ given no pulse is observed at the site. Since the traditional ground-motion models are fitted to both pulse-like and non-pulse-like ground motions, they are expected to under-predict the spectral accelerations of pulse-like ground motions and over-predict the spectral acceleration of non-pulse-like ground motions. This under-prediction of pulse-like ground motions and over-prediction of non-pulse-like ground motions can be seen in Figure 2.12, which shows the median prediction (adjusted for the inter-event residual) of $S_a(2 \text{ sec})$ along with observations from the Northridge earthquake. Figure 2.12 shows that pulse-like ground motions generally lie above the median prediction and thus have positive ϵ (i.e., under-prediction). Conversely, the non-pulse-like ground motions tend to have negative ϵ values (i.e., over-prediction). This results in model predictions with ϵ close to zero on average (i.e., unbiased prediction), but here we explicitly correct the under and over-prediction when the pulse-like motions are classified.

The over-prediction of non-pulse-like motion by ground-motion model is corrected by the same scheme used to correct the ground-motion models for pulse-like ground motions. The following equations shows the model used to correct the ground-motion models for non-pulse-like case:

$$\begin{aligned} \ln S_{a,\text{no pulse}} &= \ln \left(\frac{S_{a,\text{no pulse}}}{S_{a,\text{gmm}}} \cdot S_{a,\text{gmm}} \right) \\ &= \ln(Df \cdot S_{a,\text{gmm}}) \\ &= \ln Df + \ln S_{a,\text{gmm}}. \end{aligned} \quad (2.21)$$

The Df term in Equation 2.21 is the de-amplification factor that corrects for the over-prediction by the ground-motion models. Df was found to depend on earthquake magnitude and distance from fault. We modeled Df by fitting simple functional forms to observed ϵ values. The de-amplification of mean S_a for cases with $T > 1 \text{ sec}$ are given by:

$$\mu_{\ln Df} = \begin{cases} \max[-0.0905 \cdot \ln T \cdot g_M \cdot g_R, -0.0905 \cdot \ln 2 \cdot g_M \cdot g_R] & \text{for strike-slip} \\ -0.029 \cdot \ln T \cdot g_M \cdot g_R & \text{for non-strike-slip} \end{cases}, \quad (2.22)$$

where

$$g_M = \begin{cases} 0 & \text{if } M < 6 \\ (M - 6)/0.5 & \text{if } 6 \leq M < 6.5 \\ 1 & \text{if } M \geq 6.5 \end{cases} \quad (2.23)$$

$$g_R = \begin{cases} 10 - r_{jb} & \text{if } r_{jb} \leq 10\text{km} \\ 0 & \text{if } r_{jb} > 10\text{km} \end{cases}, \quad (2.24)$$

where r_{jb} is the Joyner-Boore distance (closest distance to the surface projection of the fault). When $T \leq 1\text{sec}$, S_a is not de-amplified.

There was little difference between the standard deviation of the residuals computed from the data and those reported in BA2008 model; therefore, we use the standard deviation from the conventional ground-motion model as the standard deviation for this non-pulse-like ground-motion model.

These models can be used along with a conventional ground-motion model to compute $\mu_{\ln S_{a,\text{no pulse}}}$ and $\sigma_{\ln S_{a,\text{no pulse}}}$, as shown in Equations 2.25 and 2.26

$$\mu_{\ln S_{a,\text{no pulse}}} = \mu_{\ln Df} + \mu_{\ln S_{a,\text{gmm}}} \quad (2.25)$$

$$\sigma_{\ln S_{a,\text{no pulse}}} = \sigma_{\ln S_{a,\text{gmm}}}. \quad (2.26)$$

These can then be used to calculate probability of exceedance given no pulse is observed at the site ($P(S_a > x | m, r, \text{no pulse})$) by using Equation 2.4. Though this model has been calibrated using the residuals from BA2008 model, it should be applicable to other ground-motion models too.

2.4 ALGORITHM TO INCLUDE THE EFFECTS OF PULSE-LIKE GROUND MOTION IN PSHA

The use of models presented earlier to account for the effect of pulse-like ground motions in PSHA is described step-by-step in algorithm 1. Note that this algorithm for PSHA is a concise version focusing primarily on the modifications to traditional PSHA.

A new variable z , representing source-to-site geometry, is introduced into the PSHA framework equation given by Equation 2.2. We define the source-to-site geometry using the parameters α, r, s for strike-slip faults and α, r, d, ϕ for non-strike-slip faults, as defined earlier. In order to do a PSHA computation one needs to sum the hazard over all possible values of z by iterating over all possible epicenter locations and computing all z parameters for each epicenter location. This is identical

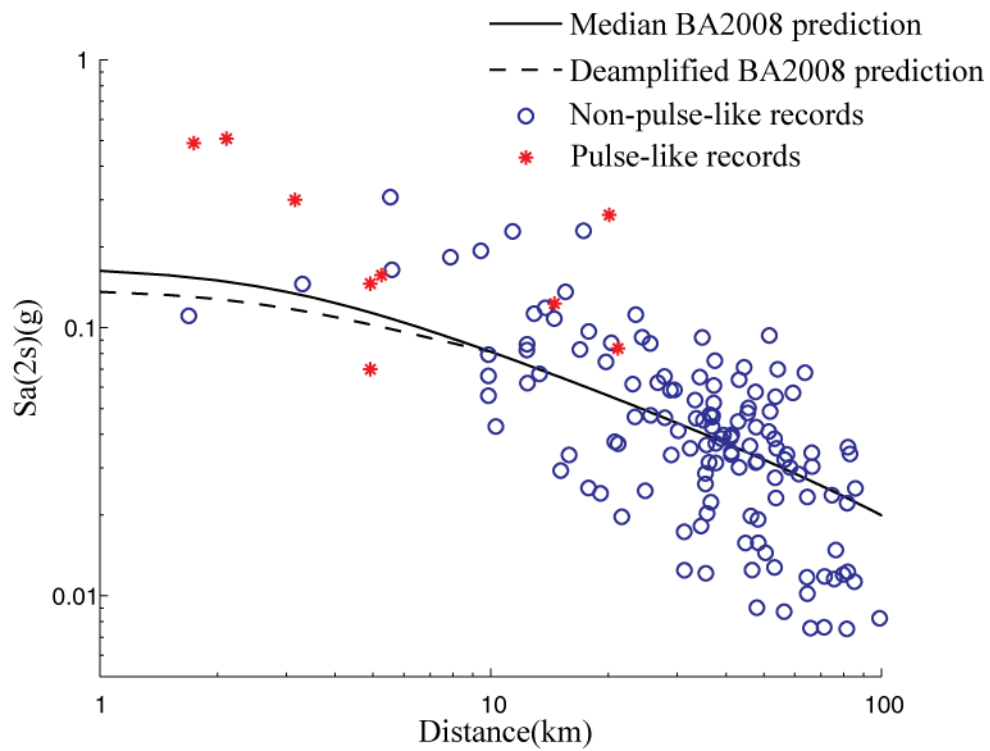


Figure 2.12 Median $S_a(2 \text{ sec})$ prediction from Boore-Atkinson 2008 model with and without the de-amplification along with the actual observations from Northridge earthquake. The Boore-Atkinson model prediction includes the inter-event residual of the Northridge earthquake.

Algorithm 1 PSHA algorithm to account for pulse-like ground motions

```
1:  $T$  = period of interest
2:  $\nu_{total} = 0$ 
3:  $\nu_{pulse} = 0$ 
4: for all faults ( $fault_i$ ) do
5:    $\alpha$  = azimuth of direction of interest – strike direction
6:    $P = 0$ ;
7:    $P_{pulse} = 0$ 
8:   for all magnitude ( $m_j$ ) and distance ( $r_k$ ) do
9:     compute  $P(S_a > x|m_j, r_k, \text{no pulse})$  from Equations 2.4, 2.25 and 2.26.
10:    compute  $P(\text{magnitude} = m_j)$  and  $P(\text{distance} = r_k)$ 
11:    for all positions of epicenter  $z_l$  do
12:      compute  $P(z = z_l)$ 
13:      compute  $P(\text{pulse}|m_j, r_k, z_l)$  from Equation 2.6 or 2.7
14:      compute  $P(\text{pulse at } \alpha|\text{pulse})$  from Equation 2.8 or 2.9.
15:       $P(\text{pulse at } \alpha) = P(\text{pulse}|m_j, r_k, z_l) * P(\text{pulse at } \alpha|\text{pulse})$ 
16:      compute  $\mu_{\ln T_p}$  and  $\sigma_{\ln T_p}$  from Equations 2.11 and 2.12
17:      for all  $T_p$  values ( $t_{pn}$ ) do
18:        compute  $P(S_a > x|m_j, r_k, z_l, \text{pulse})$  from Equations 2.3, 2.18 and 2.19 for  $T_p = t_{pn}$ .
          If  $t_{pn} < 0.6$  sec use the unmodified  $\mu_{\ln S_a, \text{gmm}}$  and  $\sigma_{\ln S_a, \text{gmm}}$  in place of  $\mu_{\ln S_a, \text{pulse}}$  and
           $\sigma_{\ln S_a, \text{pulse}}$ .
19:        compute  $P^*(S_a > x|m_j, r_k, z_l) = P(\text{pulse at } \alpha) * P(S_a > x|m_j, r_k, z_l, \text{pulse}) +$ 
           $(1 - P(\text{pulse at } \alpha)) * P(S_a > x|m_j, r_k, \text{no pulse})$ 
20:        compute  $P(T_p = t_{pn})$  by assuming  $T_p$  is log-normally distributed with  $\mu_{\ln T_p}$  and  $\sigma_{\ln T_p}$ 
21:         $P = P + P(\text{magnitude} = m_j) * P(\text{distance} = r_k) * P(z = z_l) * P(T_p = t_{pn}) * P^*(S_a > x|m_j, r_k, z_l)$ 
22:         $P_{pulse} = P_{pulse} + P(\text{magnitude} = m_j) * P(\text{distance} = r_k) * P(z = z_l) * P(T_p = t_{pn}) * P(S_a > x|m_j, r_k, z_l, \text{pulse}) * P(\text{pulse at } \alpha)$ 
23:      end for
24:    end for
25:  end for
26:   $\nu_{total} = \nu_{total} + \nu_{fault_i} * P$ 
27:   $\nu_{pulse} = \nu_{pulse} + \nu_{fault_i} * P_{pulse}$ 
28: end for
```

to the procedure used by Abrahamson (2000). A uniform distribution of epicenters over rupture length can be used if no other model is preferred, as suggested by Abrahamson (2000).

The amplification in S_a values depends on the period of the pulse, which makes T_p an important variable for hazard computation. T_p should be used as a random variable, as explained in section 2.3.3.

The proposed framework allows deaggregation of hazard to compute the likelihood that an event could have produced the exceedance of a particular threshold S_a value. Conventional PSHA allows magnitude, distance, and epsilon (ϵ) deaggregation. The framework proposed here can be used to also perform T_p deaggregation and compute the likelihood that a pulse-like ground motion caused the exceedance of a particular S_a value [i.e., $P(\text{pulse}|S_a > x)$].

The $P(\text{pulse}|S_a > x)$ can be calculated by deaggregation of hazard using ν_{pulse} and ν_{total} as shown by Equation 2.27

$$\begin{aligned} P(\text{pulse}|S_a > x) &= \frac{P(S_a > x|\text{pulse}) \cdot P(\text{pulse})}{P(S_a > x)} \\ &= \frac{\nu_{\text{pulse}}(x)}{\nu_{\text{total}}(x)}, \end{aligned} \quad (2.27)$$

where ν_{pulse} represents the rate of exceedance of S_a by pulse-like ground motions only, and ν_{total} represents the overall rate of exceedance.

2.5 EXAMPLE CALCULATIONS

Several models have been proposed in this paper for different aspects of near-fault pulse-like ground motions. Below we present some example calculations using these models.

2.5.1 PSHA for a Single Site

A full probabilistic seismic hazard analysis was done for the site shown in Figure 2.5. The site and fault parameters were chosen to mimic the conditions at a site that experienced pulse-like ground motion during the 1979 Imperial Valley earthquake. Earthquakes of magnitude 5 to 7 were considered and characteristic magnitude-recurrence relationship of Youngs and Coppersmith (1985) was used to model the probability distribution of magnitudes. The site is located at a distance 6.7 km from the fault and the fault is assumed to have a recurrence rate of 0.09 earthquakes per year. Rupture lengths of earthquakes were a function of magnitude, as determined using Wells and Coppersmith (1994). Uniformly distributed hypocenters along the rupture were assumed for PSHA computations. Hazard analysis is performed for the strike-normal orientation ($\alpha = 90^\circ$) at the site.

A PSHA was performed for a range of periods, both with and without consideration of the modifications proposed here. To summarize these results graphically, the 2% in 50 years uniform hazard spectrum from PSHA analysis is shown in Figure 2.13, along with the uniform hazard spectrum from ordinary PSHA. A third spectrum is shown based on calculations from the Somerville et al. (1997) model, later modified by Abrahamson (2000) (this approach will be referred to as the Somerville-Abrahamson model hereafter). The Somerville-Abrahamson model is currently the most widely used method to incorporate the effects of directivity pulses in hazard analysis. It is a broad-band model that decreases or increases the spectra monotonically with increasing period, in contrast to the model proposed here that predicts a narrow-band amplification around a given pulse-period. Figure 2.13 shows that the model proposed here predicts a bump-like amplification in the uniform hazard spectrum, which is broader than the original narrow-band amplification (a direct result of considering T_p as a random variable). Note that the range of periods being amplified will be a function of surrounding seismic sources, as predicted pulse periods vary as a function of the earthquake magnitude causing the ground motion. The PSHA results from a narrow-band model such as that proposed here are believed to be superior to those from a broadband model, as the results are more consistent with seismology theory (Somerville, 2005). Note that the uniform hazard spectrum is used here simply to provide a concise graphical illustration of how ground motions are amplified with varying period. This figure is not meant to imply that any single ground motion will have such a spectrum, because the uniform hazard spectrum by definition envelopes spectral values from many ground motions having varying magnitudes, distances, and pulse periods, which spreads the amplification due to pulses over a large range of periods. The spectra from a single ground motion will experience amplification in a narrower band of periods.

2.5.2 Spatial Pattern of PSHA Amplification due to Pulse-Like Ground Motion

The PSHA computations were done for a grid of sites around the same fault used in previous example. At each site, amplification due to pulse-like ground motions was computed by taking the ratio between S_a value calculated using the proposed PSHA algorithm and the conventional PSHA calculation. The map in Figure 2.14a shows the contours of the amplification of the $S_a(5 \text{ sec})$, exceeded with 2% probability in 50 years. A period of 5 sec was chosen for analysis as the models compared in this section had a large difference at this period, which made the 5-sec period an interesting point of comparison.

The contours shown in Figure 2.14 show high levels of amplification in S_a for sites located near to the fault. This shows that conventional PSHA under-predicts the hazard for near-fault sites and modification in PSHA to account for effects of near-fault pulse is necessary to correctly assess the

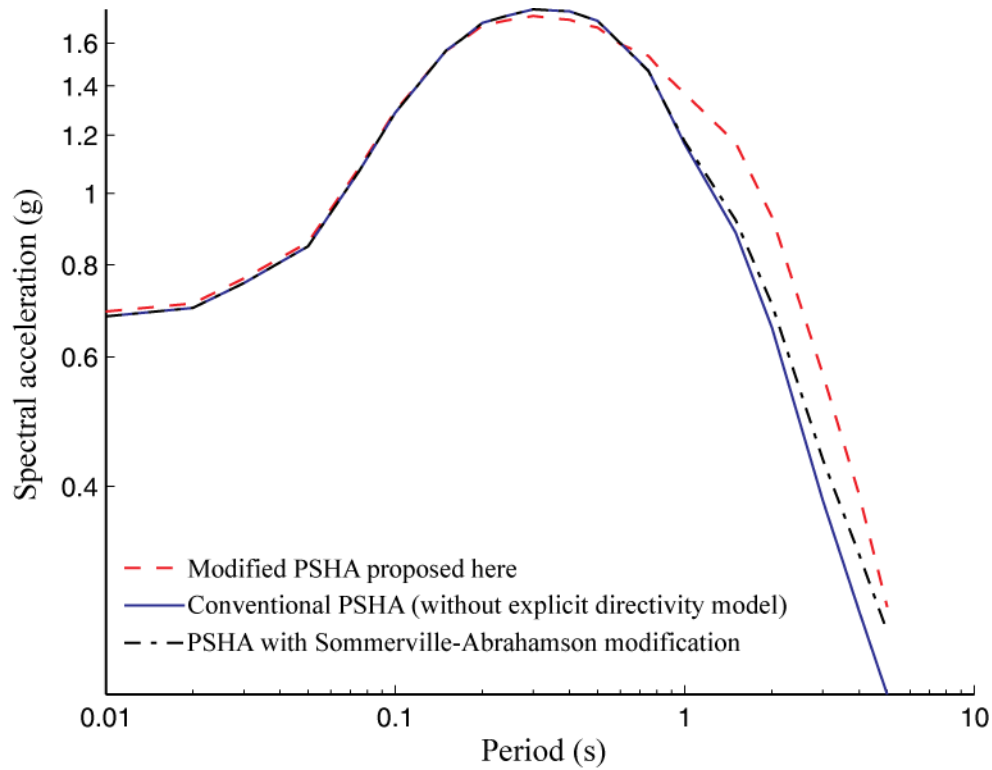


Figure 2.13 Two percent for a 50-year uniform hazard spectra from ordinary PSHA, PSHA with pulse modification suggested in this paper and PSHA with modification suggested by the Somerville-Abrahamson model for comparison. The PSHA is performed for the strike-normal orientation.

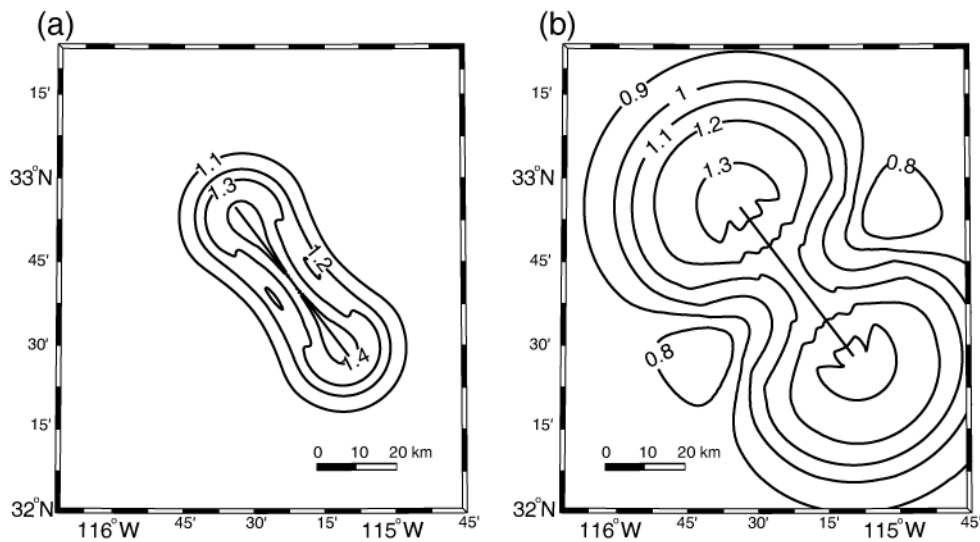


Figure 2.14 Map showing contours of amplification in 2% in 50 years $S_a(5 \text{ sec})$ by using (a) modified PSHA described in this paper, (b) using the Somerville-Abrahamson model.

hazard at such sites. Similar analysis was done for the Somerville-Abrahamson model to account for directivity. Figure 2.14b shows the contours of the amplification for 2% in 50 years $S_a(5 \text{ sec})$ when calculated by the Somerville-Abrahamson model. The proposed model shows different spatial patterns of amplification than the Somerville-Abrahamson model; it is believed that these differences are in large part due to refinements to the relationship between source-to-site geometry and directivity effects resulting from the increased observational data obtained since publication of the Somerville et al. (1997) model. Results such as these provide useful information regarding the range of distances over which one might expect directivity effects to play an important role in seismic hazard.

2.5.3 Deaggregation to Aid in Ground Motion Selection

Ground motion selection for near-fault sites is a topic that is currently under investigation, and the output from the proposed procedure may be useful to studies of such selection. Ground motion selection for a site typically involves selecting and scaling a set of ground motions to represent the hazard conditions at the site. The ground motions selected for analysis of near-fault structures should include an appropriate number of pulse-like ground motions to correctly represent the hazard conditions at site, and the framework presented here can aid in identifying appropriate ground motions for near-fault sites.

The number of pulse-like ground motions in the set of selected ground motions should reflect the probability of observing a pulse at the site. The probability of observing a pulse, given that S_a exceeds a particular value, can be obtained from Equation 2.27. Figure 2.15 shows the result of such hazard deaggregation for the site shown in Figure 2.5.

Deaggregation can also be used to find out the percentage contribution to hazard as a function of pulse period. Figure 2.16 shows the percentage contribution to 2% in 50 years $S_a(5 \text{ sec})$ hazard by different pulse periods. Figure 2.16 shows that there is a wide range of contributing pulse periods, which was expected since the presence of a pulse amplifies S_a over a range of periods. While selecting ground motions one should select pulse-like motions with pulse periods that closely represent the distribution computed by deaggregation.

2.6 CONCLUSION

A framework to include the effects of pulse-like ground motions in PSHA has been proposed. A standard ground-motion model was modified to account for the amplification in spectral acceleration due to the presence of pulse-like ground motion and the over-prediction of near-fault non-pulse-like ground motions. To calibrate the modification, a dataset was built by first classifying

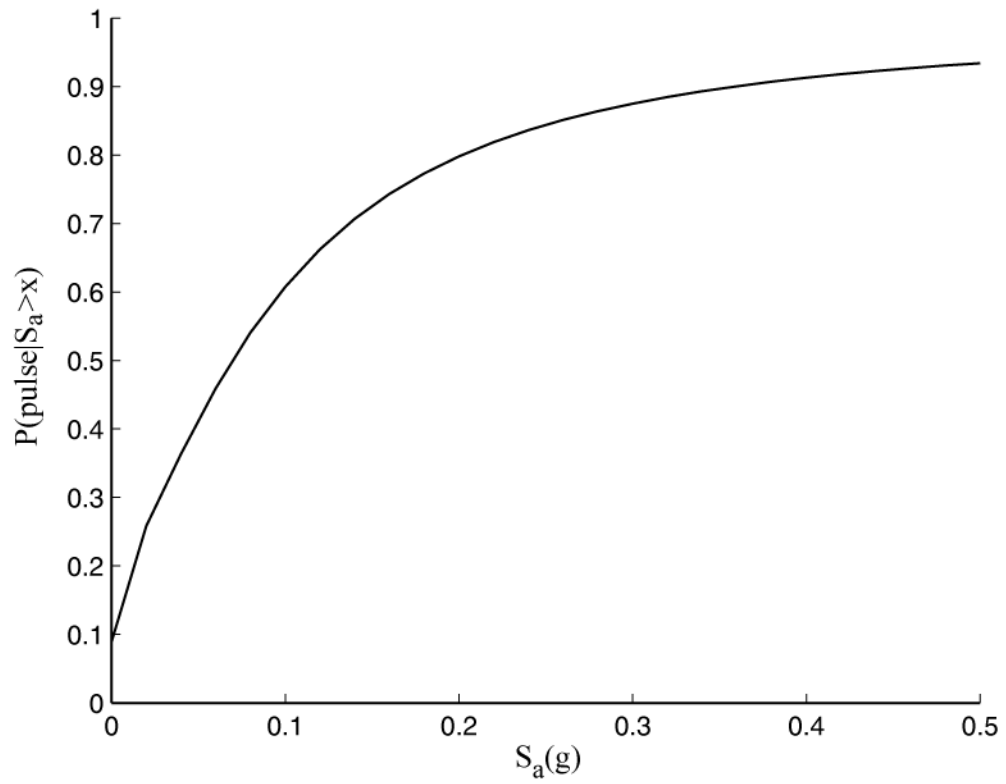


Figure 2.15 Deaggregation result showing $P(\text{pulse}|S_a(5 \text{ sec}) > x)$.

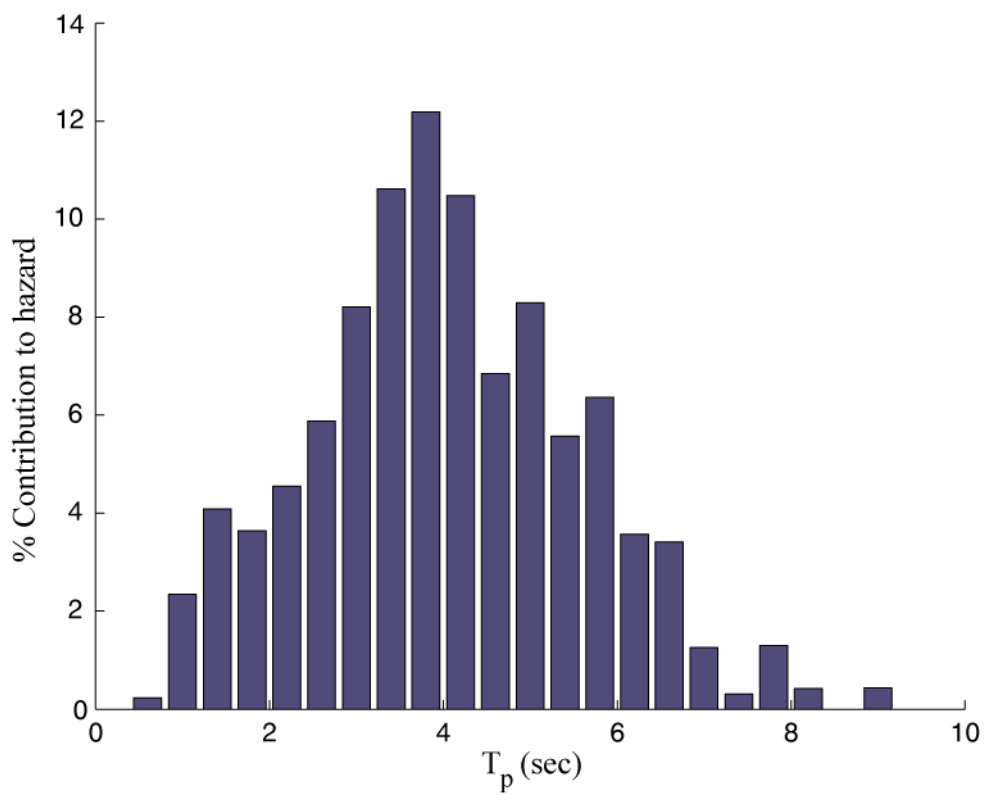


Figure 2.16 Deaggregation results showing % contribution to hazard by T_p given $S_a(5 \text{ sec}) > 0.3g$.

each ground motion in the NGA database as pulse-like or non-pulse-like, and then studying their spectra separately.

The PSHA calculation was broken down into smaller problems of finding the probability of pulse occurrence at a site given the source-to-site geometry, the probability of occurrence of a pulse in a particular orientation at the site given pulse-like ground motion is observed, the period of pulse expected at the site given the magnitude of earthquake, and the amplification of spectral acceleration given the period of an observed pulse at the site. These models were fitted using appropriate statistical techniques. All models and an algorithm to use these models to perform full PSHA computation were described. The framework is modular, which is desirable as all the models will surely need to be updated in the future as more data and knowledge become available.

Example hazard computations were performed, and the results from the approach proposed here were compared to predictions from the Somerville et al. (1997) model modified by Abrahamson (2000). The results from the two methods differ and will continued to be studied to verify that the model proposed here produces predictions more consistent with reality.

The proposed framework allows deaggregation of hazard to find the probability of observing a pulse-like ground motion given a particular level of S_a is exceeded, and the distribution of associated pulse periods. These deaggregation results are not available when using the Somerville-Abrahamson approach. These results lead to a deeper understanding of near-fault hazard and may aid in selecting appropriate ground motions for near-fault sites.

3 Regression Models for Predicting the Probability of Near-Fault Earthquake Ground Motion Pulses, and Their Period

3.1 INTRODUCTION

Near-fault ground motions may sometime contain a strong pulse at the beginning of the velocity time history. This pulse-like feature is primarily caused by forward directivity effects and are observed when the fault ruptures towards the site at a speed close to the propagation velocity of the shear waves (Somerville et al., 1997; Somerville, 2003; Spudich and Chiou, 2008). These ground motions (referred herein as “pulse-like”) place extreme demands on structures and are known to be the cause of extensive damage in previous earthquakes (e.g., Bertero et al., 1978; Anderson and Bertero, 1987; Hall et al., 1995; Iwan, 1997; Alavi and Krawinkler, 2001; Menun and Fu, 2002; Makris and Black, 2004; Mavroeidis et al., 2004; Akkar et al., 2005; Luco and Cornell, 2007). Pulse-like ground motions have higher elastic spectral acceleration (S_a) compared to ground motions without the pulse-like feature. The current ground-motion models that are used to perform probabilistic seismic hazard analysis (PSHA) do not account for the amplification in S_a caused by these ground motions. Thus the PSHA results computed using the current ground-motion models results in under-prediction of hazard at near-fault sites, where pulse-like ground motion are expected. Along with amplifying S_a , pulses also cause larger inelastic multi-degree-of-freedom (MDOF) response. Traditional intensity measures like S_a at the fundamental period of the structure are inadequate in capturing the larger nonlinear response of MDOF systems excited by pulse-like ground motions (Baker and Cornell, 2008a), which makes characterizing the risk from pulse-like ground motion difficult. The importance of accounting for the effect of pulse-like ground motion in design codes has long been recognized, but the methods to account for pulses used currently are relatively *ad hoc*. We need deeper understanding of how these pulse-like ground motions affect both the hazard and the risk before we can properly account for their effect in future design codes.

Predicting the probability of observing a pulse-like ground motion at a site is an important step

towards accounting for the effects of these ground motion in hazard computation. Modifications for the ground-motion models to predict the ground-motion intensity measure at sites when pulses are observed have been proposed in the past (e.g., Somerville et al., 1997; Spudich and Chiou, 2008). With the knowledge of probability of occurrence of pulse at the site, one can combine the prediction from traditional ground-motion models and the modified ground-motion model to come up with an estimate of hazard at the site. Equation 3.1 shows one possible way of combining the modified, and traditional ground-motion model results using the total probability theorem (e.g., Benjamin and Cornell, 1970). The term $P(S_a > x|\text{pulse})$ in Equation 3.1 is computed using the results from modified ground-motion models for pulse-like ground motions, and the term $P(S_a > x|\text{no pulse})$ is computed using the results from a traditional ground-motion models that does not account for the effects of pulses. Note that S_a depends on the period being considered and $P(S_a > x)$ depends on parameters like magnitude, distance, etc., those dependences along with the period under consideration are not explicitly included in Equation 3.1 for brevity.

$$\begin{aligned}
 P(S_a > x) &= P(S_a > x|\text{pulse}) \cdot P(\text{pulse at site}) \\
 &+ P(S_a > x|\text{no pulse}) \cdot (1 - P(\text{pulse at site}))
 \end{aligned}
 \tag{3.1}$$

As discussed above, along with amplifying S_a at moderate to large periods, pulse-like ground motions also cause amplification in the response of nonlinear MDOF systems; this amplified response cannot be completely characterized by using traditional intensity measures. It is believed that the response depends on the period of the pulse (T_p), and vector valued intensity measures including T_p can be used to characterize the nonlinear response of MDOF systems. It is also known that pulse in the ground motion amplifies the S_a in a narrow band of period (Somerville, 2003), and this narrow band amplification is centered about the period of the pulse T_p . Therefore, along with helping in characterizing the response of nonlinear MDOF systems, estimation of T_p can help in characterizing the amplification of S_a .

This paper studies and develops predictive equations for the probability of observing pulse-like ground motion at a site and the period of the pulse expected at a site. The predictive relationships developed herein can be used to improve the understanding of pulse-like ground motions and help the practitioners with problems related to hazard and risk at near-fault sites.

3.2 DATASET USED TO BUILD THE MODELS

The earthquake ground motion recordings in the NGA database (Chiou et al., 2008) were used as the base ground motion library for this study. Each ground motion in the database was classified as pulse-like or non-pulse-like using the classification algorithm proposed in Chapter 2. The classification algorithm rotates the ground motion in all orientations and classifies the ground motion in each orientation using the wavelet based classification scheme proposed by Baker (2007). A site is classified as having observed pulse-like ground motion if ground motion in any orientation is classified as pulse-like. The database consists of 3551 ground motions, of which 169 were classified as pulse-like.

3.3 PROBABILITY OF PULSE

Pulse-like ground motions caused by forward directivity effects are observed at near-fault sites, but not all near-fault sites experience pulse-like ground motion. This makes it important to estimate the probability of observing a pulse in order to correctly do PSHA calculations for near-fault sites. Forward directivity is a physical phenomenon with well-known causes, but it is hard to predict the occurrence of pulse-like ground motion at a site because of incomplete information about the source, site, and the path of wave propagation that cause this phenomenon. Due to this lack of knowledge, it is useful to develop a statistical model that agrees with the observations. Following the approach of Iervolino and Cornell (2008), the occurrence of pulse is modeled by a binary random variable (I) that takes the value 1 if pulse is observed at the site and 0 if pulse is not observed at the site (these type of variables are also called indicator variables).

3.3.1 Logistic Regression

Generalized linear models (GLMs) are generalization of the ordinary least squares regression and allow modeling variables following any distribution belonging to the exponential family of distribution (e.g., McCullagh and Nelder, 1989). A distribution belongs to exponential family if it can be written in the form:

$$f(y) = \exp(\eta y - \psi(\eta)) \cdot c(y) \quad (3.2)$$

where $f(y)$ is the probability density, η is called the natural parameter, y is the sufficient statistics, $\psi(\eta)$ is called the normalizing or the cumulant generating function, and $c(y)$ is called the carrier density. Many common probability distributions like normal distribution, Poisson distribution, binomial distribution, and gamma distribution belong to the exponential family. The GLMs use a

linear model to predict the natural parameter (η) as shown in Equation 3.3.

$$\eta = X \cdot \beta = \beta_0 + \beta_1 \cdot x_1 + \dots + \beta_p \cdot x_p \quad (3.3)$$

Here we are interested in modeling the probability of pulse occurrence, modeled by a binary random variable capable of taking the values 0 or 1 as explained above. This random variable can also be thought of as a binomial random variable that represents the number of successes (pulses) in one trial. Now the probability density of a binomial random variable is given by Equation 3.4, which can be re-written in the exponential family form as shown in Equation 3.5.

$$f(n) = \binom{N}{n} p^n (1-p)^{N-n} \quad (3.4)$$

$$f(n) = \exp\left[\left(\log \frac{p}{1-p}\right) \cdot n + N \log(1-p)\right] \cdot \binom{N}{n} \quad (3.5)$$

By comparing Equations 3.2 and 3.5 one can see that the natural parameter (η) for the binomial distribution is $\log\left(\frac{p}{1-p}\right)$, the sufficient statistic is n , the cumulant generating function is $N \log(1-p)$, and the carrier density is $\binom{N}{n}$. As shown in Equation 3.3, we model the natural parameter as a linear function of predictors, as shown in Equation 3.6. Equation 3.7 shows the function used to predict the probability of pulses as a function of various parameters (X in the equation).

$$\eta = \log \frac{p}{1-p} = X \cdot \beta \quad (3.6)$$

$$\implies p = \frac{e^{X \cdot \beta}}{1 + e^{X \cdot \beta}} = \frac{1}{1 + e^{-X \cdot \beta}} \quad (3.7)$$

$$\text{where } X \cdot \beta = \beta_0 + \beta_1 \cdot x_1 + \dots + \beta_p \cdot x_p$$

3.3.2 Fitting of the Model

Iervolino and Cornell (2008) developed a model to predict probability of pulse occurrence at a site using a dataset of pulse-like ground motion classified using the pulse classification technique of Baker (2007). Since the Baker (2007) technique classifies pulses only in the fault-normal orientation, the Iervolino and Cornell (2008) model predicts the probability of observing a pulse only in the fault-normal orientation. The classification technique used here classifies pulses in any arbitrary orientation, and thus necessitates updating the model to predict probability of observing a pulse in any orientation at the site.

Because the observation of forward directivity effects depends on source-to-site geometry, so we can narrow our search for predictor variables to different source-to-site geometry parameters.

Several source-to-site geometry parameters have been used in past to predict directivity effects at a site. Iervolino and Cornell (2008) used many combination of these parameters to fit logistic regression and compared the Akaike's information criterion (AIC) of different models to select the one with lowest AIC. The AIC is defined by Equation 3.8, where k is the number of parameters in the model, and $\ln L$ is the log likelihood of the model; the function represents the trade off between model fit and parsimony (Akaike, 1974). By increasing the number of parameters in the model, one can always improve the fit to data thus increasing log-likelihood. This improvement in fit may be due to fitting the noise in the data and is known as over-fitting the data. Models that over-fit the data are good at reproducing the data used for fitting but are bad for prediction. Minimizing the AIC tends to select parsimonious models with sufficiently high log-likelihood, thus avoiding the problem of over-fitting.

$$AIC = 2k - 2\ln L \quad (3.8)$$

Iervolino and Cornell (2008) found that closest distance from the fault (r), amount of rupture between the fault and the site (s), and the angle between the strike of the fault and line joining epicenter and the site (θ) are the best predictors for predicting probability of observing a pulse from a strike-slip fault. Analogous predictors r , d , and ϕ were found best for non-strike-slip faults. Figure 3.1 shows a diagram explaining these parameters. We consider the same parameters identified by Iervolino and Cornell (2008) even for this larger dataset as they seem to define the source-to-site geometry sufficiently well.

The logistic regression models were fitted by maximum likelihood method using the GLM function in R (R Development Core Team, 2010).

Model for Strike-Slip Faults

The NGA dataset contained 680 ground motions from strike-slip earthquakes for which all the source-to-site geometry parameters were known; out of these 41 were classified as pulse-like. This dataset of 680 ground motions was used to fit the model for strike-slip earthquakes. While fitting the model, θ turned out to be an insignificant predictor when r , s , and θ were used as predictors for the logistic regression. Generally, insignificance of a predictor in a statistical model is interpreted to mean that the predictor does not have any predictive value. As shown in Figure 3.2, when the site lies in the unshaded region, r and s can define the geometry completely, and θ (which is $\tan^{-1}(\frac{r}{s})$ in this case) is a redundant parameter not providing any new information; however, theta does provide some new information when the site lies in the shaded region of this figure. In this case, two sites with same r and s can have different θ (as shown in the figure). One needs to know the complete source and site geometry information to determine the region in which a site is located, but a quick

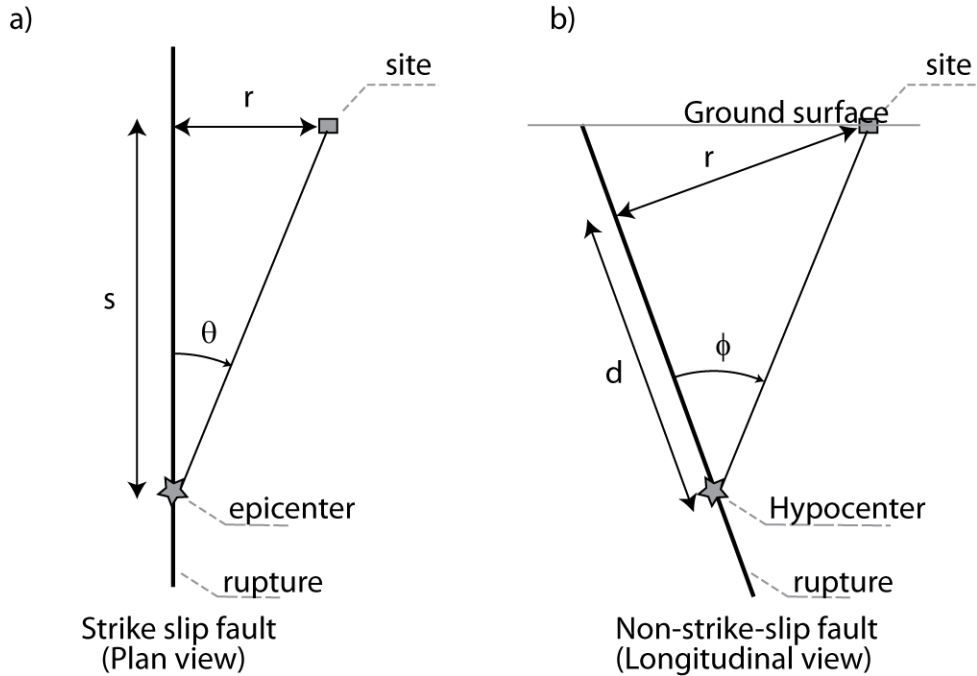


Figure 3.1 A diagram explaining the source-to-site parameters used to predict probability of pulse for (a) strike-slip fault and (b) non-strike-slip fault.(after Somerville et al., 1997).

heuristic check is sufficient to estimate the fraction of sites in the shaded area.

If one takes the ratio of $R_{epi} \cdot \cos(\theta)$ and s , where R_{epi} is the epicentral distance and s and θ are defined above, the ratio will be close to 1 when the site is located within the area where θ is redundant (unshaded region) and will be larger than 1 when the site is located in the area where θ is important (shaded region). Note that this calculation will not give us exact results because real-fault geometries are more complex than the simple straight line shown in Figure 3.1. Figure 3.3 shows the histogram of $\frac{R_{epi} \cdot \cos(\theta)}{s}$ for sites where pulses were observed, one can see that few pulse-like ground motions lie in the region where θ is important. Therefore, we may not have enough data to constrain the relationship with respect to θ , and thus θ ended up as an insignificant parameter in the regression.

As explained above, θ is insignificant because r and s alone can explain the geometry for most of the pulse-like sites. Actually any two parameters from r , s , and θ can describe the geometry completely when the site is in the unshaded region shown in Figure 3.2. So we fit logistic regression models using all possible pairs of predictors (r and s , r and θ , s and θ) and select the one with lowest AIC. The result from fitting is shown in Table 3.1, note that the result from using all three parameters is also shown for comparison.

The model with lowest AIC was selected and is shown in Equation 3.9. Here the units of r and s are in kilometers. The dataset contained r ranging from 0.07 km to 472 km and s from 0.3 km to

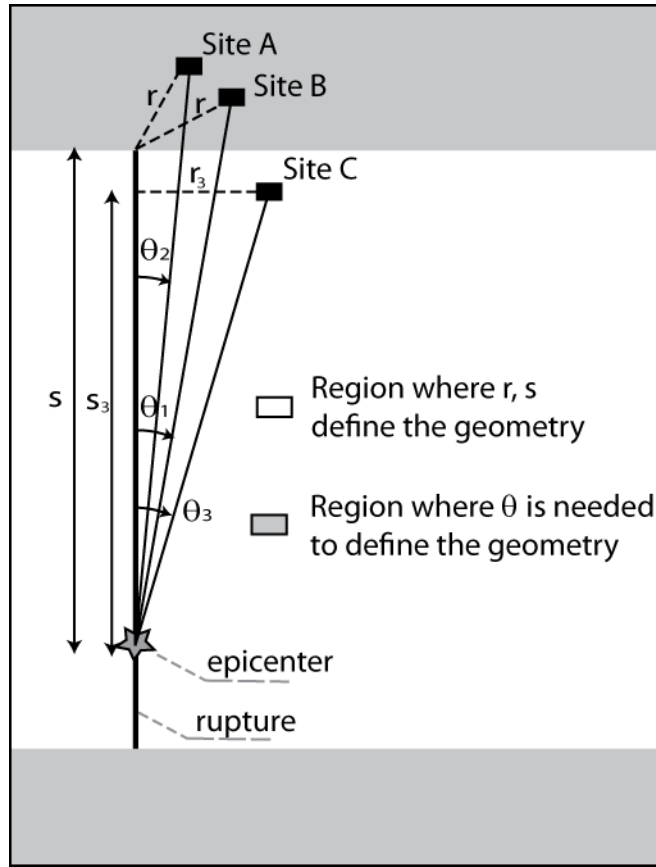


Figure 3.2 A diagram showing regions where r and s completely defines the source-to-site geometry and θ is redundant, and the region where θ is needed along with r and s to completely define the source-to-site geometry. The figure shows two sites (A and B) that have same r and s but different θ to show the importance of θ in the shaded region.

Table 3.1 AIC for strike-slip models with different predictors.

Parameters used	AIC
r, s	140.77
r, s, θ	141.34
r, θ	155.95
s, θ	250.61

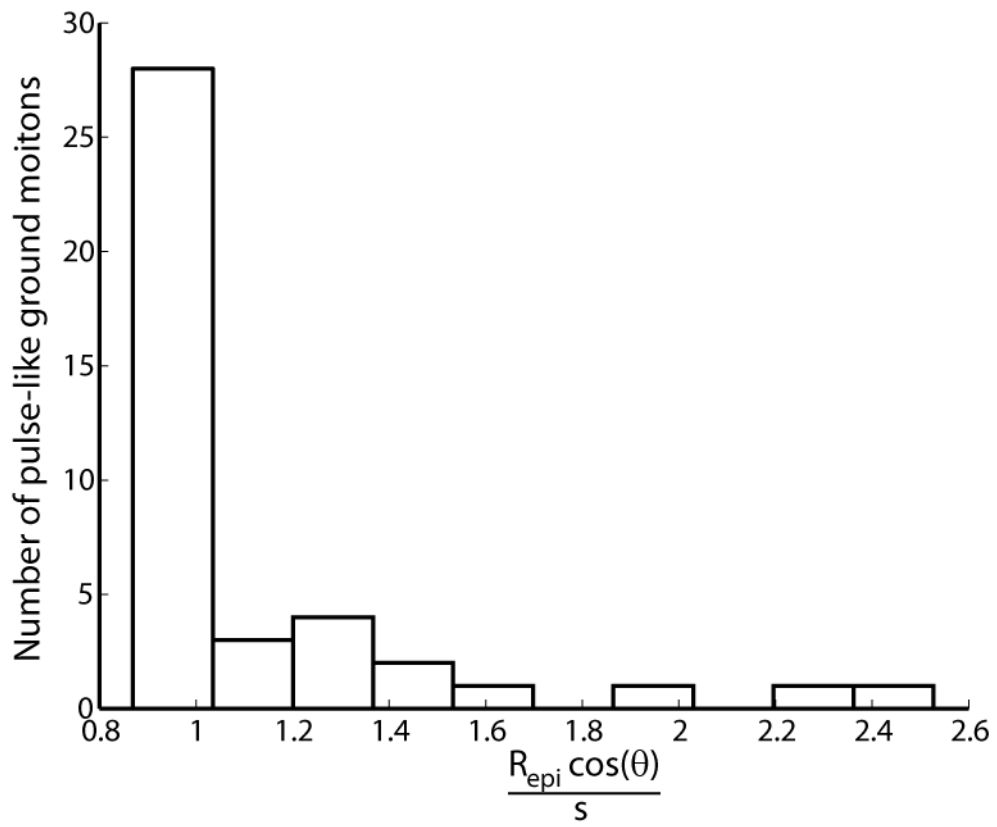


Figure 3.3 Histogram of $\frac{R_{epi} \cos(\theta)}{s}$.

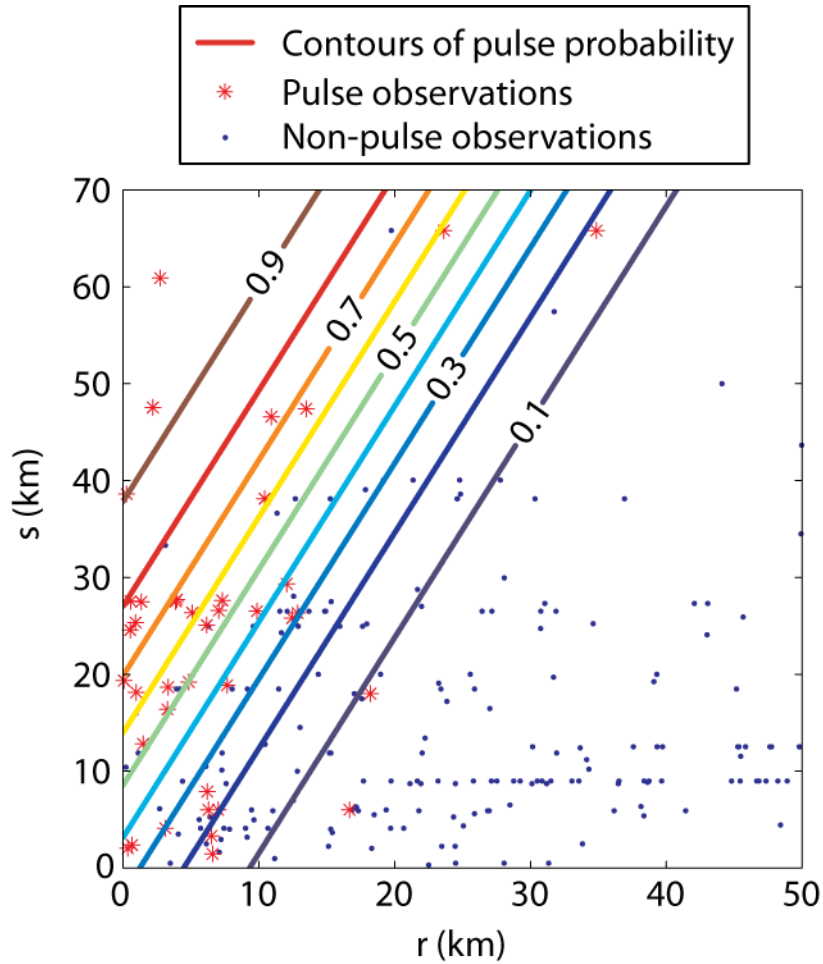


Figure 3.4 Contours of predicted probability of pulse due to an earthquake from a strike-slip fault at different r and s values.

143 km. Since the model only depends on two parameters we can look at the contours of probability in r, s space, as shown in Figure 3.4. We have superimposed the data used for regression on Figure 3.4 to visually verify the prediction. One can interpret the ratio of pulses to non-pulses in a region as an estimate of probability of observing a pulse at a site with some r and s . Figure 3.4 shows that the probability contours generally follow the trend shown by the data. One can also test the model by comparing actual pulse observation from a particular earthquake with the prediction from the model. This comparison for Imperial Valley fault is shown in Figure 3.5.

$$P(\text{pulse}) = \frac{1}{1 + e^{(0.642+0.167 \cdot r - 0.075 \cdot s)}} \quad (3.9)$$

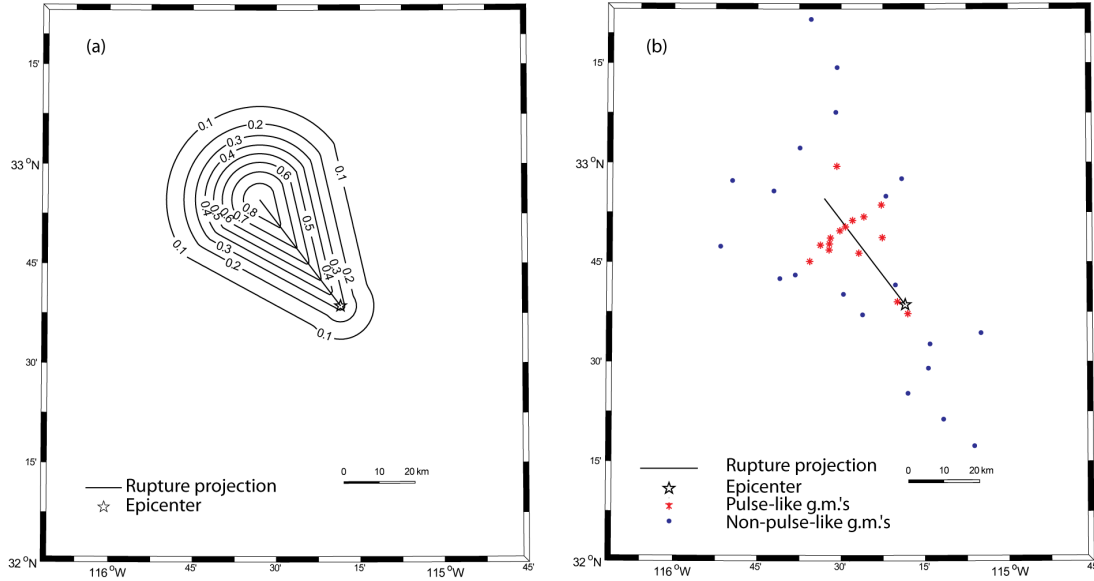


Figure 3.5 Map of Imperial Valley earthquake showing (a) contours of probability of pulse occurrence for the given rupture, and (b) sites where pulse-like ground motion was observed (from Chapter 2).

Model for non-strike-slip faults

The dataset contained 2169 non-strike-slip ground motions for which all the required parameters were known; out of these 124 were classified as pulse-like. We used the same variables selected by Iervolino and Cornell (2008) to fit the non-strike-slip model. In this case all three parameters are statistically significant. The model can be summarized by Equation 3.10. The unit for r and d is in kilometers and ϕ is degrees. The range of r values was 0.3 km to 255 km, d ranged from 0 to 70 km and ϕ ranged from 0 to 90 degrees.

$$P(\text{pulse}) = \frac{1}{1 + e^{(0.128 + 0.055 \cdot r - 0.061 \cdot d + 0.036 \cdot \phi)}} \quad (3.10)$$

Since the non-strike-slip model depends on three parameters, a simple visual verification as shown in Figure 3.4 for strike-slip fault is difficult. But we can still check the model by comparing the actual observation of pulse-like and non-pulse-like ground motion with the model prediction. Figure 3.6 shows such a comparison for the Northridge earthquake. The model predicts high probabilities in regions where pulses were actually observed during the Northridge earthquake.

3.4 PULSE PERIOD

The period of the pulse-like feature is an important parameter, as the ratio of pulse period and the structural period can be used to determine the structure's response (Anderson and Bertero, 1987;

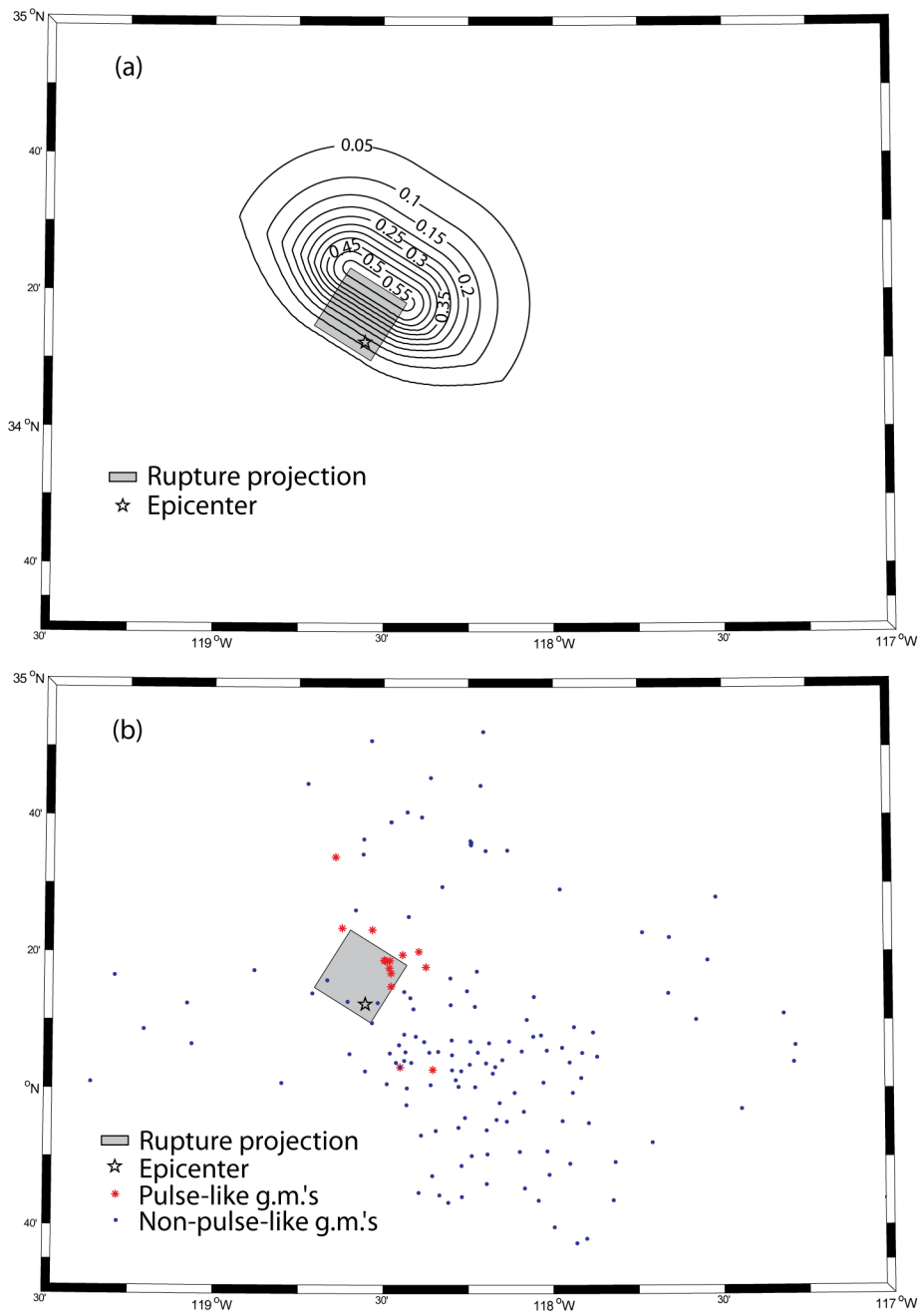


Figure 3.6 Map of Northridge earthquake showing (a) contours of probability of pulse occurrence for the given rupture, and (b) sites where pulse-like ground motion was observed (from Chapter 2).

Alavi and Krawinkler, 2001; Mavroeidis et al., 2004). The amplification of S_a due to presence of pulse also occurs in a small band of period close to the period of the pulse; this makes predicting pulse period an important part of hazard and risk computations. Several models have been proposed in the past for predicting the period of pulse-like ground motion (e.g., Mavroeidis and Papageorgiou, 2003; Alavi and Krawinkler, 2004; Fu and Menun, 2004; Bray and Rodriguez-Marek, 2004; Akkar et al., 2005). It was decided to model this relationship again as the classification algorithm of Chapter 2 used for this study identifies pulses in different orientation. With the new dataset we have information from many pulses in different orientations at the same site, data that was not available for previous studies.

3.4.1 Mixed-effects Regression

The dataset used for this study included many pulses from the same site that were identified in different orientations. Pulses at the same site but in different orientations share common source and site effects, and this commonality introduces some correlation between periods of these pulses that must be properly accounted for when fitting the model. The mixed-effect model is a popular statistical technique to capture this type of within group correlation. Equation 3.11 summarizes the mixed-effects model used here: the term y_{ij} represents the parameter of interest in j^{th} orientation of i^{th} site, $f(\cdot)$ is the functional form used for regression, η_i is the random effect term, it represents the error common to the i^{th} site, and ϵ_{ij} represents the error at i^{th} site in j^{th} orientation. Using the convention established by Abrahamson and Youngs (1992) η_i is the inter-event residual, and ϵ_{ij} is the intra-event residual.

$$y_{ij} = f(\cdot) + \eta_i + \epsilon_{ij} \quad (3.11)$$

In order to model the predictive relationship for T_p , we find a suitable functional form for the regression [$f(\cdot)$ in Equation 3.11] and fit the regression. The search for predictors is discussed below and the fitting was done by maximum likelihood method using the lme4 package (Bates and Maechler, 2010) in R (R Development Core Team, 2010).

3.4.2 Search for Predictors

Most existing predictive equations for T_p model $\ln T_p$ as a linear function of magnitude (magnitude refers to the moment magnitude of the earthquake). In seismology theory, the pulse period is related to the rise time of slip on the fault and the logarithm of rise time is proportional to magnitude, thus justifying using a linear relationship to predict $\ln T_p$ as a linear function of magnitude (Somerville, 1998; Somerville et al., 1999). Since the dataset used in this study was much bigger than those

in previous studies, we were in a position to systematically search for additional predictors. As the space of all possible functional forms is vast and it is impossible to exhaustively search for the best functional form, we reduced the search space by only considering linear combination of the predictors described below.

Magnitude of earthquake M , parameters describing the source-to-site geometry, (r,s for strike-slip faults and r,d for non-strike-slip faults) along with V_{s30} and their log, square and square root were taken as candidates to be included in the linear mixed-effect model (total of $4 \times 4 = 16$ possible predictors each, for both strike-slip and non-strike-slip faults). The dataset was divided into two parts depending on whether the source was strike-slip or not. All the pulse-like ground motions classified by the algorithm in Chapter 2 except those with $V_{s30} > 2000$ m/sec were used for this study.

A stepwise regression scheme was used to select the parameters for the final model. First all mixed-effect models with just a single predictor were fitted to predict $\ln T_p$, and the predictor with highest log-likelihood was selected. After selecting the first parameter, all possible two parameter models were constructed by combining the first selected parameter with each of the other parameters one by one. The parameter that increased the log likelihood the most was selected as the second parameter. This process was repeated until no parameter made a significant contribution to further increasing the log-likelihood of the model (a 95% level of significance was used as the cutoff). Note that the model with best log-likelihood has the best AIC too.

This scheme identified M , $\ln V_{s30}$, and \sqrt{r} as predictors for strike-slip faults and M and r^2 as predictors for non-strike-slip faults.

3.4.3 Fitting of the Model

After selecting the parameters using the forward stepwise procedure, the following model was fitted to the data.

$$\ln T_{p_{ij}} = \alpha + \beta_1 \cdot M + \beta_2 \cdot \ln V_{s30} + \beta_3 \cdot \sqrt{r} + \eta_i + \epsilon_{ij} \quad (3.12)$$

$$\ln T_{p_{ij}} = \alpha + \beta_1 \cdot M + \beta_2 \cdot r^2 + \eta_i + \epsilon_{ij} \quad (3.13)$$

Equation 3.12 shows the model for strike-slip faults, and Equation 3.13 shows the model for non-strike-slip faults. α , β_1 , β_2 and β_3 are parameters fitted using mixed-effects regression. In both models η_i (between-event error) is assumed to follow a normal distribution with mean 0 and standard deviation τ , while ϵ_{ij} (within-event error) is assumed to be normally distributed with mean 0 and standard deviation σ ; therefore, the total standard deviation of predictions from this model is

Table 3.2 Result of mixed-effects regression, for both strike-slip and non-strike-slip faults.

	SS. (eq.3.12)	NSS (eq.3.13)	NSS (eq.3.14)
α	-0.41	-7.84	-7.60
β_1	0.50	1.29	1.25
β_2	-0.37	-5×10^{-5}	-
β_3	0.12	-	-
τ	0.55	0.49	0.50
σ	0.19	0.18	0.18
σ_{total}	0.58	0.52	0.53

$\sqrt{\tau^2 + \sigma^2}$. The coefficients and the standard deviations for both the models are given in Table 3.2.

The inter-event standard deviation τ is greater than the intra-event standard deviation σ for both strike-slip and non-strike-slip models. This trend is opposite to the typical results of mixed-effect models used for ground-motion modeling where σ is greater than τ . This difference is due to the different ways in which the data is grouped. In case of ground-motion models, all the recordings from a single earthquake form a group (i.e., share a common η_i), while in the model developed here all the pulses from the same site form a group. The grouping scheme used here ensures that members of the same group share the same source, site, and path, and thus the within-group/intra-event standard deviation (σ) makes a lower contribution to the total standard deviation (σ_{total}) compared to the ground-motion models where the groups only share the source.

3.4.4 Statistical versus Practical Significance

Statistical significance of a parameter in the model suggests that the parameter has some predictive power and including it in the model is generally recommended. But with large datasets, even very small differences that may be practically insignificant become statistically significant. For example consider a group of numbers that are independently and identically sampled from a normal distribution with an unknown mean μ and standard deviation of five. With this information one may want to test the hypothesis that $\mu = 0$. If the dataset consist of 10 samples, the absolute value of sample average (\bar{X}) needs to be greater than 3.1 (i.e., $|\bar{X}| \geq 3.1$) to conclude that μ is significantly different than 0 at 95% confidence level. With a larger sample size, however, of, say, 1000 samples, the significance level threshold comes down to 0.31 (i.e., $|\bar{X}| \geq 0.31$), a difference that is statistically significant but may be practically insignificant depending on the problem. The models developed herein to predict T_p (Equations 3.12 and 3.13) consist of parameters whose coefficients are all statistically significant, but in this section we determine whether they have any practical significance.

The models for both strike-slip and non-strike-slip earthquakes use magnitude (M) as a predictor. As discussed above, it is known that $\ln T_p$ scales linearly with M , and M is the most important predictor for T_p , a fact consistent with all of the previous predictive models proposed for T_p . The non-strike-slip model uses r^2 along with M as a predictor. Pulse-like ground motions are generally expected only when $r \leq 30$ km, over this distance range the term $-5 \times 10^{-5} \cdot r^2$ varies from 0 to -0.045 ($-5 \times 10^{-5} \times 30^2$). Considering that the σ_{total} for the non-strike-slip model is 0.52, the contribution r^2 term has in the model is an order of magnitude less than the inherent uncertainty in the model, suggesting practical insignificance. Figure 3.7 shows prediction of T_p at different distances (r) made using the model using both M and r^2 (Equation 3.13) and prediction from a model for non-strike-slip faults fitted using only M as a predictor. The difference between the predictions shown in Figure 3.7 is small, so the term r^2 can be safely dropped from the model without losing predictive power. The new model for non-strike-slip fault is shown in Equation 3.14. Again the inter-event and intra-event residuals are assumed to follow normal distribution with mean 0 and standard deviation τ and σ respectively. The values of the fitted parameters and standard deviations are shown in Table 3.2.

$$\ln T_{p_{ij}} = \alpha + \beta_1 \cdot M + \eta_i + \epsilon_{ij} \quad (3.14)$$

The strike-slip model uses \sqrt{r} and $\ln V_{s30}$ along with M as predictors. One expects pulses with higher period on soil sites when compared with pulses at rock sites due to local site effects. This effect has been discussed by Bray and Rodriguez-Marek (2004) and is also evident from the regression model for strike-slip fault that predicts that T_p decreases with increase in V_{s30} . The effect of V_{s30} on T_p has some physical explanation and its contribution is non-trivial, which justifies it being practically significant. Ignoring the \sqrt{r} term from strike-slip model changes the prediction on the order of the standard deviation of the model ($0.12 \cdot \sqrt{r}$ ranges from 0 to 0.71 when r ranges from 0 to 10 km). Because this change is large and cannot be ignored, we decided to keep \sqrt{r} in the final model for strike-slip faults. The exact cause of dependence of T_p on r is not clear, but T_p may increase with distance due to attenuation of high-frequency waves or loss of pulse coherence at larger distances.

The final model for strike-slip faults is given by Equation 3.12, while the model for non strike-slip faults is given by Equation 3.14.

3.5 CONCLUSION

Pulse-like ground motions classified in Chapter 2 were used to fit predictive relationships for probability of observing pulse-like ground motion at a site and the period of the pulse expected at a site.

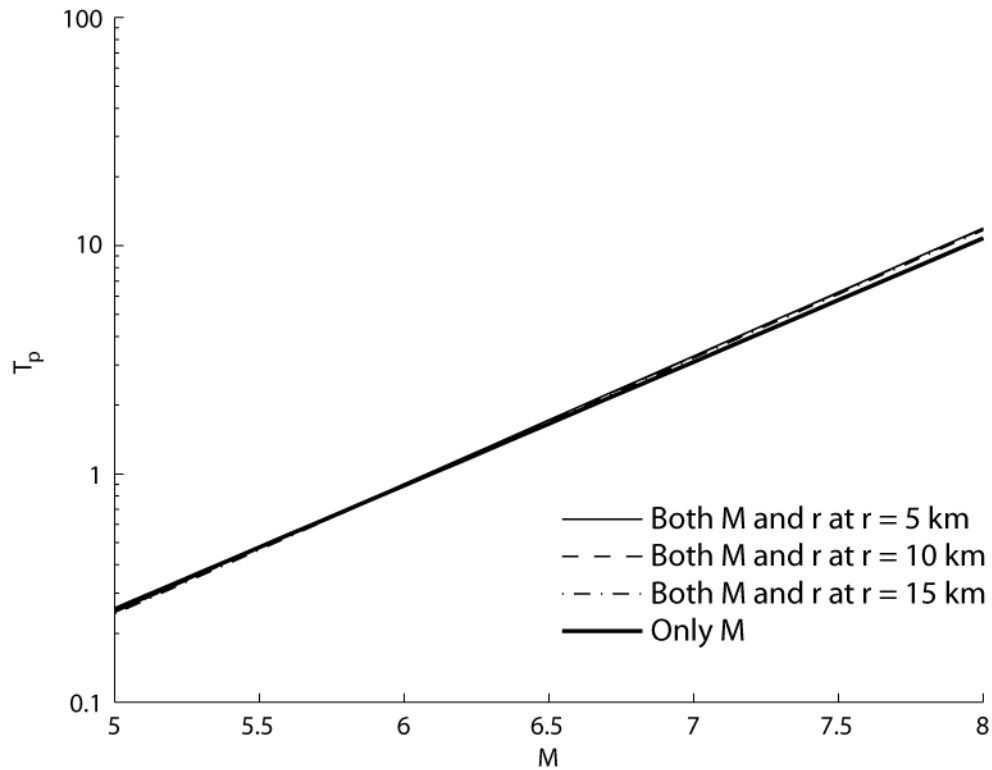


Figure 3.7 Comparison of predictions from models for non-strike-slip faults using M and r^2 as predictors and only M as predictor at different r values.

Statistical techniques were used to find appropriate functional forms for the models and effort was made to develop parsimonious models that are easy to interpret, leading to better understanding of the overall phenomenon.

Separate relationships were developed for strike-slip and non-strike-slip faults, and these relationships were very different from each other. In case of probability of pulse model, the difference was primarily due to the difference in the geometry of the fault ruptures and the different parameters used to define the source-to-site geometry. In case of the pulse period model, different parameters appear to influence the pulse period from strike-slip and non-strike-slip faults. The period of the pulse primarily depends on the magnitude of the earthquake in both cases, but the closest distance to the fault and V_{s30} also had an influence on the pulse period in case of strike-slip earthquakes. Along with having immediate practical use for hazard and risk estimation, the trends and differences between the predictive equations developed here can be useful in further understanding properties of pulse-like ground motions.

4 An Efficient Algorithm to Identify Strong Velocity Pulses in Multi-Component Ground Motions

4.1 INTRODUCTION

Given their great potential for causing damage, empirical models are needed to quantify the hazard and risk posed by these pulse-like ground motions. To calibrate such empirical models, a library of ground motions where each record is classified as pulse-like or non-pulse-like is required. Many empirical models have been developed in the past by using a version of the NGA database (Chiou et al., 2008), with each ground motion classified as pulse-like or non-pulse-like (e.g., Iervolino and Cornell, 2008; Champion and Liel, 2012, etc.), clearly showing the importance of this line of research. Early research in the field used visually classified pulses, but this approach is not reproducible and does not scale with increasing size of ground-motion databases. With the rapidly increasing size of ground-motion databases (e.g., the NGA-West2 database is over twice the size of the NGA database), there is a need for an algorithm that is both computationally efficient and reproducible.

Proposed herein is an algorithm to classify multi-component ground motions as pulse-like or non-pulse-like. The proposed algorithm uses the wavelet transform of two orthogonal components of a ground-motion time history to find orientations that are likely to contain strong pulses. The ground-motion recording is rotated to those specific orientations and wavelet coefficients of the ground motion in those selected orientations are used to extract pulses from the recorded velocity time history. A non-linear classification algorithm developed using support-vector-machines (Cortes and Vapnik, 1995; Hastie et al., 2001) uses the extracted pulse along with the PGV of the ground-motion record to classify the ground motion as pulse-like or non-pulse-like.

Classifying ground motion as pulse-like or non-pulse-like is a difficult task. There are some ground motions with clear presence or absence of visual pulses in the velocity time history that can be identified unambiguously. However, there are many ground motions that are difficult to classify

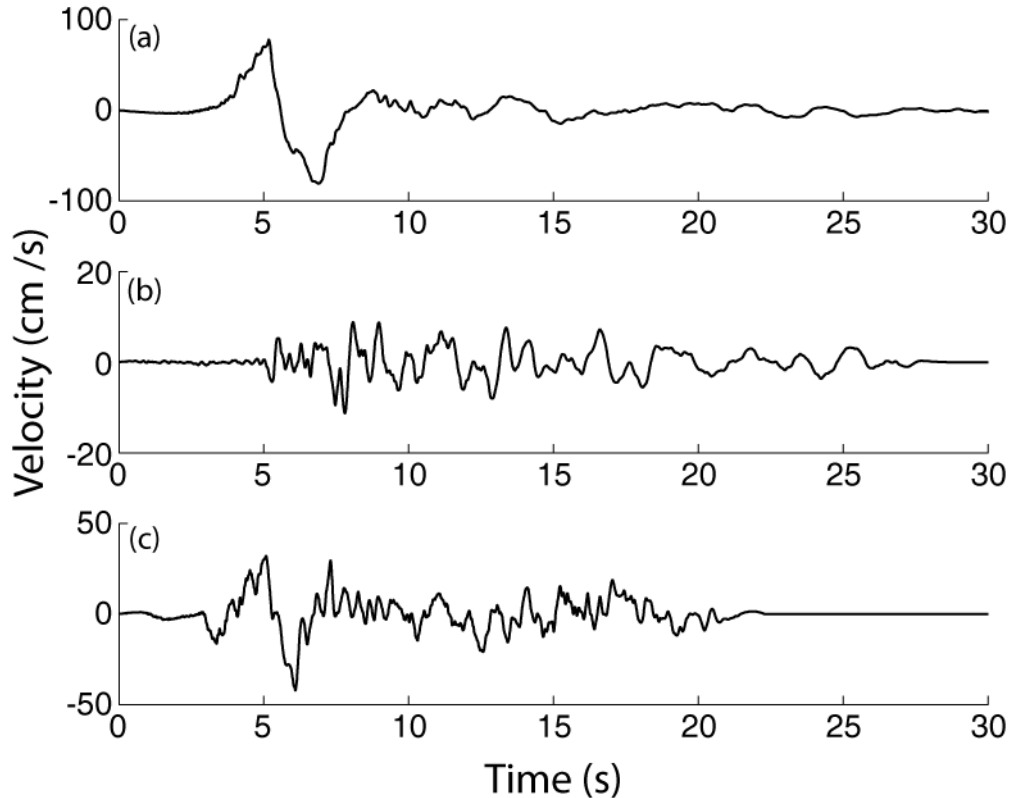


Figure 4.1 Different types of ground motions (a) clear pulse (El Centro Array # 4 recording, from the 1979 Imperial Valley earthquake), (b) clear non-pulse (Pasadena-CIT recording, from the 1971 San Fernando earthquake), and (c) an ambiguous pulse (Salton Sea Wildlife Refuge recording, from the 1987 Superstition Hills earthquake).

as a clear pulse or a clear non-pulse by only visually examining the velocity-time histories (e.g., Figure 4.1c), making manual classification of pulses subjective and make this problem challenging. An algorithm to classify pulse-like ground motions should provide defensible classifications, it should check multiple orientations for pulses, and it should be computationally efficient. The proposed algorithm improves all three aspects relative to the previous pulse classification algorithms.

The Baker (2007) pulse classification algorithm classifies a ground motion as pulse-like by examining a single component of the time history recording. The proposed algorithm improves the state-of-art by analyzing multi-component ground-motion time histories and classifying pulses in arbitrary orientations. The Baker (2007) algorithm used the wavelet transform to identify pulses in only the fault-normal component of a ground motion. It is known that pulse-like ground motions are observed in many orientations other than the fault-normal orientation (e.g., Mavroeidis and Pappageorgiou, 2002; Howard et al., 2005); furthermore the determination of fault-normal orientation may be difficult due to lack of finite fault models. Due to these difficulties, the method proposed by Baker (2007) does not classify ground motion as pulse-like when the pulse is in a non-fault-normal

orientation or when the fault-normal orientation itself is not known. Chapter 2 recommended rotating the ground motion in all non-trivial orientations and classifying each orientation as pulse-like or non-pulse-like using the Baker (2007) algorithm. The ground motion is then labeled as pulse-like if a pulse was found in any orientation. Although method of rotating the ground motion in every orientation overcomes the difficulty of identifying non-fault-normal pulses and deals with cases where the fault-normal orientation is not known, it is computationally very expensive (Changing the algorithm to the one proposed here saves several days of computation, when classifying NGA-West2 database on a desktop computer). With the Chapter 2 approach, the ground motion is labeled pulse-like if even a single orientation is classified as pulse-like. On the other hand, in order to be classified as a non-pulse-like, the ground motion should be classified as non-pulse-like in each orientation. Thus, the criteria for classification as non-pulse-like is much stricter than for classification as pulse-like if many orientations are examined. Therefore, using many orientations for classification increases the chance of false positive classifications (non-pulse-like ground motions classified as pulse-like). The proposed algorithm strikes a balance between using just one orientation and all possible orientations for classification while using an improved classification criteria to reduce the possibility of false-positive classifications. Additionally, we use the orthogonality of the wavelet transform in perpendicular orientations to dramatically reduce the computational expense of the classification procedure.

The procedure proposed here was used to classify ground motions in the NGA-West2 database (Ancheta et al., 2012), and 244 out of 8611 ground motions were classified as pulse-like. We manually filtered the 244 pulse-like ground motions using the source-to-site geometry and site condition information to prepare a list of 145 pulse-like ground motions that were most likely caused by directivity effects. The results of these classifications, along with improved models to predict the probability of pulse and its period for a given earthquake scenario, are also provided.

4.2 WAVELET TRANSFORM FOR MULTI-COMPONENT GROUND MOTION

An earthquake ground-motion time history is a non-stationary signal (i.e., both the ground motion amplitudes and frequencies change over time). The non-stationary nature of ground motion makes it rich in information, so it is difficult to find a feature like a pulse quantitatively by analyzing only the time domain representation of the signal. Since pulses have high energy in a short time interval, and the energy is also concentrated in a small frequency region (i.e., the energy is carried by a coherent pulse with a well defined frequency), a transformation of the signal in a domain that captures both time and frequency characteristics makes finding a pulse easier. Wavelet transforms

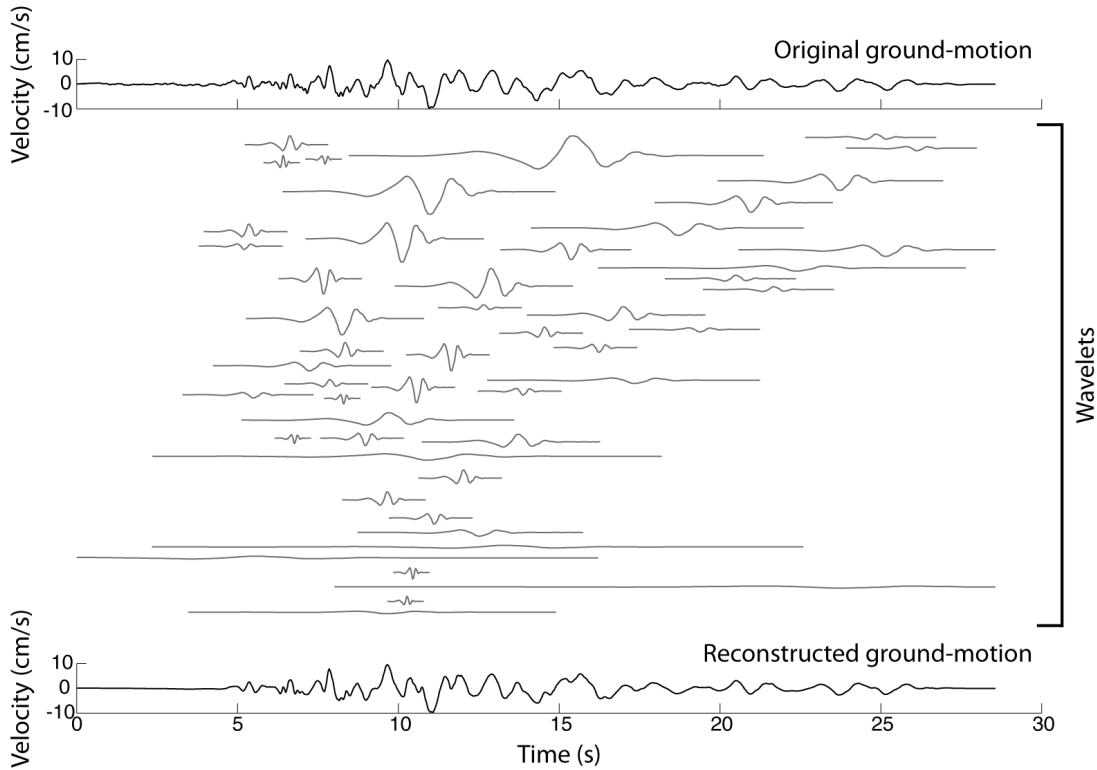


Figure 4.2 The Pasadena - CIT Athenaeum recording from 1971 San Fernando earthquake (original ground motion) is broken down into 50 wavelets using the continuous wavelet transform. The wavelets are summed together to get the reconstructed ground motion, which is an approximation of the original ground motion. The quality of approximation improves as the number of wavelets used is increased.

provide a good representation of the signal in time and frequency domains (e.g., Mallat, 1999) and, thus, are very useful for the task of pulse classification (e.g., Baker, 2007).

The wavelet transform involves representing the signal as a sum of scaled and translated mother wavelets, represented by Equation 4.1

$$\Phi_{s,l}(t) = \frac{1}{\sqrt{s}} \phi\left(\frac{t-l}{s}\right), \quad (4.1)$$

where $\phi(\cdot)$ and $\Phi_{s,l}(\cdot)$ represents the mother wavelet, and the scaled and translated wavelet respectively, as a function of time (t). These wavelets are transformed in the frequency domain by changing the scale parameter s (this amounts to stretching and contracting the mother wavelet) and in time domain by changing the parameter l (this translates the wavelet shape on the time axis). A wavelet transform breaks down the signal into a sum of such scaled and translated mother wavelets, as shown in Figures 4.2 and 4.3. Daubechies wavelet of order 4 was used as the mother wavelet in this study.

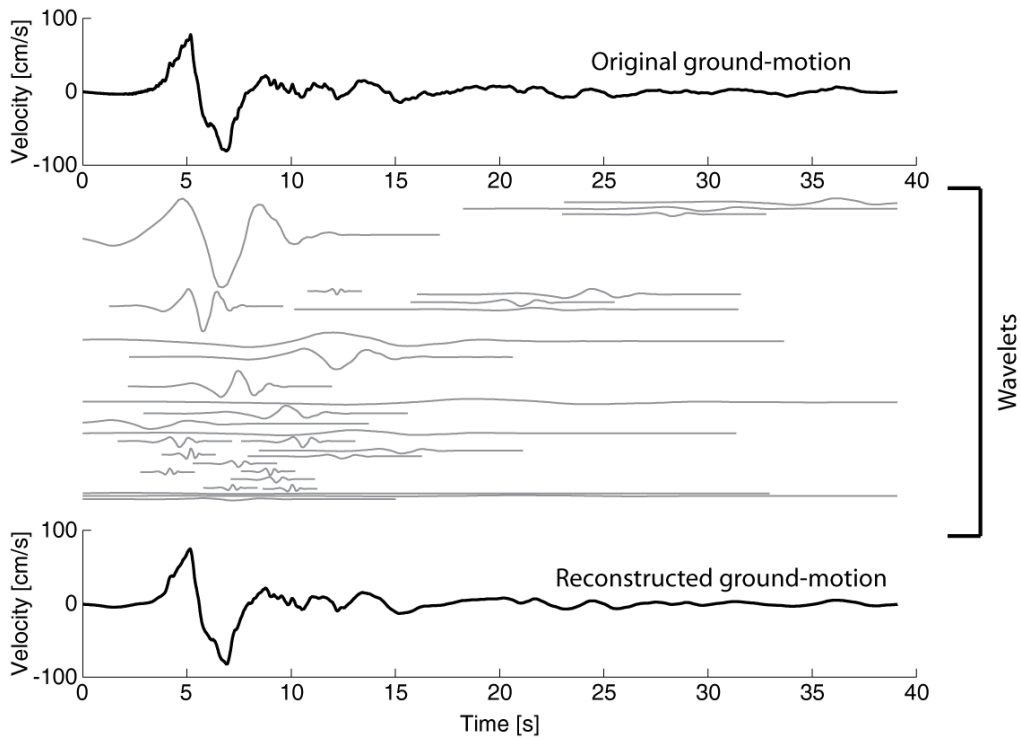


Figure 4.3 The El Centro Array #4 recording from 1979 Imperial Valley earthquake (original ground motion) is broken down into 30 wavelets using the continuous wavelet transform. The wavelets are summed together to get the reconstructed ground motion, which is an approximation of the original ground motion. Note that pulse-like ground motions are dominated by a few strong wavelets.

Mathematically, the wavelet transform is similar to the Fourier transform, but the Fourier transform decomposes the signal into a sum of sine and cosine waves whose frequency is constant with time, while the wavelet transform decomposes the signal into shapes that are localized in small time and frequency regions. This makes wavelets more suited for representing non-stationary signals like earthquake ground motion where the frequency characteristics of the signal change with time. The continuous wavelet transform coefficients for a signal $[f(t)]$ at a particular location (l) and scale (s) can be found using the integral shown in Equation 4.2.

$$c(s, l) = \int_{-\infty}^{\infty} f(t) \frac{1}{\sqrt{s}} \phi\left(\frac{t-l}{s}\right) dt \quad (4.2)$$

The scale and location associated with large amplitude coefficients are associated with a concentration of energy in a small time and frequency range, which is characteristic of a pulse; this property allows us to search for pulses efficiently. Additionally, a linear combination of wavelets can approximate any signal. So, if we use a combination of a few wavelets to describe the pulse, we can identify a wide variety of pulse shapes.

4.2.1 Efficient Wavelet Transform in Multiple Orientations

Continuous wavelet transform coefficients from two orthogonal components of a ground motion can be combined linearly to yield the coefficients for any arbitrary orientation. We used this property to compute wavelet coefficients in all orientations efficiently. This is illustrated below

$$f(t, \theta) = f_1(t) \cdot \cos(\theta) + f_2(t) \cdot \sin(\theta), \quad (4.3)$$

$$c(s, l, \theta) = \frac{1}{\sqrt{s}} \int_{-\infty}^{\infty} f(t, \theta) \phi\left(\frac{t-l}{s}\right) dt, \quad (4.4)$$

where $f_1(t)$ and $f_2(t)$ represent ground motions in orthogonal orientations. $f(t, \theta)$ represents the ground motion in an arbitrary orientation θ away from $f_1(t)$, which can be constructed using the linear combination of $f_1(t)$ and $f_2(t)$, as shown in Equation 4.3. Substituting Equation 4.3 in 4.4 we get

$$c(s, l, \theta) = \frac{1}{\sqrt{s}} \int_{-\infty}^{\infty} (f_1(t) \cdot \cos(\theta) + f_2(t) \cdot \sin(\theta)) \phi\left(\frac{t-l}{s}\right) dt, \quad (4.5)$$

$$= \frac{1}{\sqrt{s}} \int_{-\infty}^{\infty} (f_1(t) \cdot \cos(\theta)) \phi\left(\frac{t-l}{s}\right) dt + \frac{1}{\sqrt{s}} \int_{-\infty}^{\infty} (f_2(t) \cdot \sin(\theta)) \phi\left(\frac{t-l}{s}\right) dt, \quad (4.6)$$

$$= c_1(s, l) \cdot \cos(\theta) + c_2(s, l) \cdot \sin(\theta), \quad (4.7)$$

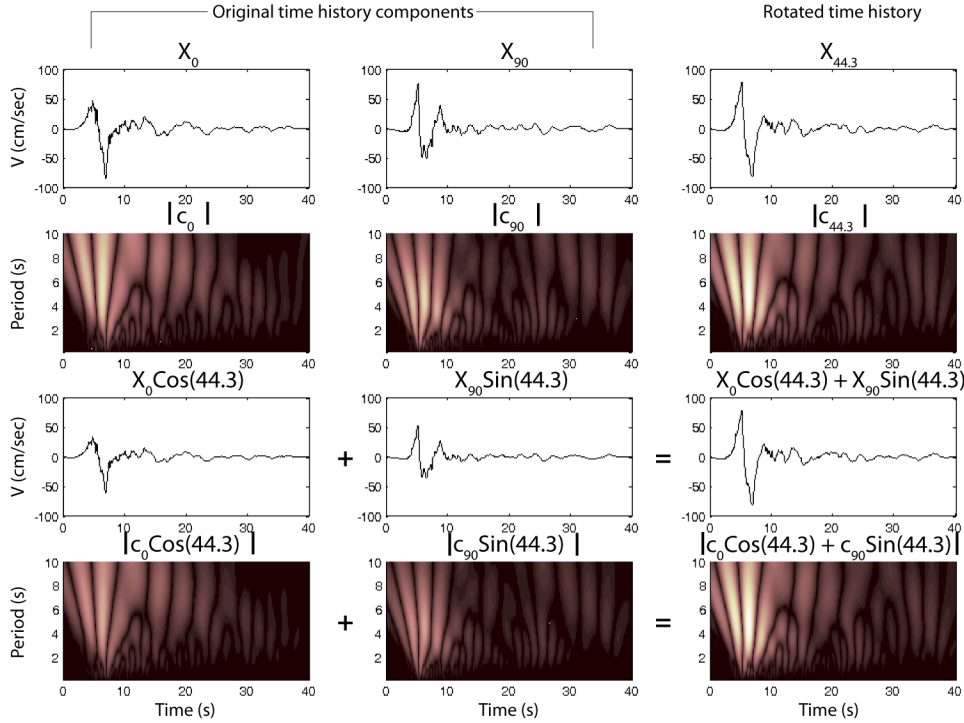


Figure 4.4 Two orthogonal components of a ground motion, labeled X_0 and X_{90} , are shown along with the absolute value of their wavelet transform coefficients, labeled $|c_0|$ and $|c_{90}|$. The wavelet coefficients c_0 and c_{90} are combined to get an estimate of $c_{44.3}$ (coefficients for ground motion in an orientation 44.3 degrees away from X_0). The wavelet coefficients computed directly using the rotated time histories are shown for comparison.

where c_1 and c_2 are the wavelet coefficients corresponding to f_1 and f_2 , respectively. This procedure is shown graphically in Figure 4.4. As the wavelet coefficient in an arbitrary orientation is $c_1 \cos(\theta) + c_2 \sin(\theta)$, the maximum value a coefficient $[c(s, l)]$ can obtain in any orientation is $\sqrt{c_1^2(s, l) + c_2^2(s, l)}$. So, using this procedure we only need to perform two wavelet transforms (of ground motions in orthogonal orientations) to find the maximum value the coefficient at each scale and location can take over all orientations.

4.3 CLASSIFICATION ALGORITHM

The continuous wavelet transform coefficients are computed for two orthogonal components of the ground motion. These coefficients are then used to compute the maximum wavelet coefficients at each location and scale over all orientations using the procedure described above. Large wavelet coefficients indicate a concentration of energy in a small time and frequency region, which is often a good indication of presence of a pulse. The Baker (2007) and Chapter 2 algorithms use the wavelet with the largest coefficient to classify the ground motion as pulse-like/non-pulse-like. Sometimes,

a wavelet other than the largest wavelet can be the dominant pulse in the ground motion. In such cases, Baker (2007) and Chapter 2 produce false negative classifications (pulse-like ground motions classified as non-pulse-like). To avoid this, we use five potential pulses for the purpose of classification. First, we select the wavelet with the largest coefficient as a potential pulse. All coefficients located in a time window of $\pm\frac{1}{2}$ the width of selected wavelet (s) are labeled as being adjacent to the pulse. Then, we find the wavelet with the largest coefficient non-adjacent to the selected coefficient as the second potential pulse. This process is repeated to select five non-adjacent potential pulses. Choosing five potential pulses lowers the probability of missing a pulse having a smaller wavelet coefficient.

For each potential pulse we rotate the velocity time history in the orientation in which the pulse was found, as determined using Equation 4.10

$$c_1(s, l) = c_{max}(s, l) \cdot \cos(\beta), \quad (4.8)$$

$$c_2(s, l) = c_{max}(s, l) \cdot \sin(\beta). \quad (4.9)$$

$$\beta = \tan^{-1} \left(\frac{c_2}{c_1} \right), \quad (4.10)$$

where $c_{max}(s, l)$ represents the maximum wavelet coefficient at scale s and location l over all orientations, and β represents the orientation in which this coefficient is found. We call the velocity time history in this orientation the “original ground motion”. The selected wavelet is then subtracted from the original ground motion to yield a “residual ground motion.” The continuous wavelet transform of the residual ground motion is used to find the wavelet with highest coefficient that has the same scale as the original wavelet and is located within a region of $\pm\frac{1}{2}s$ of the original wavelet (i.e., in a region adjacent to the selected wavelet). This wavelet is then added to the original wavelet to refine the shape of the selected pulse. We repeat this step ten times and use a combination of ten wavelets to define the shape of the extracted pulse.

After the pulse is extracted from the original ground motion, we determine whether the extracted pulse is strong enough for the record to be classified as pulse-like. We use the parameters recommended by Baker (2007) to make this determination: the energy ratio of residual and original ground motion (cumulative squared velocity is used to quantify energy), the peak ground velocity (PGV) ratio of residual and original ground motion, and the PGV of the original ground motion. These variables are selected because they directly measure the strength of the extracted pulse relative to the recorded ground motion. For example, a lower energy ratio means that the pulse subtracted from the original ground motion contributes significantly to the energy of the ground motion, while a lower PGV ratio shows that the pulse is responsible for the peak velocity of the

ground motion (because removing the pulse leads to a large reduction in PGV). The PGV of the recorded ground motion is used to avoid selecting very small ground motions where a single pulse accounts for the PGV and almost all the energy. We do not want to classify these very small PGV ground motions pulse-like as they are not of practical importance for engineers due to their small damage potential. Also, low-amplitude motions from small magnitude earthquakes often look like pulses due to their short duration, but these are not related to directivity and so are excluded.

We observed that the energy ratio and PGV are correlated, and most of the variance in these values lies along one axis, as shown in Figure 4.5. Principal component analysis was used to find the linear combination of the two variables, which captured the most variance, shown in Equation 4.11.

$$PC = 0.63 \cdot (\text{PGV ratio}) + 0.777 \cdot (\text{Energy ratio}) \quad (4.11)$$

The two variables energy ratio and PGV ratio are replaced by this linear combination that captures most of the information expressed by them together. This linear combination is referred hereafter as *PC*. Using *PC* reduces the number of variables used in the classification procedure. The reduction in dimension of the problem makes it easier to find a good classification criteria and visualize it.

We manually classified 50 pulses and 50 non-pulses in the NGA-West2 database and used support vector machines to find a criteria to separate the pulses from non-pulses. Once the criteria was found, we used it to classify more ground motions from the NGA-West2 database, and the clear mis-classifications were manually corrected. The classification scheme was re-fitted using the manually corrected data. This fitting and manual correction was iterated until a satisfactory classification result was reached. Note that only those ground motions that we thought were clearly pulses and non-pulses were used during classification. Ambiguous cases were not used even if they fitted the classification boundary.

Support vector classification boundary was fitted with a second-degree polynomial kernel using *PC* and *PGV* as the independent variables. The classification boundary was used to create the following pulse indicator (*PI*)

$$PI = -1 \cdot (13.819 + 9.384 \cdot PC^2 + 0.0004 \cdot PGV^2 - 17.189 \cdot PC - 0.625 \cdot PGV + 0.585 \cdot PC \cdot PGV). \quad (4.12)$$

The ground motion is classified as pulse-like when the *PI* is positive and is classified as a non-pulse-like if it is negative; *PI* = 0 defines the classification boundary shown in Figure 4.6.

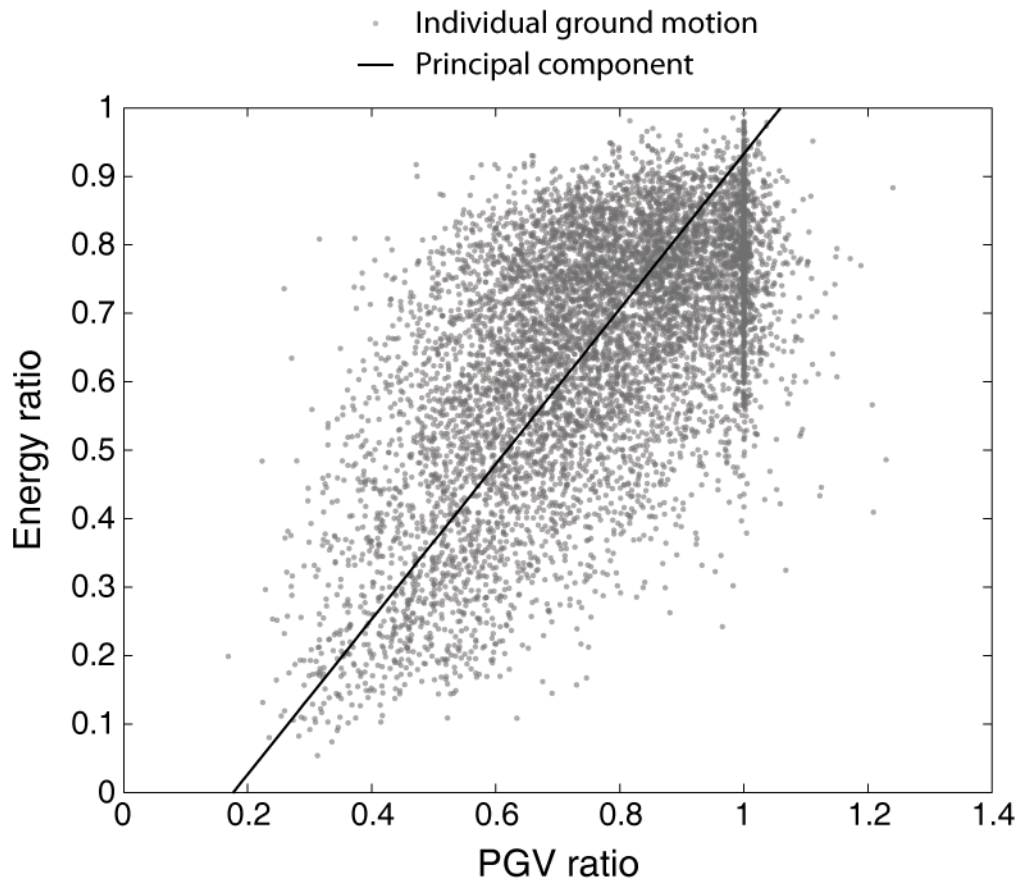


Figure 4.5 The orientation of principal component along with the energy ratio and PGV ratio from individual ground motions is shown (only the ratios from from pulse with largest wavelet coefficient is shown). Note that sometimes the PGV ratio of residual to original ground motion can be greater than 1. The points with PGV ratio equal to 1 represent those ground-motions where the extracted pulse did not cause the PGV.

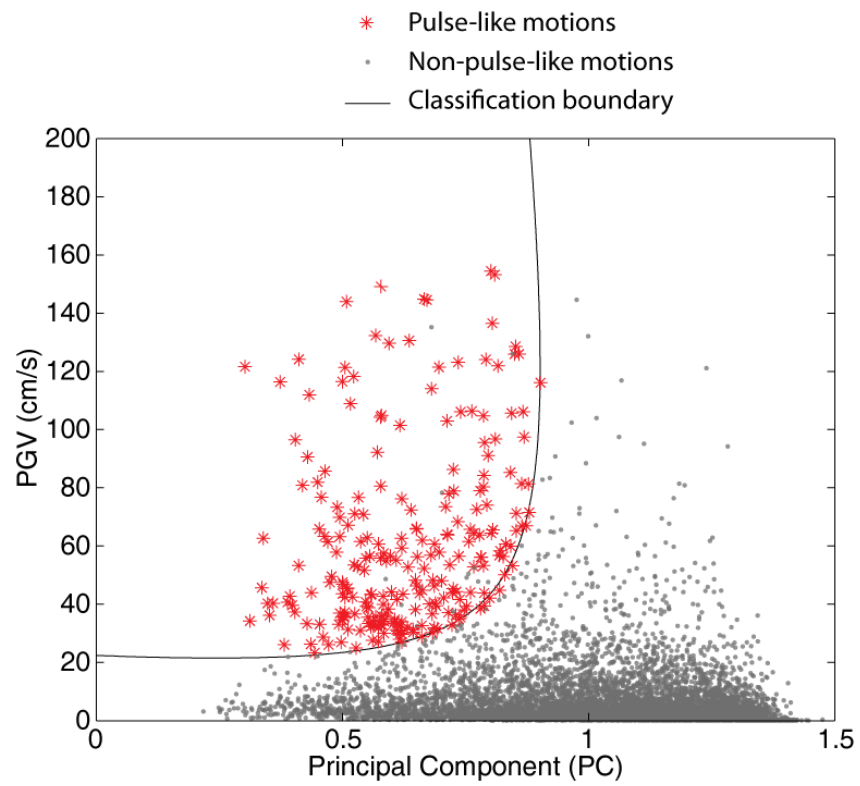


Figure 4.6 Classification boundary of Equation 4.12 shown with individual ground motions. The non-pulse-like ground motions on the positive pulse indicator side of the figure were rejected by the late arrival criteria.

4.3.1 Late Pulses

The pulses caused by directivity effects arrive early in the time-history. The algorithm described above identifies strong pulses regardless of their locations in the time histories. If we are interested in pulses caused primarily by directivity effects, we need an additional criterion to exclude late arriving pulses. Following the approach in Baker (2007), we distinguish between late and early pulses using the cumulative square velocity (CSV), defined as

$$CSV(t) = \int_0^t V^2(u) du. \quad (4.13)$$

where $V(u)$ is the velocity of the ground motion at time u . The time at which $CSV(t)$ attains $x\%$ of the total CSV of the signal is represented as $t_{x\%,orig}$ and $t_{x\%,pulse}$ for the original ground motion and the extracted pulse, respectively. We found that the early arriving pulses had $t_{17\%,orig}$ greater than the $t_{5\%,pulse}$; therefore, pulses with $t_{17\%,orig} \leq t_{5\%,pulse}$ were re-classified as non-pulse-like.

The pulse classification algorithm described above is used to classify each of the five potential pulses, and the ground motion is called pulse-like if any of the five potential pulses are classified as pulse-like. Note, sometimes more than one potential pulse can be classified as pulse-like. In that case the pulse with largest wavelet coefficient is chosen as the dominant pulse. The pulse-like ground-motions identified in the NGA-West2 database are listed in Table B.1 in Appendix B.

4.3.2 Pulse Period

The period of the pulse is an important parameter as the amplification in the response spectrum and structural response due to presence of a pulse is higher for oscillators and structures with periods close to the pulse period. Wavelets do not have a well-defined concept of period, so we use the period associated with the maximum Fourier amplitude of the wavelet as the measure of pulse period. This period is also known as pseudo-period of the wavelet (Baker, 2007). When multiple potential pulses are classified as pulse-like, we used the period of the dominant pulse (the one with highest wavelet coefficient) to represent the pulse period at a site.

4.3.3 Software Implementation

The software implementation of the proposed algorithm is released as open source under MIT license. The code can be accessed at <http://github.com/shreyshahi/PulseClassification>.

4.4 COMPARISON WITH PREVIOUSLY DEVELOPED ALGORITHMS

The algorithm proposed here differs from the Baker (2007) algorithm as the proposed algorithm uses an improved classification criteria and has the ability to handle multi-component ground motions. The proposed algorithm also examines fewer orientations than the Chapter 2 modification to classify pulses in arbitrary orientations. Here, we compare the new classification criteria and the Baker (2007) classification criteria, along with the results from the proposed algorithm with those from other algorithms.

The proposed algorithm uses a classification boundary found using support vector machines. A ground motion is called pulse-like when the pulse-indicator shown in Equation 4.12 is positive. The Baker (2007) algorithm labels a motion as pulse-like if

$$\frac{1}{1 + e^{(-23.3+14.6(\text{PGV ratio})+20.5(\text{energy ratio}))}} > 0.85, \quad (4.14)$$

and its PGV is greater than 30 cm/sec. These classification boundaries are compared in Figure 4.7. As the Baker (2007) pulse-indicator does not use PC , we show the maximum and minimum value that variable PC can take when the pulse-indicator shown by Equation 4.14 is equal to 0.85. The comparison shows that the classification boundaries agree with each other to a large extent. Though the classification regions are similar, the new classification criteria is an improvement as the threshold for PGV is obtained from the data while in Baker (2007) it was set to 30 cm/sec arbitrarily.

Most of the difference in classification results between the proposed and previous algorithms are due to the change in the PGV threshold. Also, some false positive classifications are removed, along with false negative classifications that can occur if only one potential pulse is used for classification. Figure 4.8 shows two examples where the new algorithm's classification differs from the old ones. In the first case, the ground motion has a high pulse indicator but the PGV is slightly below 30 cm/s. So, the PGV cutoff used in Baker (2007) classifies the ground motion as non-pulse-like while the proposed classification criteria classifies this as pulse-like. In the second example, the ground motion is classified as non-pulse-like by the proposed classification algorithm, but when we use the Baker (2007) algorithm in 180 different orientations, the ground motion gets classified as a pulse in 16 of them. This is a case of a false-positive classification, which is fixed by examining a smaller number of orientations. After examining several such cases, we concluded that the classification results from the proposed algorithm are consistently superior to those from the previous algorithms.

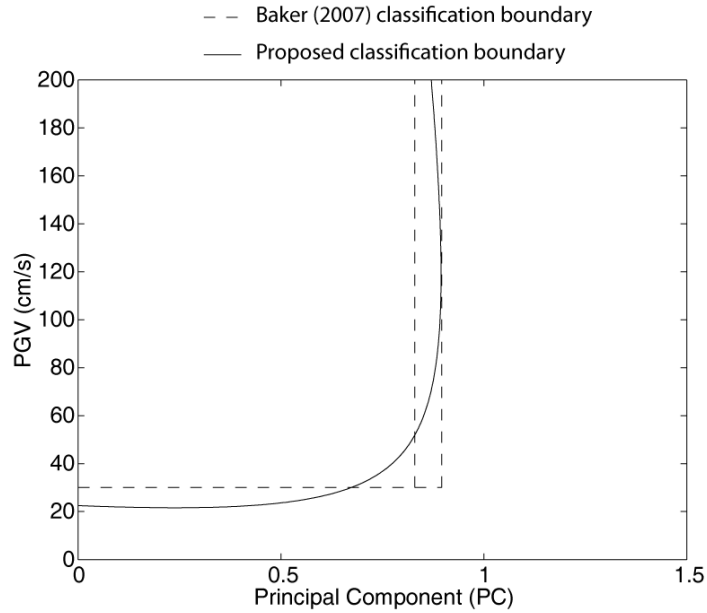


Figure 4.7 Comparison on the classification rule for the proposed algorithm and Baker (2007) algorithm. Note that the two vertical lines for Baker (2007) show the maximum and minimum values PC can take when the pulse indicator is equal to 0.85.

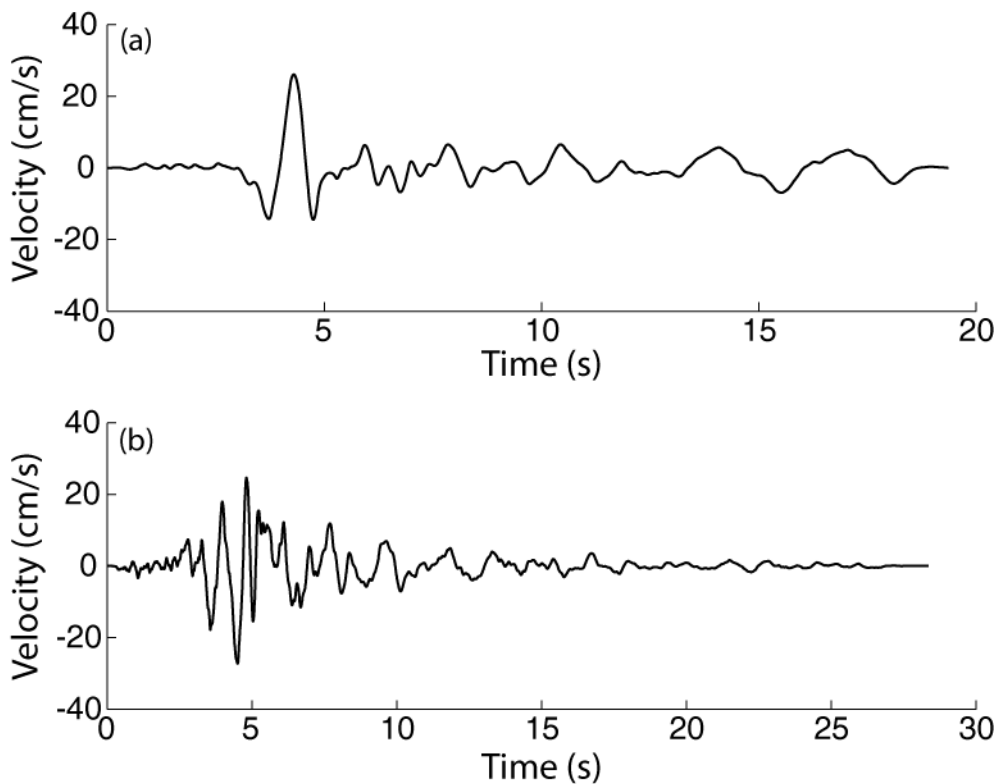


Figure 4.8 (a) A pulse-like ground motion with low PGV (SMART1 M01 recording from 1986 Taiwan earthquake), and (b) a non-pulse classified as pulse-like in a few orientations by the Chapter 2 algorithm (Agnews State Hospital recording from the 1994 Morgan Hill earthquake). For both ground motions the orientation with highest wavelet coefficient is shown.

4.5 DIRECTIVITY MODELS

Pulse-like ground motions can be caused by effects other than directivity, such as basin or soft-soil effects. To develop empirical relationships for pulses caused by directivity effects, we need to identify pulse-like ground motions caused specifically by directivity effects. To prepare a list of directivity ground motions, we manually filtered the list of pulse-like ground motions selected by the proposed algorithm to remove any ground motion that was likely not caused due to directivity effects. We mainly used the source-to-site geometry to identify directivity ground motions from the list of pulse-like ground motions. Ground motions on soft soils with multiple large cycles in the time history were also removed, as it generally indicates presence of soft-soil effects. Studies like Chioccarelli and Iervolino (2010), Bradley and Cubrinovski (2011) and Bradley (2012) were used to aid in manual classification of ground motions from specific earthquakes. A list of pulse-like ground motions classified by the proposed algorithm along with manually filtered list of directivity pulses is provided online (http://www.stanford.edu/~bakerjw/pulse_classification_v2/Pulse-like-records.html). This list of directivity ground motions was used to fit the following models.

4.5.1 Model for Pulse Period

A pulse-like ground motion causes an amplification in the response spectra over a narrow band of periods that is centered about the pulse period (Somerville, 2003). This makes the pulse period a very important parameter. Various researchers have proposed models for the period of the pulse (e.g., Mavroeidis and Papageorgiou, 2003; Somerville, 2003; Bray and Rodriguez-Marek, 2004; Baker, 2007) and most of them model the natural log of pulse period as linearly dependent on moment magnitude (M) of the earthquake. We re-fit this relationship using the directivity pulses identified in the NGA-West2 database. The relationship modeling pulse period (T_p) as a function of earthquake magnitude is shown in Equation 4.15 and the standard deviation of the residual from linear regression is given by Equation 4.16.

$$\ln T_p = -6.207 + 1.075M, \quad (4.15)$$

$$\sigma_{\ln T_p} = 0.61. \quad (4.16)$$

This model is similar to the other published models mentioned above.

4.5.2 Model for Probability of Directivity Pulse

In order to account for directivity effects in hazard analysis, we need a model to predict the probability of observing a directivity pulse at a near-fault site. Several researchers have proposed models for probability of pulse at a site in past (e.g., Iervolino and Cornell, 2008). These past models were fit using lists of pulse-like ground motions, which were used as a surrogate for ground motions with directivity pulses. We re-fit these relationships using the new refined list of directivity pulses, as it should give a better estimate of the probability of observing directivity effects at a site. Several functional forms were explored to find one that predicts with sufficient accuracy. As only 145 directivity pulses were used for the regression, special attention was given to how the predictions extrapolate for cases with little data. We used logistic regression to model the probability of a directivity pulse at a site (see Chapter 2 for detailed explanation of why logistic regression is used for modeling the probability of pulse).

Iervolino and Cornell (2008) compared linear combinations of several predictor variables and found that source-to-site geometry parameters R , s , and θ for strike-slip ruptures and R , d , and ϕ for non-strike-slip ruptures resulted in the best models for predicting the probability of a pulse. These parameters are explained graphically in Figure 4.9. The dataset used to fit these relationships did not include many events with very long ruptures. For cases with large s , these previous models predict very high probability of pulses even at large distances (R), which is not supported by data or by theoretical predictions of directivity. So, we tried several functional forms to fit a model whose predictions extrapolates well for conditions with little data. The models were compared with each others using their AIC (Akaike, 1974) and their predictions for long ruptures. A summary of the models tested in this study and their AIC is given in Table 4.1. For strike-slip faults the models shown in Equations 4.17 and 4.18 had the best AIC (261.02 and 261.73, respectively).

$$P(\text{directivity}|R, s, \theta, \text{strike-slip}) = \frac{1}{1 + \exp(\alpha_0 + \alpha_1 R + \alpha_2 s + \alpha_3 \theta)} \quad (4.17)$$

$$P(\text{directivity}|R, s, \theta, \text{strike-slip}) = \frac{1}{1 + \exp(\alpha_0 + \alpha_1 R + \alpha_2 \sqrt{s} + \alpha_3 \theta)} \quad (4.18)$$

Comparing the contours of predicted probabilities from these two equations, which are shown in Figure 4.10 for fault rupture lengths of 50 km and 200 km, we note that Equation 4.18 extrapolates better for larger ruptures, while the results from both equations are similar for smaller ruptures. For non-strike-slip faults, the model using R , \sqrt{d} , and ϕ had the lowest AIC, so we decided to select it over other models.

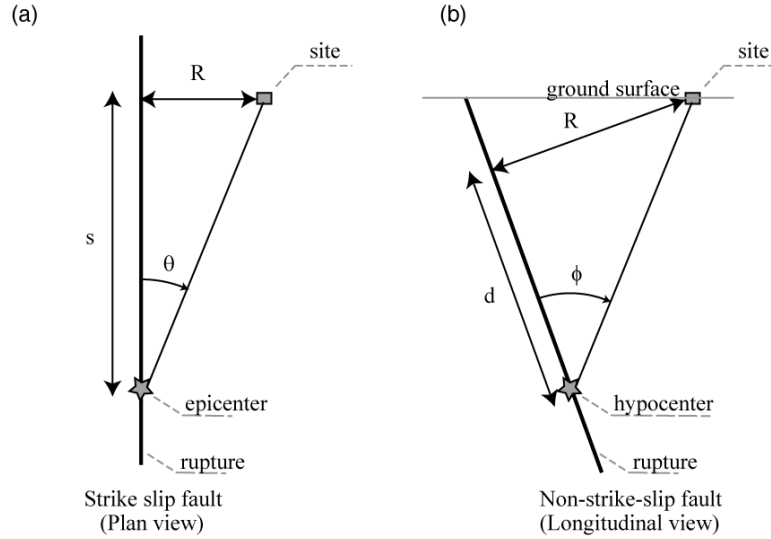


Figure 4.9 Parameters used to fit the logistic regressions for (a) strike-slip and (b) non-strike-slip faults.

The models for probability of directivity pulse are given by Equations 4.19 for strike-slip ruptures and 4.20 for non-strike-slip ruptures.

$$P(\text{directivity}|R, s, \theta, \text{strike-slip}) = \frac{1}{1 + \exp(0.7897 + 0.1378R - 0.3533\sqrt{s} + 0.020\theta)} \quad (4.19)$$

$$P(\text{directivity}|R, d, \phi, \text{non-strike-slip}) = \frac{1}{1 + \exp(1.483 + 0.124R - 0.688\sqrt{d} + 0.022\phi)} \quad (4.20)$$

4.6 PULSE MODELS

Sometimes the effect of pulse-like ground motions on a structure is assumed to be similar, regardless of the cause of the pulse (e.g., Champion and Liel, 2012). If no distinction is made between directivity and non-directivity cases, pooling the directivity and non-directivity pulses together to fit models may be preferred to allow more data to be used in fitting. We re-fit the relationships to predict the probability of a pulse and its period using the entire dataset of pulse-like ground motions.

Table 4.1 Details of logistic regression models tested to predict the probability of directivity pulse at a site.

Parameters	Fault type	AIC
R, s	strike slip	265.03
R, \sqrt{s}	strike slip	263.32
$R, \ln(s)$	strike slip	264.33
R, s, θ	strike slip	261.02
R, \sqrt{s}, θ	strike slip	261.73
$R, \ln(s), \theta$	strike slip	263.51
R, d, ϕ	non strike-slip	613.39
R, d	non strike-slip	627.28
R, \sqrt{d}, ϕ	non strike-slip	607.10
R, d, ϕ , no intercept	non strike-slip	612.03
R, \sqrt{d}, ϕ , no intercept	non strike-slip	614.26

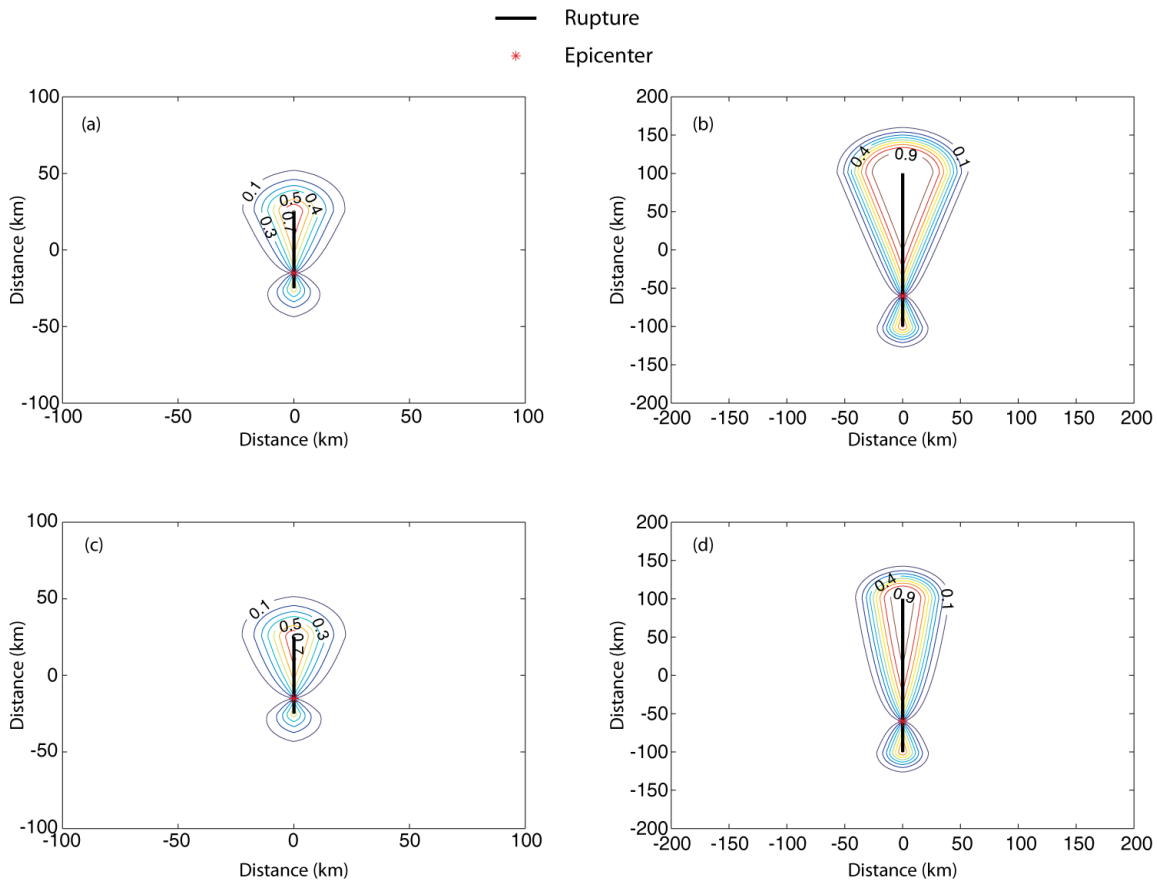


Figure 4.10 Probability of directivity pulse contours. Predictions from Equation 4.17 for rupture of length (a) 50 km and (b) 200 km. Prediction from Equation 4.18 for rupture of length (c) 50 km and (d) 200 km.

The period of a pulse can be predicted using the equations shown below:

$$\ln T_p = -6.51 + 1.11M, \quad (4.21)$$

$$\sigma_{\ln T_p} = 0.57. \quad (4.22)$$

The models proposed to predict the probability of a directivity pulse at the site were re-fit using the entire dataset to predict the probability of observing a pulse-like ground motion at a site. Equations 4.23 and 4.24 describe the model for strike-slip and non strike-slip sites.

$$P(\text{pulse}|R, s, \theta, \text{strike-slip}) = \frac{1}{1 + e^{0.457+0.126R-0.244\sqrt{s}+0.013\theta}} \quad (4.23)$$

$$P(\text{pulse}|R, d, \phi, \text{non-strike-slip}) = \frac{1}{1 + e^{0.304+0.072R-0.208\sqrt{d}+0.021\phi}} \quad (4.24)$$

4.7 CONCLUSION

An algorithm to classify multi-component ground motions as pulse-like or non-pulse-like has been described. The proposed algorithm significantly improves the accuracy and the computational cost of some previous algorithms. The approach uses wavelet transform results from two orthogonal components of ground motions to identify potential pulses from all orientations. These pulses are then classified using a new criterion developed using support vector machines. The algorithm was used to classify all 8611 ground motions in the NGA-West2 database and 244 pulse-like ground motions were identified. These pulse-like ground motions were then manually filtered to identify 145 ground motions most likely caused by directivity effects.

The classified ground motions were used to fit models to predict the period and probability of observing a directivity pulse. Limitations of the dataset were recognized and care was taken to choose functional forms that extrapolate well for cases that were ill constrained by data. We also recognized that in some engineering applications the distinction between directivity and non-directivity pulses may not be important. For such cases fitting the models using a combined dataset of directivity and non-directivity pulses improved the quality of the models, as more data is used. Alternate models fitted using both directivity and non-directivity pulses are also provided.

With increasing size of ground-motion databases, there is an ever increasing need for better and faster algorithms to process them. We hope that the speed and accuracy advantage of the proposed algorithm will allow us to process larger amounts of data and thus help further expand our knowledge of near-fault pulses.

5 Explicit Inclusion of Directivity Effects in Ground-Motion Models

5.1 INTRODUCTION

As noted earlier, directivity effects causes larger than normal ground-motion intensity at near-fault sites and have been known to cause extensive damage in previous earthquakes. Significant amplification in ground-motion intensity makes accounting for directivity effects very important in near-fault hazard assessment. Several methods to modify ground-motion model predictions to account for directivity amplification have been proposed in the past (e.g, Somerville et al., 1997; Spudich and Chiou, 2008; Rowshandel, 2006), but they are correction factors for already existing ground-motion models and are not included explicitly in the models. It is known that directivity effects are more common in near-fault region and the probability of observing directivity effects decreases with increase of distance between the rupture and the site (Iervolino and Cornell, 2008, e.g.,). Along with dependence on distance, the amplification from directivity effects occurs in a band of periods that depends on the earthquake magnitude (sometimes referred as narrow-band amplification, e.g., Somerville, 2003). Since the ground-motion models are fitted using a database that consists of some ground-motion records with directivity effects, the interaction between directivity amplification, magnitude and distance may affect the magnitude and distance scaling relationship of the ground-motion models. Thus, inclusion of directivity effects may lead to changes in the magnitude and distance scaling relationships, which can also affect prediction of non-directivity ground-motion intensity. This change cannot be properly accounted for by adding correction factors on top of existing ground-motion models. The method introduced in Chapter 2, tries to correct the magnitude and distance scaling using simple statistical models, but it is preferable to account for these factors while fitting ground-motion models rather than correcting for it later.

We fitted two ground-motion models: with and without explicit directivity terms. The functional forms proposed by Campbell and Bozorgnia (2008) was used for the non-directivity ground-motion model and the coefficients were re-fitted using a subset of NGA-West2 database being

used to update the Campbell and Bozorgnia (2008) ground-motion model. For the ground-motion model with directivity effects, the Campbell and Bozorgnia (2008) functional form was used for the non-directivity component of the ground-motion model and a simplified form of the amplification model from Chapter 2 was used to model the directivity amplification. The predictions from the directivity and non-directivity ground-motion models were studied in detail and the differences were highlighted. The NGA-West2 database used for fitting the models consists of 8611 earthquake ground-motion recordings from 334 events. This database expands the original NGA database (Chiou et al., 2008) by adding recordings from several shallow crustal earthquakes post-2003. The results from Chapter 4 were used to identify 145 directivity pulses in the database.

Directivity effects depends on the source-to-site geometry, which necessitates the use of source-to-site geometry parameters in the ground-motion models. Use of source-to-site geometry in seismic hazard analysis is not common, so for some studies this information may not be available. Also, in a PSHA, one needs to take expectations over all parameters used in the ground-motion model (e.g., Kramer, 1996; McGuire, 2004). Expectation over source-to-site geometry is generally performed by integrating over possible hypocenter location on the fault plane (Abrahamson, 2000). Thus to use the ground-motion model proposed in this study, one would have to change PSHA software to include integration over hypocenter locations. We anticipate that due to these and other factors, some users of the ground-motion models will prefer a model without the new source-to-site geometry parameters. Since the complete ground-motion model is fitted to the data, dropping the directivity terms will change the ground-motion model prediction and may make the predictions biased with respect to the data used for fitting. We propose models to predict the expected value of directivity effects given a smaller set of parameters (those used in Campbell and Bozorgnia, 2008). In addition, a method is presented to use these average directivity predictions to get unbiased prediction of ground motion when the source-to-site parameters are unknown.

Note that the ground-motion model we present in this paper was fitted empirically using the NGA-West2 database; therefore, the predictions are constrained by data used for fitting. The NGA ground-motion models on the other hand are augmented by simulations and theoretical considerations so that they extrapolate well and provide reasonable prediction of ground-motion intensity, even for cases which are outside the range of data (e.g., Abrahamson and Silva, 2008). The purpose of the models presented here is to demonstrate the procedure of fitting ground-motion models and to study the changes due to inclusion of directivity effects. They are not intended to improve or replace the NGA ground motion models.

5.2 GROUND-MOTION MODELS

To study the changes in ground-motion intensity prediction due to explicit inclusion of directivity effects, two separate ground-motion models (with and without directivity effects) were fitted. These models are described in Equations 5.1 and 5.2 below.

$$\ln Sa_{ij} = f(M_i, R_j, T, Vs30_j, \Theta, \dots) + \eta_i + \epsilon_{ij} \quad (5.1)$$

$$\ln Sa_{ij} = f(M_i, R_j, T, Vs30_j, \tilde{\Theta}, \dots) + I_{directivity} \cdot \ln Amp(T, T_p) + \eta_i + \epsilon_{ij} \quad (5.2)$$

These models will be referred hereafter as CBR (Campbell and Bozorgnia Refitted using NGA-West2 database) and CBSB (Campbell and Bozorgnia with Shahi and Baker directivity model), respectively. The term $f(M_i, R_j, T, Vs30_j, \Theta, \dots)$ in the equations above denotes a ground-motion model without any directivity terms (Campbell and Bozorgnia, 2008, in this study). $I_{directivity}$ is an indicator variable (0/1 variable) indicating presence or absence of a directivity pulse. The $\ln Amp(T, T_p)$ term denotes a model that predicts the amplification in the spectral acceleration at a period T given the observation of directivity pulse of period (T_p), as shown by the equation below

$$\ln Amp(T, T_p) = b_0 \exp \left(b_1 \left(\ln \left(\frac{T}{T_p} \right) - b_2 \right)^2 \right). \quad (5.3)$$

The value of $I_{directivity}$ and T_p were computed for each ground-motion record used to fit the ground-motion models using the method described in Chapter 4. Note that functional forms similar to Equation 5.3 has been used in the past to model narrow-band effects (e.g., Ruiz-García and Miranda, 2004, 2006). Following the convention used to describe ground-motion models, we use subscript i to denote the i^{th} event and the subscript j to denote the j^{th} recording from the i^{th} event in Equations 5.1 and 5.2. The parameters Θ and $\tilde{\Theta}$ in Equations 5.1 and 5.2, respectively, refer to the model coefficients estimated from regression.

5.2.1 Base Ground-Motion Model

We use the Campbell and Bozorgnia (2008) functional form as the base ground-motion model for both the CBR and CBSB models described above. The Campbell and Bozorgnia (2008) ground-motion model predicts the median value of $\ln Sa$ using the following general equation

$$\ln \hat{S}a = f_{mag} + f_{dis} + f_{flt} + f_{hng} + f_{site} + f_{sed} \quad (5.4)$$

where the magnitude term is modeled as

$$f_{mag} = \begin{cases} c_0 + c_1M; & M \leq 5.5 \\ c_0 + c_1M + c_2(M - 5.5) & 5.5 < M \leq 6.5 \\ c_0 + c_1M + c_2(M - 5.5) + c_3(M - 6.5) & M > 6.5 \end{cases} \quad (5.5)$$

where M represents the earthquake magnitude. The distance term is

$$f_{dis} = (c_4 + c_5M) \ln(\sqrt{R_{rup}^2 + c_6^2}) \quad (5.6)$$

where R_{rup} represents the closest distance between the rupture and the site. Note that sometimes we use the variable R in place of R_{rup} for brevity. The fault term is given by

$$f_{flt} = c_7 F_{RV} f_{flt,Z} + C_8 F_{NM} \quad (5.7)$$

F_{RV} is an indicator variable representing reverse or reverse oblique faulting. F_{RV} is 1 when rake lies between 30 to 150 degrees (reverse or reverse oblique faulting) and is 0 otherwise. F_{NM} represents normal or normal oblique faulting and takes the value 1 when rake is between -150 to -30 degrees. $f_{flt,Z}$ depends on the depth to top of the rupture (Z_{tor}) and is defined below

$$f_{flt,Z} = \begin{cases} Z_{tor} & Z_{tor} < 1 \\ 1 & Z_{tor} \geq 1 \end{cases} \quad (5.8)$$

The hanging wall term is given by the equations

$$f_{hng} = c_9 f_{hng,R} f_{hng,M} f_{hng,Z} f_{hng,\delta} \quad (5.9)$$

$$f_{hng,R} = \begin{cases} 1 & R_{JB} = 0 \\ \frac{\max(R_{rup}, \sqrt{R_{JB}^2 + 1}) - R_{JB}}{\max(R_{rup}, \sqrt{R_{JB}^2 + 1})} & R_{JB} > 0, Z_{tor} < 1 \\ (R_{rup} - R_{JB}) / R_{rup} & R_{JB} > 0, Z_{tor} \geq 1 \end{cases} \quad (5.10)$$

$$f_{hng,M} = \begin{cases} 0 & M \leq 6.0 \\ 2(M - 6.0) & 6.0 < M < 6.5 \\ 1 & M \geq 6.5 \end{cases} \quad (5.11)$$

$$f_{hng,Z} = \begin{cases} 0 & Z_{tor} \geq 20 \\ (20 - Z_{tor}) / 20 & 0 \leq Z_{tor} < 20 \end{cases} \quad (5.12)$$

$$f_{hmg,\delta} = \begin{cases} 1 & \delta \leq 70 \\ (90 - \delta)/20 & \delta > 70 \end{cases} \quad (5.13)$$

where R_{JB} is the closest distance between the site and the surface projection of the rupture plane, and δ is the dip of the fault. The shallow site response term is given by

$$f_{site} = \begin{cases} c_{10} \ln \left(\frac{V_{s30}}{k_1} \right) + k_2 \left\{ \ln \left[A_{1100} + c \left(\frac{V_{s30}}{k_1} \right)^n \right] - \ln [A_{1100} + c] \right\} & V_{s30} < k_1 \\ (c_{10} + k_2 n) \ln \left(\frac{V_{s30}}{k_1} \right) & k_1 \leq V_{s30} < 1100 \\ (c_{10} + k_2 n) \ln \left(\frac{1100}{k_1} \right) & V_{s30} \geq 1100 \end{cases} \quad (5.14)$$

V_{s30} refers to the time averaged shear wave velocity in the top 30 m of the site profile and A_{1100} is the median estimate of PGA on a rock outcrop ($V_{s30} = 1100$ m/sec). We used the Campbell and Bozorgnia (2008) model to estimate the A_{1100} values for each recording. The basin response term is given by the equation

$$f_{sed} = \begin{cases} c_{11}(Z_{2.5} - 1) & Z_{2.5} < 1 \\ 0 & 1 \leq Z_{2.5} \leq 3 \\ c_{12} k_3 e^{-0.75[1 - e^{-0.25(Z_{2.5}-3)}]} & Z_{2.5} > 3 \end{cases} \quad (5.15)$$

where $Z_{2.5}$ refers to the depth to the 2.5 km/sec shear-wave velocity horizon, also referred as the sediment depth.

The variables c_1 to c_{12} are the model coefficients, which are obtained through mixed-effects regression.

5.3 FITTING THE GROUND-MOTION MODELS

A subset of the NGA-West2 database, updated using the Campbell and Bozorgnia (2008) model, was used to statistically fit the models shown in Equations 5.1 and 5.2. The ground-motion models were fitted using mixed-effects regression to model the inter (between) and intra (within) event errors (e.g., Brillinger and Preisler, 1985). The mixed-effects regression was performed using a stable iterative technique proposed by Abrahamson and Youngs (1992) and the least squares fitting was performed using stochastic gradient descent algorithm (Zhang, 2004). The CBR model (Equation 5.1) was fitted first. The regression procedure was validated by comparing the results from this algorithm with the published Campbell and Bozorgnia (2008) results. This was followed by fitting of

CBSB model (Equation 5.2). The coefficients of CBSB models were compared with those from the CBR model, and the coefficients that did not produce appreciable change in the model prediction were labeled as fixed. The CBSB model was refitted, and the coefficients identified as fixed were set to their values in CBR model. The stochastic-gradient-descent and the iterative mixed effects fitting algorithms introduce randomness in the fitting procedure. Thus, small changes in fitted coefficients can occur due to random chance. The fixing of coefficients removes some of these small random changes, which isolates significant changes due to explicit inclusion of directivity effects thus allowing a better comparison of the two ground-motion models.

5.3.1 Fitting CBR

The CBR model shown in Equation 5.1 was fitted using the algorithm described above. The regression was done to predict the RotD50 spectral acceleration (Sa_{RotD50}), which is defined as the median value of spectral acceleration at a period over all orientation (Boore, 2010, see) at 21 different periods and the fitted model coefficients at each period are presented in Table 5.1. Note that we do not re-estimate the parameters k_1 , k_2 , and k_3 , their values from Campbell and Bozorgnia (2008) are used. Regression without any constraints leads to coefficients that predicts over saturation of ground-motion intensity with respect to magnitude (intensity decreasing with increase in magnitude) at low periods. Though there is some support for over saturation of ground-motion intensity with respect to magnitude (e.g., Schmedes et al., 2006), the evidence in data is weak and there is a lack of scientific consensus on this topic (e.g., Abrahamson et al., 2008, notes that none of the NGA modelers allowed over saturation in their models). Following the recommendation of Campbell and Bozorgnia (2008), we set the coefficient $c_3 = -c_1 - c_2 - c_5 \ln(c_6)$ at periods where regression leads to coefficients that predicts over saturation of intensity with magnitude. Apart from correcting for over saturation at some periods, no other post processing or smoothing was applied to the model coefficients, which are presented in Table 5.1.

Handling of missing parameters

We adopted a policy of not using any recording that had missing values of any parameters, except $Z_{2.5}$, in the regression. The $Z_{2.5}$ values are not known for many records in the NGA-West2 database. Thus, throwing these records away would significantly reduce the number of data-points and adversely impact the quality of regression results. For the records with missing $Z_{2.5}$ values, the sediment effect (f_{sed} in Campbell and Bozorgnia, 2008) and the gradient of the f_{sed} coefficients (c_{11}, c_{12}) used in the stochastic gradient descent algorithm were both set to 0. Thus, only the records with known $Z_{2.5}$ values were used to fit the values of c_{11} and c_{12} , while all recordings (even with

Table 5.1 Coefficients for the CBR ground-motion model.

T(s)	c_0	c_1	c_2	c_3	c_4	c_5	c_6	c_7	c_8	c_9	c_{10}	c_{11}	c_{12}
0.01	-1.729	0.510	-0.444	-0.378	-2.208	0.178	5.779	0.239	-0.426	0.675	1.017	-0.030	0.292
0.02	-1.693	0.511	-0.450	-0.377	-2.222	0.180	5.758	0.230	-0.446	0.697	1.062	-0.027	0.282
0.03	-1.569	0.509	-0.426	-0.396	-2.258	0.179	5.766	0.210	-0.442	0.731	1.125	-0.036	0.310
0.05	-1.227	0.519	-0.412	-0.441	-2.363	0.188	5.890	0.164	-0.507	0.803	1.248	-0.032	0.342
0.075	-0.670	0.527	-0.433	-0.493	-2.546	0.203	7.116	0.129	-0.585	0.819	1.442	-0.077	0.350
0.1	-0.327	0.519	-0.439	-0.496	-2.552	0.200	8.033	0.120	-0.510	0.813	1.546	-0.054	0.318
0.15	-0.145	0.504	-0.460	-0.453	-2.487	0.188	8.800	0.146	-0.404	0.765	1.789	-0.067	0.424
0.2	-0.496	0.495	-0.394	-0.454	-2.302	0.173	7.704	0.167	-0.247	0.706	2.000	-0.008	0.445
0.25	-0.894	0.511	-0.332	-0.456	-2.219	0.167	6.695	0.230	-0.167	0.642	2.149	0.001	0.345
0.3	-1.158	0.519	-0.347	-0.377	-2.117	0.162	6.183	0.220	-0.207	0.676	2.273	-0.034	0.292
0.4	-1.443	0.525	-0.287	-0.361	-2.101	0.165	5.493	0.285	-0.158	0.619	2.408	0.030	0.237
0.5	-2.534	0.689	-0.461	-0.236	-2.017	0.151	5.024	0.316	-0.126	0.590	2.369	0.006	0.183
0.75	-4.800	1.025	-0.767	-0.136	-1.985	0.155	4.294	0.354	-0.068	0.647	1.978	0.002	0.101
1	-6.388	1.237	-0.830	-0.140	-1.990	0.144	4.207	0.395	0.105	0.545	1.467	0.094	0.140
1.5	-8.705	1.536	-0.953	-0.197	-1.999	0.148	4.219	0.366	0.021	0.527	0.373	0.215	0.085
2	-9.742	1.617	-0.735	-0.427	-2.015	0.148	4.409	0.358	0.032	0.402	-0.471	0.212	0.034
3	-10.652	1.606	-0.106	-0.937	-1.857	0.124	4.633	0.264	-0.043	0.129	-0.795	0.148	0.010
4	-11.323	1.581	0.276	-1.175	-1.821	0.119	4.647	0.152	-0.020	-0.112	-0.783	0.087	0.053
5	-11.797	1.583	0.532	-1.386	-1.719	0.110	4.723	-0.024	-0.091	-0.230	-0.756	0.010	0.038
7.5	-12.623	1.548	0.525	-1.123	-1.730	0.126	4.520	-0.094	-0.404	-0.354	-0.669	0.028	0.068
10	-13.128	1.608	0.166	-0.811	-1.752	0.125	4.165	-0.301	-0.224	-0.383	-0.476	0.195	0.080

missing $Z_{2.5}$) were used to fit other coefficients.

Due to the low number of records in NGA-West2 database with known $Z_{2.5}$ values, we had less confidence in the sediment effect coefficients fitted empirically. Therefore, the comparisons shown below uses $Z_{2.5}$ value of 2 km to forcibly set the value of f_{sed} to 0 for each comparison case. All the comparison shown below assumes a vertical strike-slip fault rupture (dip = 90, rake = 180).

Comparison of magnitude scaling

The magnitude scaling is compared for intensity predictions at periods of 0.1, 0.2, 1, and 3 sec when R_{rup} and R_{jb} are 30 km (vertical fault) and V_{s30} is 760 m/sec. Figure 5.1 shows the comparison of $Sa_{GMRotI50}$ prediction from Campbell and Bozorgnia (2008) and Sa_{RotD50} prediction from CBR model. The magnitude scaling of both models are very similar, and the predictions are within a factor of 1.66. For comparison, the original NGA models are generally within a factor of 1.5 to 2 of each other for similar cases (Abrahamson et al., 2008). Given that there is expected variability due to modeling a different intensity measure and using a different database, we conclude that the results are reasonably close to each other.

Comparison of distance scaling

The distance scaling of CBR and Campbell and Bozorgnia (2008) is compared for the case when magnitude is 7 and V_{s30} is 760 m/sec. Figure 5.2 shows the comparison of predictions from Campbell and Bozorgnia (2008) and CBR models as a function of distance. Both models show very

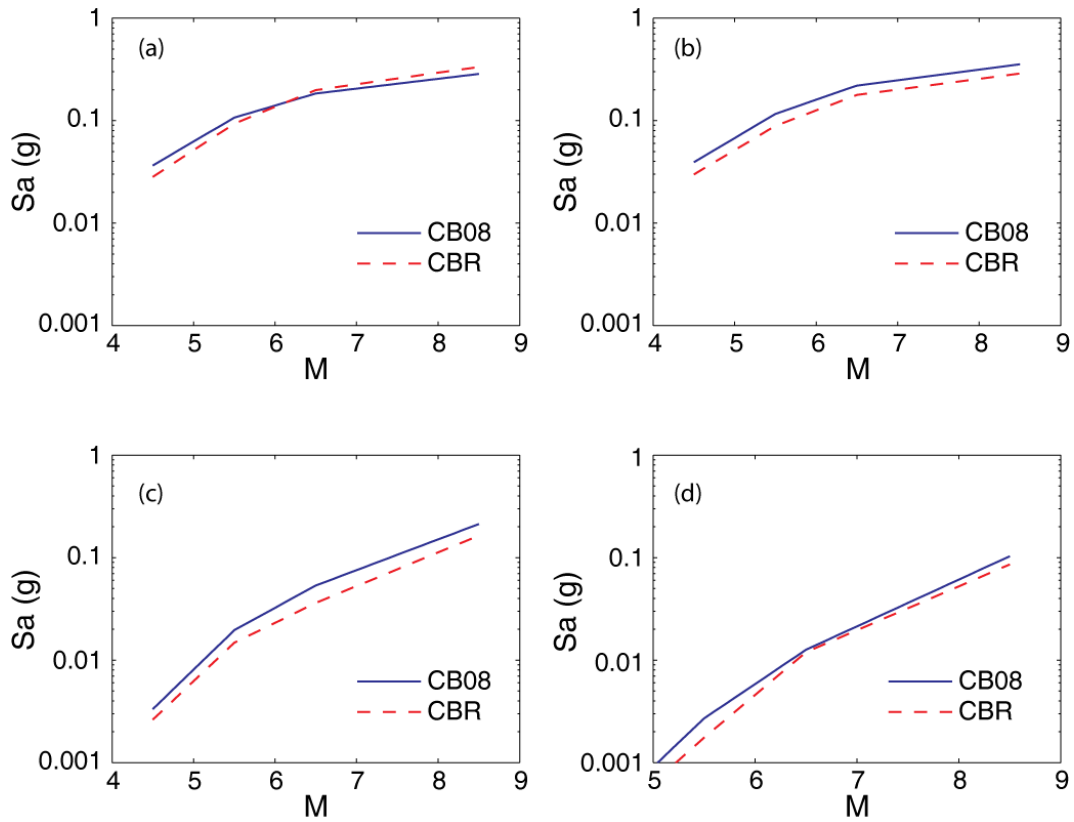


Figure 5.1 Comparison of magnitude scaling of the Campbell and Bozorgnia (2008) and CBR model fitted in this study, for $R_{rup} = 30$ km, $V_{s30} = 760$ m/sec and periods (a) 0.1 sec, (b) 0.2 sec, (c) 1 sec, and (d) 3 sec.

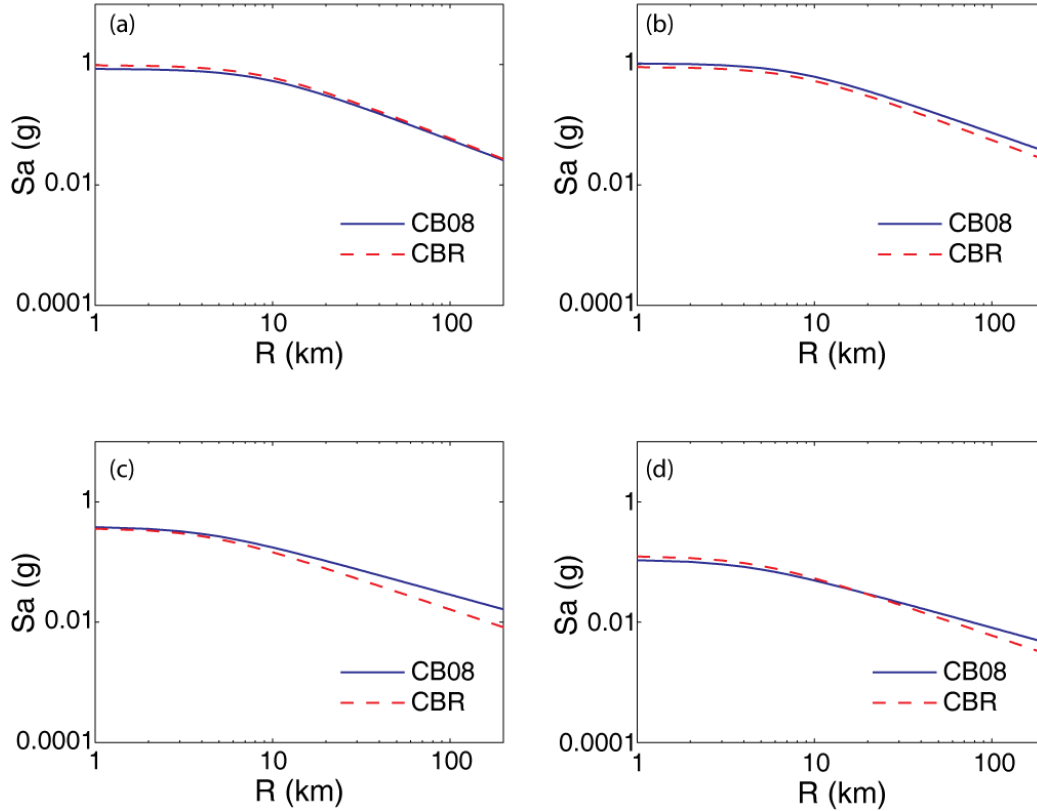


Figure 5.2 Comparison of distance scaling of the Campbell and Bozorgnia (2008) and CBR model fitted in this study for $M = 7$, $V_{s30} = 760$ m/sec and periods (a) 0.1 sec, (b) 0.2 sec, (c) 1 sec and (d) 3 sec.

similar distance scaling and are within a factor of 1.6.

Comparison of V_{s30} scaling

The V_{s30} scaling of CBR and Campbell and Bozorgnia (2008) is compared when magnitude is 7 and R_{rup} and R_{jb} are 30 km. Figure 5.3 shows the predictions from Campbell and Bozorgnia (2008) and CBR models as a function of V_{s30} . The predictions are close to each other and are within a factor of 1.6 from each other.

Comparison of response spectra predictions

The median response spectra predicted by Campbell and Bozorgnia (2008) and the CBR model are compared for strike-slip earthquakes of magnitudes 5,6, 6.5, and 7.5 at R_{rup} and R_{jb} of 10 km at a rock site. The comparison is shown in Figure 5.4 and the predictions are within a factor of 1.5 of each other. Note that the median response spectra predicted by CBR model is not smooth. Smoothing of coefficients, which is a common post-processing used in the NGA models, was not

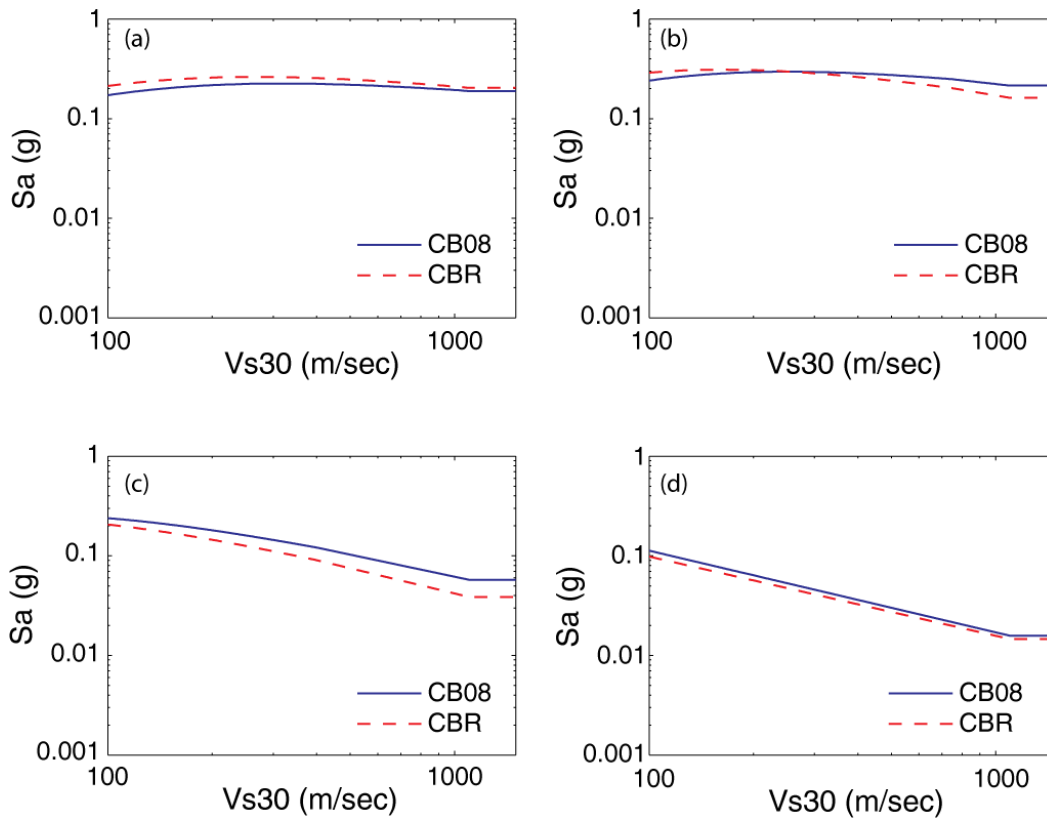


Figure 5.3 Comparison of V_{s30} scaling of the Campbell and Bozorgnia (2008) and CBR model fitted in this study for $M = 7$, $R_{rup} = 30$ km and periods (a) 0.1 sec, (b) 0.2 sec, (c) 1 sec, and (d) 3 sec.

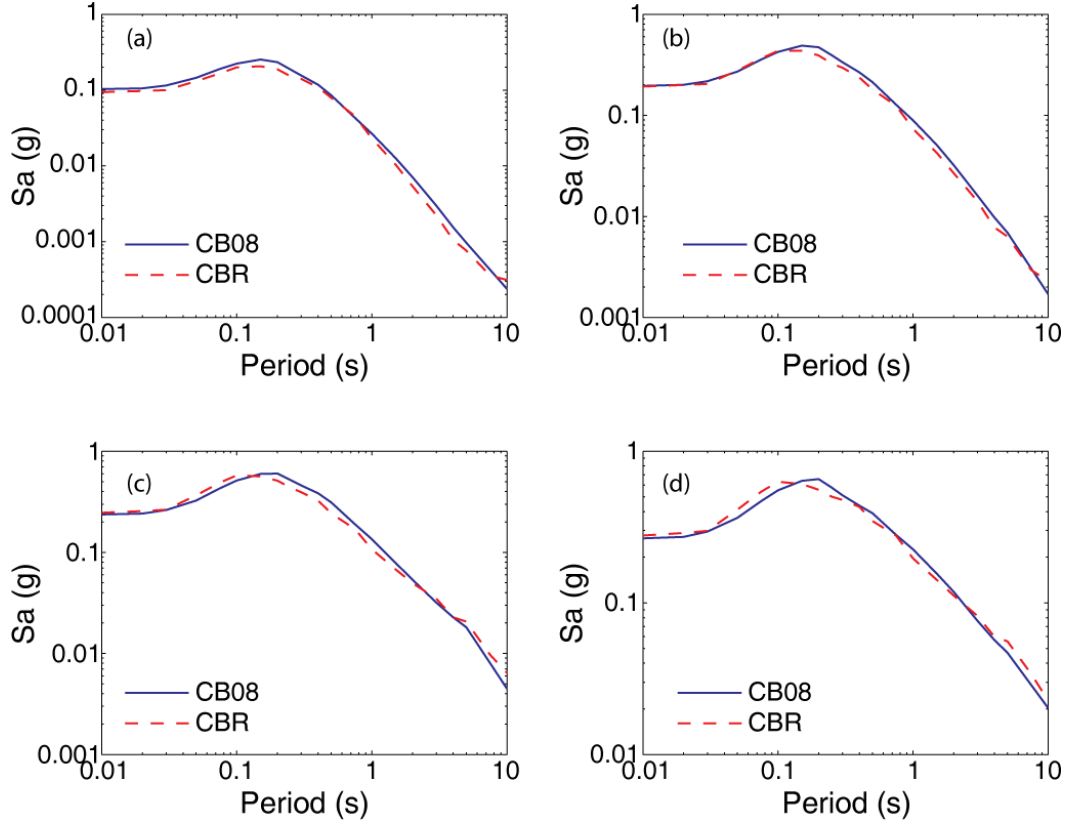


Figure 5.4 Comparison of the median response spectra predicted by Campbell and Bozorgnia (2008) and CBR model for (a) $M = 5$, (b) $M = 6$, (c) $M = 6.5$, and (d) $M = 7.5$.

done after the CBR regression.

Validation of fitting algorithm

The Campbell and Bozorgnia (2008) ground motion model was fitted to predict the $Sa_{GMRot150}$ intensity of a ground motion, while the CBR model was fitted to predict the Sa_{RotD50} intensity. Since the $Sa_{GMRot150}$ and Sa_{RotD50} intensity measures are generally close to each other (e.g., Boore, 2010), we expect the prediction from Campbell and Bozorgnia (2008) and CBR to be similar. The comparison of magnitude, distance and V_{s30} scaling shows that the two models are close to each other within reasonable error.

5.3.2 Fitting the CBSB Model

After validating the mixed-effects regression algorithm, we used it to fit the CBSB ground-motion model (Equation 5.2). The list of directivity pulses (records with $I_{directivity} = 1$) and their periods required to fit CBSB model were taken from Chapter 4. The CBSB model coefficients were fitted empirically in two stages. In the first stage, mixed-effects regression was performed without any

constraints. After the first regression the coefficients were compared with those from the CBR model to find the coefficients that produced significant changes in the ground-motion intensity prediction. To check the significance of parameters, all parameters were set to their CBR values, and each coefficient was changed one at a time to their value found in the first stage of CBSB regression. Using this method we were able to isolate the change in median intensity prediction due to change in each parameter. Changes in coefficients c_1 , c_2 , c_3 , c_4 , c_5 , c_7 , and c_8 produced significant change in the median prediction of ground-motion intensity, and these coefficients were labeled as important parameters. We refitted the CBSB model keeping the non-important parameters fixed to their CBR values. The fixing of coefficient was performed to isolate the change in models to only those coefficients that results in significant changes in the prediction. This makes the comparison between the two models easier as explained earlier.

The directivity model described in Equation 5.3 uses coefficients b_0 , b_1 , and b_2 , which are period independent; other ground-motion model coefficients (c_0 to c_{12}) depend on the spectral acceleration period. Fitting of period-dependent and independent coefficients together makes this regression more complex than that for regular ground-motion models, and an iterative technique was used. Initially, all coefficients were allowed to change with period. In the next step the values of coefficients c_0 to c_{12} were fixed to that in the previous model, and period-independent coefficients, b_0 , b_1 , and b_2 were fitted using data pooled across all periods. Finally c_0 to c_{12} were re estimated from regression with fixed period-independent coefficients b_0 , b_1 , and b_2 . The last two steps were repeated until the coefficients converged to their final values. The coefficients estimated from the final regression are presented in Tables 5.2 and 5.3.

Directivity amplification

As explained above, presence of a directivity pulse amplifies the spectral acceleration (Sa) in a band of periods close to the period of the pulse. Thus, we expect a ground-motion model accounting for directivity effects to predict a different spectral shape than that predicted by a ground-motion model without any explicit directivity terms. Figure 5.5 shows the median response spectra predicted by the CBR and the CBSB models from a strike-slip earthquake of magnitude 6.5 at a distance of 10 km ($R_{jb} = R_{rup}$ for vertical strike-slip fault). For this comparison the $I_{directivity}$ is set to 1 and T_p is set to 2.2 sec (median T_p for $M = 6.5$). Note that specifying values of $I_{directivity}$ and T_p assumes occurrence of a particular pulse. Although one can assume occurrence of a particular pulse when computing ground-motion intensity from a specified scenario, when predicting ground motions from a future earthquake one does not know the value of $I_{directivity}$ and T_p . In this case $I_{directivity}$ and T_p can be treated as random variables, and $I_{directivity}$ can be modeled as a Bernoulli random

Table 5.2 Coefficients for the CBSB ground-motion model.

T(s)	c_0	c_1	c_2	c_3	c_4	c_5	c_6	c_7	c_8	c_9	c_{10}	c_{11}	c_{12}
0.01	-1.729	0.510	-0.440	-0.396	-2.278	0.185	5.779	0.227	-0.493	0.675	1.017	-0.030	0.292
0.02	-1.693	0.519	-0.455	-0.390	-2.299	0.186	5.758	0.214	-0.510	0.697	1.062	-0.027	0.282
0.03	-1.569	0.509	-0.418	-0.419	-2.321	0.187	5.766	0.199	-0.516	0.731	1.125	-0.036	0.310
0.05	-1.227	0.523	-0.389	-0.491	-2.467	0.201	5.890	0.143	-0.584	0.803	1.248	-0.032	0.342
0.075	-0.670	0.536	-0.397	-0.571	-2.673	0.220	7.116	0.092	-0.707	0.819	1.442	-0.077	0.350
0.1	-0.327	0.526	-0.383	-0.611	-2.705	0.225	8.033	0.082	-0.657	0.813	1.546	-0.054	0.318
0.15	-0.145	0.511	-0.428	-0.531	-2.606	0.206	8.800	0.116	-0.500	0.765	1.789	-0.067	0.424
0.2	-0.496	0.495	-0.393	-0.473	-2.352	0.182	7.704	0.162	-0.297	0.706	2.000	-0.008	0.445
0.25	-0.894	0.508	-0.363	-0.474	-2.246	0.172	6.695	0.226	-0.230	0.642	2.149	0.001	0.345
0.3	-1.158	0.525	-0.425	-0.331	-2.177	0.172	6.183	0.233	-0.259	0.676	2.273	-0.034	0.292
0.4	-1.443	0.524	-0.340	-0.307	-2.135	0.173	5.493	0.298	-0.200	0.619	2.408	0.030	0.237
0.5	-2.534	0.679	-0.471	-0.207	-2.032	0.160	5.024	0.316	-0.141	0.590	2.369	0.006	0.183
0.75	-4.800	1.000	-0.778	-0.130	-1.986	0.159	4.294	0.354	-0.076	0.647	1.978	0.002	0.101
1	-6.388	1.207	-0.835	-0.126	-1.992	0.156	4.207	0.385	0.097	0.545	1.467	0.094	0.140
1.5	-8.705	1.503	-0.956	-0.204	-1.997	0.157	4.219	0.358	0.008	0.527	0.373	0.215	0.085
2	-9.742	1.581	-0.743	-0.444	-2.014	0.157	4.409	0.343	0.024	0.402	-0.471	0.212	0.034
3	-10.652	1.564	-0.114	-0.966	-1.841	0.133	4.633	0.260	-0.054	0.129	-0.795	0.148	0.010
4	-11.323	1.543	0.264	-1.223	-1.794	0.124	4.647	0.152	-0.032	-0.112	-0.783	0.087	0.053
5	-11.797	1.535	0.547	-1.454	-1.677	0.116	4.723	-0.021	-0.122	-0.230	-0.756	0.010	0.038
7.5	-12.623	1.487	0.662	-1.312	-1.632	0.126	4.520	-0.096	-0.494	-0.354	-0.669	0.028	0.068
10	-13.128	1.552	0.298	-1.006	-1.733	0.128	4.165	-0.294	-0.358	-0.383	-0.476	0.195	0.080

Table 5.3 Period-independent coefficients of the directivity terms.

b_0	0.72
b_1	-1.10
b_2	-0.19

variable with probability of directivity pulse given by Equation 5.16 given below

$$P(\text{directivity}) = \begin{cases} \frac{1}{1+\exp(0.790+0.138R_{rup}-0.353\sqrt{s}+0.020\theta)} & \text{strike-slip fault,} \\ \frac{1}{1+\exp(1.483+0.124R_{rup}-0.688\sqrt{d}+0.022\phi)} & \text{non-strike-slip fault.} \end{cases} \quad (5.16)$$

T_p can be described by a log-normal distribution with $\mu_{\ln T_p}$ and $\sigma_{\ln T_p}$, described by Equations 5.17 and 5.18 below

$$\mu_{\ln T_p} = -6.207 + 1.075M, \quad (5.17)$$

$$\sigma_{\ln T_p} = 0.61. \quad (5.18)$$

See Chapter 4 for more details about these equations. The median ground-motion intensities when T_p and $I_{\text{directivity}}$ are unknown can be computed by taking a expectation over the random variables as shown by Equations 5.19 and 5.20

$$\ln \hat{S}a = E_{I_{\text{directivity}}, T_p | M, R, V s30 \dots} [f(M, R, T, V s30, \dots) + I_{\text{directivity}} * \ln \text{Amp}(T, T_p)], \quad (5.19)$$

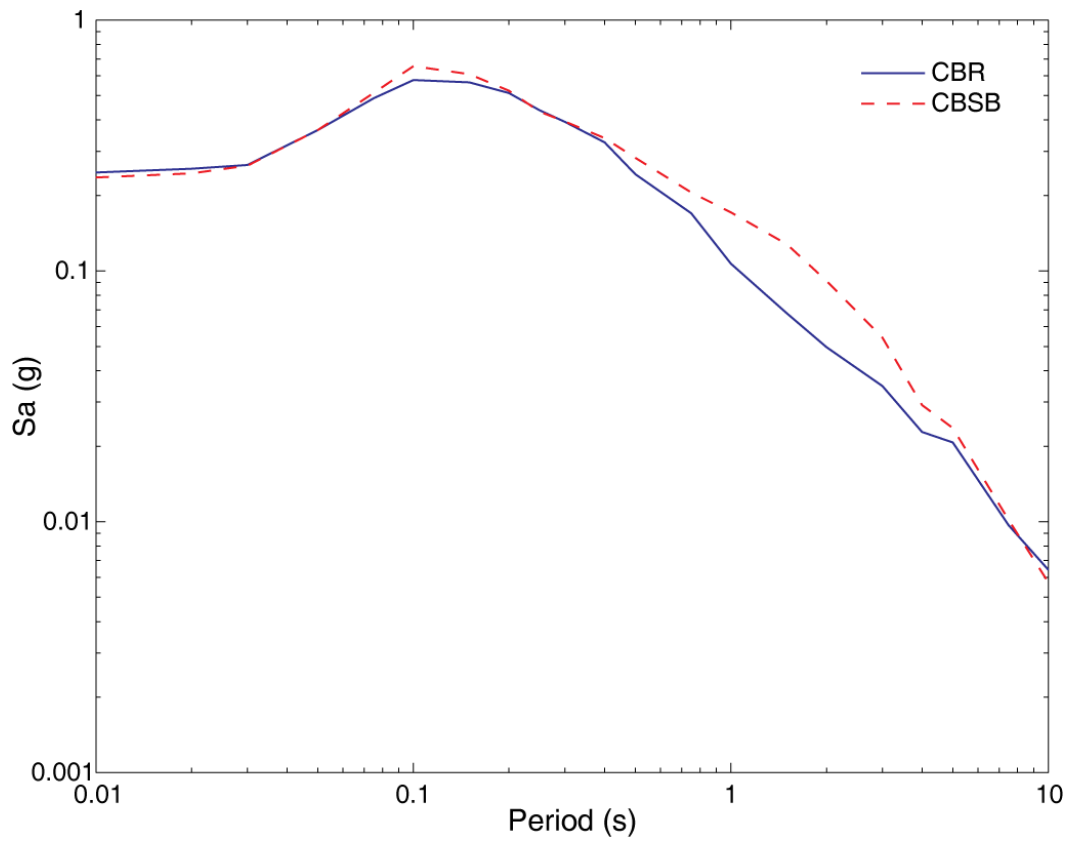


Figure 5.5 Comparison of the median response spectra predicted by CBSB and CBR models when a directivity pulse of period 2.2 sec is assumed to have occurred.

$$\ln \hat{S}a = f(M, R, T, Vs30, \dots) + P(\text{directivity} | M, R, T, Vs30, \dots) * E_{T_p | M}(\ln Amp(T, T_p)). \quad (5.20)$$

where the distribution of T_p given M and the probability of pulse are computed using the Equations 5.16, 5.17, and 5.18. Note that the probability of pulse computation requires the knowledge of source-to-site geometry (location of hypocenter and the site relative to the rupture). If the geometry information is not known, another expectation over the locations can be performed, as discussed below. Closed-form solution of the expectation of $\ln Amp(T, T_p)$ over $T_p | M$ exists and is derived in Appendix C. Thus, we can compute the expectation shown in Equation 5.20 using a closed form equation rather than doing a numerical integration. Figure 5.6 shows the response spectra predicted by Equation 5.20, for an earthquake with magnitude of 6.5 at a distance of 10 km and a source-to-site geometry that has a probability of observing a directivity pulse of 0.6. For comparison, the CBR spectra and the CBSB spectra for a particular pulse observation are also shown.

Figure 5.6 shows that when the period of pulse is known the CBSB model amplifies a small region of periods close to the pulse period and the amplification can be large (up to 2 times). When the pulse occurrence is uncertain, the magnitude of amplification decreases and a wider range of period is now amplified (as the pulse period is random). One should note that even in the uncertain T_p and $I_{\text{directivity}}$ case the amplification can be up to 1.3 times.

Deamplificaiton

The CBR ground-motion model was fitted to provide prediction of ground motion under the absence of any information about directivity pulses (information like occurrence of a directivity pulse, period of the pulse, etc.). When some information related to directivity pulses is known, the CBSB model is fitted to provide prediction of ground-motion intensity. Thus, if the CBSB model shows amplification with respect to the CBR model when a directivity pulse is observed (i.e., $I_{\text{directivity}} = 1$), it should predict deamplification with respect to the CBR model given the information that pulse is not observed. Figure 5.7 compares the median spectra predicted by CBSB with CBR for a strike-slip earthquake with magnitude 7.5 and distance 1 km and 20 km. The $I_{\text{directivity}}$ parameter in CBSB is set to 0 to obtain the prediction for a particular case when a directivity pulse is not observed at the site. The CBSB model predicts lower ground-motion intensities than the CBR model, but the deamplification is stronger at 1 km than at 20 km, which is expected as the probability of observing directivity pulses is very low at 20 km. Therefore, in the absence of any information about

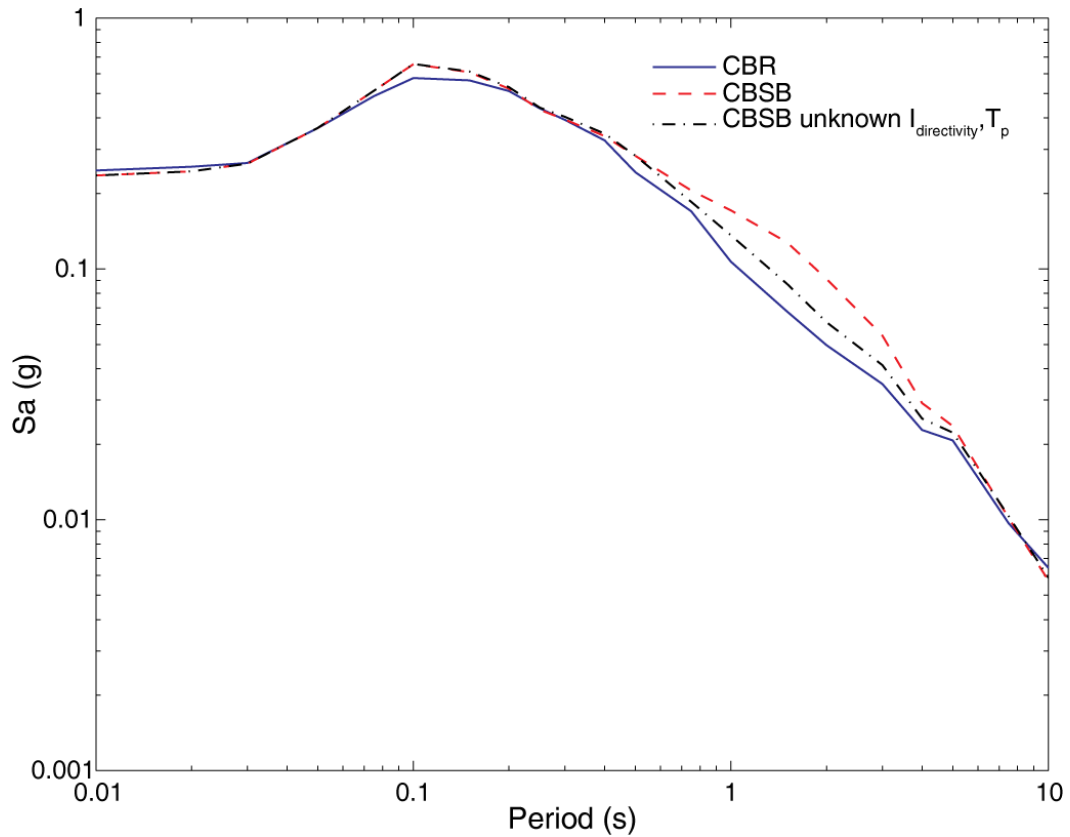


Figure 5.6 Comparison of the median response spectra predicted by CBR model and the CBSB model when a directivity pulse of period 2.2 sec is assumed to have occurred and when pulse occurrence is considered uncertain. For the uncertain pulse, case P(directivity) is assumed to be 0.6 and the T_p follows the log-normal distribution described by Equations 5.17 and 5.18.

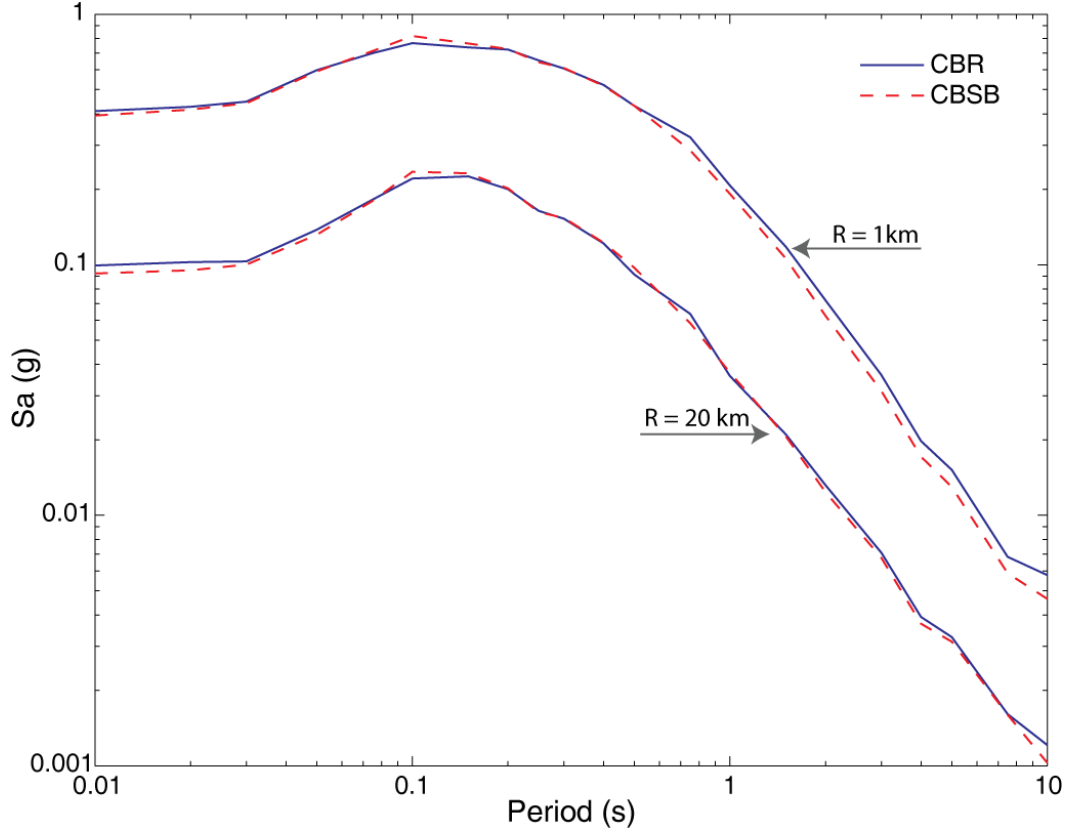


Figure 5.7 Comparison of the median response spectra predicted by CBR model and the CBSB model when $I_{directivity}$ is set to 0. The comparisons are for $R_{rup} = 1$ km and $R_{rup} = 20$ km.

directivity pulses the CBR model predicts the intensity that is closer to the no-pulse prediction of CBSB model.

5.4 AVERAGE DIRECTIVITY AMPLIFICATION

The CBSB ground-motion model as presented in Equation 5.2 assumes the knowledge of directivity pulse occurrence (i.e., the value of $I_{directivity}$) and its period (T_p). When predicting the ground motion from a future earthquake, the value of these parameters are unknown. Although the values of $I_{directivity}$ and T_p are unknown, it is reasonable to assume some knowledge about the scenario of interest (even the most basic ground-motion models assume knowledge of M , R). In this case, the expected value of $\ln Sa$ conditioned on available information can be used as a prediction for ground-motion intensity from a future earthquake. When location of the rupture and the hypocenter is known, Equation 5.20 gives the mean $\ln Sa$. Rupture location and hypocenter location are not known from future earthquake, so to use Equation 5.20 further expectation over possible rupture

and hypocenter location may be needed. Although it is common in PSHA computations to take expectation over possible future fault rupture locations, taking expectation over possible hypocenter locations is not as common. Taking expectation over possible hypocenter locations is recommended in literature (e.g., Abrahamson, 2000), but it adds considerable computational overhead and is only required when accounting for directivity effects. Significant computational savings can be achieved by pre-computing the average directivity amplification ($\ln Amp$) over possible source-to-site geometries. We modified the CBSB ground motion model to use pre-computed average directivity amplification, as shown by Equation 5.21 below

$$\ln Sa = f(M, R, T, Vs30, \dots) + \begin{cases} I_{directivity} \cdot \ln Amp(T, T_p) & \text{known } I_{directivity}, T_p \\ \mu_{\ln Amp|M,R,T,\dots} & \text{unknown } I_{directivity}, T_p \end{cases} \quad (5.21)$$

The average directivity ($\mu_{\ln Amp|M,R,T,\dots}$) can be computed by taking the expectation given all known parameters. Next, we will compute the average directivity amplification assuming the knowledge of parameters used in the base ground-motion model (Campbell and Bozorgnia, 2008). Note that this case assumes the minimum possible knowledge as without these parameters no prediction can be made. If some parameters required by the base ground-motion model are unknown, relationships proposed by Kaklamanos et al. (2011) can be used to guess appropriate values.

5.4.1 Average Directivity Computation

The average directivity amplification can be computed either empirically using the NGA-West2 database used to fit the ground-motion models in this study or by using the probability distributions for each parameter and computing the expectation through numerical integration. As only 145 directivity pulses were found in the NGA-West2 database, there is a high probability that the distribution of important parameters in the database may be biased as a result of small sample effects. Since the ground-motion models are fitted to predict future earthquakes and not just to predict the recordings in the database, averaging over a biased distribution may lead to biased ground-motion intensity prediction from future earthquakes. To prevent this bias we decided to compute the expected directivity amplification through numerical integration using the probability distribution of each parameter.

Strike-slip ruptures

To compute the expected value of $I_{directivity} \ln Amp(T, T_p)$, it is necessary to compute the average directivity amplification. The $I_{directivity}$ and T_p terms are modeled by Equations 5.16 to 5.18. For

strike-slip ruptures the probability of directivity depends on R , s , and θ , and the distribution of T_p depends on magnitude (M). Given this information we can compute the directivity amplification expected at a site given only the values of M , R , and T . Note that the source-to-site geometry parameters depends on the dip of the fault. Since this study only aims to illustrate the procedure to include directivity effects in ground-motion models and not propose a new ground-motion model, for simplicity we present results for faults with dip of 90 degrees (vertical strike-slip faults). Similar calculations can be done for faults with different dips.

Given the values of M , R (for vertical faults $R = R_{rup} = R_{jb}$), and T , expectation over s , θ and T_p needs to be taken to compute the conditional average directivity amplification as shown by Equation 5.22 below:

$$\mu(\ln Amp|M,R,T) = \int_s \int_\theta \int_{T_p} P(pulse|R, s, \theta, M) \ln Amp(T, T_p) P(s, \theta, T_p|M, R, T) dT_p \cdot d\theta \cdot ds. \quad (5.22)$$

In the expectation integral shown in Equation 5.22, the pulse period only depends on magnitude; therefore, the expectation can be split as shown below

$$\mu(\ln Amp|M,R,T) = \left(\int_s \int_\theta P(pulse|R, s, \theta, M) P(s, \theta|M, R) d\theta \cdot ds \right) \left(\int_{T_p} \ln Amp(T, T_p) P(T_p|M) dT_p \right). \quad (5.23)$$

The integration over T_p is shown in Appendix C. The integration over the geometry parameters (s , θ) is more involved and its computation is described below.

Given a magnitude M and closest distance R , several source-to-site geometries are possible. The values of s and θ depend on the rupture length, location of site relative to the rupture and the location of hypocenter on the fault rupture. Therefore, the integration over s and θ in Equation 5.23 can be computed using the following:

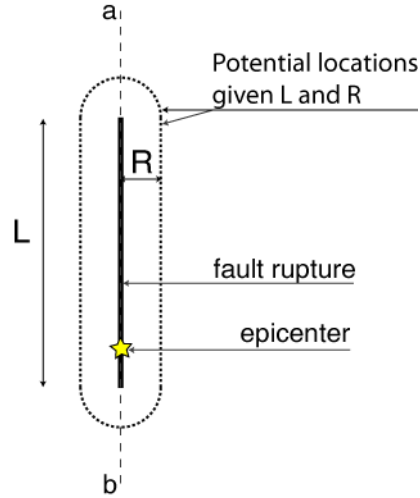


Figure 5.8 Diagram showing location of sites at a distance R from a vertical strike-slip rupture. Note in this case R is both the R_{jb} and R_{rup} .

$$\left(\int_s \int_\theta P(pulse|R, s, \theta, M) P(s, \theta|M, R) d\theta \cdot ds \right)$$

$$= \int_L \int_z \int_{loc} P(pulse|L, z, loc, M, R) P(L, z, loc|M, R) dloc \cdot dz \cdot dL \quad (5.24)$$

$$= \int_L \int_z \int_{loc} P(pulse|L, z, loc) P(loc|z, L, M, R) P(z|L, M, R) P(L|M, R) dloc \cdot dz \cdot dL \quad (5.25)$$

$$= \int_L \int_z \int_{loc} P(pulse|L, z, loc) P(loc|L, R) P(z|L) P(L|M) dloc \cdot dz \cdot dL \quad (5.26)$$

where L is the length of rupture that is assumed to follow the distribution described by Wells and Coppersmith (1994), given the value of M (it is independent of R). z represents the location of hypocenter and is assumed to be distributed uniformly over the rupture plane (following Abrahamson, 2000). Note that given L , the hypocenter distribution is independent of other parameters. There is some evidence that hypocenter location can follow a distribution other than uniform (e.g., Mai et al., 2005) and any distribution can be used in the equation above. We chose uniformly distributed hypocenters as it is commonly used in practice and also simplifies the computation. The parameter loc represents the location of site at a distance R from the rupture, as shown in Figure 5.8. All sites at a distance of R from the rupture are assumed to have equal probability. For a dipping fault, the fault width will also have an influence on the location of sites at a distance of R from the fault, but for the vertical fault considered here it has no effect.

Figure 5.10 shows the average directivity amplification at different distances (R) and periods (T) as a function of the magnitude (M). The location of the peak of average amplification, along

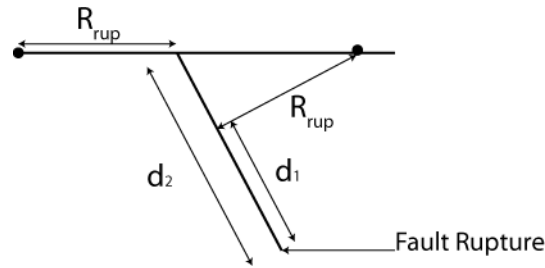


Figure 5.9 Diagram showing difference in the value of parameter d for sites at same closest distance on hanging wall (d_1) and foot wall (d_2).

the magnitude axis, is period dependent. This was expected as larger magnitude ruptures produce directivity pulses with higher periods and thus amplify the spectral acceleration at higher periods. A similar relationship between directivity amplification, magnitude, and spectral acceleration periods can be seen in Figure 5.11. Figure 5.12 shows the decay in directivity amplification with distance, which is a direct result of decrease in probability of directivity with distance.

Non-strike-slip ruptures

The computation of average directivity for non-strike-slip ruptures is similar to the strike-slip case described above. As mentioned above, the fault width becomes an important parameter for dipping faults. The distribution of fault width given the magnitude M is computed using Wells and Coppersmith (1994). As shown in Figure 5.9, a site at distance R on hanging wall side has a different d than that on the foot-wall side. Thus, the geometry parameters have different distributions on the hanging-wall and foot-wall sides. Since the hanging-wall flag is a standard input to the Campbell and Bozorgnia (2008) model, different average directivity values for hanging walls and foot walls can be computed. Wells and Coppersmith (1994) report different distributions for rupture length and width given M for normal and reverse faults. Although the directivity model used here does not discriminate between normal and reverse cases, using Wells and Coppersmith (1994) to compute distribution of rupture length and width will produce different average directivity amplification results for normal and reverse faults.

5.4.2 Fitting Functional Forms to Average Directivity Amplification

To use the average directivity ground-motion model shown in Equation 5.21 we need to fit models to predict the average directivity amplification.

Table 5.4 Coefficients for the average directivity amplification model.

T(s)	a_0	a_1	a_2	a_3	a_4
0.01	-9.39	0.15	3.94	-0.54	4.57
0.02	-13.56	0.15	4.17	-0.51	5.62
0.03	-12.41	0.15	3.65	-0.51	5.63
0.05	-10.68	0.15	3.00	-0.50	5.63
0.075	-9.09	0.15	2.49	-0.50	5.64
0.1	-7.85	0.15	2.13	-0.50	5.64
0.15	-5.89	0.15	1.62	-0.50	5.63
0.2	-4.26	0.15	1.23	-0.51	5.61
0.25	-2.73	0.14	0.90	-0.52	5.57
0.3	-1.03	0.14	0.55	-0.54	5.49
0.4	5.04	0.15	-0.64	-0.55	4.91
0.5	6.71	0.15	-0.96	-0.50	4.87
0.75	8.78	0.15	-1.32	-0.42	4.95
1	10.12	0.15	-1.52	-0.37	5.06
1.5	11.94	0.14	-1.77	-0.31	5.28
2	13.25	0.13	-1.93	-0.27	5.46
3	15.24	0.12	-2.16	-0.22	5.65
4	16.82	0.11	-2.34	-0.17	5.65
5	18.16	0.11	-2.49	-0.12	5.45
7.5	20.29	0.10	-2.74	-0.02	2.56
10	20.70	0.10	-2.78	-0.00	25.89

Strike-slip ruptures

A functional form to predict the average directivity for vertical strike-slip faults is shown below

$$\mu_{(\ln Amp|M,R,T)} = \frac{1}{1 + \exp(a_0 + a_1 R + a_2 M)} \exp(a_3(M - a_4)^2) \quad (5.27)$$

The first term in the equation above is influenced by the functional form used to predict the probability of a directivity pulse (Equation 5.16). The second term is related to the functional form of the expected value of $\ln Amp(T, T_p)$ given M derived in Appendix C. The coefficients of this model (a_0 to a_4) are period dependent and were found by minimizing square errors at each period (T) separately. Table 5.4 lists the coefficients at 21 different periods, and Figures 5.10, 5.11, and 5.12 compare the fitted function with computed values of average directivity using Equation 5.22. To use this model at other periods one can use linear interpolation to find the average directivity amplification at the period of interest.

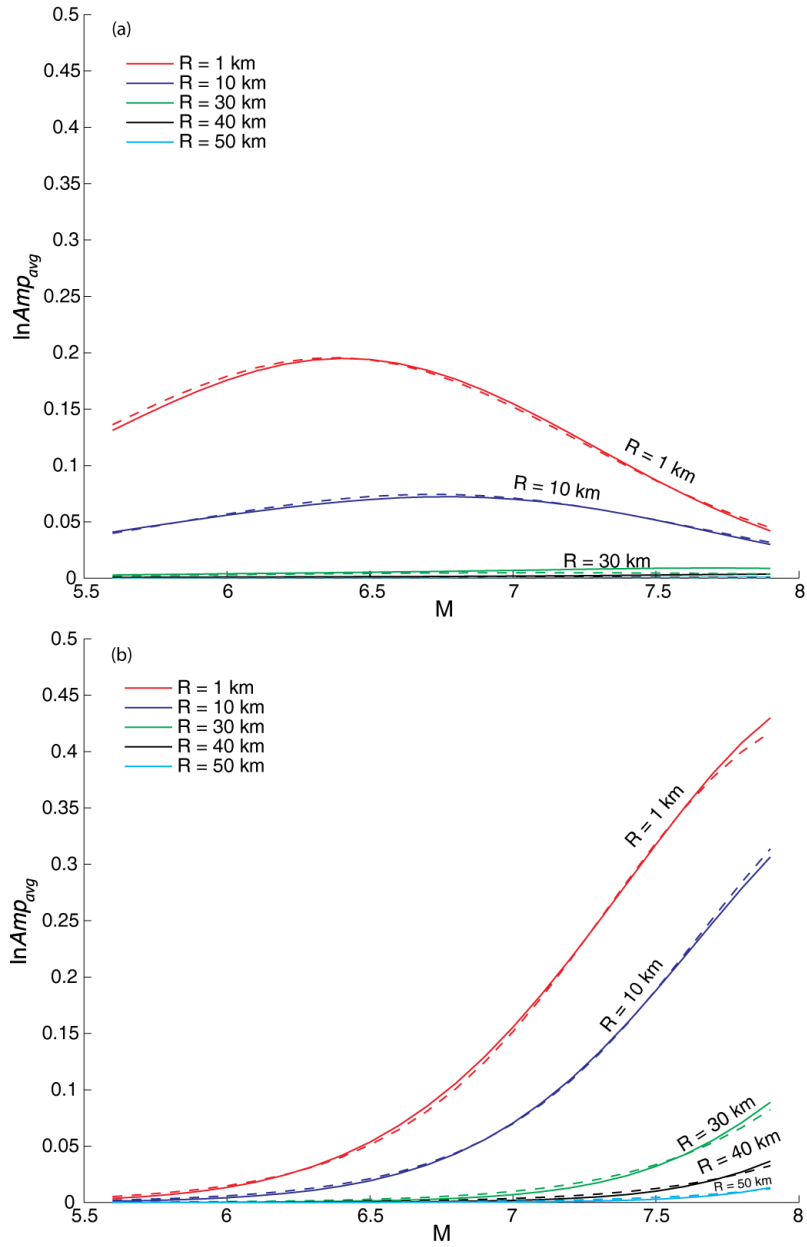


Figure 5.10 Comparison of average directivity computed using Equation 5.22 (solid lines) and predictions from Equation 5.27 (dashed lines). The comparison is shown as a function of M at various R values. The period is 1 sec in (a) and 7.5 sec in (b).

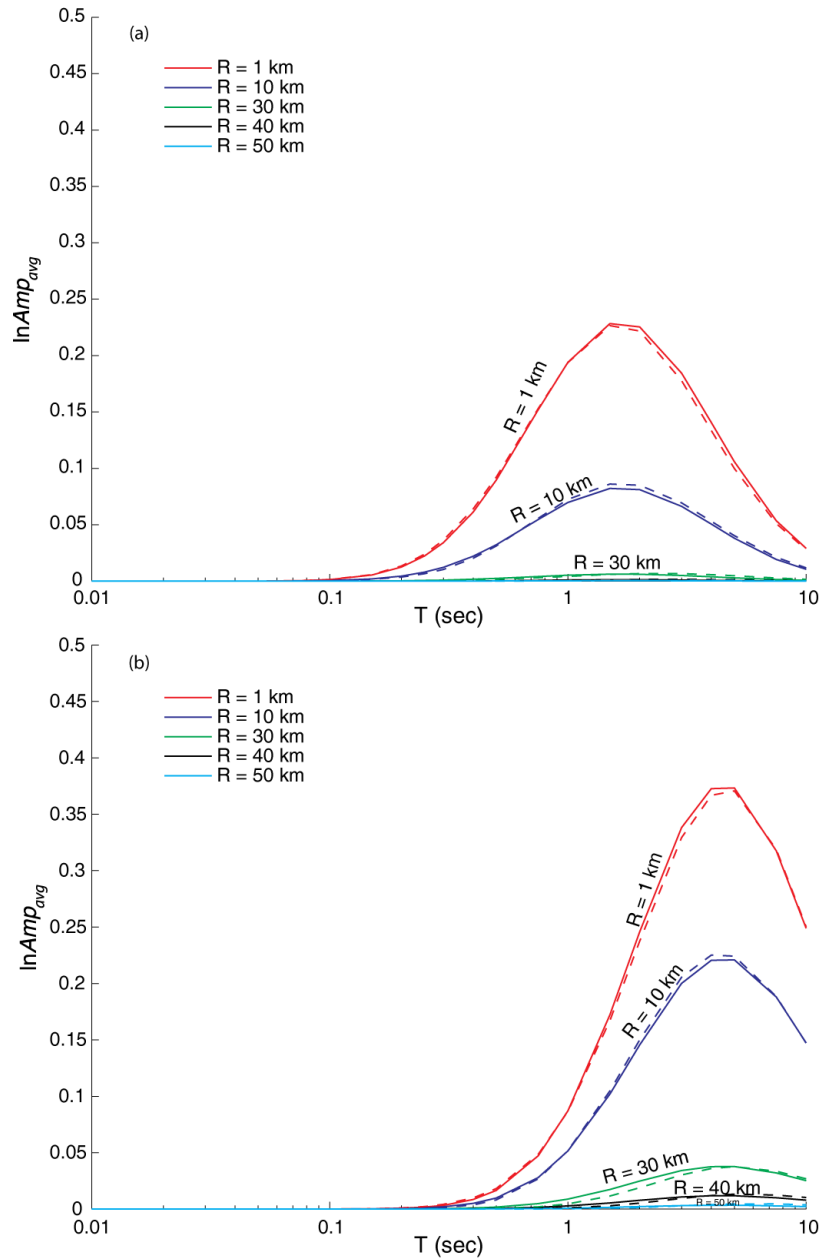


Figure 5.11 Comparison of average directivity computed using Equation 5.22 (solid lines) and predictions from Equation 5.27 (dashed lines). The comparison is shown as a function of T at various R values. The magnitude (M) is 6.5 in (a) and 7.5 in (b).

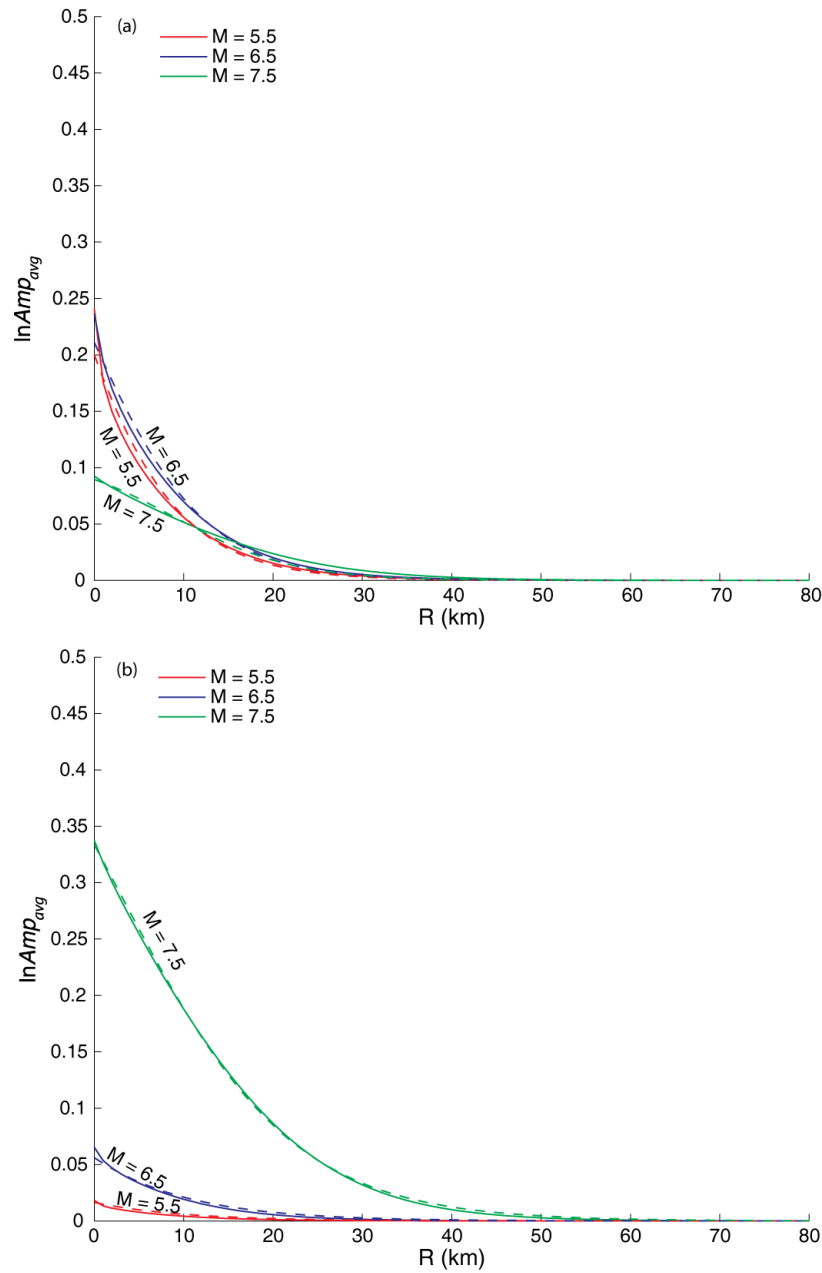


Figure 5.12 Comparison of average directivity computed using Equation 5.22 (solid lines) and predictions from Equation 5.27 (dashed lines). The comparison is shown as a function of R at various M values. The period is 1 sec in (a) and 7.5 sec in (b).

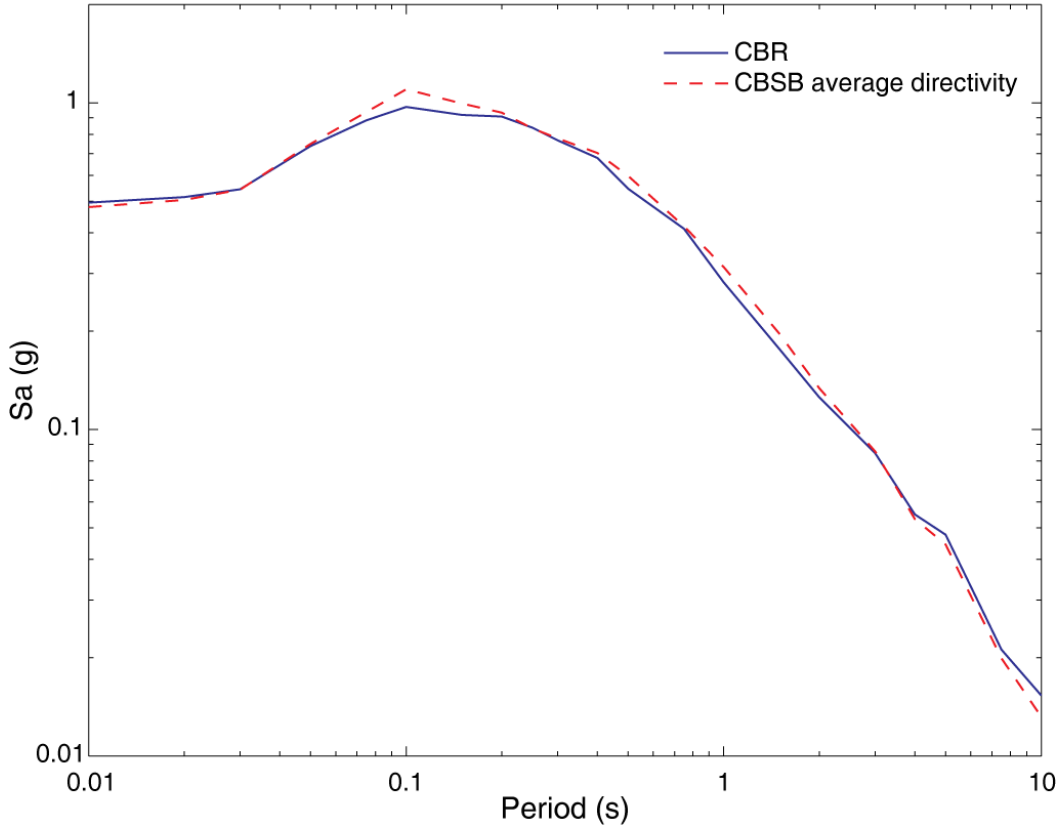


Figure 5.13 Comparison of prediction from CBR and CBSB model when directivity parameters are unknown. The comparison is shown for a vertical strike-slip rupture of magnitude 6.5. The site is 1 km away from the rupture and the site has $V_{s30} = 760$ m/sec and $Z_{2.5} = 2$ km.

5.5 COMPARISON OF GROUND-MOTION PREDICTIONS

5.5.1 Median Predictions from CBR and CBSB with Average Directivity

Figure 5.13 shows median spectra predicted by the CBR model and CBSB model when $I_{directivity}$, T_p and hypocenter location are unknown (using Equation 5.22). The CBR model is fitted to give unbiased prediction with respect to the subset of NGA-West2 database used for fitting when directivity effects are ignored, while CBSB with average directivity model separates the directivity and non-directivity parts of the ground-motion model. The average directivity model was computed through numerical integration using the probability distribution of each parameter given M , R , and T , as explained above. This numerical integration approach was taken to avoid any bias due to small sample effects in the dataset. The close agreement between the predictions from CBR and CBSB with average directivity models in Figure 5.13, may point to lack of any significant bias in the sampling of directivity parameters in the subset of NGA-West2 database used to fit the models.

5.5.2 Comparison of CBSB Predictions under Different Levels of Information

The prediction from CBSB model at three different sites shown in Figure 5.14 are compared. The parameters used in CBR model have the same values at all the sites ($M = 6.5$, $R = 0$ km, $Z_{tor} = 0$, $Z_{2.5} = 2$ km, $\delta = 90$, $\lambda = 180$, $V_{s30} = 760$ m/sec) while the directivity parameter s is different at different sites (θ is 0 at all sites). The comparisons are made for two cases when the location of epicenter is unknown (case 1) and when it is known (case 2). For these comparisons we have assumed the length and location of rupture to be known. The length of rupture is taken to be 29 km, which is the median length for a magnitude 6.5 earthquake according to Wells and Coppersmith (1994).

Under the assumption of uniformly distributed epicenter along the fault length, sites A and C are equivalent to each other due to symmetry. Thus, we expect the predicted spectra from CBSB model at sites A and C to be the same. Note that site A and C are equivalent under a more general assumption of epicenter location having a distribution symmetric about the middle of the fault. Site B is located in the middle of the rupture so the maximum value s can take is half of rupture length, while this is equal to rupture length for sites A and C. Thus, we expect the average amplification due to directivity at site B to be lower than sites A and C when the epicenter location is unknown. Figure 5.15 shows the median response spectra prediction at the three sites from CBSB and CBR model. The median response spectra predicted by CBSB model at sites A and C are equal to each other as expected, while the prediction at site B is lower than that at A and C, which is also in line with expectation. Note that the CBR prediction—which ignores directivity effects—is lower than CBSB prediction at all sites in a range of periods from 0.3 sec to 4 sec.

Figure 5.16 shows the median spectra prediction at the three sites in Figure 5.14 when the epicenter is assumed to be located at the location of site C. In this case s is 0 at site C, half the rupture length at site B, and equal to the rupture length at site A. The figure shows largest spectral accelerations at site A followed by B and lowest Sa at site C. Again, the prediction from CBR model is shown for comparison.

5.5.3 Standard Deviations from the Ground-Motion Models

Table 5.5 shows the estimates of standard deviation of total error (i.e., between-event error + within-event error) for the CBR model, the CBSB model assuming the occurrence of pulse and its period is known and the CBSB model when the occurrence of pulse and its period are unknown. Residuals of predictions from each model were computed using the subset of NGA-West2 database used for fitting, and the standard deviations were estimated empirically from them. The standard deviation of total error (σ) of both the CBSB and CBR models are similar to each other at low periods, and

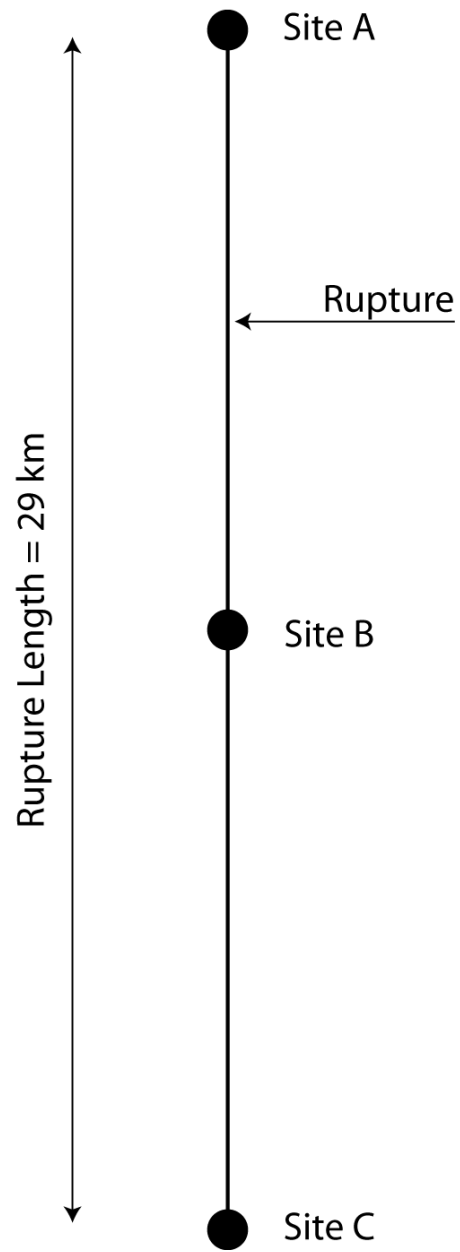


Figure 5.14 The three sites and fault rupture used for comparison of the CBSB model prediction.

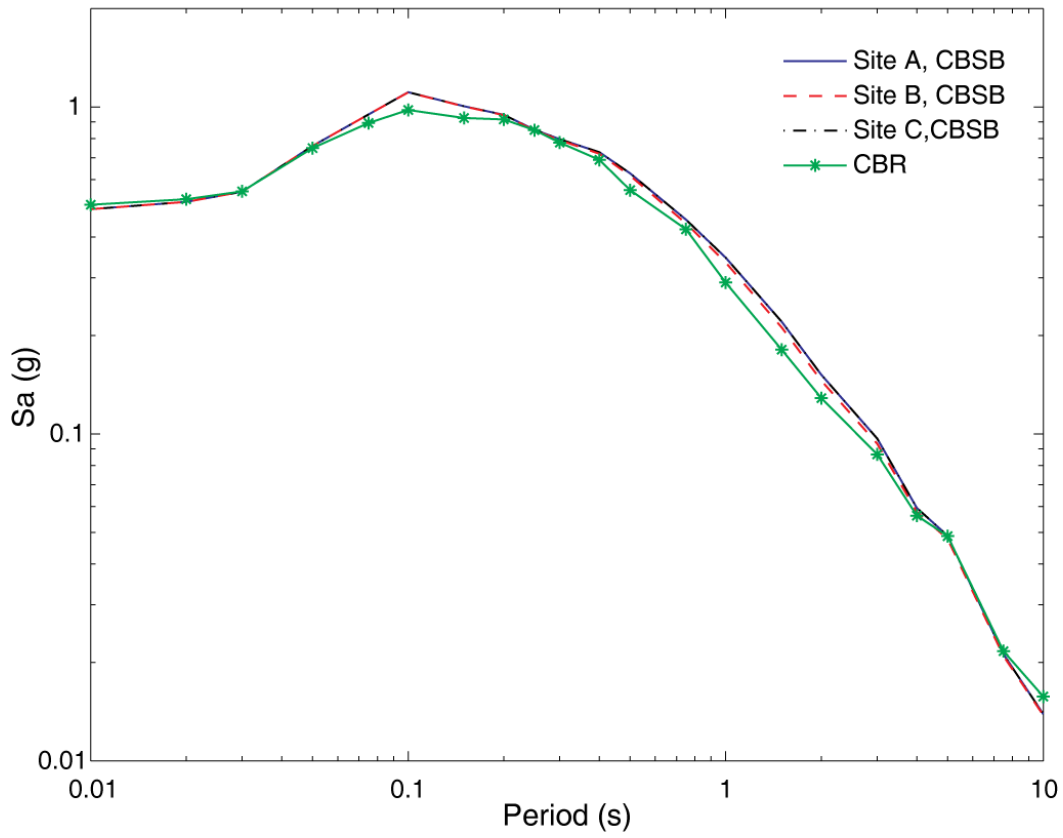


Figure 5.15 Comparison of median prediction from the CBSB model when the epicenter location is unknown for the three sites shown in Figure 5.14 . Median spectra prediction from the CBR model is also shown for comparison.

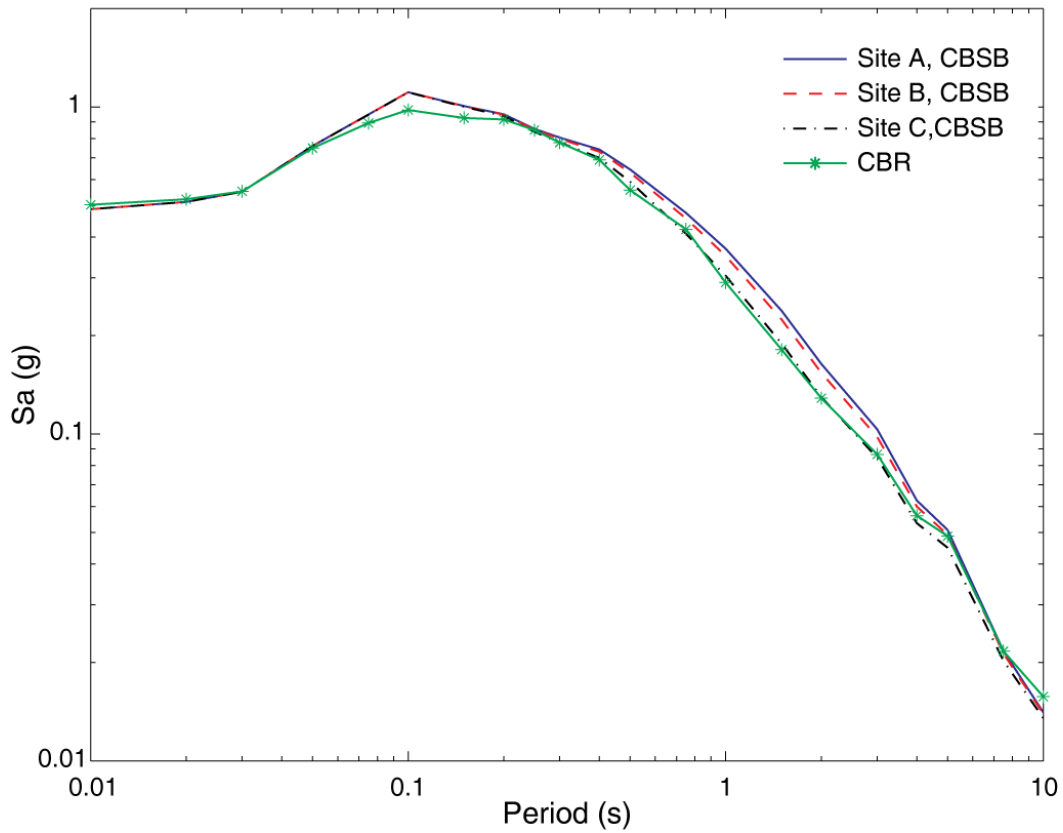


Figure 5.16 Comparison of median prediction from the CBSB model when the epicenter location is known for the three sites shown in Figure 5.14. The epicenter is assumed to be located at the location of site C. Median spectra prediction from the CBR model is also shown for comparison.

Table 5.5 Standard deviation of total error (σ) for different models considered in the study.

T(s)	CBR	CBSB	
		known $I_{directivity}$ and T_p	unknown $I_{directivity}$ and T_p
0.01	0.540	0.541	0.541
0.02	0.544	0.546	0.546
0.03	0.557	0.558	0.558
0.05	0.600	0.603	0.603
0.075	0.649	0.655	0.655
0.1	0.660	0.668	0.668
0.15	0.617	0.619	0.620
0.2	0.592	0.591	0.592
0.25	0.575	0.573	0.574
0.3	0.591	0.589	0.590
0.4	0.609	0.608	0.610
0.5	0.633	0.633	0.634
0.75	0.674	0.671	0.675
1	0.684	0.680	0.685
1.5	0.664	0.658	0.665
2	0.645	0.640	0.646
3	0.642	0.634	0.643
4	0.636	0.626	0.637
5	0.644	0.629	0.647
7.5	0.666	0.640	0.669
10	0.635	0.611	0.635

there is a modest decrease in σ of about 3.8% at high periods when information about observation of pulse and its period is known. When the $I_{directivity}$ and T_p are unknown the CBSB model and CBR models have similar σ . The reduction in σ shows improvement in model prediction from incorporating new parameters. Directivity effects are most prominent at sites near the fault and the spectral acceleration amplification affects larger periods. Thus, if the model improvement is a result of better accounting of directivity effects, the sigma reduction should be higher at sites close to the fault and at larger periods. Figure 5.17 shows model σ as the function of R_{rup} at 0.2 and 2.0 sec spectral acceleration periods. Loess or local regression (e.g., Hastie et al., 2001) was used to compute the expected value of residuals ($E[residual]$) and square residuals ($E[residual^2]$) as a non-parametric function of R_{rup} . These non-parametric estimates were then used to compute the σ ($\sqrt{E[residual]^2 - E[residual^2]}$) as a function of R_{rup} , as shown in the figure. As expected, most of the sigma reduction occurs at sites close to the fault and at higher periods.

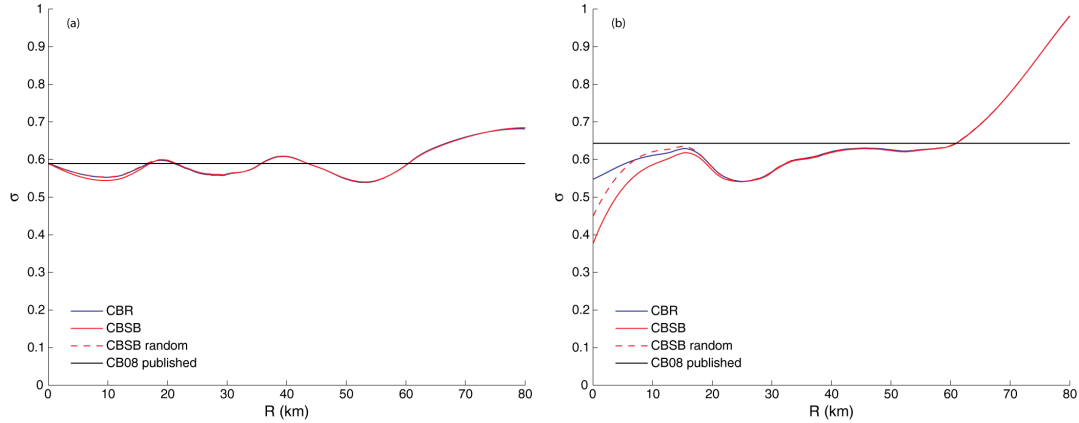


Figure 5.17 Comparison of σ of residuals from the CBR, CBSB, and CBSB models with random/unknown T_p and $I_{directivity}$ as a function of R_{rup} for (a) $T = 0.2$ sec and (b) $T = 2$ sec. Published values of σ from Campbell and Bozorgnia (2008) are also shown for comparison.

5.6 CONCLUSION

A method to explicitly include directivity effects in ground-motion models has been proposed and studied. Two ground-motion models, with and without explicit directivity terms, were fitted using the NGA-West2 database. The ground-motion models were compared to each other and changes due to inclusion of directivity terms were studied in detail.

The ground-motion model with explicit directivity terms uses some parameters that may not be known in some cases. We proposed to use the expected value of the ground-motion model prediction conditioned on available information as a prediction of ground-motion intensity in such cases. Several example predictions under different levels of information were studied in this report. We found that the median and standard deviation of the predictions from both directivity and non-directivity ground-motion models were similar to each other when no information regarding the directivity parameters were available. The directivity ground-motion model was able to differentiate between different source-to-site geometries and provided better prediction of ground-motion intensity when such information was available, however.

The method proposed here expands the ability of ground-motion models to incorporate additional predictor variables in the Sa predictions, while giving a reasonable prediction when the values of the extra variables are not known.

6 Approximate Deaggregation Results for Hazard Consistent Ground Motion Selection in Near-Fault Regions

6.1 INTRODUCTION

Design of structures requires estimation of structural response or *EDP* from future ground-motions expected at the design seismic hazard level. The *EDP* from a future earthquake is unknown because of uncertainty in several factors, such as material properties, structural model parameters, ground-motion input, etc. Of these, the uncertainty in future ground-motion is responsible for most of the uncertainty in *EDP* (e.g., Padgett and DesRoches, 2007; Katsanos et al., 2010). Lack of knowledge about source, site, and path effects makes the ground-motion time history from a future earthquake random or uncertain. Thus, to model the distribution of future *EDP*, a set of ground motions representing ground-shaking at the selected hazard level is generally used as input to nonlinear time history analysis. Generally, sets of recorded ground-motion time histories that have intensity similar to the selected hazard level and were produced by events similar to the ones causing the hazard are used to represent future ground motion at the site (e.g., Shome et al., 1998; Bommer and Acevedo, 2004). Deaggregation of PSHA results (e.g., Bazzurro and Cornell, 1999) is used to find the probability distribution over the earthquake scenarios responsible for exceedance of the selected hazard level. The recorded time histories from earthquakes similar to scenarios with high deaggregated probability (or most likely scenarios causing the hazard exceedance) can be selected for nonlinear analysis.

Libraries of recorded time histories, though growing in size, are generally sparse with respect to the large magnitude nearby events of most importance to engineers. This makes finding a large set of ground motions for several earthquake scenarios difficult. In practice, surrogate strategies like matching to a target spectra, scaling of time histories, etc., are often used to overcome the sparseness of ground-motion database (e.g., Beyer and Bommer, 2007; Kottke and Rathje, 2008;

Baker, 2011; Jayaram et al., 2011; Lin, 2012). Sets of simulated or spectrally modified ground-motion time histories representing the hazard level of interest are also used as input to nonlinear dynamic analysis in practice (e.g., Hancock et al., 2006; Al Atik and Abrahamson, 2010), but we will focus on selection of recorded time-histories from past earthquakes in this chapter.

In this study we consider ground-motion selection at near-fault sites, focusing on selecting sets of ground-motions that properly account for the effects of near-fault directivity. Directivity effects can cause ground motions with a large velocity pulse at the beginning of the time history (Mavroudis et al., 2004; Baker, 2007) and the presence of a velocity pulse has a significant effect on the response of the structure (e.g., Bertero et al., 1978; Anderson and Bertero, 1987; Hall et al., 1995; Iwan, 1997; Alavi and Krawinkler, 2001; Menun and Fu, 2002; Makris and Black, 2004; Mavroudis et al., 2004; Akkar et al., 2005; Luco and Cornell, 2007). To properly account for the effect of directivity pulses on structural response, the selected set of hazard consistent ground-motions must contain appropriate number of pulse-like ground motions, where the number of pulse-like ground motions can be chosen to reflect the probability that the selected hazard level is exceeded due to a directivity pulse. Also, the period of the pulse has a significant effect on structural response (e.g., Alavi and Krawinkler, 2001; Champion and Liel, 2012). Thus, the periods of the pulses in the selected set of records should also be consistent with the expected distribution causing hazard exceedance. The probability that a directivity pulse causes the hazard exceedance and the distribution of pulse periods causing this exceedance can be computed using PSHA deaggregation as demonstrated in Chapter 2.

A PSHA computation properly accounting for directivity effects is needed to compute the deaggregated distributions of pulse occurrence ($I_{directivity}$) and pulse period (T_p). Accounting for directivity effects in PSHA is computationally expensive and not common in practice. Though PSHA with directivity effects is not common yet, there is an immediate need for guidance regarding ground motion selection in near-fault regions. In this chapter we study the results from PSHA computations with and without explicit inclusion of directivity effects to derive relationships that can help approximately estimate the $I_{directivity}$ and T_p deaggregation using only the results from common non-directivity PSHA computations.

6.2 PROBABILITY OF DIRECTIVITY PULSE CAUSING EXCEEDANCE OF A GIVEN SA LEVEL

The number of pulse-like ground motions in the set selected for structural analysis should reflect the probability of directivity pulse occurrence, conditioned on hazard exceedance at the site ($I_{directivity}$ deaggregation). The PSHA computations were performed at eight sites shown in Figure 6.1 around

a 60km long fault to study the $I_{directivity}$ and T_p deaggregation. Figures 6.2 and 6.3 shows the result of $I_{directivity}$ deaggregation conditioned on $Sa(3s)$ exceedance at the considered sites. These figures show that the probability of a pulse causing the Sa exceedance is dependent on the source-site geometry and decreases with increasing distance from the fault. Also, directivity pulses have higher likelihood of causing hazard exceedance at sites located at the end of the fault than at sites located in the middle of the fault. Tables 6.1 and 6.2 show the $I_{directivity}$ deaggregation results conditioned at Sa with 2% in 50 years and 10% in 50-year probability of exceedance at several periods. The tables show that along with source-to-site geometry dependence, $P(directivity|S_a > x)$ also depends on spectral acceleration period. For the case under consideration, the $P(directivity)$ peaks at a period of 3 sec at all distances and decreases away from it.

To derive a relationship which approximately capture these complex dependencies, we start with the exact equation to compute $P(directivity|S_a > x)$ and then add approximations.

$P(directivity|S_a > x)$ can be computed using the law of total probability as shown below

$$P(directivity|S_a > x) = \int_M \int_R P(directivity|S_a > x, m, r) f_{M,R}(m, r) dm dr. \quad (6.1)$$

Here, contribution from different earthquake scenarios, i.e., magnitudes (M) and distances (R), are combined together to compute the $P(directivity|S_a > x)$. $f_{M,R}(m, r)$ represents the joint distribution of M and R . As a first approximation we assume that only one scenario contributes to the hazard and that scenario is assumed to be the one with magnitude \bar{M} and distance \bar{R} , where \bar{M} is the mean of the deaggregated magnitude distribution (or $\int_M m f_M(m|S_a > x) dm$) and \bar{R} is the mean of the deaggregated distance distribution ($\int_R r f_R(r|S_a > x) dr$). Here, $f_M(m|S_a > x)$ and $f_R(r|S_a > x)$ represents the deaggregated magnitude and distance distributions respectively. Thus, $f_{M,R}(m, r)$ is assumed to be a delta function that is 0 everywhere except at $m = \bar{M}$ and $r = \bar{R}$. Using this approximation in Equation 6.1 we get

$$P(directivity|S_a > x) \approx P(directivity|S_a > x, \bar{M}, \bar{R}). \quad (6.2)$$

Note that assuming linearity of $P(directivity|S_a > x, \bar{M}, \bar{R})$ near \bar{M} and \bar{R} , leads to the same result as shown in Appendix D. Using Bayes' rule we can write

$$P(directivity|S_a > x) \approx P(directivity|S_a > x, \bar{M}, \bar{R}) \quad (6.3)$$

$$= \frac{P(S_a > x|directivity, \bar{M}, \bar{R})P(directivity|\bar{M}, \bar{R})}{P(S_a > x|\bar{M}, \bar{R})} \quad (6.4)$$

Finally, we use the average deaggregated magnitude and distance from common non-directivity

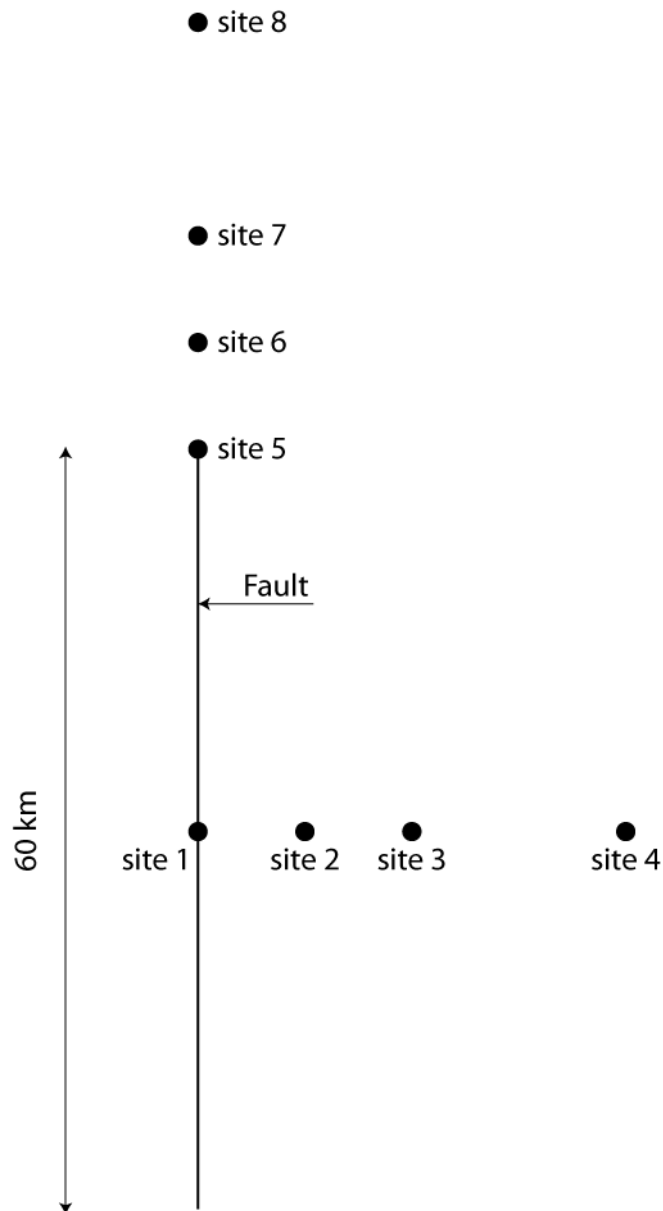


Figure 6.1 Location of the eight sites where PSHA was performed. Sites 1 and 5 are 0 km away from the fault, 2 and 6 are 5 km away, 3 and 7 are 10 km away and sites 4 and 8 are 20 km away. The fault is 60 km long and 12 km wide vertical strike-slip fault. With earthquakes assumed to occur at a rate of 0.09 per year. Magnitudes from 5 to 7 were considered for the study and Gutenberg-Richter b parameter was assumed to be 0.91. Note that the source parameters were selected to represent Imperial fault as in Chapter 2.

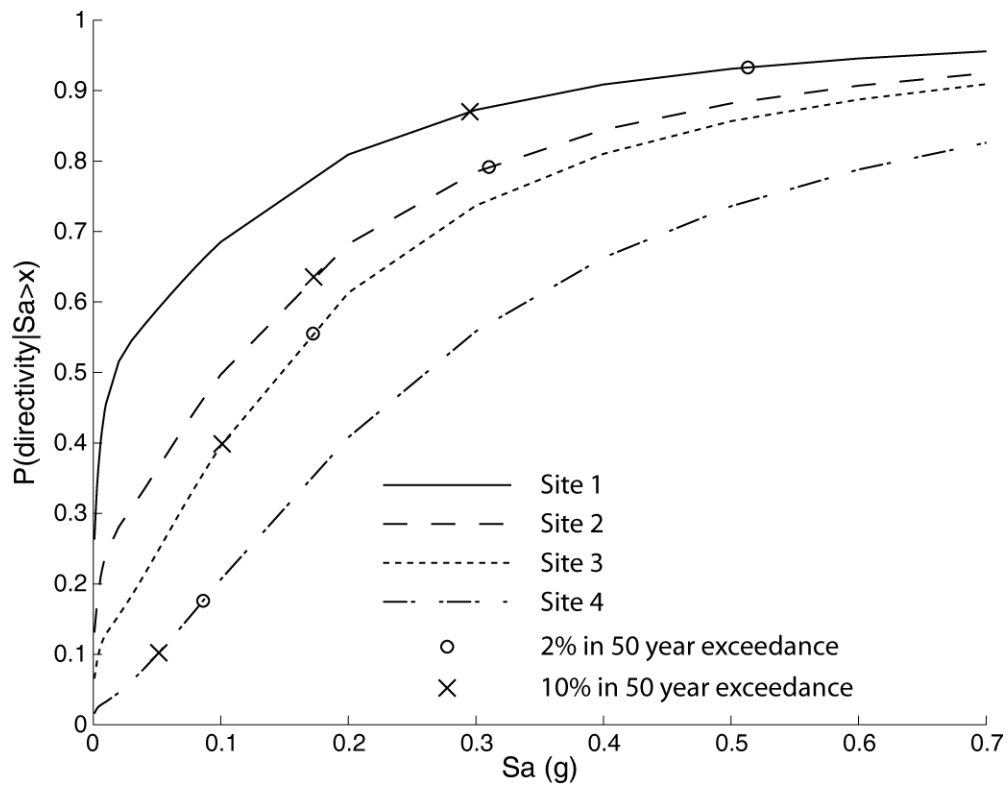


Figure 6.2 $P(\text{directionality} | Sa > x)$ conditioned on different $Sa(3s)$ levels for sites 1 to 4. The 2% in 50 years hazard is highlighted at each site by a circle and the 10% in 50 years hazard level is highlighted by a cross.

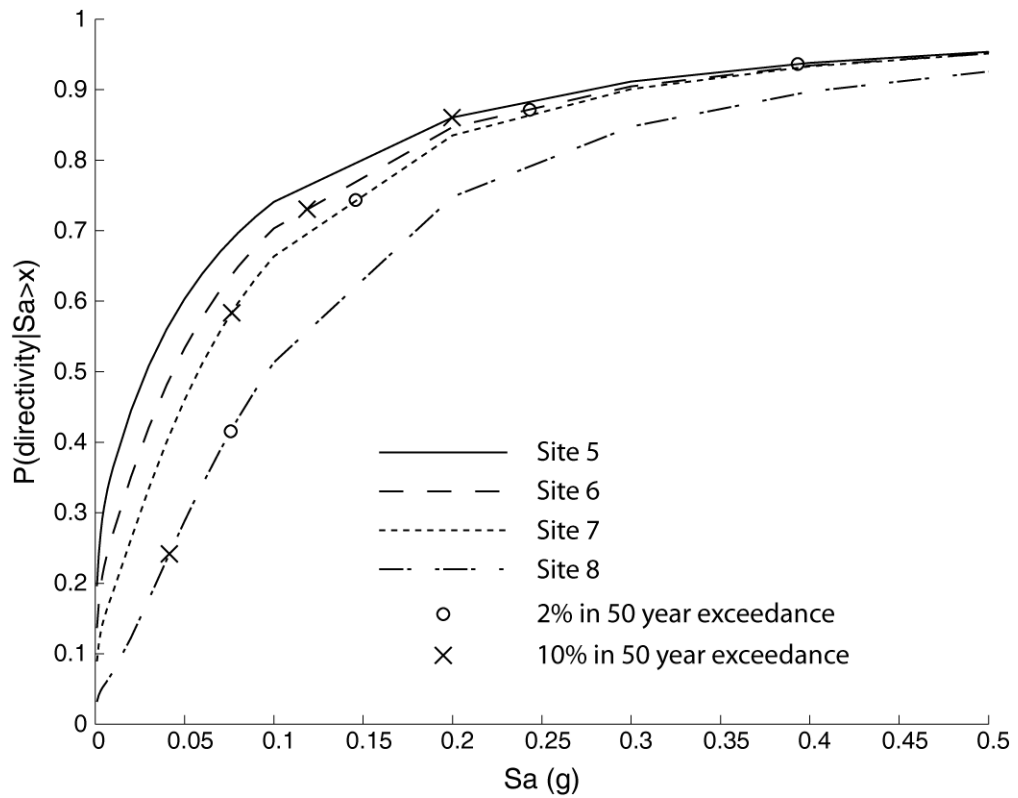


Figure 6.3 $P(\text{directionality} | Sa > x)$ conditioned on different $Sa(3s)$ levels for sites 5 to 8. The 2% in 50 years hazard is highlighted at each site by a circle and the 10% in 50 years hazard level is highlighted by a cross.

PSHA (say \bar{M}_{nd} and \bar{R}_{nd}) to approximate the \bar{M} and \bar{R} in Equation 6.4 to obtain

$$P(\text{directivity}|S_a > x) \approx \frac{P(S_a > x|\text{directivity}, \bar{M}_{nd}, \bar{R}_{nd})P(\text{directivity}|\bar{M}_{nd}, \bar{R}_{nd})}{P(S_a > x|\bar{M}_{nd}, \bar{R}_{nd})} \quad (6.5)$$

Here $P(S_a > x|\text{directivity}, \bar{M}_{nd}, \bar{R}_{nd})$ can be computed using the CBSB model described in Chapter 5 (with $I_{\text{directivity}} = 1$), $P(\text{directivity}|\bar{M}_{nd}, \bar{R}_{nd})$ can be computed by averaging $P(\text{directivity})$ at the site from various possible rupture scenarios of magnitude \bar{M}_{nd} at distance \bar{R}_{nd} . A Monte Carlo simulation can be used to simulate different ruptures with rupture length sampled from the Wells and Coppersmith (1994) distribution (given magnitude = \bar{M}_{nd}) and rupture locations sampled from an equi-probable distribution of locations on the fault with closest distance between site the rupture being equal to \bar{R}_{nd} . The $P(\text{directivity})$ for each scenario can be computed using equations developed in Chapter 4. Finally, the law of total probability can be used to compute $P(S_a > x|\bar{M}_{nd}, \bar{R}_{nd})$, as shown below

$$\begin{aligned} P(S_a > x|\bar{M}_{nd}, \bar{R}_{nd}) &= P(\text{directivity}|\bar{M}_{nd}, \bar{R}_{nd}) \\ &\quad \cdot P(S_a > x|\text{directivity}, \bar{M}_{nd}, \bar{R}_{nd}) \\ &+ (1 - P(\text{directivity}|\bar{M}_{nd}, \bar{R}_{nd})) \\ &\quad \cdot P(S_a > x|\text{no-directivity}, \bar{M}_{nd}, \bar{R}_{nd}). \end{aligned} \quad (6.6)$$

where $P(S_a > x|\text{directivity}, \bar{M}_{nd}, \bar{R}_{nd})$ can be computed using the CBSB model from Chapter 5, setting $I_{\text{directivity}}$ to 1, and $P(S_a > x|\text{no-directivity}, \bar{M}_{nd}, \bar{R}_{nd})$ can be computed using the CBSB model with $I_{\text{directivity}}$ set to 0. $P(\text{directivity}|\bar{M}_{nd}, \bar{R}_{nd})$ is computed using the Monte Carlo simulation described above. No information other than non-directivity PSHA deaggregations and relationships developed herein is needed for this computation. Note that the CBSB model requires T_p as an input but some computations are not conditioned on any T_p (e.g., $P(S_a > x|\text{directivity}, \bar{M}_{nd}, \bar{R}_{nd})$). To use CBSB models without conditioning on T_p we use the law of total probability as shown below

$$\begin{aligned} P(S_a > x|\text{directivity}, \bar{M}_{nd}, \bar{R}_{nd}) &= \int_{T_p} P(S_a > x|\text{directivity}, T_p, \bar{M}_{nd}, \bar{R}_{nd}) \\ &\quad \cdot f_{T_p}(t_p|\bar{M}_{nd})dt_p. \end{aligned} \quad (6.7)$$

where $f(T_p|\bar{M}_{nd})$ is the conditional distribution of the pulse period given magnitude = \bar{M}_{nd} as defined in Chapter 4.

Table 6.1 $P(\text{directivity})$ conditioned on 2% for a 50-year hazard at different periods and site locations.

Site	Distance	$T = 1\text{s}$	$T = 3\text{s}$	$T = 5\text{s}$
Site 1	0 km	0.86	0.93	0.90
Site 2	5 km	0.64	0.79	0.72
Site 3	10 km	0.40	0.56	0.49
Site 4	20 km	0.11	0.18	0.14
Site 5	0 km	0.85	0.94	0.92
Site 6	5 km	0.75	0.87	0.83
Site 7	10 km	0.59	0.75	0.72
Site 8	20 km	0.25	0.42	0.36

Table 6.2 $P(\text{directivity})$ conditioned on 10% for a 50-year hazard at different periods and site locations.

Site	Distance	$T = 1\text{s}$	$T = 3\text{s}$	$T = 5\text{s}$
Site 1	0 km	0.79	0.87	0.82
Site 2	5 km	0.52	0.64	0.58
Site 3	10 km	0.30	0.40	0.34
Site 4	20 km	0.07	0.10	0.08
Site 5	0 km	0.77	0.86	0.82
Site 6	5 km	0.63	0.74	0.71
Site 7	10 km	0.45	0.58	0.53
Site 8	20 km	0.17	0.24	0.21

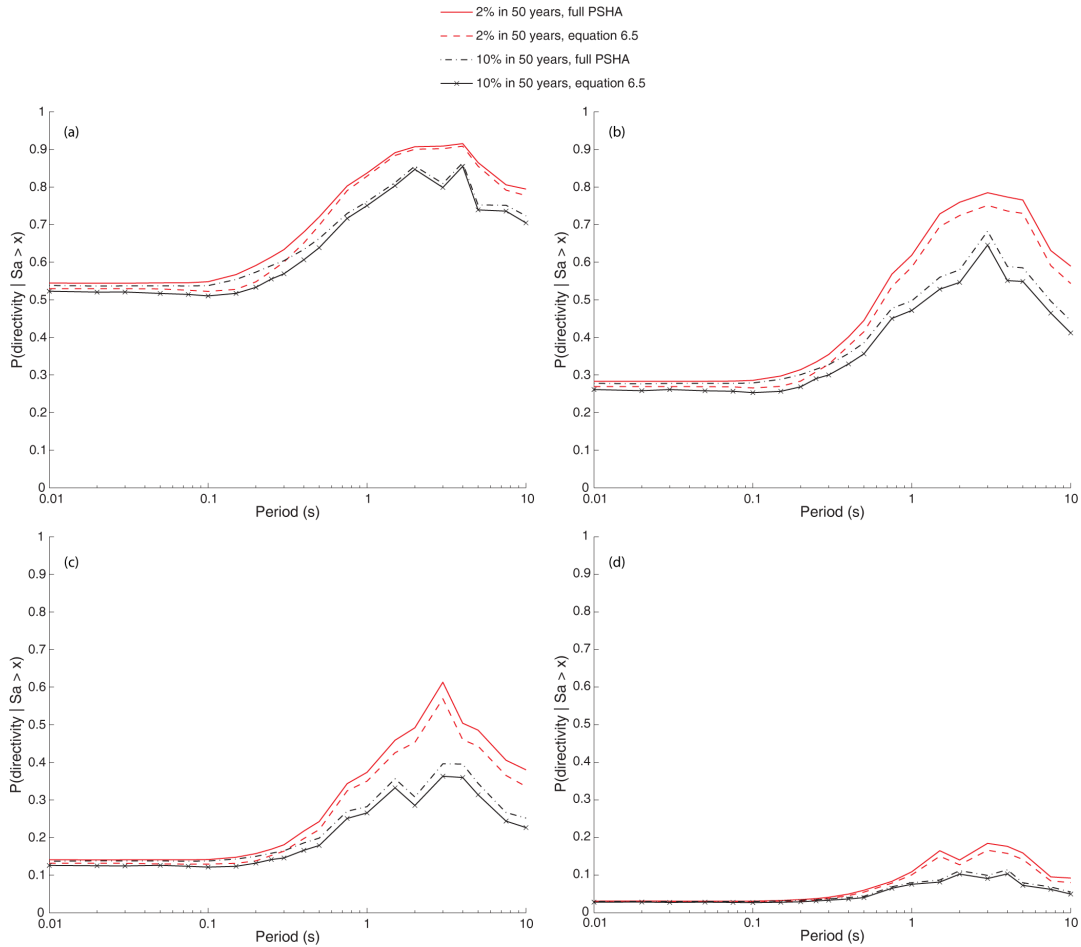


Figure 6.4 The deaggregated probability that a directivity pulse caused exceedance of hazard is plotted as a function of period. Estimates of the deaggregated pulse probability from a full directivity PSHA and Equation 6.5 are compared for different hazard levels at (a) site 1, (b) site 2, (c) site 3, and (d) site 4.

In Figure 6.4, $P(\text{directionality} | S_a > x)$ computed using deaggregation from PSHA considering directivity effects is compared with the prediction from Equation 6.5 at different sites. This figure shows that although several approximations are made between Equations 6.1 and 6.5, the $P(\text{directionality} | S_a > x)$ prediction from Equation 6.5 gives a reasonable estimate that captures most of the trends discussed above. Note that plots in Figure 6.4 are not a smooth function of period because the coefficients of the CBSB model were not smoothed, as described in Chapter 5.

6.3 PERIODS OF PULSE-LIKE GROUND MOTIONS CONDITIONED AT A GIVEN S_A LEVEL

As discussed earlier, the period of the pulse has a significant effect on the response of structures. Thus, properly representing future observations of pulse periods in the selected set of time histories

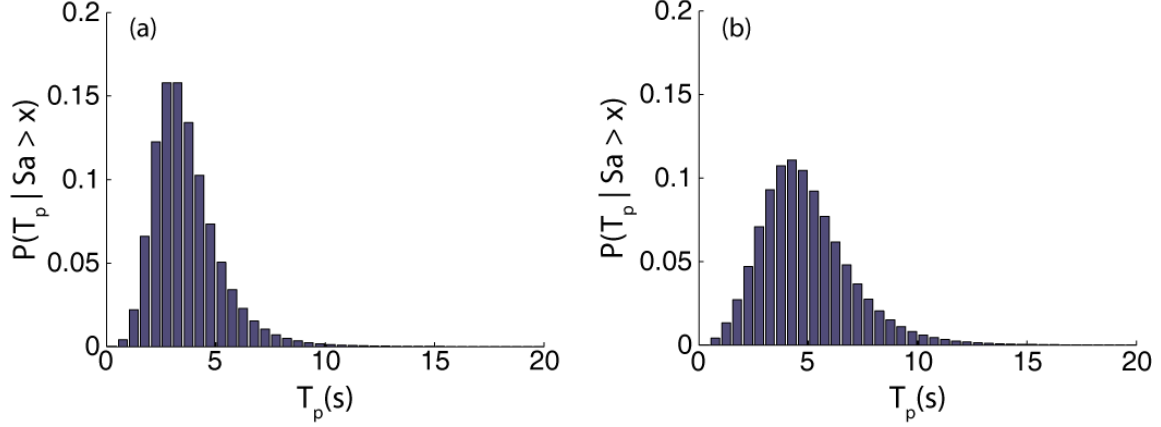


Figure 6.5 T_p deaggregation at site 1, for S_a with 2% in 50 years exceedance probability. Results are for spectral acceleration periods (a) 3 sec and (b) 5 sec.

is important to improve the estimate of future EDP . Since the pulse period (T_p) is modeled as a random variable for a given earthquake magnitude (e.g., Chapters 2, 3, and 4), ground-motions with several T_p values contribute to the hazard, as shown in Figure 6.5.

As a wide range of T_p s can cause S_a exceedance, it is important when selecting ground motions to consider the full deaggregated T_p distribution, and not just the central tendencies like the mean of the distribution. We follow the same procedure as above to derive an approximate deaggregated T_p distribution ($f_{T_p}(t_p|S_a > x)$), which uses only the deaggregation results from the common non-directivity PSHA. Using the law of total probability, the $f_{T_p}(t_p|S_a > x)$ can be expressed as a combination of contributions from different earthquake scenarios as shown below

$$f_{T_p}(t_p|S_a > x) = \int_M \int_R f_{T_p}(t_p|S_a > x, m, r) f_{M,R}(m, r) dm dr. \quad (6.8)$$

Note that T_p for a non-pulse-like ground motion is not defined. The occurrence of a directivity pulse is assumed throughout the derivation; for brevity, this is not mentioned in the list of conditioning variables. Again we make the simplifying assumption that the hazard is dominated by a single event with magnitude \bar{M} at a distance \bar{R} . Using this assumption and Bayes' rule, we get

$$f_{T_p}(t_p|S_a > x) \approx f_{T_p}(t_p|S_a > x, \bar{M}, \bar{R}) \quad (6.9)$$

$$= \frac{P(S_a > x|t_p, \bar{M}, \bar{R}) f_{T_p}(t_p|\bar{M}, \bar{R})}{P(S_a > x|\bar{M}, \bar{R})} \quad (6.10)$$

As the distribution of T_p only depends on earthquake magnitude and not on distance, the above

equation can be rewritten as

$$f_{T_p}(t_p|S_a > x) \approx \frac{P(S_a > x|t_p, \bar{M}, \bar{R})f_{T_p}(t_p|\bar{M})}{P(S_a > x|\bar{M}, \bar{R})} \quad (6.11)$$

Finally, we use the average deaggregated magnitude and distance from common non-directivity PSHA (\bar{M}_{nd} and \bar{R}_{nd}) to approximate the \bar{M} and \bar{R} in Equation 6.11 to get

$$f_{T_p}(t_p|S_a > x) \approx \frac{P(S_a > x|t_p, \bar{M}_{nd}, \bar{R}_{nd})f_{T_p}(t_p|\bar{M})}{P(S_a > x|\bar{M}_{nd}, \bar{R}_{nd})}. \quad (6.12)$$

Here $P(S_a > x|t_p, \bar{M}_{nd}, \bar{R}_{nd})$ can be computed using the CBSB ground-motion model (with $I_{directivity}=1$), $f_{T_p}(t_p|\bar{M})$ is given by a lognormal distribution with mean and variance given by relationships from Chapter 4, and $P(S_a > x|\bar{M}_{nd}, \bar{R}_{nd})$ can again be computed using the CBSB model.

Figure 6.6 shows the deaggregated distribution of T_p conditioned on S_a exceeding the 2% in 50 years hazard level and 10% in 50 years hazard level computed using full PSHA deaggregation and from Equation 6.12. The figure shows that Equation 6.12 provides reasonable approximation.

6.4 NUMBER OF GROUND MOTIONS NEEDED

To properly account for the effects of pulse-like ground-motions, enough records need to be selected to match the deaggregated distribution of T_p and $I_{directivity}$. Since the fraction of pulse-like records in the selected set should reflect the $P(directivity|S_a > x)$, the total number of selected records should at least equal $\frac{1}{P(directivity|S_a > x)}$ times the number of pulse-like records in the set, where the number of pulse-like records in the selected set should be enough to approximate the deaggregated T_p distribution. It is difficult to give guidance on how many records are needed to approximate the shape of the distribution, as the variance of the deaggregated distribution differs widely from case to case (as can be seen in Figure 6.5). Engineering judgment should be used after hazard deaggregation to judge the number of records needed to approximate the T_p distribution.

6.5 CONCLUSION

A method to approximately compute the $I_{directivity}$ and T_p deaggregation without performing the full PSHA computation with directivity effects is proposed. These deaggregated distributions can aid

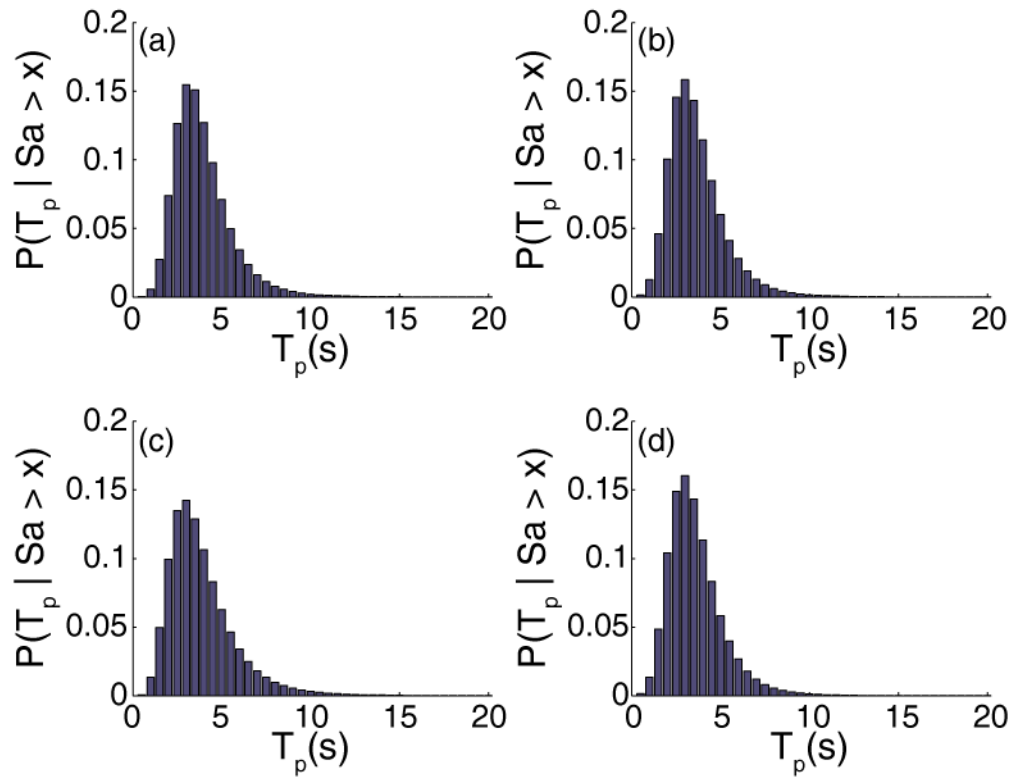


Figure 6.6 The deaggregated T_p distribution computed through deaggregation of a full directivity PSHA is shown for S_a with (a) 2% in 50 years exceedance probability and (c) 10% in 50 years exceedance probability. This can be compared with the approximate distribution computed using Equation 6.12 for S_a with (b) 2% in 50 years exceedance probability and (d) 10% in 50 years exceedance probability. This figure shows results for site 1 and spectral acceleration period (T) of 3 sec.

in ground-motion selection for near-fault sites after accounting for directivity effects. The approximate relationships were derived by starting from the exact equation that utilizes the directivity-based PSHA procedure of Chapter 2, and adding approximations until results could be obtained using standard PSHA results. The approximate estimates were compared with results from full directivity PSHA and were found to be adequate for the cases considered here. Since PSHA with directivity effects is not common yet, the models proposed here fill an urgent need to provide guidance about near-fault ground-motion selection using only information that is readily available from standard PSHA calculations.

7 NGA-West2 Models for Ground-Motion Directionality

7.1 INTRODUCTION

Structures designed to resist seismic loads are generally designed considering ground motion in the horizontal plane. However, the acceleration response spectrum, which is the intensity-measure used for design, is defined as the maximum response of a damped SDOF system at different periods when excited by a single component of the ground motion (5% damping is assumed throughout, also Sa in this report refers to pseudo spectral acceleration). Even though two-dimensional ground motions are considered for design, the intensity measure is defined to represent single component of the ground motion. Various methods have been proposed to compute an intensity measure representative of the two-dimensional horizontal ground motion. These methods include using the geometric mean of the acceleration response spectra computed using two orthogonal components of ground motion, using the median or maximum value of response spectra over all orientations at each period, etc. (Boore et al., 2006; Boore, 2010)

The NGA-West2 program, coordinated by PEER, will produce refined models for predicting the median ground-motion response spectra of a ground motion when rotated over all horizontal orientations (Bozorgnia et al., 2012); this is referred to as the Sa_{RotD50} spectrum (Boore, 2010). It is well known that ground-motion intensity is not uniform in all orientations. In some cases ground motions can be polarized, and intensity in one orientation can be significantly stronger than in other orientations (e.g., Kubo and Penzien, 1979; Huang et al., 2008). This phenomenon is often referred as “directionality” of ground motion. Due to ground motion directionality, some engineers believe that the maximum spectral acceleration over all orientations ($Sa_{RotD100}$) is a more meaningful intensity measure than Sa_{RotD50} for structural design (e.g., NEHRP, 2009). Thus, different definitions of ground-motion intensities will be used to build ground-motion models (Sa_{RotD50}) and for structural design ($Sa_{RotD100}$). The need to use a consistent intensity-measure throughout the

design process (e.g., Baker and Cornell, 2006; Beyer and Bommer, 2006) requires models to convert between the two definitions of intensity measures. Additionally, there is interest in whether the $Sa_{RotD100}$ is observed in random orientations or has preferential alignment in, for example, near-fault ground motions. This also has potentially important implications for structural design.

Several researchers have modeled the ratio of different intensity measures, which can be used as a multiplicative factor to convert between them (e.g., Beyer and Bommer, 2006; Watson-Lamprey and Boore, 2007; Huang et al., 2008, 2010). Most of these studies used subsets of the NGA database (Chiou et al., 2008) and focused on the ratios involving the older $Sa_{GMRot150}$ definition of response spectrum. In this study we used over 3000 ground motions from the expanded NGA-West2 database to build empirical models for the ratio of $Sa_{RotD100}$ to Sa_{RotD50} and the probability distribution of orientations in which the $Sa_{RotD100}$ is observed. The model predicting the ratio of $Sa_{RotD100}$ to Sa_{RotD50} can be used as a multiplicative factor that when used with the NGA-West2 ground-motion models can predict the $Sa_{RotD100}$ at a site. The proposed models are compared with older models and differences are discussed.

As defined, the $Sa_{RotD100}$ values at different periods may occur in differing orientations; therefore, it is highly unlikely that any single orientation will have Sa as large as the $Sa_{RotD100}$ at all periods. Since nonlinear response of a MDOF system is related to Sa at a range of periods, using $Sa_{RotD100}$ as the spectrum of a single ground motion component may lead to conservative estimates of structural demand. To address this, the relationship between the orientation of $Sa_{RotD100}$ at different periods is studied in detail and this information is used to compute more realistic target spectra for single ground motion components. Example computation and discussion of several alternate target spectra is included.

7.2 GROUND-MOTION INTENSITY AND DIRECTIONALITY

As discussed above, Sa measures the response of a SDOF oscillator in a single orientation and cannot completely represent the intensity in two dimensions if the ground motion is polarized. Several intensity measures have been proposed in the past to better account for two dimensional intensity of ground motions while not sacrificing the ease of use that comes with using a scalar intensity measure. Early efforts to account for the two-dimensional intensity of ground motion used the geometric mean of response spectra computed using two orthogonal components of the ground motion (sometimes referred as Sa_{GM}). Generally, the two orientations in which the ground motion was recorded (“as-recorded orientations”), or the fault-normal and fault-parallel orientations, are used for computing Sa_{GM} . Using the as-recorded orientations of the ground motion makes the ground-motion intensity dependent on the orientation of the recording instrument, which is often

arbitrary (though the practical effect on Sa is often not major). The fault-normal and fault-parallel orientations are important for near-fault sites, as near-fault effects are generally observed in these orientations (directivity in fault-normal and fling in fault-parallel for strike-slip earthquakes), but these orientations have no special significance for sites located far from the fault.

To remove the dependence of intensity measures on arbitrarily selected orientations, Boore et al. (2006) introduced $Sa_{GMRotDnn}$ and $Sa_{GMRotInn}$ intensity measures, which are orientation independent definitions of ground-motion intensity. $Sa_{GMRotDnn}$ is defined as the nn^{th} percentile of the geometric means of the response spectra from all orthogonal components of the ground motion at a specified period. The $Sa_{GMRotDnn}$ spectrum uses the geometric means from different orientations at different periods and does not represent any particular observation of two components of the ground motion. $Sa_{GMRotInn}$ addresses this problem by defining the intensity measure as the geometric mean of response spectra at the specific orientation with a spectrum closest to the $Sa_{GMRotDnn}$ spectrum across a range of periods. This definition uses the geometric mean spectrum of two specific ground motion components that were observed at the site. The 2008 version of NGA ground-motion models were developed to predict the $Sa_{GMRotI50}$ at a site (Abrahamson et al., 2008).

Though the $Sa_{GMRotInn}$ spectrum captures information from multiple orientations and is orientation and period independent, it is difficult to compute. Boore (2010) proposed a new set of IM called Sa_{RotDnn} and Sa_{RotInn} . Sa_{RotDnn} is defined as the nn^{th} percentile of the spectral acceleration at each period over all orientations. Like $Sa_{GMRotDnn}$, the nn^{th} percentile spectral acceleration at each period may occur in different orientations. Sa_{RotInn} addresses this by defining the intensity to be the spectral acceleration in the orientation most representative of the Sa_{RotDnn} spectrum. Since maximum intensity at each period may occur in different orientations and Sa_{RotInn} spectrum uses a single orientation of the ground motion, the Sa_{RotI50} spectrum can be greater than the $Sa_{RotI100}$ spectrum at some periods (Boore, 2010). This is considered a shortcoming of the Sa_{RotInn} definition. Due to its simple and orientation-independent definition, the Sa_{RotDnn} intensity measure has become popular. The new ground-motion models being developed as part of the NGA-West2 project will predict Sa_{RotD50} values, but the NEHRP (2009) provisions use $Sa_{RotD100}$ intensity for seismic design.

In general, constructing a single response spectrum to represent two-dimensional ground-motion intensity involves reducing information in two dimensions to one, which results in loss of some information. Different definitions of ground-motion intensity capture different pieces of this information and thus may be appropriate for different tasks. If the ground motion is unpolarized, then it will have equal intensity in all orientations (i.e., no directionality). In an almost no-polarization

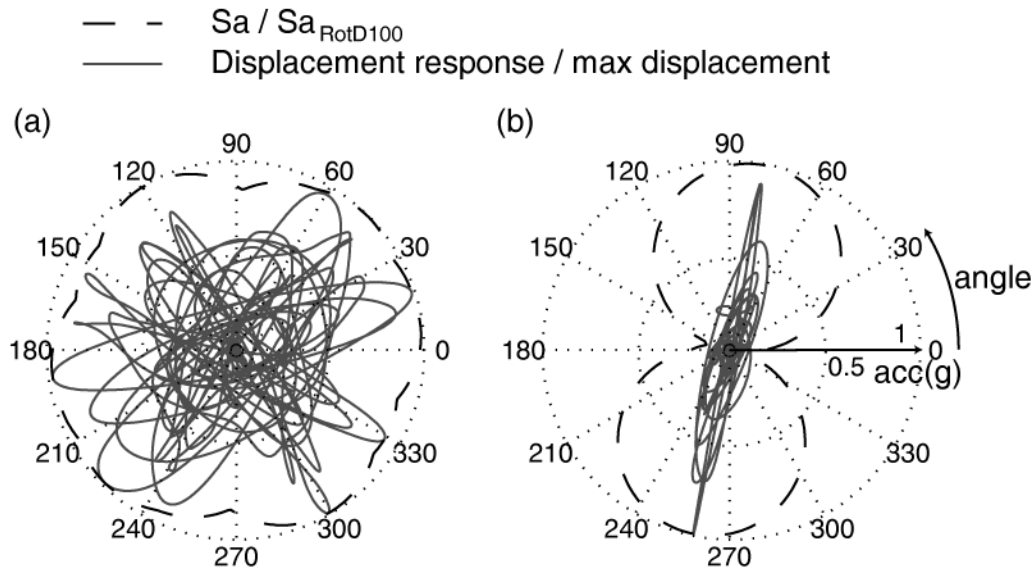


Figure 7.1 Displacement response trace ($T = 1$ sec) and spectral acceleration in all orientations (a) when ground motion is almost unpolarized (HWA031 recording from 1999 Chi-Chi-04 earthquake) and (b) when the ground motion is almost completely polarized (Gilroy Array#6 recording from 1984 Morgan Hill earthquake).

case, illustrated in figure 7.1a, all definitions of ground-motion intensity will give similar result. Hence, the ratio of $Sa_{RotD100}$ to Sa_{RotD50} will be close to 1. However, if the ground motion is strongly polarized, as illustrated in Figure 7.1b, the various definitions of Sa will differ significantly in value. In this case, different definitions of intensity measures will give different results and the ratio of $Sa_{RotD100}$ to Sa_{RotD50} can be shown to equal $\sqrt{2} = 1.414$. A ground motion record generally lies between these two extreme cases and the $Sa_{RotD100}$ to Sa_{RotD50} ratio lies between 1 and 1.414 as shown in Figure 7.2. Therefore, the intensity of ground motion computed using Sa_{RotD50} or $Sa_{RotD100}$ can differ for various ground motions, with the difference ranging from 0 to 41% of the Sa_{RotD50} intensity.

The polarization of ground motion, also referred as directionality of ground motion, causes this discrepancy among different definitions of response spectra. Thus, in this study the models used to convert between different spectral acceleration definitions are referred to as directionality models.

7.3 RATIO OF $Sa_{RotD100}$ TO Sa_{RotD50}

As discussed earlier, the NEHRP (2009) provisions use $Sa_{RotD100}$ as the intensity measure for design, while the NGA-West2 ground-motion models are being developed to predict Sa_{RotD50} intensity. Thus, models to convert between the two definitions are needed to allow the use of consistent definition of IM throughout the design process.

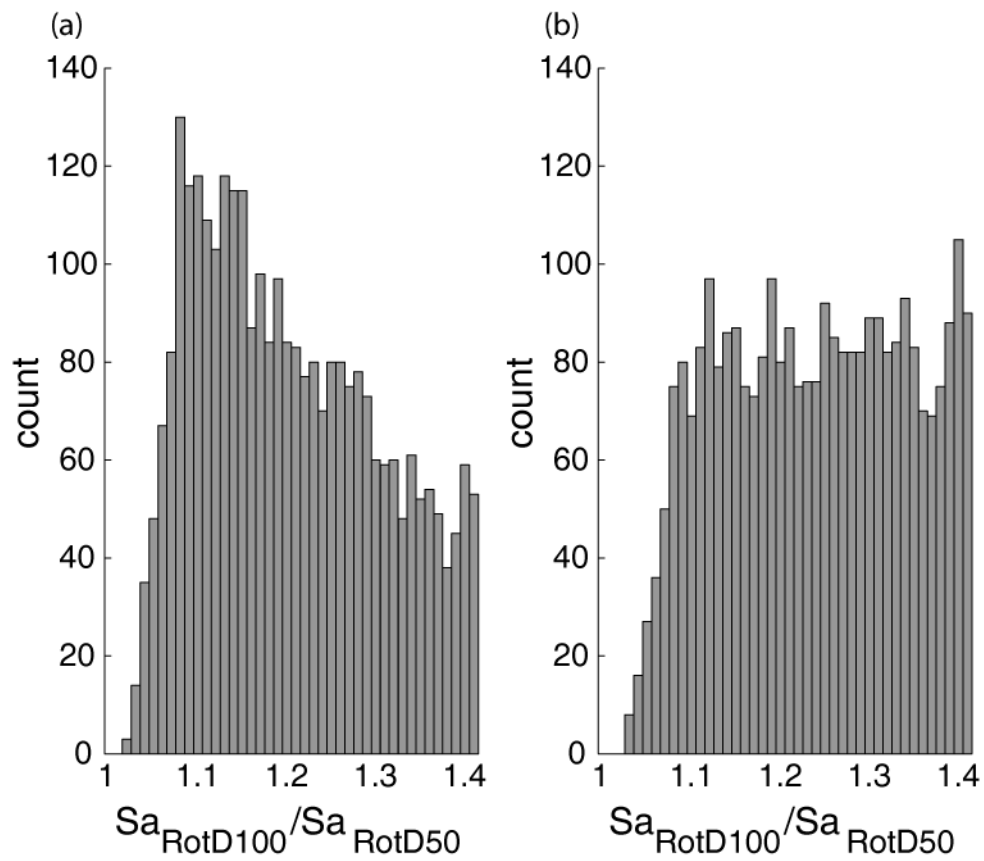


Figure 7.2 Histogram of observed ratios of $Sa_{RotD100}$ and Sa_{RotD50} in the NGA-West2 database for (a) $T = 0.2$ sec and (b) $T = 1$ sec.

We computed the ratio of $Sa_{RotD100}$ to Sa_{RotD50} for each ground motion in the subset of NGA-West2 database being used to develop the Abrahamson-Silva ground-motion model. The geometric mean of these ratios can be used as a multiplicative factor to convert Sa_{RotD50} intensity to $Sa_{RotD100}$ and its logarithm as an additive factor to convert $\ln Sa_{RotD50}$ to $\ln Sa_{RotD100}$. As ground-motion intensities are assumed to be log-normally distributed and the ground-motion models predict the natural log of intensity, the geometric mean of the ratios is a more natural estimator than the arithmetic mean, as shown in Equations 7.1 to 7.3.

$$Sa_{RotD100} = \frac{Sa_{RotD100}}{Sa_{RotD50}} \cdot Sa_{RotD50} \quad (7.1)$$

$$\ln Sa_{RotD100} = \ln \left(\frac{Sa_{RotD100}}{Sa_{RotD50}} \right) + \ln Sa_{RotD50} \quad (7.2)$$

$$E[\ln Sa_{RotD100}] = E \left[\ln \left(\frac{Sa_{RotD100}}{Sa_{RotD50}} \right) \right] + E[\ln Sa_{RotD50}] \quad (7.3)$$

where $E[\cdot]$ represents the expected value or mean value. Mixed-effects regression (e.g., Searle, 1971; Brillinger and Preisler, 1985; Abrahamson and Youngs, 1992) is used to estimate the $\ln(Sa_{RotD100}/Sa_{RotD50})$ while accounting for any earthquake-specific effects in the ratio of $Sa_{RotD100}$ and Sa_{RotD50} . The empirically computed geometric mean of $Sa_{RotD100}/Sa_{RotD50}$ from mixed-effects regression at different periods is shown in Figure 7.3. Table 7.1 shows the estimated $E[\ln(Sa_{RotD100}/Sa_{RotD50})]$ along with the between-event standard deviation (τ) and within-event standard deviation (ϕ) (standard-deviation notation following Al Atik et al., 2010). The low values of τ show that the event terms for $\ln(Sa_{RotD100}/Sa_{RotD50})$ are close to zero, or the event terms for $\ln Sa_{RotD100}$ and $\ln Sa_{RotD50}$ are almost same as each other and thus cancel out. This was expected, as the amplification/deamplification due to common source effects should be shared by both Sa_{RotD50} and $Sa_{RotD100}$. Results computed using different subsets of the NGA-West2 database used to develop other ground-motion models were found to be consistent with each other.

7.3.1 Comparison with Other Models

Several researchers have computed estimates for the ratio of $Sa_{RotD100}$ to $Sa_{GMRotI50}$ in past (e.g., Beyer and Bommer, 2006; Watson-Lamprey and Boore, 2007; Huang et al., 2008, 2010). To compare the older ratios of $Sa_{RotD100}$ to $Sa_{GMRotI50}$ with the $Sa_{RotD100}$ to Sa_{RotD50} ratios computed in this study, we used the factors proposed by Boore (2010) to convert the proposed $Sa_{RotD100}/Sa_{RotD50}$ ratios to $Sa_{RotD100}/Sa_{GMRotI50}$ ratios. Figure 7.4 compares our converted $Sa_{RotD100}$ to $Sa_{GMRotI50}$ ratios with previous results. Most of these models agree with each other

Table 7.1 Fitted values of $\ln(Sa_{RotD100}/Sa_{RotD50})$ with the within-event standard deviation (ϕ), between-event standard deviation (τ), and total standard deviation (σ), estimated by mixed-effects regression. Note that the estimates are for mean of $\ln(Sa_{RotD100}/Sa_{RotD50})$ and geometric mean of $Sa_{RotD100}/Sa_{RotD50}$ and the reported standard deviations are for $\ln(Sa_{RotD100}/Sa_{RotD50})$ estimates.

T(s)	$\ln\left(\frac{Sa_{RotD100}}{Sa_{RotD50}}\right)$	$\frac{Sa_{RotD100}}{Sa_{RotD50}}$	ϕ	τ	σ_{total}
0.01	0.176	1.19	0.08	0.01	0.08
0.02	0.175	1.19	0.08	0.01	0.08
0.03	0.172	1.19	0.08	0.01	0.08
0.05	0.171	1.19	0.08	0.01	0.08
0.075	0.172	1.19	0.08	0.01	0.08
0.1	0.172	1.19	0.08	0.01	0.08
0.15	0.182	1.20	0.08	0.01	0.08
0.2	0.187	1.21	0.08	0.01	0.08
0.25	0.196	1.22	0.08	0.01	0.08
0.3	0.198	1.22	0.08	0.01	0.08
0.4	0.206	1.23	0.08	0.01	0.08
0.5	0.206	1.23	0.09	0.01	0.09
0.75	0.213	1.24	0.08	0.01	0.08
1	0.216	1.24	0.08	0.01	0.08
1.5	0.217	1.24	0.08	0.01	0.08
2	0.218	1.24	0.08	0.01	0.08
3	0.221	1.25	0.08	0.01	0.08
4	0.231	1.26	0.08	0.01	0.08
5	0.235	1.26	0.08	0.02	0.08
7.5	0.251	1.28	0.08	0.02	0.08
10	0.258	1.29	0.07	0.03	0.08

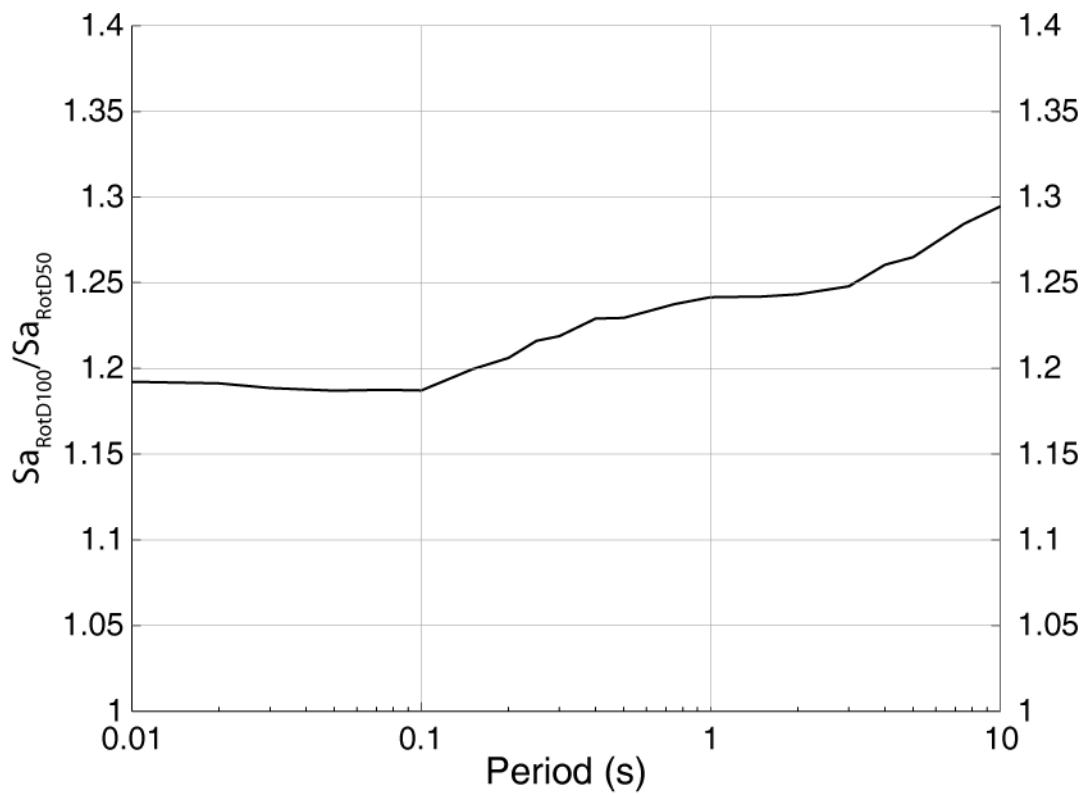


Figure 7.3 Geometric mean of the observed ratio of $Sa_{RotD100}$ to Sa_{RotD50} estimated by mixed-effects regression using NGA-West2 database.

in both the magnitude of the ratios and their trend with period. The one exception is the ratios proposed in NEHRP (2009) provisions.

The NEHRP (2009) $Sa_{RotD100}/Sa_{GMRotI50}$ ratios are based on the ratio of observed $Sa_{RotD100}$ values in recorded ground motions to the prediction of $Sa_{GMRotI50}$ by a ground-motion model. Modeling the ratio of an observed value to a predicted value—rather than the ratio of an observed value to an observed value—has some flaws. The NGA models were carefully fitted to provide an unbiased estimate of ground-motion intensity from future earthquakes. However, the dataset used to fit the ground-motion models is not an unbiased sample of earthquakes (e.g., there are many more ground motions from the 1999 M=7.6 Chi-Chi, Taiwan, earthquake in the NGA database compared to other earthquakes). Statistical techniques such as mixed-effects regression have been used to overcome these biases in the dataset while fitting the NGA ground-motion models.

The ratios recommended by NEHRP (2009) provisions effectively readjust the NGA ground-motion models, which undoes careful calculations that goes into building a ground-motion model. For example, a particular earthquake can produce higher average ground-motion intensities than the unbiased ground-motion model estimate due to random chance (any effect not accounted for by the ground-motion model can be modeled as random chance). The ratios of observed $Sa_{RotD100}$ to the predicted Sa_{RotD50} for such an earthquake will be higher than the ratio of observed $Sa_{RotD100}$ to observed Sa_{RotD50} , as the first ratio will also include the random earthquake effect, which is carefully removed by the mixed-effects regression used to fit ground-motion models. Modeling $Sa_{RotD100}/Sa_{RotD50}$ as the ratio of observed $Sa_{RotD100}$ to observed Sa_{RotD50} , and using the prediction from a ground-motion model as an estimate for $E[\ln Sa_{RotD50}]$ in Equation 7.3 allows us to leverage the results from careful fitting of ground-motion models and provides a better estimate of $Sa_{RotD100}$ from a future earthquake.

Huang et al. (2008, 2010) reported that ground motion from Chi-Chi earthquake had a significant effect on the geometric mean of the ratio of observed $Sa_{RotD100}$ to $Sa_{GMRotI50}$ values predicted by ground-motion models; therefore, they reported different sets of results for datasets with and without the Chi-Chi records. As shown in Figure 7.5, the presence or absence of Chi-Chi records did not change the geometric mean of observed $Sa_{RotD100}$ to observed Sa_{RotD50} significantly, indicating that the observed to observed ratio are more stable across different earthquake events compared to the observed to predicted ratio.

7.3.2 Dependence of $Sa_{RotD100}/Sa_{RotD50}$ on Other Parameters

Figures 7.2 and 7.3 showed that the geometric mean value of $Sa_{RotD100}/Sa_{RotD50}$ depends on spectral acceleration period. We also investigated its dependence on other seismological parameters,

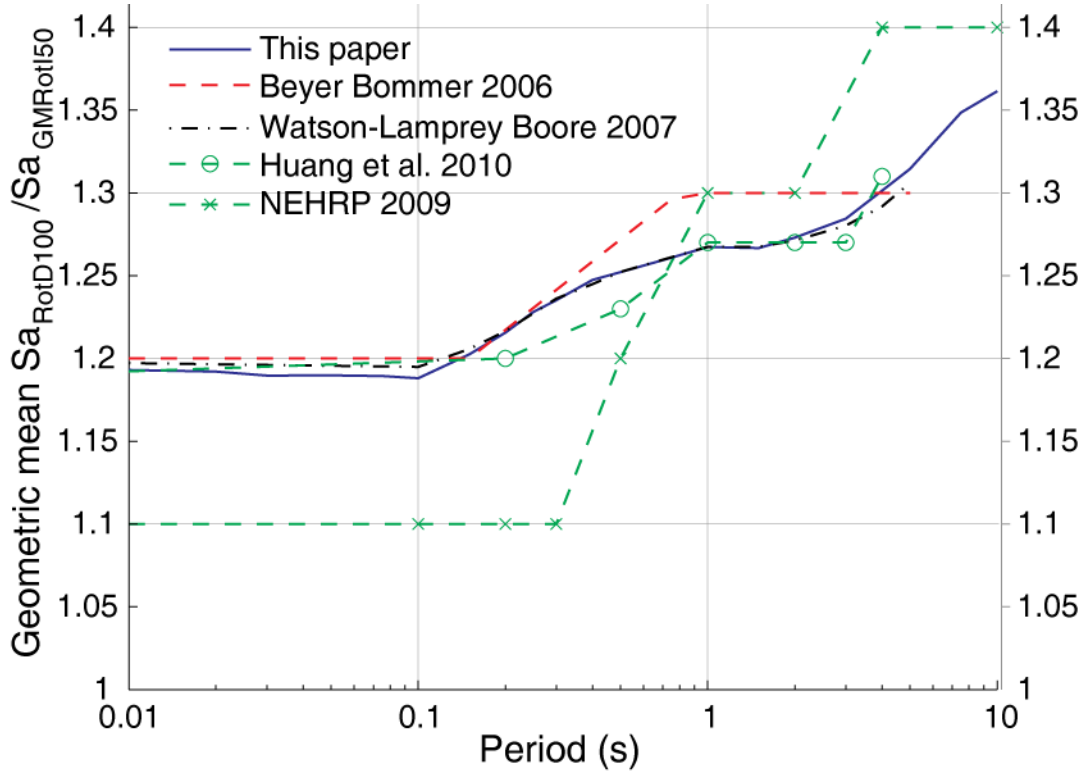


Figure 7.4 Comparison of various models for geometric mean $Sa_{RotD100}/Sa_{GMRotI50}$ ratios.

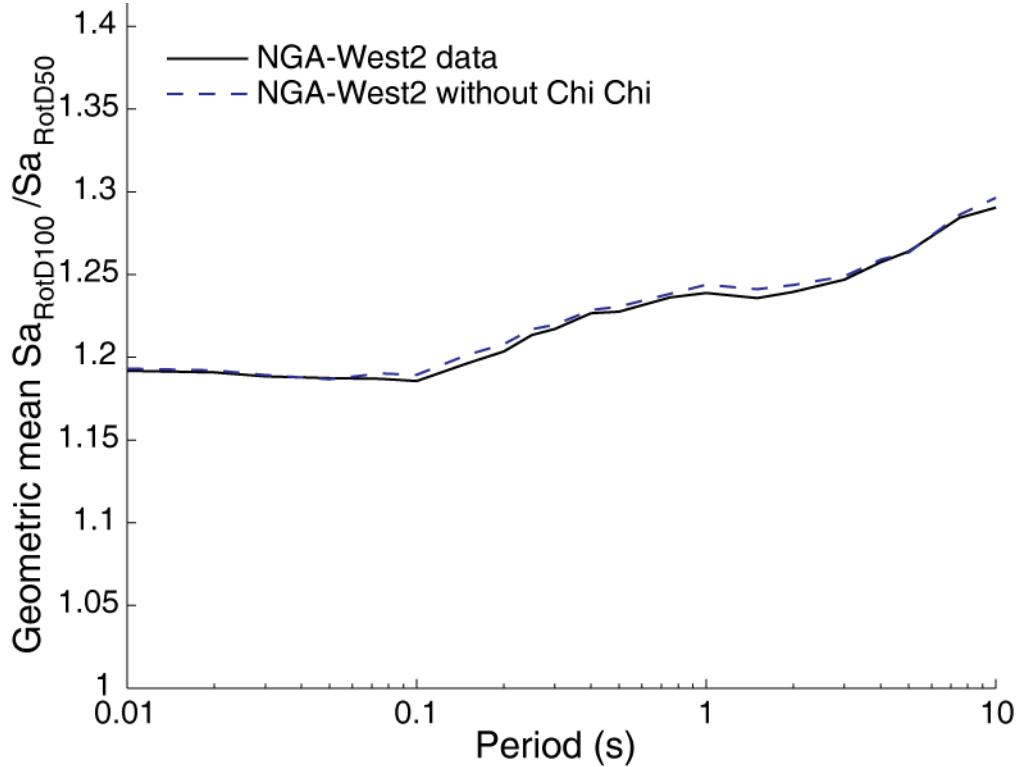


Figure 7.5 Comparison of the geometric means of $Sa_{RotD100}/Sa_{RotD50}$ estimated using datasets with and without the 1999 M=7.6 Chi-Chi ground motions.

such as earthquake magnitude, closest distance between source and the site, and some directivity parameters. We studied the dependence of this ratio on other seismological parameters and fitted several regression models using variable selection techniques, such as forward selection, backward elimination, etc. After examining the practical and statistical significance of different models, we decided to develop a model for $\ln(Sa_{RotD100}/Sa_{RotD50})$ that was a linear function of R_{rup} (closest distance between rupture and site). Other parameters such as magnitude, directivity predictor terms, etc., had no appreciable predictive power. The linear model, shown in Equation 7.4, contains a coefficient a_0 that varies with period and a coefficient a_1 that is constant for all periods, which is estimated to be -1.614×10^{-4} . Coefficient a_0 is the same as the $\ln(Sa_{RotD100}/Sa_{RotD50})$ values presented in Table 7.1. Note that this relationship was fitted using data with closest distance less than 200 km and over 90% of the data had closest distance less than 100 km. So, we do not recommend use of these models for distances larger than 200 km.

$$E \left[\ln \left(\frac{Sa_{RotD100}}{Sa_{RotD50}} \right) \right] = a_0 + a_1 \cdot (R_{rup} - 60) \quad (7.4)$$

The difference between the results from using a distance-dependent model or using a non-distance-dependent model is small, as can be seen in Figure 7.6. Thus, we report both the geometric mean of the ratio of $Sa_{RotD100}$ and Sa_{RotD50} and the coefficient a_0 from equation 7.4 at different periods in table 7.1. Either of the two models can be used depending on the level of precision required. This view is echoed in the similar earlier study by Watson-Lamprey and Boore (2007), who noted slight distance, magnitude, and radiation pattern dependence, but stated that “for most engineering applications the conversion factors independent of those variables can be used.” The results are reported at discrete set of periods and coefficients at other periods can be estimated by interpolating these results.

7.4 ORIENTATION OF $SA_{ROT D100}$

Structural systems generally have different resistance to seismic loads in different orientations. For these systems, the orientation in which the maximum spectral acceleration occurs is also important. We define the orientation of $Sa_{RotD100}$ as the minimum angle between the strike of the fault and the orientation of $Sa_{RotD100}$. This orientation, referred as α hereafter, ranges from 0 to 90 degrees where $\alpha = 0$ represents the strike-parallel orientation and $\alpha = 90$ represent the strike-normal orientation. These orientations are often close to the fault-normal and fault-parallel orientation, and in most cases can be taken as an approximation to them.

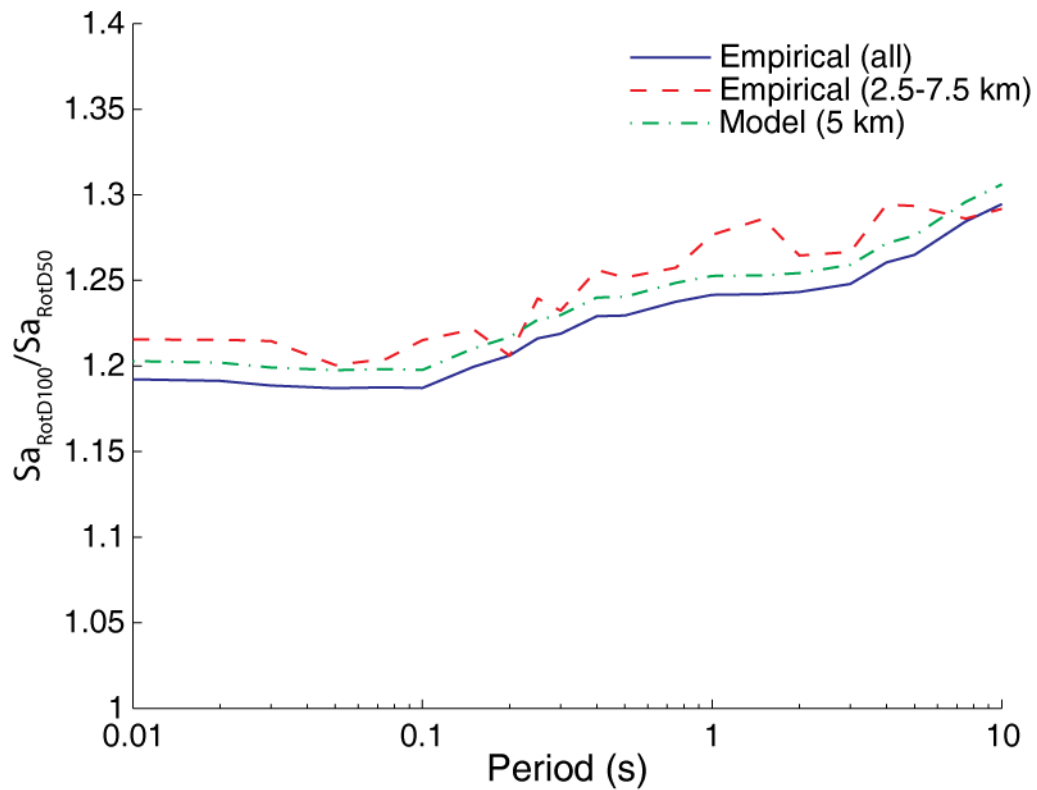


Figure 7.6 Prediction of $Sa_{RotD100}/Sa_{RotD50}$ by the distance dependent model in Equation 7.4 for $R = 5$ km, compared with the non-distance dependent estimates of $Sa_{RotD100}/Sa_{RotD50}$ given in Table 7.1 and the empirical geometric mean of $Sa_{RotD100}/Sa_{RotD50}$ ratio using only the data with closest distance between 2.5 to 7.5 km.

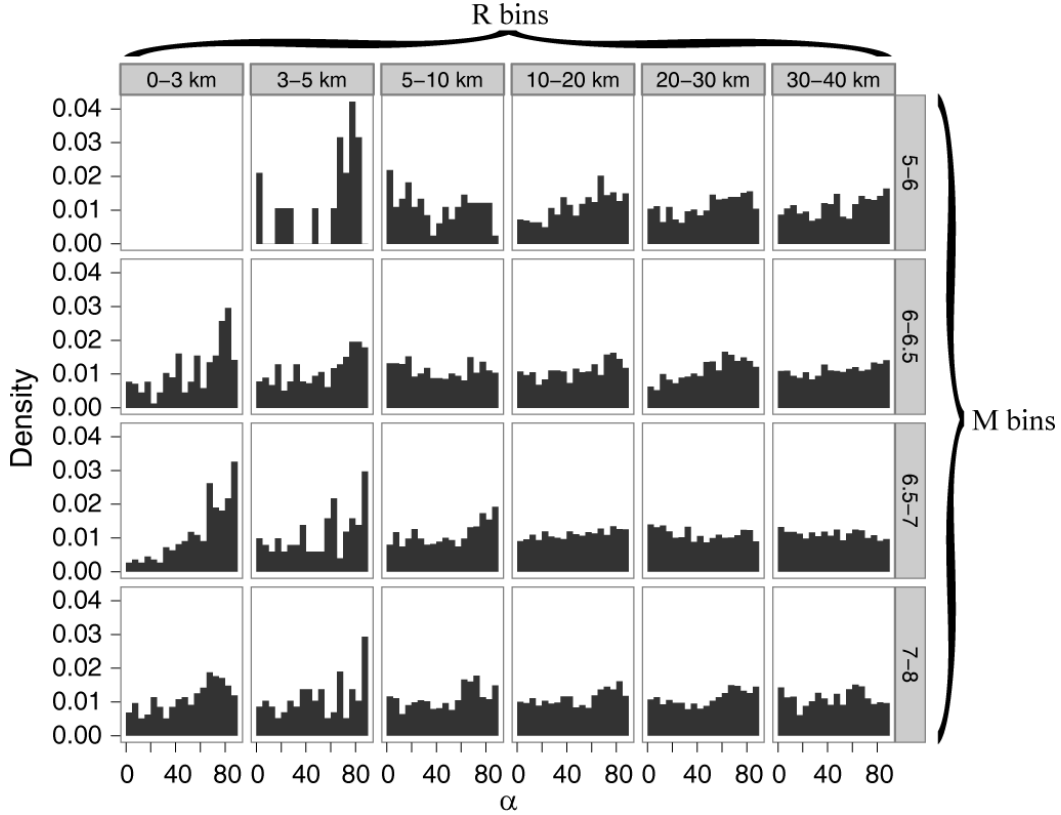


Figure 7.7 Probability density of α ($Sa_{RotD100}$ orientations) in different M , R_{rup} bins.

To study these orientations, we computed α for each ground motion in our database at 21 periods, and then binned the data according to different seismological parameters and examined the distribution of α in each bin. Figure 7.7 shows the distribution of α in different M and R_{rup} bins. α is closer to the strike-normal orientation ($\alpha = 90$) more often than to the strike-parallel orientation ($\alpha = 0$) when the site is located within 5 km of the fault. On the other hand, when R_{rup} is greater than 5 km, α is almost uniformly distributed. The magnitude bins do not seem to have any significant influence on the distribution of α . To examine the effect of period on $Sa_{RotD100}$ orientation (α), we binned all the data within 5 km of the fault by period. Histograms of α in different period bins are shown in Figure 7.8. The distribution of α is nearly uniform for periods less than 1 sec, while orientations close to strike-normal are more frequent than strike-parallel for periods larger than 1 sec.

After examining histograms of α binned by several parameters, we decided to model the distribution of α as uniform for sites when R_{rup} is greater than 5 km or when the spectral-acceleration period under consideration is less than 1 sec. For other cases ($R_{rup} < 5$ km and $T \geq 1$ sec) the data was pooled and the distribution was modeled empirically by counting the number of α observed in 10-degree bins. This empirically computed distribution is presented in Table 7.2.

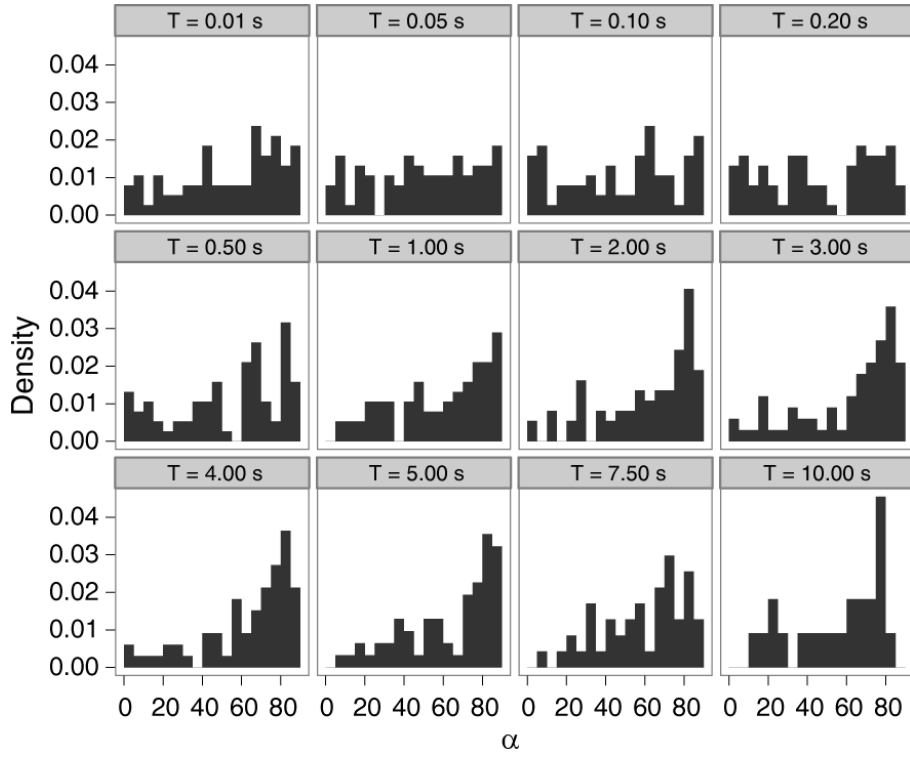


Figure 7.8 Probability density of α for sites with $R_{rup} < 5$ km, binned by period (sec).

Table 7.2 Probability density of α for $R_{rup} < 5$ km and $T \geq 1$ sec.

Orientations (degrees)	Probability
0-10	0.031
10-20	0.055
20-30	0.070
30-40	0.067
40-50	0.080
50-60	0.100
60-70	0.106
70-80	0.233
80-90	0.258

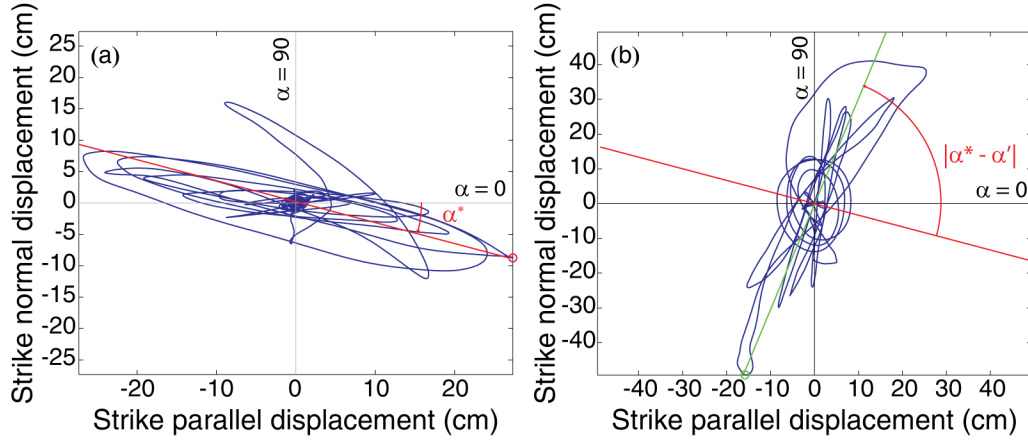


Figure 7.9 Displacement response trace to the EI Centro differential array recording from the 1979 Imperial Valley earthquake. The period of the SDOF oscillator is (a) $T^* = 1.5$ sec and (b) $T' = 3$ sec. The orientations of $Sa_{RotD100}$ along with the difference between these orientations at the two periods ($|\alpha^* - \alpha'|$) is also shown.

7.4.1 Relationship between $Sa_{RotD100}$ Orientations at Different Periods

Figure 7.9 shows the polarization of displacement response and orientation of $Sa_{RotD100}$ intensity from an example ground motion at two different periods (say T^* and T'). The $Sa_{RotD100}$ intensity at different periods may occur in different orientations and the difference in orientation ($|\alpha^* - \alpha'|$ in Figure 7.9) can be used to study the relationship between the $Sa_{RotD100}$ orientations at different periods. This knowledge can be used to construct more realistic single orientation target spectra, as shown below.

The difference in the orientation of $Sa_{RotD100}$ at two periods has a lot of uncertainty and can take any value between 0 degrees (i.e., the orientation at both period are the same) to 90 degrees (i.e., the $Sa_{RotD100}$ occurs in orthogonal orientations at the two periods). Figure 7.10 shows the histogram of the difference in $Sa_{RotD100}$ orientation ($|\alpha^* - \alpha'|$) at two different periods. The probability distribution of $|\alpha^* - \alpha'|$ depends on the periods under consideration $|\alpha^* - \alpha'|$ is more likely to be close to 0 degrees when the periods are closer to each other. Thus, the average difference between the orientations increases with increasing difference between the periods.

After examining histograms at several sets of periods, the truncated exponential distribution was selected to model the distribution of $|\alpha^* - \alpha'|$. The truncated exponential distribution is described in equation 7.5 below

$$f(x) = \begin{cases} \frac{\lambda e^{-\lambda x}}{1 - e^{-90\lambda}}; & x \leq 90 \\ 0 & \text{otherwise} \end{cases} \quad (7.5)$$

The distribution depends on the parameter λ , which is estimated here using the maximum likelihood method. The estimated parameters are presented in Table 7.3. When $T^* = T'$, $\lambda \rightarrow \infty$, thus the

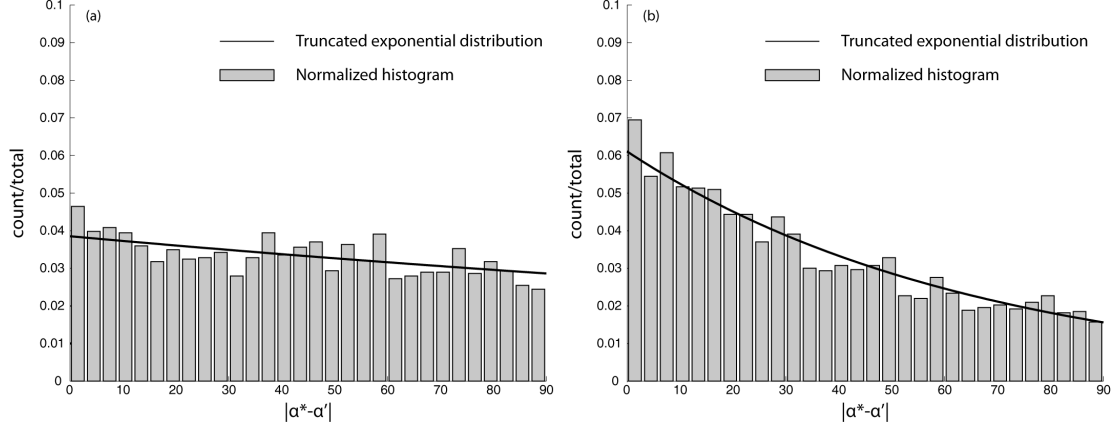


Figure 7.10 Distribution of $|\alpha^* - \alpha'|$ as predicted by the truncated exponential model is compared with the normalized histogram for (a) $T^* = 2$ sec and $T' = 0.1$ sec and (b) $T^* = 2$ sec and $T' = 1$ sec.

probability density becomes a Dirac-delta function centered at 0 degrees. Figure 7.10 shows the comparison of the fitted distribution with empirical histograms for two periods.

7.5 SA AT ARBITRARY ORIENTATIONS

A model to predict Sa in an arbitrary orientation is needed to compute single orientation conditional spectra. Here we study the Sa in an orientation ϕ degrees away from the $Sa_{RotD100}$ orientation. This Sa is referred hereafter as Sa_ϕ . An empirical model for the ratio of Sa_ϕ/Sa_{RotD50} is developed, which can be used as a multiplicative factor with a ground-motion model prediction of Sa_{RotD50} to get a prediction for Sa_ϕ . The spectral acceleration in each orientation was computed for all the ground-motion recordings used in this study. This dataset was used to empirically compute the geometric mean of the Sa_ϕ/Sa_{RotD50} . As the event terms from mixed-effects regression for $\ln(Sa_{RotD100}/Sa_{RotD50})$ were found to be close to 0, we ignored the inter-event terms and pooled the data across different earthquakes and estimated the Sa_ϕ/Sa_{RotD50} using geometric means of the pooled data. The $Sa_{RotD100}/Sa_{RotD50}$ values estimated using mixed-effects regression (Table 7.1) and empirical geometric means (values corresponding to $\phi = 0$ in Table 7.4) vary slightly but are practically identical.

Figure 7.11 shows the modeled ratio for three different periods. As expected the ratio is highest at $\phi = 0$, where it is same as $Sa_{RotD100}$, and decreases with increase of ϕ . Table 7.4 presents the geometric mean of $\frac{Sa_\phi}{Sa_{RotD50}}$ at ϕ values from 0 to 90 degrees at 5-degree intervals for 21 periods. Predictions at other periods and ϕ values can be found by interpolating these results.

Table 7.3 Estimated values of the parameter λ for the truncated exponential model.

T'	T''																					
	0.01	0.02	0.03	0.05	0.07	0.10	0.15	0.20	0.25	0.30	0.40	0.50	0.75	1.00	1.50	2.00	3.00	4.00	5.00	7.50	10.00	
0.01	∞	0.579	0.186	0.070	0.042	0.031	0.022	0.021	0.020	0.020	0.020	0.018	0.014	0.013	0.010	0.007	0.004	0.005	0.007	0.007	0.007	0.007
0.02	∞	0.579	0.188	0.071	0.042	0.031	0.022	0.021	0.019	0.020	0.020	0.018	0.014	0.013	0.010	0.007	0.004	0.005	0.007	0.007	0.007	0.007
0.03	0.186	0.188	∞	0.072	0.042	0.030	0.022	0.021	0.019	0.019	0.019	0.018	0.013	0.012	0.009	0.007	0.004	0.006	0.007	0.007	0.007	0.007
0.05	0.070	0.071	0.072	∞	0.041	0.028	0.020	0.019	0.017	0.017	0.016	0.015	0.010	0.010	0.007	0.006	0.004	0.005	0.005	0.006	0.006	0.005
0.07	0.042	0.042	0.042	0.041	∞	0.031	0.019	0.017	0.016	0.016	0.015	0.013	0.009	0.009	0.007	0.005	0.003	0.004	0.004	0.004	0.004	0.005
0.10	0.031	0.031	0.030	0.028	0.031	∞	0.020	0.015	0.014	0.014	0.011	0.011	0.009	0.007	0.005	0.003	0.003	0.003	0.003	0.003	0.003	0.003
0.15	0.022	0.022	0.022	0.020	0.019	0.017	∞	0.019	0.013	0.013	0.010	0.009	0.006	0.005	0.003	0.002	0.000	0.001	0.002	0.002	0.002	0.002
0.20	0.021	0.021	0.021	0.019	0.017	0.016	0.015	∞	0.021	0.016	0.013	0.011	0.007	0.005	0.003	0.003	0.001	0.002	0.003	0.003	0.002	0.002
0.25	0.020	0.019	0.019	0.017	0.016	0.014	0.013	0.021	∞	0.026	0.015	0.010	0.007	0.005	0.004	0.004	0.003	0.003	0.003	0.003	0.002	0.002
0.30	0.020	0.020	0.019	0.017	0.016	0.014	0.013	0.016	0.026	∞	0.019	0.013	0.007	0.007	0.005	0.003	0.004	0.004	0.004	0.005	0.004	0.005
0.40	0.020	0.020	0.020	0.016	0.015	0.011	0.010	0.013	0.015	0.019	∞	0.024	0.011	0.010	0.008	0.005	0.004	0.006	0.007	0.005	0.005	0.005
0.50	0.018	0.018	0.018	0.015	0.013	0.011	0.009	0.011	0.010	0.013	0.024	∞	0.016	0.013	0.008	0.007	0.004	0.005	0.005	0.005	0.005	0.005
0.75	0.014	0.014	0.014	0.012	0.010	0.009	0.006	0.007	0.007	0.007	0.011	0.016	∞	0.022	0.013	0.011	0.006	0.008	0.009	0.009	0.009	0.009
1.00	0.013	0.013	0.012	0.010	0.009	0.007	0.005	0.005	0.005	0.005	0.007	0.010	0.013	∞	0.020	0.015	0.010	0.010	0.010	0.010	0.010	0.010
1.50	0.010	0.010	0.009	0.007	0.007	0.005	0.003	0.003	0.004	0.005	0.008	0.008	0.013	0.020	∞	0.024	0.012	0.011	0.012	0.012	0.013	0.013
2.00	0.007	0.007	0.007	0.006	0.005	0.003	0.002	0.003	0.004	0.003	0.005	0.007	0.011	0.015	0.024	∞	0.019	0.016	0.016	0.016	0.016	0.014
3.00	0.004	0.004	0.004	0.004	0.003	0.003	0.000	0.001	0.001	0.003	0.004	0.004	0.006	0.010	0.012	0.019	∞	0.029	0.024	0.019	0.017	0.017
4.00	0.005	0.005	0.006	0.005	0.004	0.003	0.001	0.002	0.003	0.004	0.006	0.005	0.008	0.010	0.011	0.016	0.024	∞	0.040	0.025	0.021	0.021
5.00	0.007	0.007	0.007	0.005	0.004	0.003	0.002	0.003	0.003	0.005	0.007	0.005	0.009	0.010	0.012	0.015	0.024	0.040	∞	0.034	0.027	0.027
7.50	0.007	0.007	0.007	0.006	0.004	0.003	0.002	0.002	0.003	0.004	0.005	0.005	0.009	0.011	0.013	0.016	0.019	0.025	0.034	∞	0.034	0.034
10.00	0.007	0.007	0.007	0.005	0.005	0.003	0.002	0.002	0.003	0.005	0.005	0.005	0.009	0.010	0.013	0.014	0.017	0.021	0.027	0.027	0.027	∞

Table 7.4 Geometric mean of $\frac{S_{a\phi}}{S_{a_{RotD50}}}$ at various values of ϕ and T .

	ϕ (degrees)																		
	0	5	10	15	20	25	30	35	40	45	50	55	60	65	70	75	80	85	90
0.01	1.192	1.188	1.175	1.154	1.127	1.096	1.061	1.026	0.993	0.963	0.939	0.919	0.903	0.891	0.882	0.874	0.869	0.865	0.864
0.02	1.191	1.187	1.174	1.154	1.127	1.095	1.061	1.026	0.993	0.964	0.939	0.920	0.904	0.892	0.882	0.875	0.869	0.866	0.865
0.03	1.188	1.184	1.171	1.151	1.124	1.093	1.059	1.025	0.992	0.963	0.940	0.921	0.906	0.893	0.884	0.877	0.872	0.868	0.867
0.05	1.187	1.183	1.170	1.150	1.123	1.091	1.058	1.024	0.992	0.964	0.941	0.923	0.908	0.896	0.887	0.880	0.874	0.871	0.870
0.07	1.187	1.183	1.170	1.150	1.123	1.091	1.058	1.024	0.992	0.965	0.942	0.923	0.908	0.896	0.887	0.879	0.874	0.871	0.870
0.10	1.186	1.181	1.168	1.148	1.122	1.091	1.058	1.024	0.993	0.965	0.941	0.922	0.906	0.893	0.882	0.874	0.868	0.865	0.864
0.15	1.196	1.192	1.179	1.159	1.133	1.101	1.067	1.032	0.998	0.967	0.939	0.915	0.895	0.880	0.867	0.858	0.851	0.847	0.845
0.20	1.204	1.199	1.187	1.166	1.140	1.109	1.074	1.038	1.003	0.968	0.938	0.910	0.887	0.869	0.854	0.843	0.835	0.830	0.829
0.25	1.213	1.209	1.196	1.176	1.149	1.117	1.082	1.044	1.006	0.969	0.935	0.905	0.879	0.859	0.841	0.828	0.819	0.813	0.812
0.30	1.217	1.213	1.200	1.180	1.153	1.120	1.084	1.046	1.008	0.970	0.935	0.902	0.874	0.850	0.830	0.814	0.803	0.796	0.794
0.40	1.227	1.222	1.209	1.189	1.162	1.129	1.093	1.053	1.013	0.972	0.934	0.899	0.868	0.841	0.819	0.802	0.789	0.781	0.779
0.50	1.228	1.223	1.210	1.190	1.163	1.130	1.094	1.054	1.013	0.972	0.933	0.896	0.863	0.835	0.811	0.792	0.780	0.773	0.770
0.75	1.236	1.232	1.219	1.198	1.171	1.138	1.100	1.059	1.017	0.974	0.933	0.893	0.857	0.825	0.798	0.776	0.761	0.752	0.749
1.00	1.239	1.234	1.222	1.201	1.173	1.140	1.102	1.061	1.017	0.973	0.931	0.891	0.854	0.822	0.795	0.773	0.757	0.748	0.745
1.50	1.236	1.231	1.219	1.198	1.171	1.138	1.100	1.059	1.016	0.973	0.932	0.892	0.855	0.823	0.795	0.773	0.757	0.748	0.744
2.00	1.240	1.235	1.222	1.201	1.174	1.140	1.102	1.061	1.018	0.974	0.930	0.889	0.851	0.817	0.789	0.766	0.750	0.740	0.737
3.00	1.247	1.243	1.229	1.209	1.180	1.146	1.108	1.066	1.021	0.975	0.929	0.885	0.845	0.809	0.778	0.753	0.734	0.723	0.719
4.00	1.257	1.253	1.240	1.219	1.190	1.156	1.116	1.073	1.026	0.977	0.929	0.881	0.837	0.796	0.761	0.730	0.708	0.693	0.688
5.00	1.264	1.259	1.246	1.225	1.196	1.161	1.121	1.077	1.029	0.979	0.928	0.877	0.828	0.781	0.740	0.704	0.677	0.658	0.652
7.50	1.284	1.280	1.266	1.245	1.215	1.180	1.138	1.091	1.039	0.985	0.928	0.869	0.810	0.753	0.699	0.650	0.608	0.577	0.565
10.00	1.290	1.286	1.272	1.250	1.221	1.184	1.141	1.093	1.041	0.985	0.927	0.867	0.806	0.746	0.688	0.635	0.589	0.555	0.542

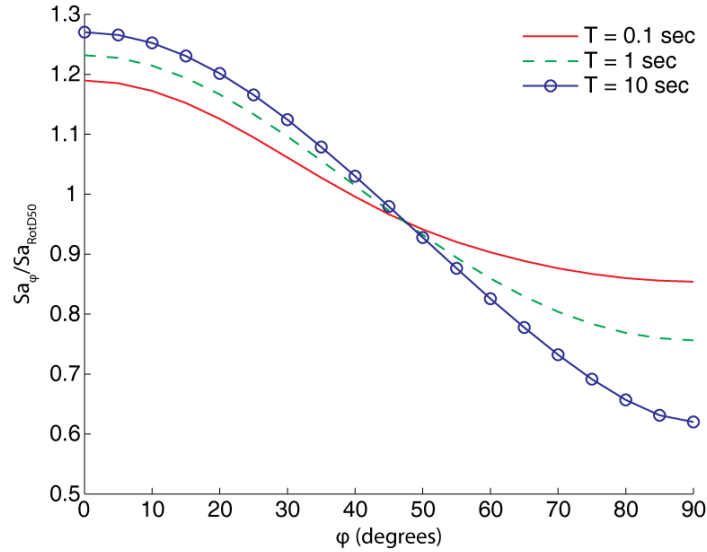


Figure 7.11 The geometric mean of $\frac{S a_{\phi}}{S a_{RotD50}}$ as a function of ϕ for different periods.

7.6 EXAMPLE TARGET SPECTRA

As discussed above, the $S a_{RotD100}$ spectrum is an envelope over spectra from all orientations at each period. Figure 7.9 shows that the $S a_{RotD100}$ value may be observed in very different orientations, even at two periods that are close to each other; therefore, it is very unlikely to observe $S a_{RotD100}$ at multiple periods in a single orientation. Thus, using $S a_{RotD100}$ as a target design spectrum may result in conservative estimates of *EDPs*, which depends on multiple periods (e.g., peak floor acceleration, inter-storey drift ratio etc.). The conditional mean spectra approach (e.g., Baker, 2011) can be used to compute more realistic single orientation target spectra for design. The conditional mean spectra is the expected value of the ground-motion intensity conditioned upon some information. Here we study the computation of two such target spectra conditioned on a specific orientation and on a $S a_{RotD100}$ observation in a specific period.

7.6.1 Spectra Conditioned on Orientation

Structures generally have different load resistance in different orientations. If some orientation is more important than other orientations, then the expected value of $S a$ in that particular orientation can be used as an appropriate target spectrum. Since this response spectrum is conditioned on a single orientation, it does not suffer from the problem of having $S a$ from different orientations at different periods, as in case of the $S a_{RotD100}$ spectra.

The target spectrum conditioned on an orientation, θ degrees away from strike-parallel orientation can be computed using the Equations 7.6 to 7.8 below

$$E[Sa|\theta] = \int_0^{90} E[Sa_\theta|\alpha] \cdot P(\alpha) d\alpha \quad (7.6)$$

$$= \int_0^{90} E[Sa_{\theta-\alpha}] \cdot P(\alpha) d\alpha \quad (7.7)$$

$$= \int_0^{90} \frac{Sa_{\theta-\alpha}}{Sa_{RotD50}} \cdot \hat{S}a_{RotD50} \cdot P(\alpha) d\alpha \quad (7.8)$$

where α represents the orientation in which the $Sa_{RotD100}$ is observed at the period for which computation is being done, and $\hat{S}a_{RotD50}$ represents the Sa_{RotD50} prediction from a ground-motion model. Table 7.4 gives the values of $\frac{Sa_{\theta-\alpha}}{Sa_{RotD50}}$ at different periods and $\phi = \theta - \alpha$ orientations, while Table 7.2 describes the probability distribution of α [i.e. $P(\alpha)$].

Spectra conditioned in the strike-normal and strike-parallel orientations are compared with corresponding Sa_{RotD50} and $Sa_{RotD100}$ in Figure 7.12. These computations were done for an earthquake of magnitude 7 and at a site with a V_{s30} of 760 m/sec and located 2.5 km away from the rupture. The Boore and Atkinson (2008) model prediction was used to estimate Sa_{RotD50} (i.e., $\hat{S}a_{RotD50}$ in equation 7.8). It should be noted that Boore and Atkinson (2008) model predicts for an $Sa_{GMRotI50}$ intensity, but Sa_{RotD50} and $Sa_{GMRotI50}$ intensities are expected to be close to each other (e.g., $Sa_{RotD50}/Sa_{GMRotI50}$ is within a factor of 1.06, Boore, 2010).

7.6.2 Spectra Conditioned on the Orientation of $Sa_{RotD100}$ at a Given Period

Since, the orientation of $Sa_{RotD100}$ is random, the spectrum conditioned on a single orientation can never be as large as $Sa_{RotD100}$ at any period. Structural response is often primarily driven by the ground-motion intensity at a single period. Thus, if a single period is more important than others, a more appropriate target spectrum could be the one conditioned on the orientation in which $Sa_{RotD100}$ is observed at the important period (say, T^*). If the spectrum is conditioned on $Sa_{RotD100}$ orientation at the period T^* (i.e., orientation α^*), the expected value of the Sa at a different period, say, T' , can be computed using Equations 7.9 to 7.11 below

$$E[SaT'|\alpha^*] = \int_0^{90} E[SaT'|\alpha', \alpha^*] P(\alpha'|\alpha^*) d\alpha' \quad (7.9)$$

$$= \int_0^{90} E[SaT'_{|\alpha^*-\alpha'}|\alpha', \alpha^*] P(|\alpha' - \alpha^*|) d\alpha' \quad (7.10)$$

$$= \int_0^{90} \frac{Sa_{\alpha^*-\alpha'}}{Sa_{RotD50}} \cdot \hat{S}a_{RotD50} P(|\alpha' - \alpha^*|) d\alpha' \quad (7.11)$$

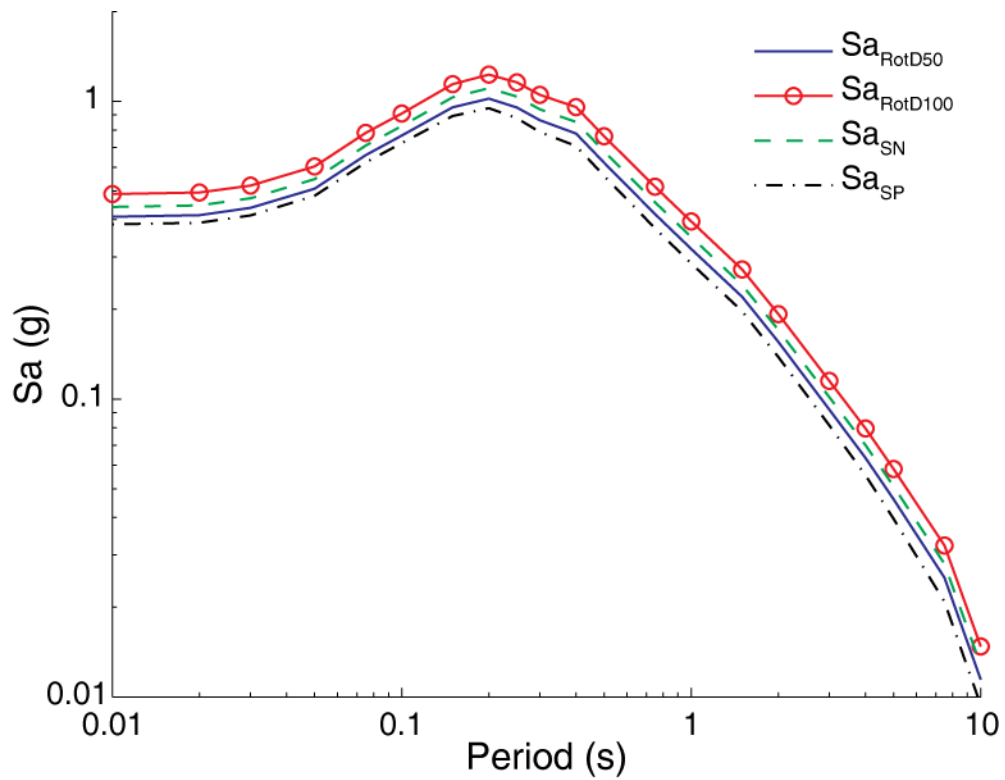


Figure 7.12 Comparison of the median predicted $Sa_{RotD100}$ and Sa_{RotD50} spectra with spectra conditioned in strike-normal and strike-parallel orientations. All results are for an earthquake with magnitude 7, at distance of 2.5 km and $V_{s30} = 760$ m/sec.

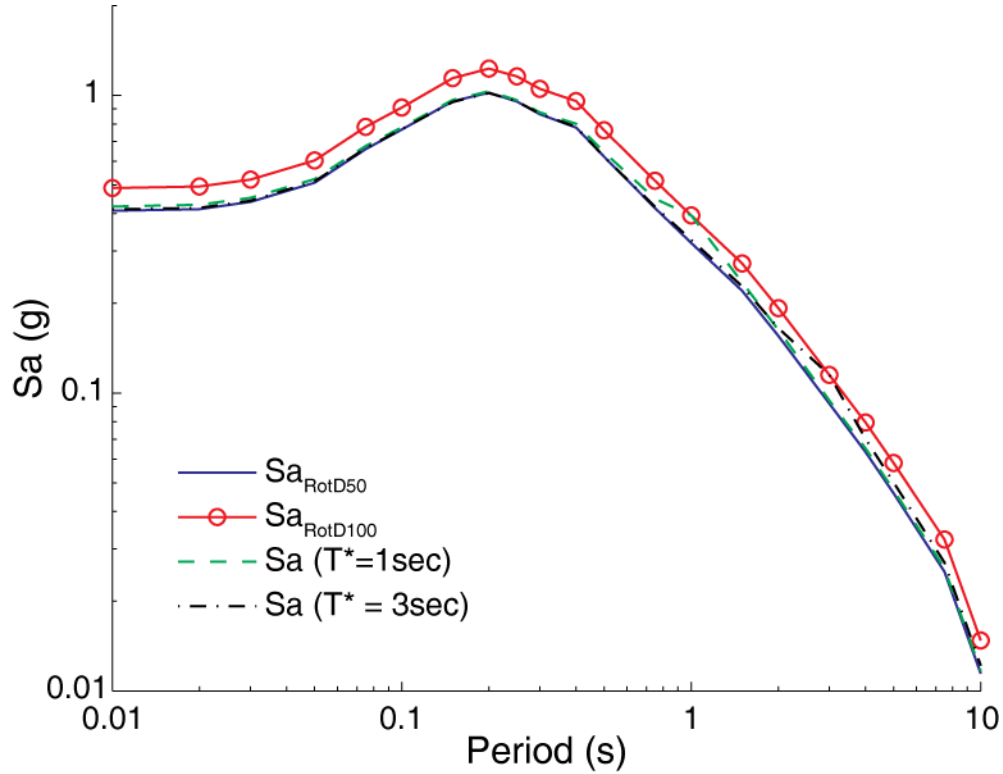


Figure 7.13 Comparison of the $Sa_{RotD100}$ and Sa_{RotD50} spectra with spectra conditioned on $Sa_{RotD100}$ orientation at $T^* = 1$ sec and $T^* = 3$ sec. All results are for an earthquake with magnitude 7, at distance of 2.5 km and $V_{s30} = 760$ m/sec.

where $\frac{Sa_{\alpha^*-\alpha'}}{Sa_{RotD50}}$ is given by Table 7.4 for different values of $\phi = |\alpha^* - \alpha'|$ and periods (T'). $\hat{S}a_{RotD50}$ is the prediction from a ground-motion model, and $P(|\alpha' - \alpha^*|)$ is modeled by the truncated exponential distribution with the parameter λ for the pair of periods T' and T^* given in Table 7.3.

Spectra conditioned on the $Sa_{RotD100}$ orientations at $T^* = 1$ sec and $T^* = 3$ sec are compared with the Sa_{RotD50} and $Sa_{RotD100}$ in Figure 7.13. These computation were done for an earthquake of magnitude 7 and at a site with V_{s30} of 760 m/sec located 2.5 km away from the rupture. Again the Boore and Atkinson (2008) model prediction was used to estimate Sa_{RotD50} .

7.7 CONCLUSION

This study examined different methods of representing the intensity of ground motion in the horizontal plane using a response spectrum that is a one-dimensional representation of ground-motion intensity. We focused on two orientation-independent representations of the response spectrum: Sa_{RotD50} and $Sa_{RotD100}$. The new ground-motion models being developed as part of the NGA-West2 project will predict the Sa_{RotD50} spectrum at a site due to a future earthquake, while the NEHRP (2009) provisions recommend using $Sa_{RotD100}$ for seismic design. We have proposed a

model to predict the ratio of $Sa_{RotD100}$ to Sa_{RotD50} , which can be used as a multiplicative factor with the Sa_{RotD50} predictions from the new NGA-West2 ground-motion models to predict the $Sa_{RotD100}$ ground-motion intensity. The proposed model was compared and was found to be consistent with similar models built in the past, though the proposed model advances that earlier work by using a larger dataset, utilizing the recently adopted Sa_{RotD50} definition instead of $Sa_{GMRotI50}$, and using mixed-effects regression to account for inter-event terms. The differences between the proposed model and corresponding NEHRP (2009) ratios were also explained. One important observation from this work is that the current NEHRP ratio of 1.1 at small periods is incorrect and should be approximately 1.2; this result is confirmed by other studies.

Along with modeling the ratio of $Sa_{RotD100}$ to Sa_{RotD50} , we also modeled the probability distribution of orientations in which the $Sa_{RotD100}$ intensity is observed relative to the strike of the fault. The orientations of $Sa_{RotD100}$ were observed to be uniformly distributed when the closest distance between the fault and the site was greater than 5 km, or if the period under consideration was less than 1 sec. Only for the cases when the site was within 5 km of the fault and at periods greater than 1 sec was the orientation of $Sa_{RotD100}$ more likely to be closer to the strike-normal than strike-parallel direction. The relationship between the orientations of $Sa_{RotD100}$ at different periods was also studied, and the difference between the orientation was modeled using a truncated exponential distribution. Together these models can help solve a practical problem of converting between two important intensity measures while helping deepen the understanding of the directionality of ground motions by studying the distribution of orientations in which $Sa_{RotD100}$ occurs and dependence of the $Sa_{RotD100}$ to Sa_{RotD50} ratio on different seismological parameters. Spectra conditioned on an orientation and on the orientation in which $Sa_{RotD100}$ is observed at a particular period were discussed. Example computations of these spectra using the models developed in the study were also presented.

It is anticipated that these results will help bridge the gap between the work of seismic hazard analysts, who typically use Sa_{GM} or Sa_{RotD50} values, and engineers, some of whom prefer to work with $Sa_{RotD100}$ response spectra.

8 Conclusion

This report focused on developing probabilistic frameworks to account for directivity and directionality effects in seismic risk assessment. Accounting for these effects in seismic risk assessment requires models to predict the probability of observing these effects at a site, models to predict their effect on ground-motion intensity, and an algorithm to combine these models to compute seismic risk. Contributions have been made in all of these areas. The following sections summarize briefly the important findings, limitations, and suggested future work related to this dissertation.

8.1 PRACTICAL IMPLICATIONS AND CONTRIBUTIONS

8.1.1 Framework to Include Directivity Effects in Seismic Hazard Assessment

Pulse-like ground motions caused by directivity effects amplify the ground-motion intensity and thus increase seismic hazard. While methods to include directivity effects in seismic hazard computation have been proposed (e.g., Abrahamson, 2000; Tothong et al., 2007), the framework introduced in Chapter 2 of this report significantly improves and extends them. The Abrahamson (2000) method uses a broadband amplification model to account for amplification in Sa response spectra due to presence of a directivity pulse. The current framework amplifies the ground-motion intensity in a narrow-band of period, which is known to be a better representation of the Sa amplification due to directivity effects (e.g., Somerville, 2003). The dependence of the amplified periods on magnitude is also modeled and accounted properly in the proposed framework. The approach reported herein is similar to Tothong et al. (2007), but several data constrained models required for the computation are also proposed. The orientations in which directivity pulses are observed was also studied in Chapters 2 and 4. This information was used to study the probability of pulse observation in an arbitrary orientation relative to the strike of the fault. Using these models, the proposed framework can be used to compute the seismic hazard in an arbitrary orientation.

8.1.2 Models to Predict Probability of Pulse Occurrence and its Period

Models to predict the probability of pulse occurrence at a site were studied in Chapters 2, 3 and 4. These models extend the models developed by Iervolino and Cornell (2008), which were fitted using pulses classified by the Baker (2007) algorithm and thus predicted the probability of observing a pulse in only the fault-normal orientation at the site. The probability of pulse models developed in this study used multi-orientation classification algorithms developed in Chapters 2 and 4 to study the probability of pulse occurrence at a site in any orientation. Several functional forms were considered for the models, and a detailed explanation of the selected logistic regression model was given in Chapter 3.

The recently expanded NGA-West2 database was used to develop a new probability of pulse model in Chapter 4. Special attention was given to long rupture cases, which are sparse in the dataset used for fitting (there are only two earthquakes with ruptures longer than 200 km in the NGA-West2 database). Recognizing that the models are not well constrained by data in this important region, we chose a functional form that extrapolates well for very long ruptures without sacrificing the goodness of fit to observed data.

The new pulse-classification data from the NGA-West2 database was also used to update the model to predict the period of the pulse. This result was consistent with earlier studies (e.g., Mavroeidis and Papageorgiou, 2003; Somerville, 2003; Bray and Rodriguez-Marek, 2004; Baker, 2007).

8.1.3 Algorithm to Identify Pulse-Like Ground Motions

The pulse-like ground motions used to fit the directivity models developed in this study were selected from a database of ground-motion recordings using quantitative algorithms. Manual selection of pulses, which has been used in previous studies (e.g., Mavroeidis and Papageorgiou, 2003; Fu and Menun, 2004; Akkar et al., 2005) can introduce some bias due to subjective nature of the procedure, particularly in ambiguous cases. Because the number of near-fault ground motions with directivity pulses in both the NGA and NGA-West2 databases are small, any bias in selection of pulses can be amplified while fitting empirical models. Thus, quantitative algorithms were preferred. Also with increasing size of ground-motion databases, manual classification will soon become obsolete due to the complexity of the process. This further motivates building a quantitative pulse-classification procedure.

Two algorithms were developed herein to classify multicomponent pulses in ground motions. The method proposed in Chapter 2 used the Baker (2007) pulse-classification algorithm and classified each orientation of the ground motion as pulse-like or non-pulse-like. This method extends the

applicability of the Baker (2007) algorithm to cases where models for the faults are not available and computation of the fault normal orientation is not possible. Also, it can identify all orientations in which pulses were observed at the site. This information allowed for the development of orientation-dependent directivity models.

The deficiencies of the Baker (2007) algorithm and the initial generalization presented in Chapter 2 were discussed in detail in Chapter 4, and a new algorithm that addresses these problems was presented in Chapter 4. The proposed algorithm improved the previous classification criteria by using principal component analysis and support vector machines. This allowed us to determine the PGV threshold for pulses automatically from the data, which was an improvement over the arbitrary PGV threshold used in Baker (2007). The new algorithm improves both the false-positive and false-negative classifications, which can occur when using the method proposed in Chapter 2, while significantly improving the speed of computation.

Pulse-like ground motions in the NGA database classified using the Baker (2007) algorithm have been used in several studies (e.g., Iervolino and Cornell, 2008; Champion and Liel, 2012, etc.). It is hoped that the pulse-like ground motions in the NGA-West2 database classified herein will help facilitate further such studies in the future.

8.1.4 Including Directivity Effects in Ground-Motion Models

Although it has been known that directivity effects amplify spectral accelerations significantly, they are not accounted for in standard ground-motion models. The amplification of ground-motion intensity due to the presence of a directivity pulse occurs in a band of periods centered around the period of the pulse. The observations of pulse-like ground motions at near-fault sites and their periods are random. Thus, when data from different sites and earthquakes are pooled to fit a ground-motion model, the amplification in intensity gets “smeared out” (Tothong et al., 2007). This smearing of amplification makes it challenging to isolate the directivity effects. The ability to identify individual pulses and their periods allowed us to account for them carefully and thus overcome the smearing effect and fit a ground-motion model with explicit directivity terms.

The parameters used to model directivity effects are not commonly used in seismic hazard studies. Thus, in some cases these parameters may not be known. This can restrict the applicability of the ground-motion models for some projects. A new approach of using conditional expectation with missing parameters for ground-motion prediction was proposed in Chapter 5. This approach gives reasonable Sa predictions, even with missing directivity parameters. These conditional expectations, or average directivity amplifications, were pre-computed for a variety of cases. The average directivity models make the conditional expectation computation practical for common

PSHA cases. The proposed methods were used to fit a ground-motion model with directivity effects and the predictions were compared and contrasted with a non-directivity ground-motion model.

As ground-motion models are widely used in both research and practice, it is hoped that these results can lead to more widespread adoption of directivity predictions within models.

8.1.5 Study of Hazard Deaggregation Accounting for Directivity Effects

Seismic hazard deaggregation was used to compute the probability of pulse occurrence and the probability distribution of pulse period (T_p) conditioned on several levels of Sa . This information can be used to select hazard consistent sets of ground-motion records for structural analysis. For example, the fraction of pulse-like ground motions in the record set can be estimated using the deaggregated probability of pulse. The change in deaggregated probability distributions with change in site geometry was studied in detail. These results help in more intuitive understanding of the amplification in seismic hazard due to directivity pulses by identifying the scenarios contributing to the hazard. Results from this study have been used by Champion and Liel (2012) to compute collapse fragility curves after accounting for directivity effects. Recommendations based on results from this study were also used to select pulse-like ground motions for the PEER Transportation Research Program (Baker et al., 2011).

8.1.6 Ratio of $Sa_{RotD100}$ to Sa_{RotD50}

The new ground-motion models being developed as part of the NGA-West2 project will predict the Sa_{RotD50} intensity of ground motion while the NEHRP (2009) provisions recommend using $Sa_{RotD100}$ intensity of the ground motion for structural design. The need to use a consistent intensity measure throughout the design process motivated the study of $Sa_{RotD100}$ to Sa_{RotD50} ratios. Some previous studies have modeled the ratio of different intensity measures (e.g., Beyer and Bommer, 2006; Watson-Lamprey and Boore, 2007; Huang et al., 2008, 2010) but they used the older NGA database and focused on ratios with respect to the $Sa_{GMRotI50}$ intensity measure. The current study improves upon the previous studies by using the expanded NGA-West2 database and using mixed-effects regression to model the $Sa_{RotD100}/Sa_{RotD50}$ ratios accounting for inter- and intra-event residuals. The dependence of $Sa_{RotD100}/Sa_{RotD50}$ on several seismological parameters was studied and a distance dependent model for these ratios was also proposed. The models developed in this study were compared with earlier models, and the flaw of modeling ratios of observed intensity to ground-motion prediction as proposed in NEHRP (2009) was discussed. These ratios can be used with the upcoming NGA-West2 ground-motion models to obtain predictions of $Sa_{RotD100}$.

8.1.7 Orientation of $Sa_{RotD100}$ and Single Orientation Conditional Spectra

Along with the ratio of $Sa_{RotD100}$ to Sa_{RotD50} , the orientation in which $Sa_{RotD100}$ is observed was also studied in detail. The dependence of $Sa_{RotD100}$ orientation on several seismological parameters was studied, and a model for distribution of $Sa_{RotD100}$ dependent on distance and spectral acceleration period was proposed. As the $Sa_{RotD100}$ orientation for a given ground motion can be different at each period, modeling the joint distribution of $Sa_{RotD100}$ orientations at different periods is essential to study single orientation spectra. The difference in $Sa_{RotD100}$ orientation at two different periods was used to model the joint distribution of $Sa_{RotD100}$ orientation (α). A truncated exponential distribution was fit to the observed $|\alpha^* - \alpha'|$ values at pairs of periods T^* and T' using the maximum likelihood method. It is hoped that these models will help in further understanding of $Sa_{RotD100}$ orientations and will help in computing more realistic target design spectra.

A model to predict spectral acceleration in arbitrary orientations relative to the $Sa_{RotD100}$ orientation was developed, and a method to compute spectra conditioned on a single orientation was proposed. Example computations of spectrum in strike-normal orientation and the orientation of $Sa_{RotD100}$ at a particular period was presented. These spectra were compared with the $Sa_{RotD100}$ and the Sa_{RotD50} spectra. The spectrum proposed in this study is a more realistic representation of the ground-motion intensity than the $Sa_{RotD100}$ spectrum. We hope that our results will lead to better understanding of the directionality of ground motion and aid in development of improved target spectra for risk assessment.

8.2 LIMITATIONS AND FUTURE WORK

8.2.1 Data Limitations

The NGA-West2 ground-motion database is a large database with more than 8500 earthquake ground-motion recordings from over 300 earthquakes, but it only contains 244 pulse-like ground motions. As the models developed herein are primarily empirical, their quality depends on the data used to fit the models. To improve the applicability of the models, choices were made during selection of functional forms to make reasonable predictions in conditions for which data was not available. For example, sites at the end of long ruptures have high probabilities of experiencing directivity effects, but the number of earthquakes with long rupture lengths in the NGA-West2 database was too small to properly constrain the model in this important region. Thus, the choice of probability of the pulse model was dictated by the need to have reasonable predictions when the rupture is very long without sacrificing the goodness of fit to the data. The choices made to fit a model that extrapolates well when data is not present are subjective. More work needs to be

done to quantitatively verify the models in important regions with few data points. Using simulated ground-motion recordings can be a possible method to verify some of these assumptions. When using simulated ground motions to verify the models, care should be taken to verify that the simulations are consistent with the available empirical data.

We recognize the limitations of the dataset and thus deliberately designed both the directivity and directionality frameworks to be modular. Splitting the task in several smaller models facilitates replacing component models when new data or knowledge is available. One example of this replacement was presented here, where the models developed using the original NGA database in Chapter 2 were updated by some new models developed using the expanded NGA-West2 database while keeping the overall framework the same.

Also, due to the focus of the NGA-West2 project on California, all of the events in the database are from active crustal regions. Thus, the models developed in this dissertation are only applicable in regions where hazard is dominated by active crustal earthquakes. To build models for other regions, for example subduction zones or stable continental regions, the procedure presented here will have to be repeated with data from the region of interest.

8.2.2 Classification of Directivity Pulses

Though pulse-like ground motions are generally caused by directivity effects, they can also be caused due to other phenomena such as basin effects. The pulse classification algorithm proposed in Chapter 4 improves the performance of previous algorithms and produces defensible classifications, but it does not discriminate between different causes of pulse-like ground motions. Thus, currently identification of directivity pulses is done in two steps, where the automated algorithm classifies a large number of ground motions in a database as pulse-like or non-pulse-like in the first step. Then the smaller subset of pulse-like ground motions are classified manually as directivity pulses and non-directivity pulses. In this study the 244 pulse-like ground motions identified in the NGA-West2 database were manually classified as directivity or non-directivity pulses. The source-to-site geometry, site conditions, and velocity time history for the orientation in which the strongest pulse was found were used to aid in this classification. Initial classifications were put online and feedback was sought from several experts. Though the classifications were checked by several people, there is still some chance of ignoring some effects in the process due to the subjective nature of the work. If a parameter used to predict the probability of pulse is also used to classify ground motion as directivity pulse, then there is a chance that the probability models will be affected by any subjective bias introduced during the classification step. This makes the task of identifying directivity pulses challenging. Directivity parameters like *IDP* (the isochrone directivity predictor, Spudich and

Chiou, 2008) or ξ (effective fraction of fault area that ruptures towards the site, Rowshandel, 2006), which are not used in our models, can be used to identify directivity pulses. As most directivity parameters are correlated to each other, using different parameters in classification algorithm and models will not guarantee unbiased models. More research is needed in future to automate the separation of pulse-like ground motions into directivity and non-directivity pulses.

Though there is some possibility that directivity models presented in Chapter 4 may be affected by some subjective bias, it does not limit the applicability of the proposed framework. Often it is assumed that all pulse-like ground motions cause similar structural response regardless of the cause of the pulse (e.g., Champion and Liel, 2012). Thus, in these studies, models developed using pulse-like ground motions that were classified automatically can be used instead.

Another limitation of the classification algorithm is that it produces binary classification. The difference between records that just miss and those that just pass the classification threshold may be smaller than what the binary classification suggests. A more continuous approach to pulse classification may be a better representation of pulses in nature. Though changing the classification from binary to continuous may improve the models, it will add considerable computation to the PSHA framework. As, another integration over the continuous pulse parameter will be needed. More research is needed to examine whether the benefits from a continuous classification approach outweigh the added computational cost.

8.2.3 Ground-Motion Model with Directivity Effects

Since ground-motion models are widely used, they are often used to predict ground-motion intensity in situations outside the range of data used to fit them. Thus the ground-motion developers often augment the data with analytical models and select functional forms to develop a model whose predictions can extrapolate well. The ground-motion models developed in Chapter 5 were pure empirical fits to data, and minimal post processing was applied to the coefficients estimated by mixed-effects regression. Thus, the models cannot be guaranteed to work well outside the range of data used for fitting.

Though several ground-motion models have been developed in with much more focus on extrapolation issues (e.g. Boore and Atkinson, 2008; Idriss, 2008; Chiou and Youngs, 2008; Abrahamson and Silva, 2008; Campbell and Bozorgnia, 2008), including directivity terms in such a ground-motion model introduces new challenges. While directivity effects are primarily near-fault effects, making good predictions far from the fault is also important for a ground-motion model. Thus, care has to be taken to not sacrifice the quality of prediction far from the fault to improve the near-fault predictions. More research needs to be done before the ground-motion models developed

in Chapter 5 can be used universally.

8.2.4 Ground Motion Selection

Some recommendations regarding ground motion selection and target spectrum computation were proposed herein. Recommendations for ground motion selection were derived using laws of probability to estimate deaggregation of T_p and probability of pulse in Chapters 2 and 6. More realistic single orientation target spectrum that can be used for ground motion selection were introduced in Chapter 7. The recommendations are mathematically consistent; however, the effects of following these recommendations were not studied in detail. Detailed study of the difference in *EDP* distribution for a structure when subjected to a set of ground motions selected following the proposed recommendations and a control set of ground motions needs to be done.

Another challenge with selecting pulse-like ground motion is the limitations of the dataset. As the number of pulse-like ground motions is small, selecting a set to match deaggregated probability distributions is difficult. Augmenting the recorded pulse-like ground motions with artificial ones can help with this problem; however, more research may be needed to create artificial pulse-like ground motions with characteristics similar to real ones.

Despite their limitations, these recommendations are still valuable and have been used to select sets of pulse-like ground motions (e.g., Baker et al., 2011; Champion and Liel, 2012). that being said, more work needs to be done to turn these recommendations into an unambiguous algorithm that can be readily used in practice.

8.3 CONCLUDING REMARKS

This report proposes a framework to account for near-fault effects like directivity and directionality in seismic risk assessment. This framework was designed to be modular to ease the upgrading of individual models in the future. All the empirical models required for the computations and some example computations are also presented. It must be noted that the quality of empirical models depends on the quality of data. Though the dataset used in this study was the largest ever used to study directivity effects, data for some important cases like long fault ruptures was sparse. Recognizing this limitation, effort was made to utilize the data to the fullest and build models that can extrapolate reasonably well. Some practical recommendations for ground motion selection at near fault sites are also presented. Though these recommendations serve an urgent need, more research is required to quantify the effects of following these recommendation on *EDP* estimation. Given the importance of directivity and directionality effects in the near-fault region and the mathematical consistency and versatility of the current framework, further research seems warranted to study

some of the limitations and formalize these results to make them more accessible to practicing engineers.

APPENDIX A Pulse-Like Ground Motions Classified using Method Describe in Chapter 2

List of pulse-like ground motions identified using the method described in Chapter 2 is provided in Table A.1 below.

Table A.1 List of pulse-like ground motions.

SI No.	NGA Record Number	EQID	Earthquake Name	Year	Station Name
1	20	17	Northern Calif-03	1954	Ferndale City Hall
2	77	30	San Fernando	1971	Pacoima Dam (upper left abut)
3	96	32	Managua, Nicaragua-02	1972	Managua, ESSO
4	126	41	Gazli, USSR	1976	Karakyr
5	143	46	Tabas, Iran	1978	Tabas
6	150	48	Coyote Lake	1979	Gilroy Array #6
7	158	50	Imperial Valley-06	1979	Aeropuerto Mexicali
8	159	50	Imperial Valley-06	1979	Agrarias
9	161	50	Imperial Valley-06	1979	Brawley Airport
10	170	50	Imperial Valley-06	1979	EC County Center FF
11	171	50	Imperial Valley-06	1979	El Centro - Meloland Geot. Array
12	173	50	Imperial Valley-06	1979	El Centro Array #10
13	174	50	Imperial Valley-06	1979	El Centro Array #11
14	178	50	Imperial Valley-06	1979	El Centro Array #3
15	179	50	Imperial Valley-06	1979	El Centro Array #4
16	180	50	Imperial Valley-06	1979	El Centro Array #5
17	181	50	Imperial Valley-06	1979	El Centro Array #6
18	182	50	Imperial Valley-06	1979	El Centro Array #7
19	183	50	Imperial Valley-06	1979	El Centro Array #8
20	184	50	Imperial Valley-06	1979	El Centro Differential Array
21	185	50	Imperial Valley-06	1979	Holtville Post Office

SI No.	NGA Record Number	EQID	Earthquake Name	Year	Station Name
22	250	61	Mammoth Lakes-06	1980	Long Valley Dam (Upr L Abut)
23	285	68	Irpinia, Italy-01	1980	Bagnoli Irpinio
24	292	68	Irpinia, Italy-01	1980	Sturno (STN)
25	316	73	Westmorland	1981	Parachute Test Site
26	319	73	Westmorland	1981	Westmorland Fire Sta
27	407	80	Coalinga-05	1983	Oil City
28	415	80	Coalinga-05	1983	Transmitter Hill
29	418	82	Coalinga-07	1983	Coalinga-14th & Elm (Old CHP)
30	448	90	Morgan Hill	1984	Anderson Dam (Downstream)
31	451	90	Morgan Hill	1984	Coyote Lake Dam (SW Abut)
32	459	90	Morgan Hill	1984	Gilroy Array #6
33	496	97	Nahanni, Canada	1985	Site 2
34	503	100	Taiwan SMART1(40)	1986	SMART1 C00
35	504	100	Taiwan SMART1(40)	1986	SMART1 E01
36	505	100	Taiwan SMART1(40)	1986	SMART1 I01
37	506	100	Taiwan SMART1(40)	1986	SMART1 I07
38	508	100	Taiwan SMART1(40)	1986	SMART1 M07
39	517	101	N. Palm Springs	1986	Desert Hot Springs
40	527	101	N. Palm Springs	1986	Morongo Valley Fire Station
41	529	101	N. Palm Springs	1986	North Palm Springs Post Office
42	568	108	San Salvador	1986	Geotech Investig Center
43	569	108	San Salvador	1986	National Geographical Inst
44	585	110	Baja California	1987	Cerro Prieto
45	614	113	Whittier Narrows-01	1987	Downey - Birchdale
46	615	113	Whittier Narrows-01	1987	Downey - Co Maint Bldg
47	645	113	Whittier Narrows-01	1987	LB - Orange Ave
48	692	113	Whittier Narrows-01	1987	Santa Fe Springs - E.Joslin
49	721	116	Superstition Hills-02	1987	El Centro Imp. Co. Cent
50	732	118	Loma Prieta	1989	APEEL 2 - Redwood City
51	759	118	Loma Prieta	1989	Foster City - APEEL 1
52	763	118	Loma Prieta	1989	Gilroy - Gavilan Coll.
53	764	118	Loma Prieta	1989	Gilroy - Historic Bldg.
54	766	118	Loma Prieta	1989	Gilroy Array #2
55	767	118	Loma Prieta	1989	Gilroy Array #3
56	771	118	Loma Prieta	1989	Golden Gate Bridge
57	778	118	Loma Prieta	1989	Hollister Diff. Array
58	779	118	Loma Prieta	1989	LGPC
59	783	118	Loma Prieta	1989	Oakland - Outer Harbor Wharf

SI No.	NGA Record Number	EQID	Earthquake Name	Year	Station Name
60	784	118	Loma Prieta	1989	Oakland - Title & Trust
61	787	118	Loma Prieta	1989	Palo Alto - SLAC Lab
62	796	118	Loma Prieta	1989	SF - Presidio
63	799	118	Loma Prieta	1989	SF Intern. Airport
64	802	118	Loma Prieta	1989	Saratoga - Aloha Ave
65	803	118	Loma Prieta	1989	Saratoga - W Valley Coll.
66	808	118	Loma Prieta	1989	Treasure Island
67	825	123	Cape Mendocino	1992	Cape Mendocino
68	828	123	Cape Mendocino	1992	Petrolia
69	838	125	Landers	1992	Barstow
70	879	125	Landers	1992	Lucerne
71	900	125	Landers	1992	Yermo Fire Station
72	963	127	Northridge-01	1994	Castaic - Old Ridge Route
73	982	127	Northridge-01	1994	Jensen Filter Plant
74	983	127	Northridge-01	1994	Jensen Filter Plant Generator
75	1003	127	Northridge-01	1994	LA - Saturn St
76	1004	127	Northridge-01	1994	LA - Sepulveda VA Hospital
77	1009	127	Northridge-01	1994	LA - Wadsworth VA Hospital North
78	1013	127	Northridge-01	1994	LA Dam
79	1044	127	Northridge-01	1994	Newhall - Fire Sta
80	1045	127	Northridge-01	1994	Newhall - W Pico Canyon Rd.
81	1050	127	Northridge-01	1994	Pacoima Dam (downstr)
82	1051	127	Northridge-01	1994	Pacoima Dam (upper left)
83	1052	127	Northridge-01	1994	Pacoima Kagel Canyon
84	1063	127	Northridge-01	1994	Rinaldi Receiving Sta
85	1084	127	Northridge-01	1994	Sylmar - Converter Sta
86	1085	127	Northridge-01	1994	Sylmar - Converter Sta East
87	1086	127	Northridge-01	1994	Sylmar - Olive View Med FF
88	1106	129	Kobe, Japan	1995	KJMA
89	1108	129	Kobe, Japan	1995	Kobe University
90	1114	129	Kobe, Japan	1995	Port Island (0 m)
91	1119	129	Kobe, Japan	1995	Takarazuka
92	1120	129	Kobe, Japan	1995	Takatori
93	1147	136	Kocaeli, Turkey	1999	Ambarli
94	1148	136	Kocaeli, Turkey	1999	Arcelik
95	1158	136	Kocaeli, Turkey	1999	Duzce
96	1161	136	Kocaeli, Turkey	1999	Gebze
97	1176	136	Kocaeli, Turkey	1999	Yarimca

SI No.	NGA Record Number	EQID	Earthquake Name	Year	Station Name
98	1182	137	Chi-Chi, Taiwan	1999	CHY006
99	1193	137	Chi-Chi, Taiwan	1999	CHY024
100	1197	137	Chi-Chi, Taiwan	1999	CHY028
101	1202	137	Chi-Chi, Taiwan	1999	CHY035
102	1244	137	Chi-Chi, Taiwan	1999	CHY101
103	1329	137	Chi-Chi, Taiwan	1999	ILA037
104	1402	137	Chi-Chi, Taiwan	1999	NST
105	1403	137	Chi-Chi, Taiwan	1999	NSY
106	1410	137	Chi-Chi, Taiwan	1999	TAP003
107	1411	137	Chi-Chi, Taiwan	1999	TAP005
108	1463	137	Chi-Chi, Taiwan	1999	TCU003
109	1464	137	Chi-Chi, Taiwan	1999	TCU006
110	1466	137	Chi-Chi, Taiwan	1999	TCU008
111	1468	137	Chi-Chi, Taiwan	1999	TCU010
112	1471	137	Chi-Chi, Taiwan	1999	TCU015
113	1472	137	Chi-Chi, Taiwan	1999	TCU017
114	1473	137	Chi-Chi, Taiwan	1999	TCU018
115	1475	137	Chi-Chi, Taiwan	1999	TCU026
116	1476	137	Chi-Chi, Taiwan	1999	TCU029
117	1477	137	Chi-Chi, Taiwan	1999	TCU031
118	1479	137	Chi-Chi, Taiwan	1999	TCU034
119	1480	137	Chi-Chi, Taiwan	1999	TCU036
120	1481	137	Chi-Chi, Taiwan	1999	TCU038
121	1482	137	Chi-Chi, Taiwan	1999	TCU039
122	1483	137	Chi-Chi, Taiwan	1999	TCU040
123	1484	137	Chi-Chi, Taiwan	1999	TCU042
124	1485	137	Chi-Chi, Taiwan	1999	TCU045
125	1486	137	Chi-Chi, Taiwan	1999	TCU046
126	1487	137	Chi-Chi, Taiwan	1999	TCU047
127	1489	137	Chi-Chi, Taiwan	1999	TCU049
128	1490	137	Chi-Chi, Taiwan	1999	TCU050
129	1492	137	Chi-Chi, Taiwan	1999	TCU052
130	1493	137	Chi-Chi, Taiwan	1999	TCU053
131	1494	137	Chi-Chi, Taiwan	1999	TCU054
132	1496	137	Chi-Chi, Taiwan	1999	TCU056
133	1497	137	Chi-Chi, Taiwan	1999	TCU057
134	1498	137	Chi-Chi, Taiwan	1999	TCU059
135	1499	137	Chi-Chi, Taiwan	1999	TCU060

SI No.	NGA Record Number	EQID	Earthquake Name	Year	Station Name
136	1501	137	Chi-Chi, Taiwan	1999	TCU063
137	1502	137	Chi-Chi, Taiwan	1999	TCU064
138	1503	137	Chi-Chi, Taiwan	1999	TCU065
139	1505	137	Chi-Chi, Taiwan	1999	TCU068
140	1510	137	Chi-Chi, Taiwan	1999	TCU075
141	1511	137	Chi-Chi, Taiwan	1999	TCU076
142	1514	137	Chi-Chi, Taiwan	1999	TCU081
143	1515	137	Chi-Chi, Taiwan	1999	TCU082
144	1516	137	Chi-Chi, Taiwan	1999	TCU083
145	1519	137	Chi-Chi, Taiwan	1999	TCU087
146	1523	137	Chi-Chi, Taiwan	1999	TCU094
147	1524	137	Chi-Chi, Taiwan	1999	TCU095
148	1525	137	Chi-Chi, Taiwan	1999	TCU096
149	1526	137	Chi-Chi, Taiwan	1999	TCU098
150	1528	137	Chi-Chi, Taiwan	1999	TCU101
151	1529	137	Chi-Chi, Taiwan	1999	TCU102
152	1530	137	Chi-Chi, Taiwan	1999	TCU103
153	1531	137	Chi-Chi, Taiwan	1999	TCU104
154	1533	137	Chi-Chi, Taiwan	1999	TCU106
155	1537	137	Chi-Chi, Taiwan	1999	TCU111
156	1541	137	Chi-Chi, Taiwan	1999	TCU116
157	1546	137	Chi-Chi, Taiwan	1999	TCU122
158	1548	137	Chi-Chi, Taiwan	1999	TCU128
159	1550	137	Chi-Chi, Taiwan	1999	TCU136
160	1595	137	Chi-Chi, Taiwan	1999	WGK
161	1602	138	Duzce, Turkey	1999	Bolu
162	1605	138	Duzce, Turkey	1999	Duzce
163	1752	155	Northwest China-03	1997	Jiashi
164	1853	160	Yountville	2000	Napa Fire Station #3
165	2114	169	Denali, Alaska	2002	TAPS Pump Station #10
166	2457	172	Chi-Chi, Taiwan-03	1999	CHY024
167	2461	172	Chi-Chi, Taiwan-03	1999	CHY028
168	2466	172	Chi-Chi, Taiwan-03	1999	CHY035
169	2495	172	Chi-Chi, Taiwan-03	1999	CHY080
170	2507	172	Chi-Chi, Taiwan-03	1999	CHY101
171	2618	172	Chi-Chi, Taiwan-03	1999	TCU065
172	2627	172	Chi-Chi, Taiwan-03	1999	TCU076
173	2650	172	Chi-Chi, Taiwan-03	1999	TCU116

SI No.	NGA Record Number	EQID	Earthquake Name	Year	Station Name
174	2734	173	Chi-Chi, Taiwan-04	1999	CHY074
175	3317	175	Chi-Chi, Taiwan-06	1999	CHY101
176	3473	175	Chi-Chi, Taiwan-06	1999	TCU078
177	3474	175	Chi-Chi, Taiwan-06	1999	TCU079
178	3475	175	Chi-Chi, Taiwan-06	1999	TCU080
179	3548	118	Loma Prieta	1989	Los Gatos - Lexington Dam

APPENDIX B Pulse-Like Ground Motions Classified using Method Described in Chapter 4

List of pulse-like ground motions identified using the method described in Chapter 4 is provided in Table B.1 below.

Table B.1 List of pulse-like ground motions.

SI No.	NGA Record Number	EQID	Earthquake Name	Year	Station Name
1	20	17	Northern Calif-03	1954	Ferndale City Hall
2	77	30	San Fernando	1971	Pacoima Dam (upper left abut)
3	143	46	Tabas, Iran	1978	Tabas
4	147	48	Coyote Lake	1979	Gilroy Array #2
5	148	48	Coyote Lake	1979	Gilroy Array #3
6	149	48	Coyote Lake	1979	Gilroy Array #4
7	150	48	Coyote Lake	1979	Gilroy Array #6
8	159	50	Imperial Valley-06	1979	Agrarias
9	161	50	Imperial Valley-06	1979	Brawley Airport
10	170	50	Imperial Valley-06	1979	EC County Center FF
11	171	50	Imperial Valley-06	1979	El Centro - Meloland Geot. Array
12	173	50	Imperial Valley-06	1979	El Centro Array #10
13	178	50	Imperial Valley-06	1979	El Centro Array #3
14	179	50	Imperial Valley-06	1979	El Centro Array #4
15	180	50	Imperial Valley-06	1979	El Centro Array #5
16	181	50	Imperial Valley-06	1979	El Centro Array #6
17	182	50	Imperial Valley-06	1979	El Centro Array #7
18	184	50	Imperial Valley-06	1979	El Centro Differential Array
19	185	50	Imperial Valley-06	1979	Holtville Post Office
20	204	51	Imperial Valley-07	1979	El Centro Array #6
21	250	61	Mammoth Lakes-06	1980	Long Valley Dam (Upr L Abut)
22	285	68	Irpinia, Italy-01	1980	Bagnoli Irpinio
23	292	68	Irpinia, Italy-01	1980	Sturmo (STN)
24	316	73	Westmorland	1981	Parachute Test Site
25	319	73	Westmorland	1981	Westmorland Fire Sta
26	372	77	Coalinga-02	1983	Anticline Ridge Free-Field
27	373	77	Coalinga-02	1983	Anticline Ridge Pad

SI No.	NGA Record Number	EQID	Earthquake Name	Year	Station Name
28	415	80	Coalinga-05	1983	Transmitter Hill
29	418	82	Coalinga-07	1983	Coalinga-14th & Elm (Old CHP)
30	451	90	Morgan Hill	1984	Coyote Lake Dam - Southwest Abutment
31	459	90	Morgan Hill	1984	Gilroy Array #6
32	503	100	Taiwan SMART1(40)	1986	SMART1 C00
33	504	100	Taiwan SMART1(40)	1986	SMART1 E01
34	505	100	Taiwan SMART1(40)	1986	SMART1 I01
35	506	100	Taiwan SMART1(40)	1986	SMART1 I07
36	507	100	Taiwan SMART1(40)	1986	SMART1 M01
37	508	100	Taiwan SMART1(40)	1986	SMART1 M07
38	510	100	Taiwan SMART1(40)	1986	SMART1 O07
39	527	101	N. Palm Springs	1986	Morongo Valley Fire Station
40	566	107	Kalamata, Greece-02	1986	Kalamata (bsmt) (2nd trigger)
41	568	108	San Salvador	1986	Geotech Investig Center
42	569	108	San Salvador	1986	National Geographical Inst
43	595	113	Whittier Narrows-01	1987	Bell Gardens - Jaboneria
44	611	113	Whittier Narrows-01	1987	Compton - Castlegate St
45	614	113	Whittier Narrows-01	1987	Downey - Birchdale
46	615	113	Whittier Narrows-01	1987	Downey - Co Maint Bldg
47	645	113	Whittier Narrows-01	1987	LB - Orange Ave
48	668	113	Whittier Narrows-01	1987	Norwalk - Imp Hwy, S Grnd
49	692	113	Whittier Narrows-01	1987	Santa Fe Springs - E.Joslin
50	722	116	Superstition Hills-02	1987	Kornbloom Road (temp)
51	723	116	Superstition Hills-02	1987	Parachute Test Site
52	725	116	Superstition Hills-02	1987	Poe Road (temp)
53	738	118	Loma Prieta	1989	Alameda Naval Air Stn Hanger
54	758	118	Loma Prieta	1989	Emeryville, Pacific Park #2, Free Field
55	764	118	Loma Prieta	1989	Gilroy - Historic Bldg.
56	766	118	Loma Prieta	1989	Gilroy Array #2
57	767	118	Loma Prieta	1989	Gilroy Array #3
58	783	118	Loma Prieta	1989	Oakland - Outer Harbor Wharf
59	784	118	Loma Prieta	1989	Oakland - Title & Trust
60	796	118	Loma Prieta	1989	SF - Presidio
61	802	118	Loma Prieta	1989	Saratoga - Aloha Ave
62	803	118	Loma Prieta	1989	Saratoga - W Valley Coll.
63	808	118	Loma Prieta	1989	Treasure Island
64	825	123	Cape Mendocino	1992	Cape Mendocino
65	828	123	Cape Mendocino	1992	Petrolia
66	838	125	Landers	1992	Barstow
67	879	125	Landers	1992	Lucerne
68	900	125	Landers	1992	Yermo Fire Station
69	982	127	Northridge-01	1994	Jensen Filter Plant
70	983	127	Northridge-01	1994	Jensen Filter Plant Generator
71	1003	127	Northridge-01	1994	LA - Saturn St
72	1004	127	Northridge-01	1994	LA - Sepulveda VA Hospital
73	1013	127	Northridge-01	1994	LA Dam
74	1044	127	Northridge-01	1994	Newhall - Fire Sta
75	1045	127	Northridge-01	1994	Newhall - W Pico Canyon Rd.
76	1050	127	Northridge-01	1994	Pacoima Dam (downstr)

SI No.	NGA Record Number	EQID	Earthquake Name	Year	Station Name
77	1051	127	Northridge-01	1994	Pacoima Dam (upper left)
78	1052	127	Northridge-01	1994	Pacoima Kagel Canyon
79	1054	127	Northridge-01	1994	Pardee - SCE
80	1063	127	Northridge-01	1994	Rinaldi Receiving Sta
81	1084	127	Northridge-01	1994	Sylmar - Converter Sta
82	1085	127	Northridge-01	1994	Sylmar - Converter Sta East
83	1086	127	Northridge-01	1994	Sylmar - Olive View Med FF
84	1106	129	Kobe, Japan	1995	KJMA
85	1114	129	Kobe, Japan	1995	Port Island (0 m)
86	1119	129	Kobe, Japan	1995	Takarazuka
87	1120	129	Kobe, Japan	1995	Takatori
88	1148	136	Kocaeli, Turkey	1999	Arcelik
89	1161	136	Kocaeli, Turkey	1999	Gebze
90	1165	136	Kocaeli, Turkey	1999	Izmit
91	1176	136	Kocaeli, Turkey	1999	Yarimca
92	1182	137	Chi-Chi, Taiwan	1999	CHY006
93	1193	137	Chi-Chi, Taiwan	1999	CHY024
94	1244	137	Chi-Chi, Taiwan	1999	CHY101
95	1402	137	Chi-Chi, Taiwan	1999	NST
96	1403	137	Chi-Chi, Taiwan	1999	NSY
97	1462	137	Chi-Chi, Taiwan	1999	TCU
98	1464	137	Chi-Chi, Taiwan	1999	TCU006
99	1470	137	Chi-Chi, Taiwan	1999	TCU014
100	1471	137	Chi-Chi, Taiwan	1999	TCU015
101	1472	137	Chi-Chi, Taiwan	1999	TCU017
102	1473	137	Chi-Chi, Taiwan	1999	TCU018
103	1475	137	Chi-Chi, Taiwan	1999	TCU026
104	1476	137	Chi-Chi, Taiwan	1999	TCU029
105	1477	137	Chi-Chi, Taiwan	1999	TCU031
106	1478	137	Chi-Chi, Taiwan	1999	TCU033
107	1479	137	Chi-Chi, Taiwan	1999	TCU034
108	1480	137	Chi-Chi, Taiwan	1999	TCU036
109	1481	137	Chi-Chi, Taiwan	1999	TCU038
110	1482	137	Chi-Chi, Taiwan	1999	TCU039
111	1483	137	Chi-Chi, Taiwan	1999	TCU040
112	1485	137	Chi-Chi, Taiwan	1999	TCU045
113	1486	137	Chi-Chi, Taiwan	1999	TCU046
114	1487	137	Chi-Chi, Taiwan	1999	TCU047
115	1489	137	Chi-Chi, Taiwan	1999	TCU049
116	1491	137	Chi-Chi, Taiwan	1999	TCU051
117	1492	137	Chi-Chi, Taiwan	1999	TCU052
118	1493	137	Chi-Chi, Taiwan	1999	TCU053
119	1496	137	Chi-Chi, Taiwan	1999	TCU056
120	1498	137	Chi-Chi, Taiwan	1999	TCU059
121	1501	137	Chi-Chi, Taiwan	1999	TCU063
122	1502	137	Chi-Chi, Taiwan	1999	TCU064
123	1503	137	Chi-Chi, Taiwan	1999	TCU065
124	1505	137	Chi-Chi, Taiwan	1999	TCU068
125	1510	137	Chi-Chi, Taiwan	1999	TCU075

SI No.	NGA Record Number	EQID	Earthquake Name	Year	Station Name
126	1511	137	Chi-Chi, Taiwan	1999	TCU076
127	1514	137	Chi-Chi, Taiwan	1999	TCU081
128	1515	137	Chi-Chi, Taiwan	1999	TCU082
129	1519	137	Chi-Chi, Taiwan	1999	TCU087
130	1520	137	Chi-Chi, Taiwan	1999	TCU088
131	1523	137	Chi-Chi, Taiwan	1999	TCU094
132	1524	137	Chi-Chi, Taiwan	1999	TCU095
133	1525	137	Chi-Chi, Taiwan	1999	TCU096
134	1526	137	Chi-Chi, Taiwan	1999	TCU098
135	1528	137	Chi-Chi, Taiwan	1999	TCU101
136	1529	137	Chi-Chi, Taiwan	1999	TCU102
137	1530	137	Chi-Chi, Taiwan	1999	TCU103
138	1531	137	Chi-Chi, Taiwan	1999	TCU104
139	1548	137	Chi-Chi, Taiwan	1999	TCU128
140	1550	137	Chi-Chi, Taiwan	1999	TCU136
141	1595	137	Chi-Chi, Taiwan	1999	WGK
142	1602	138	Duzce, Turkey	1999	Bolu
143	1605	138	Duzce, Turkey	1999	Duzce
144	1752	155	Northwest China-03	1997	Jiashi
145	1853	160	Yountville	2000	Napa Fire Station #3
146	2114	169	Denali, Alaska	2002	TAPS Pump Station #10
147	2457	172	Chi-Chi, Taiwan-03	1999	CHY024
148	2466	172	Chi-Chi, Taiwan-03	1999	CHY035
149	2495	172	Chi-Chi, Taiwan-03	1999	CHY080
150	2618	172	Chi-Chi, Taiwan-03	1999	TCU065
151	2627	172	Chi-Chi, Taiwan-03	1999	TCU076
152	2628	172	Chi-Chi, Taiwan-03	1999	TCU078
153	2734	173	Chi-Chi, Taiwan-04	1999	CHY074
154	3317	175	Chi-Chi, Taiwan-06	1999	CHY101
155	3473	175	Chi-Chi, Taiwan-06	1999	TCU078
156	3475	175	Chi-Chi, Taiwan-06	1999	TCU080
157	3548	118	Loma Prieta	1989	Los Gatos - Lexington Dam
158	3634	100	Taiwan SMART1(40)	1986	SMART1 I02
159	3635	100	Taiwan SMART1(40)	1986	SMART1 I03
160	3636	100	Taiwan SMART1(40)	1986	SMART1 I04
161	3637	100	Taiwan SMART1(40)	1986	SMART1 I05
162	3638	100	Taiwan SMART1(40)	1986	SMART1 I06
163	3639	100	Taiwan SMART1(40)	1986	SMART1 I08
164	3640	100	Taiwan SMART1(40)	1986	SMART1 I09
165	3641	100	Taiwan SMART1(40)	1986	SMART1 I11
166	3642	100	Taiwan SMART1(40)	1986	SMART1 I12
167	3643	100	Taiwan SMART1(40)	1986	SMART1 M02
168	3644	100	Taiwan SMART1(40)	1986	SMART1 M03
169	3645	100	Taiwan SMART1(40)	1986	SMART1 M04
170	3646	100	Taiwan SMART1(40)	1986	SMART1 M05
171	3647	100	Taiwan SMART1(40)	1986	SMART1 M06
172	3649	100	Taiwan SMART1(40)	1986	SMART1 M09
173	3650	100	Taiwan SMART1(40)	1986	SMART1 M10
174	3652	100	Taiwan SMART1(40)	1986	SMART1 M12

SI No.	NGA Record Number	EQID	Earthquake Name	Year	Station Name
175	3655	100	Taiwan SMART1(40)	1986	SMART1 O04
176	3656	100	Taiwan SMART1(40)	1986	SMART1 O05
177	3657	100	Taiwan SMART1(40)	1986	SMART1 O06
178	3658	100	Taiwan SMART1(40)	1986	SMART1 O08
179	3660	100	Taiwan SMART1(40)	1986	SMART1 O11
180	3744	123	Cape Mendocino	1992	Bunker Hill FAA
181	3746	123	Cape Mendocino	1992	Centerville Beach, Naval Fac
182	3755	125	Landers	1992	Lucerne
183	3763	129	Kobe, Japan	1995	Port Island (83 m)
184	3965	176	Tottori, Japan	2000	TTR008
185	4040	178	Bam, Iran	2003	Bam
186	4065	179	Parkfield-02, CA	2004	PARKFIELD - EADES
187	4097	179	Parkfield-02, CA	2004	Slack Canyon
188	4098	179	Parkfield-02, CA	2004	Parkfield - Cholame 1E
189	4100	179	Parkfield-02, CA	2004	Parkfield - Cholame 2WA
190	4101	179	Parkfield-02, CA	2004	Parkfield - Cholame 3E
191	4102	179	Parkfield-02, CA	2004	Parkfield - Cholame 3W
192	4103	179	Parkfield-02, CA	2004	Parkfield - Cholame 4W
193	4107	179	Parkfield-02, CA	2004	Parkfield - Fault Zone 1
194	4113	179	Parkfield-02, CA	2004	Parkfield - Fault Zone 9
195	4115	179	Parkfield-02, CA	2004	Parkfield - Fault Zone 12
196	4116	179	Parkfield-02, CA	2004	Parkfield - Fault Zone 14
197	4126	179	Parkfield-02, CA	2004	Parkfield - Stone Corral 1E
198	4211	180	Niigata, Japan	2004	NIG021
199	4228	180	Niigata, Japan	2004	NIGH11
200	4451	262	Montenegro, Yugo.	1979	Bar-Skupstina Opstine
201	4458	262	Montenegro, Yugo.	1979	Ulcinj - Hotel Olimpic
202	4480	274	L'Aquila, Italy	2009	L'Aquila - V. Aterno - Centro Valle
203	4482	274	L'Aquila, Italy	2009	L'Aquila - V. Aterno -F. Aterno
204	4483	274	L'Aquila, Italy	2009	L'Aquila - Parking
205	4716	277	Wenchuan, China	2008	Deyangbaima
206	4816	277	Wenchuan, China	2008	Mianzuqingping
207	4847	278	Chuetsu-oki	2007	Joetsu Kakizakiku Kakizaki
208	4850	278	Chuetsu-oki	2007	Yoshikawaku Joetsu City
209	4856	278	Chuetsu-oki	2007	Kashiwazaki City Center
210	4874	278	Chuetsu-oki	2007	Oguni Nagaoka
211	4875	278	Chuetsu-oki	2007	Kariwa
212	4879	278	Chuetsu-oki	2007	Yan Sakuramachi City watershed
213	4889	278	Chuetsu-oki	2007	Joetsu Otemachi
214	4891	278	Chuetsu-oki	2007	Iizuna Imokawa
215	4896	278	Chuetsu-oki	2007	Kashiwazaki NPP, Service Hall Array 2.4 m depth
216	4897	278	Chuetsu-oki	2007	SERVICE HALL:50.8 M DEPTH
217	5658	279	Iwate	2008	IWTH26
218	5810	279	Iwate	2008	Machimukai Town
219	5832	280	El Mayor-Cucapah	2010	TAMAULIPAS
220	6877	146	Joshua Tree, CA	1992	Indio - Jackson Road
221	6887	281	Darfield, New Zealand	2010	Christchurch Botanical Gardens
222	6897	281	Darfield, New Zealand	2010	DSLCL
223	6906	281	Darfield, New Zealand	2010	GDLC

SI No.	NGA Record Number	EQID	Earthquake Name	Year	Station Name
224	6911	281	Darfield, New Zealand	2010	HORC
225	6927	281	Darfield, New Zealand	2010	LINC
226	6928	281	Darfield, New Zealand	2010	LPCC
227	6942	281	Darfield, New Zealand	2010	NNBS North New Brighton School
228	6959	281	Darfield, New Zealand	2010	Christchurch Resthaven
229	6960	281	Darfield, New Zealand	2010	Riccarton High School
230	6962	281	Darfield, New Zealand	2010	ROLC
231	6966	281	Darfield, New Zealand	2010	Shirley Library
232	6969	281	Darfield, New Zealand	2010	Styx Mill Transfer Station
233	6975	281	Darfield, New Zealand	2010	TPLC
234	8064	346	Christchurch, New Zealand	2011	Christchurch Cathedral College
235	8066	346	Christchurch, New Zealand	2011	Christchurch Hospital
236	8067	346	Christchurch, New Zealand	2011	Christchurch Cashmere High School
237	8090	346	Christchurch, New Zealand	2011	Hulverstone Drive Pumping Station
238	8119	346	Christchurch, New Zealand	2011	Pages Road Pumping Station
239	8123	346	Christchurch, New Zealand	2011	Christchurch Resthaven
240	8130	346	Christchurch, New Zealand	2011	Shirley Library
241	8158	346	Christchurch, New Zealand	2011	LPCC
242	8161	280	El Mayor-Cucapah	2010	El Centro Array #12
243	8164	138	Duzce, Turkey	1999	IRIGM 487
244	8606	280	El Mayor-Cucapah	2010	Westside Elementary School

APPENDIX C Expected Value of $\ln Amp$ Given M

Below is a closed-form solution of the expectation of $\ln Amp(T, T_p)$ over $T_p|M$ as needed in Equation 5.20 is derived below.

$$E_{T_p|M}[\ln Amp] = \int_{-\infty}^{+\infty} b_0 e^{b_1 \left(\ln \frac{T}{T_p} - b_2 \right)^2} P(\ln T_p|M) d \ln T_p \quad (C.1)$$

$$P(\ln T_p|M) = \frac{1}{\sqrt{2\pi\sigma_{\ln T_p}}} e^{-\frac{1}{2\sigma_{\ln T_p}^2} (\ln T_p - \mu_{\ln T_p})^2} \quad (\text{normal distribution}) \quad (C.2)$$

Substituting $\ln T_p$ with x .

$$E_{T_p|M}[\ln Amp] = \int_{-\infty}^{+\infty} b_0 e^{b_1 (\ln T - x - b_2)^2} \frac{1}{\sqrt{2\pi\sigma_x}} e^{-\frac{1}{2\sigma_x^2} (x - \mu_x)^2} dx \quad (C.3)$$

substituting $c = \ln T - b_2$

$$E_{T_p|M}[\ln Amp] = \frac{b_0}{\sqrt{2\pi\sigma_x^2}} \int_{-\infty}^{+\infty} e^{b_1 (c-x)^2} e^{-\frac{1}{2\sigma_x^2} (x - \mu_x)^2} dx \quad (C.4)$$

$$= \frac{b_0}{\sqrt{2\pi\sigma_x^2}} \int_{-\infty}^{+\infty} e^{b_1 (c^2 + x^2 - 2cx)} e^{-\frac{1}{2\sigma_x^2} (x^2 + \mu_x^2 - 2x\mu_x)} dx \quad (C.5)$$

$$= \frac{b_0}{\sqrt{2\pi\sigma_x^2}} \int_{-\infty}^{+\infty} e^{\left(b_1 c^2 + b_1 x^2 - 2b_1 cx - \frac{1}{2\sigma_x^2} x^2 - \frac{1}{2\sigma_x^2} \mu_x^2 + \frac{2}{2\sigma_x^2} x\mu_x \right)} dx \quad (C.6)$$

$$= \frac{b_0}{\sqrt{2\pi\sigma_x^2}} \int_{-\infty}^{+\infty} e^{\frac{1}{2\sigma_x^2} (2\sigma_x^2 b_1 c^2 + 2\sigma_x^2 b_1 x^2 - 4\sigma_x^2 b_1 cx - x^2 - \mu_x^2 + 2x\mu_x)} dx \quad (C.7)$$

Substitute $2\sigma_x^2 b_1 = d$

$$E_{T_p|M}[\ln Amp] = \frac{b_0}{\sqrt{2\pi\sigma_x^2}} \int_{-\infty}^{+\infty} e^{\frac{1}{2\sigma_x^2}(dc^2+dx^2-2dcx-x^2-\mu_x^2+2x\mu_x)} dx \quad (C.8)$$

$$= \frac{b_0}{\sqrt{2\pi\sigma_x^2}} \int_{-\infty}^{+\infty} e^{\frac{1}{2\sigma_x^2}(x^2(d-1)-2x(dc-\mu_x)+(dc^2-\mu_x^2))} dx \quad (C.9)$$

$$= \frac{b_0}{\sqrt{2\pi\sigma_x^2}} \int_{-\infty}^{+\infty} e^{\frac{d-1}{2\sigma_x^2}\left(x^2-\frac{2x(dc-\mu_x)}{d-1}+\frac{(dc^2-\mu_x^2)}{d-1}\right)} dx \quad (C.10)$$

$$= \frac{b_0}{\sqrt{2\pi\sigma_x^2}} \int_{-\infty}^{+\infty} e^{-\frac{1-d}{2\sigma_x^2}\left(x^2-\frac{2x(dc-\mu_x)}{d-1}+\left(\frac{dc-\mu_x}{d-1}\right)^2-\left(\frac{dc-\mu_x}{d-1}\right)^2+\frac{(dc^2-\mu_x^2)}{d-1}\right)} dx \quad (C.11)$$

$$= \frac{b_0}{\sqrt{2\pi\sigma_x^2}} \int_{-\infty}^{+\infty} e^{-\frac{1-d}{2\sigma_x^2}\left(x^2-\frac{2x(dc-\mu_x)}{d-1}+\left(\frac{dc-\mu_x}{d-1}\right)^2\right)} e^{-\frac{1-d}{2\sigma_x^2}\left(\frac{(dc^2-\mu_x^2)}{d-1}-\left(\frac{dc-\mu_x}{d-1}\right)^2\right)} dx \quad (C.12)$$

Substitute $\alpha = \frac{(dc^2-\mu_x^2)}{d-1} - \left(\frac{dc-\mu_x}{d-1}\right)^2$

$$E_{T_p|M}[\ln Amp] = \frac{b_0}{\sqrt{2\pi\sigma_x^2}} \int_{-\infty}^{+\infty} e^{-\frac{1-d}{2\sigma_x^2}\left(x^2-\frac{2x(dc-\mu_x)}{d-1}+\left(\frac{dc-\mu_x}{d-1}\right)^2\right)} e^{-\frac{1-d}{2\sigma_x^2}\alpha} dx \quad (C.13)$$

$$= \frac{b_0}{\sqrt{2\pi\sigma_x^2}} e^{-\frac{1-d}{2\sigma_x^2}\alpha} \int_{-\infty}^{+\infty} e^{-\frac{1-d}{2\sigma_x^2}\left(x^2-\frac{2x(dc-\mu_x)}{d-1}+\left(\frac{dc-\mu_x}{d-1}\right)^2\right)} dx \quad (C.14)$$

$$= \frac{b_0}{\sqrt{2\pi\sigma_x^2}} e^{-\frac{1-d}{2\sigma_x^2}\alpha} \sqrt{2\pi \left(\frac{\sigma_x}{\sqrt{d-1}}\right)^2} \int_{-\infty}^{+\infty} \frac{1}{\sqrt{2\pi \left(\frac{\sigma_x}{\sqrt{d-1}}\right)^2}} e^{-\frac{1-d}{2\sigma_x^2}\left(x-\left(\frac{dc-\mu_x}{d-1}\right)\right)^2} dx \quad (C.15)$$

Now $\frac{1}{\sqrt{2\pi \left(\frac{\sigma_x}{\sqrt{d-1}}\right)^2}} e^{-\frac{1-d}{2\sigma_x^2}\left(x-\left(\frac{dc-\mu_x}{d-1}\right)\right)^2}$ is the normal probability density function with mean $\frac{dc-\mu_x}{d-1}$ and standard deviation $\frac{\sigma_x}{\sqrt{d-1}}$, so the integration in Equation C.15 is equal to 1.

Thus,

$$E_{T_p|M}[\ln Amp] = \frac{b_0}{\sqrt{2\pi\sigma_x^2}} e^{-\frac{1-d}{2\sigma_x^2}\alpha} \sqrt{2\pi \left(\frac{\sigma_x}{\sqrt{d-1}}\right)^2} \quad (C.16)$$

$$= \frac{b_0}{\sqrt{d-1}} e^{-\frac{1-d}{2\sigma_x^2}\alpha} \quad (C.17)$$

where

$$x = \ln T_p \tag{C.18}$$

$$d = 2\sigma_x^2 b_1 \tag{C.19}$$

$$c = \ln T - b_2 \tag{C.20}$$

$$\alpha = \frac{(dc^2 - \mu_x^2)}{d - 1} - \left(\frac{dc - \mu_x}{d - 1} \right)^2 \tag{C.21}$$

APPENDIX D Approximations Made in Chapter 6

The derivation here shows that the approximations made in Equations 6.2 and 6.9 in Chapter 6 were first order approximations around \bar{m} and \bar{r} .

Using the total probability theorem the $P(\text{directivity}|S_a > x)$ can be expressed as shown below

$$P(\text{directivity}|S_a > x) = \int_M \int_R P(\text{directivity}|S_a > x, m, r) f_{M,R}(m, r) dm dr \quad (\text{D.1})$$

$$= E_{M,R}[P(\text{directivity}|S_a > x, m, r)] \quad (\text{D.2})$$

where $E_{M,R}[\cdot]$ represents the expected value over M and R . Now $P(\text{directivity}|S_a > x, m, r)$ can be written as an infinite sum using the Taylor series expansion about the mean magnitude (\bar{m}) and distance (\bar{r}) as shown below

$$\begin{aligned} P(\text{directivity}|S_a > x, m, r) &= P(\text{directivity}|S_a > x, \bar{m}, \bar{r}) \\ &+ (m - \bar{m}) \frac{\partial}{\partial m} P(\text{directivity}|S_a > x, m, r) \Big|_{\bar{m}, \bar{r}} \\ &+ (r - \bar{r}) \frac{\partial}{\partial r} P(\text{directivity}|S_a > x, m, r) \Big|_{\bar{m}, \bar{r}} \\ &+ \frac{1}{2} \left[(m - \bar{m})^2 \frac{\partial^2}{\partial m^2} P(\text{directivity}|S_a > x, m, r) \Big|_{\bar{m}, \bar{r}} \right. \\ &+ 2(m - \bar{m})(r - \bar{r}) \frac{\partial^2}{\partial m \partial r} P(\text{directivity}|S_a > x, m, r) \Big|_{\bar{m}, \bar{r}} \\ &\left. + (r - \bar{r})^2 \frac{\partial^2}{\partial r^2} P(\text{directivity}|S_a > x, m, r) \Big|_{\bar{m}, \bar{r}} \right] + \dots \quad (\text{D.3}) \end{aligned}$$

Ignoring the second and higher order terms we get a first order approximation of $P(\text{directivity}|S_a >$

x, m, r) as shown below

$$\begin{aligned}
P(\text{directivity}|S_a > x, m, r) &\approx P(\text{directivity}|S_a > x, \bar{m}, \bar{r}) \\
&+ (m - \bar{m}) \frac{\partial}{\partial m} P(\text{directivity}|S_a > x, m, r) \Big|_{\bar{m}, \bar{r}} \\
&+ (r - \bar{r}) \frac{\partial}{\partial r} P(\text{directivity}|S_a > x, m, r) \Big|_{\bar{m}, \bar{r}} \quad (\text{D.4})
\end{aligned}$$

Plugging the first order approximation of $P(\text{directivity}|S_a > x, m, r)$ from Equation D.4 in Equation D.2 we get

$$\begin{aligned}
E_{M,R}[P(\text{directivity}|S_a > x, m, r)] &\approx E_{M,R} \left[P(\text{directivity}|S_a > x, \bar{m}, \bar{r}) \right. \\
&+ (m - \bar{m}) \frac{\partial}{\partial m} P(\text{directivity}|S_a > x, m, r) \Big|_{\bar{m}, \bar{r}} \\
&\left. + (r - \bar{r}) \frac{\partial}{\partial r} P(\text{directivity}|S_a > x, m, r) \Big|_{\bar{m}, \bar{r}} \right] \quad (\text{D.5})
\end{aligned}$$

Using the linearity of expectation operator Equation D.5 can be re-written as

$$\begin{aligned}
E_{M,R}[P(\text{directivity}|S_a > x, m, r)] &\approx P(\text{directivity}|S_a > x, \bar{m}, \bar{r}) \\
&+ \frac{\partial}{\partial m} P(\text{directivity}|S_a > x, m, r) \Big|_{\bar{m}, \bar{r}} E_{M,R}[(m - \bar{m})] \\
&+ \frac{\partial}{\partial r} P(\text{directivity}|S_a > x, m, r) \Big|_{\bar{m}, \bar{r}} E_{M,R}[(r - \bar{r})] \quad (\text{D.6})
\end{aligned}$$

Now $E_{M,R}[(m - \bar{m})]$ is same as $E_{M,R}[m] - \bar{m} = \bar{m} - \bar{m} = 0$. Similarly $E_{M,R}[(r - \bar{r})] = 0$. Plugging this in Equation D.6 we get

$$E_{M,R}[P(\text{directivity}|S_a > x, m, r)] \approx P(\text{directivity}|S_a > x, \bar{m}, \bar{r}) \quad (\text{D.7})$$

Plugging Equation D.7 into Equation D.2 gives

$$P(\text{directivity}|S_a > x) \approx P(\text{directivity}|S_a > x, \bar{m}, \bar{r}) \quad (\text{D.8})$$

which is the desired approximation used in equation 6.2 in chapter 6.

This same procedure can be used to show that the approximation used in Equation 6.9 was a first-order approximation.

References

- Abrahamson, N., G. Atkinson, D. Boore, Y. Bozorgnia, K. Campbell, B. Chiou, I. M. Idriss, W. Silva, and R. Youngs (2008). Comparisons of the NGA ground-motion relations. *Earthquake Spectra* 24(1), 45–66.
- Abrahamson, N. and W. Silva (2008). Summary of the Abrahamson & Silva NGA ground-motion relations. *Earthquake Spectra* 24(1), 67–97.
- Abrahamson, N. A. (1988). Statistical properties of peak ground accelerations recorded by the SMART 1 array. *Bulletin of the Seismological Society of America* 78(1), 26–41.
- Abrahamson, N. A. (2000). Effects of rupture directivity on probabilistic seismic hazard analysis. In *Sixth International Conference on Seismic Zonation*, Oakland, California, pp. 151–156. Earthquake Engineering Research Inst.
- Abrahamson, N. A. and L. Al Atik (2010). Scenario spectra for design ground motions and risk calculation. In *9th US National and 10th Canadian Conference on Earthquake Engineering*, Toronto, Canada, pp. 12.
- Abrahamson, N. A. and R. R. Youngs (1992). A stable algorithm for regression analysis using the random effects model. *Bulletin of the Seismological Society of America* 82(1), 505–510.
- Akaike, H. (1974). A new look at the statistical model identification. *IEEE Transactions on Automatic Control* 19(6), 716 – 723.
- Akkar, S., U. Yazgan, and P. Gulkan (2005). Drift estimates in frame buildings subjected to near-fault ground motions. *Journal of Structural Engineering* 131(7), 1014–1024.
- Al Atik, L. and N. Abrahamson (2010). An improved method for nonstationary spectral matching. *Earthquake Spectra* 26(3), 601–617.
- Al Atik, L., N. Abrahamson, J. J. Bommer, F. Scherbaum, F. Cotton, and N. Kuehn (2010). The variability of ground-motion prediction models and its components. *Seismological Research Letters* 81(5), 794–801.
- Alavi, B. and H. Krawinkler (2001). Effects of near-fault ground motions on frame structures. Technical Report Blume Center Report 138, Stanford, California.
- Alavi, B. and H. Krawinkler (2004). Behavior of moment-resisting frame structures subjected to

- near-fault ground motions. *Earthquake Engineering & Structural Dynamics* 33(6), 687–706.
- Ancheta, T., Y. Bozorgnia, R. Darragh, W. Silva, B. Chiou, J. Stewart, D. Boore, R. Graves, N. Abrahamson, K. Campbell, I. Idriss, R. Youngs, and G. Atkinson (2012). PEER NGA-West2 database: A database of ground motions recorded in shallow crustal earthquakes in active tectonic regions. In *15th World conference on earthquake engineering*, Lisbon, Portugal, pp. 6.
- Anderson, J. C. and V. Bertero (1987). Uncertainties in establishing design earthquakes. *Journal of Structural Engineering* 113(8), 1709–1724.
- Baker, J., T. Lin, S. Shahi, and N. Jayaram (2011). New ground motion selection procedures and selected motions for the PEER Transportation Research Program. Technical report, Pacific Earthquake Engineering Research Center, Berkeley, California.
- Baker, J. W. (2007). Quantitative classification of Near-Fault ground motions using wavelet analysis. *Bulletin of the Seismological Society of America* 97(5), 1486–1501.
- Baker, J. W. (2011). The conditional mean spectrum: a tool for ground motion selection. *Journal of Structural Engineering* 3(137), 322–331.
- Baker, J. W. and C. A. Cornell (2005). A vector-valued ground motion intensity measure consisting of spectral acceleration and epsilon. *Earthquake Engineering & Structural Dynamics* 34(10), 1193–1217.
- Baker, J. W. and C. A. Cornell (2006). Which spectral acceleration are you using? *Earthquake Spectra* 22(2), 293–312.
- Baker, J. W. and C. A. Cornell (2008a). Vector-valued intensity measures for pulse-like near-fault ground motions. *Engineering structures* 30(4), 1048–1057.
- Baker, J. W. and C. A. Cornell (2008b). Vector-valued intensity measures incorporating spectral shape for prediction of structural response. *Journal of Earthquake Engineering* 12(4), 534–554.
- Bates, D. and M. Maechler (2010). *lme4: Linear mixed-effects models using S4 classes*. R package version 0.999375-33.
- Bazzurro, P. and C. A. Cornell (1999). Disaggregation of seismic hazard. *Bulletin of the Seismological Society of America* 89(2), 501–520.
- Bazzurro, P. and C. A. Cornell (2002). Vector-valued probabilistic seismic hazard analysis. In *U.S. National Conference on Earthquake Engineering (7th : 2002 : Boston, Mass.)*, Boston, MA, pp. 10.
- Benjamin, J. R. and C. A. Cornell (1970). *Probability, Statistics, and Decision for Civil Engineers*. New York: McGraw-Hill.
- Bertero, V., S. Mahin, and R. Herrera (1978). Aseismic design implications of near-fault San Fernando earthquake records. *Earthquake Engineering & Structural Dynamics* 6(1), 31–42.

- Beyer, K. and J. J. Bommer (2006). Relationships between median values and between aleatory variabilities for different definitions of the horizontal component of motion. *Bulletin of the Seismological Society of America* 96(4A), 1512–1522.
- Beyer, K. and J. J. Bommer (2007). Selection and scaling of real accelerograms for bi-directional loading: A review of current practice and code provisions. *Journal of Earthquake Engineering* 11, 13–45.
- Bommer, J. and A. Acevedo (2004). The use of real earthquake accelerograms as input to dynamic analysis. *Journal of Earthquake Engineering* 8(spec01), 43–91.
- Bommer, J., P. Stafford, and J. Alarcón (2009). Empirical equations for the prediction of the significant, bracketed, and uniform duration of earthquake ground motion. *Bulletin of the Seismological Society of America* 99(6), 3217–3233.
- Boore, D. M. (2010). Orientation-independent, nongeometric-mean measures of seismic intensity from two horizontal components of motion. *Bulletin of the Seismological Society of America* 100(4), 1830–1835.
- Boore, D. M. and G. M. Atkinson (2007). Boore-Atkinson NGA ground motion relations for the geometric mean horizontal component of peak and spectral ground motion parameters. Technical report, Pacific Earthquake Engineering Research Center, Berkeley, California.
- Boore, D. M. and G. M. Atkinson (2008). Ground-Motion prediction equations for the average horizontal component of PGA, PGV, and 5%-Damped PSA at spectral periods between 0.01 s and 10.0 s. *Earthquake Spectra* 24(1), 99–138.
- Boore, D. M., J. Watson-Lamprey, and N. A. Abrahamson (2006). Orientation-Independent measures of ground motion. *Bulletin of the Seismological Society of America* 96(4A), 1502–1511.
- Bozorgnia, Y., N. Abrahamson, K. Campbell, B. Rowshandel, and T. Shantz (2012). NGA-West2: A comprehensive research program to update ground motion prediction equations for shallow crustal earthquakes in active tectonic regions. In *15th World conference on earthquake engineering*, Lisbon, Portugal, pp. 6.
- Bradley, B. A. (2012). Strong ground motion characteristics observed in the 4 September 2010 Darfield, New Zealand earthquake. *Soil Dynamics and Earthquake Engineering* 42(0), 32 – 46.
- Bradley, B. A. and M. Cubrinovski (2011). Near-source strong ground motions observed in the 22 February 2011 Christchurch earthquake. *Seismological Research Letters* 82(6), 853 – 865.
- Bray, J. D. and A. Rodriguez-Marek (2004). Characterization of forward-directivity ground motions in the near-fault region. *Soil Dynamics and Earthquake Engineering* 24(11), 815–828.
- Brillinger, D. R. and H. K. Preisler (1985). Further analysis of the Joyner-Boore attenuation data. *Bulletin of the Seismological Society of America* 75(2), 611–614.

- Campbell, K. W. and Y. Bozorgnia (2008). NGA ground motion model for the geometric mean horizontal component of PGA, PGV, PGD and 5% damped linear elastic response spectra for periods ranging from 0.01 to 10 s. *Earthquake Spectra* 24(1), 139–171.
- Champion, C. and A. Liel (2012). The effect of near-fault directivity on building seismic collapse risk. *Earthquake Engineering & Structural Dynamics* 41(10), 1391–1409.
- Chioccarelli, E. and I. Iervolino (2010). Near-source seismic demand and pulse-like records: A discussion for L’Aquila earthquake. *Earthquake Engineering & Structural Dynamics* 39(9), 1039–1062.
- Chiou, B., R. Darragh, N. Gregor, and W. Silva (2008). NGA project strong-motion database. *Earthquake Spectra* 24(1), 23–44.
- Chiou, B. S. J. and R. R. Youngs (2008). An NGA model for the average horizontal component of peak ground motion and response spectra. *Earthquake Spectra* 24(1), 173–215.
- Cornell, C. and H. Krawinkler (2000). Progress and challenges in seismic performance assessment. *PEER Center News* 3(2).
- Cornell, C. A. (1968). Engineering seismic risk analysis. *Bulletin of the Seismological Society of America* 58(5), 1583–1606.
- Cortes, C. and V. Vapnik (1995). Support-vector networks. *Machine Learning* 20, 273–297.
- Deierlein, G. (2004). Overview of a comprehensive framework for earthquake performance assessment. In *International Workshop on Performance-Based Seismic Design Concepts and Implementation*, Bled, Slovenia, pp. 15–26.
- Fu, Q. and C. Menun (2004). Seismic-environment-based simulation of near-fault ground motions. In *Proceedings, 13th World Conference on Earthquake Engineering*, Vancouver, Canada, pp. 15.
- Hall, J. F., T. H. Heaton, M. W. Halling, and D. J. Wald (1995). Near-source ground motion and its effects on flexible buildings. *Earthquake Spectra* 11(4), 569–605.
- Hancock, J., J. Watson-Lamprey, N. A. Abrahamson, J. J. Bommer, A. Markatis, E. McCoy, and R. Mendis (2006). An improved method of matching response spectra of recorded earthquake ground motion using wavelets. *Journal of earthquake engineering* 10, 67–89.
- Hastie, T., R. Tibshirani, and J. H. Friedman (2001). *The elements of statistical learning: data mining, inference, and prediction*. New York: Springer.
- Housner, G. and D. Hudson (1958). The port hueneme earthquake of march 18, 1957. *Bulletin of the Seismological Society of America* 48(2), 163–168.
- Howard, J. K., C. A. Tracy, and R. G. Burns (2005). Comparing observed and predicted directivity in Near-Source ground motion. *Earthquake Spectra* 21(4), 1063–1092.
- Huang, Y., A. Whittaker, and N. Luco (2010). Maximum spectral demand in the United States,

- USGS open file report xxx-xxxx. pp. 217.
- Huang, Y., A. S. Whittaker, and N. Luco (2008). Maximum spectral demands in the near-fault region. *Earthquake Spectra* 24(1), 319–341.
- Idriss, I. M. (2008). An NGA empirical model for estimating the horizontal spectral values generated by shallow crustal earthquakes. *Earthquake Spectra* 24(1), 217–242.
- Iervolino, I. and C. A. Cornell (2008). Probability of occurrence of velocity pulses in near-source ground motions. *Bulletin of the Seismological Society of America* 98(5), 2262–2277.
- Iwan, W. (1997). Drift spectrum: measure of demand for earthquake ground motions. *Journal of Structural Engineering* 123(4), 397–404.
- Jayaram, N. and J. W. Baker (2008). Statistical tests of the joint distribution of spectral acceleration values. *Bulletin of the Seismological Society of America* 98(5), 2231–2243.
- Jayaram, N., T. Lin, and J. Baker (2011). A computationally efficient ground-motion selection algorithm for matching a target response spectrum mean and variance. *Earthquake Spectra* 27(3), 797–815.
- Kaklamanos, J., L. G. Baise, and D. M. Boore (2011). Estimating unknown input parameters when implementing the NGA ground-motion prediction equations in engineering practice. *Earthquake Spectra* 27(4), 1219–1235.
- Katsanos, E., A. Sextos, and G. Manolis (2010). Selection of earthquake ground motion records: A state-of-the-art review from a structural engineering perspective. *Soil Dynamics and Earthquake Engineering* 30(4), 157–169.
- Kottke, A. and E. M. Rathje (2008). A semi-automated procedure for selecting and scaling recorded earthquake motions for dynamic analysis. *Earthquake Spectra* 24(4), 911–932.
- Kramer, S. L. (1996). *Geotechnical earthquake engineering*. Upper Saddle River, N.J.: Prentice Hall.
- Kubo, T. and J. Penzien (1979). Analysis of three-dimensional strong ground motions along principal axes, san fernando earthquake. *Earthquake Engineering & Structural Dynamics* 7(3), 265–278.
- Kutner, M. H., C. Nachtsheim, and J. Neter (2004). *Applied linear regression models*. Boston; New York: McGraw-Hill/Irwin.
- Lin, T. (2012). *Advancement of hazard-consistent ground motion selection methodology*. Ph. D. thesis, Stanford University.
- Lin, T., C. Haselton, and J. Baker (2012a). Conditional spectrum based ground-motion selection, Part 1 : Hazard consistency for risk based assessment. *Earthquake Engineering & Structural Dynamics* (in review).

- Lin, T., C. Haselton, and J. Baker (2012b). Conditional spectrum based ground-motion selection, Part 2: Intensity based assessment and evaluation of alternate target spectra. *Earthquake Engineering & Structural Dynamics* (in review).
- Luco, N. and C. A. Cornell (2007). Structure-specific scalar intensity measures for near-source and ordinary earthquake ground motions. *Earthquake Spectra* 23(2), 357–392.
- MacRae, G., D. Morrow, and C. Roeder (2001). Near-fault ground motion effects on simple structures. *Journal of Structural Engineering* 127(9), 996–1004.
- Mai, P. M., P. Spudich, and J. Boatwright (2005). Hypocenter locations in finite-source rupture models. *Bulletin of the Seismological Society of America* 95(3), 965–980.
- Makris, N. and C. J. Black (2004). Dimensional analysis of bilinear oscillators under pulse-type excitations. *Journal of Engineering Mechanics* 130(9), 1019–1031.
- Mallat, S. G. (1999). *A wavelet tour of signal processing*, Volume 2nd. San Diego: Academic Press.
- Mavroeidis, G. and A. Papageorgiou (2002). Near-source strong ground motion: characteristics and design issues. In *Proc. of the Seventh US National Conf. on Earthquake Engineering (7NCEE)*, Boston, Massachusetts, pp. 21–25.
- Mavroeidis, G. P., G. Dong, and A. S. Papageorgiou (2004). Near-fault ground motions, and the response of elastic and inelastic single-degree-of-freedom (SDOF) systems. *Earthquake Engineering & Structural Dynamics* 33(9), 1023–1049.
- Mavroeidis, G. P. and A. S. Papageorgiou (2003). A mathematical representation of near-fault ground motions. *Bulletin of the Seismological Society of America* 93(3), 1099–1131.
- McCullagh, P. and J. A. Nelder (1989). *Generalized Linear Models*. New York: Chapman & Hall.
- McGuire, R. K. (2004). *Seismic Hazard and Risk Analysis*. Berkeley: Earthquake Engineering Research Institute.
- Menun, C. and Q. Fu (2002). An analytical model for near-fault ground motions and the response of SDOF systems. In *Proceedings, 7th U.S. National Conference on Earthquake Engineering*, Boston, MA, pp. 10.
- Moehle, J. and G. G. Deierlein (2004). A framework methodology for performance-based earthquake engineering. In *Proc. of International Workshop on Performance-Based Design*, Vancouver, Canada, pp. 13.
- NEHRP (2009). *NEHRP Recommended Provisions for Seismic Regulations for New Buildings and Other Structures*. FEMA P-750. Federal Emergency Management Agency, Washington, D.C.
- Padgett, J. and R. DesRoches (2007). Sensitivity of seismic response and fragility to parameter uncertainty. *Journal of Structural Engineering* 133(12), 1710–1718.

- Power, M., B. Chiou, N. Abrahamson, Y. Bozorgnia, T. Shantz, and C. Roblee (2008). An overview of the NGA project. *Earthquake Spectra* 24(1), 3–21.
- R Development Core Team (2010). *R: A Language and Environment for Statistical Computing*. Vienna, Austria: R Foundation for Statistical Computing. ISBN 3-900051-07-0.
- Rowshandel, B. (2006). Incorporating source rupture characteristics into Ground-Motion hazard analysis models. *Seismological Research Letters* 77(6), 708–722.
- Ruiz-García, J. and E. Miranda (2004). Inelastic displacement ratios for design of structures on soft soils sites. *Journal of Structural Engineering* 130(12), 2051–2061.
- Ruiz-García, J. and E. Miranda (2006). Inelastic displacement ratios for evaluation of structures built on soft soil sites. *Earthquake engineering & structural dynamics* 35(6), 679–694.
- Schmedes, J., R. J. Archuleta, and R. Madariaga (2006). Oversaturation of Peak Ground Velocity Along Strike Slip Faults. *AGU Fall Meeting Abstracts*, 246.
- Searle, S. (1971). *Linear Models*. New York-London: John Wiley & Sons.
- Shome, N., C. A. Cornell, P. Bazzurro, and J. E. Carballo (1998). Earthquakes, records, and non-linear responses. *Earthquake Spectra* 14(3), 469–500.
- Somerville, P., K. Irikura, R. Graves, S. Sawada, D. Wald, N. Abrahamson, Y. Iwasaki, T. Kagawa, N. Smith, and A. Kowada (1999). Characterizing crustal earthquake slip models for the prediction of strong ground motion. *Seismological Research Letters* 70, 59–80.
- Somerville, P. G. (1998). Development of an improved representation of near fault ground motions. In *SIMP 98, Seminar on Utilization of Strong-Motion Data*, Oakland, CA, pp. 20.
- Somerville, P. G. (2003). Magnitude scaling of the near fault rupture directivity pulse. *Physics of the earth and planetary interiors* 137(1), 201–212.
- Somerville, P. G. (2005). Engineering characterization of near fault ground motion. In *2005 New Zealand Society for Earthquake Engineering Conference*, Taupo, New Zealand, pp. 8.
- Somerville, P. G., N. F. Smith, R. W. Graves, and N. A. Abrahamson (1997). Modification of empirical strong ground motion attenuation relations to include the amplitude and duration effects of rupture directivity. *Seismological Research Letters* 68(1), 199–222.
- Somerville, P. G. and H. K. Thio (2005). Probabilistic vector-valued seismic hazard analysis for near-fault ground motions. Technical report.
- Spudich, P. and B. S. J. Chiou (2008). Directivity in NGA earthquake ground motions: Analysis using isochrone theory. *Earthquake Spectra* 24(1), 279–298.
- Stewart, J. P., N. A. Abrahamson, G. M. Atkinson, J. Baker, D. M. Boore, Y. Bozorgnia, K. W. Campbell, C. D. Comartin, I. M. Idriss, M. Lew, M. Mehrain, J. P. Moehle, F. Naeim, and T. A. Sabol (2011). Representation of bi-directional ground motions for design spectra in building

- codes. *Earthquake Spectra* 27(3), 927–937.
- Tothong, P., C. A. Cornell, and J. W. Baker (2007). Explicit-directivity-pulse inclusion in probabilistic seismic hazard analysis. *Earthquake Spectra* 23(4), 867–891.
- Travasarou, T., J. Bray, and N. Abrahamson (2003). Empirical attenuation relationship for arias intensity. *Earthquake engineering & structural dynamics* 32(7), 1133–1155.
- Vamvatsikos, D. and C. A. Cornell (2002). Incremental dynamic analysis. *Earthquake Engineering & Structural Dynamics* 31(3), 491–514.
- Vamvatsikos, D. and C. A. Cornell (2004). Applied incremental dynamic analysis. *Earthquake Spectra* 20(2), 523–553.
- Watson-Lamprey, J. and D. M. Boore (2007). Beyond SaGMROtI: conversion to SaArb, SaSN, and SaMaxRot. *Bulletin of the Seismological Society of America* 97(5), 1511–1524.
- Wells, D. L. and K. J. Coppersmith (1994). New empirical relationships among magnitude, rupture length, rupture width, rupture area, and surface displacement. *Bulletin of the Seismological Society of America* 84(4), 974–1002.
- Youngs, R. R. and K. Coppersmith (1985). Implications of fault slip rates and earthquake recurrence models to probabilistic seismic hazard analysis. *Bulletin of the Seismological Society of America* 75(4), 939–964.
- Zhang, T. (2004). Solving large scale linear prediction problems using stochastic gradient descent algorithms. In *Proceedings of the twenty-first international conference on Machine learning, ICML '04*, New York, NY, pp. 8.

PEER REPORTS

PEER reports are available as a free PDF download from http://peer.berkeley.edu/publications/peer_reports_complete.html. Printed hard copies of PEER reports can be ordered directly from our printer by following the instructions at http://peer.berkeley.edu/publications/peer_reports.html. For other related questions about the PEER Report Series, contact the Pacific Earthquake Engineering Research Center, 325 Davis Hall mail code 1792, Berkeley, CA 94720. Tel.: (510) 642-3437; Fax: (510) 665-1655; Email: peer_editor@berkeley.edu

- PEER 2013/21** *Seismic Design and Performance of Bridges with Columns on Rocking Foundations.* Grigorios Antonellis and Marios Panagiotou. September 2013.
- PEER 2013/20** *Experimental and Analytical Studies on the Seismic Behavior of Conventional and Hybrid Braced Frames.* Jiun-Wei Lai and Stephen A. Mahin. September 2013.
- PEER 2013/19** *Toward Resilient Communities: A Performance-Based Engineering Framework for Design and Evaluation of the Built Environment.* Michael William Mieler, Bozidar Stojadinovic, Robert J. Budnitz, Stephen A. Mahin and Mary C. Comerio. September 2013.
- PEER 2013/18** *Identification of Site Parameters that Improve Predictions of Site Amplification.* Ellen M. Rathje and Sara Navidi. July 2013.
- PEER 2013/17** *Response Spectrum Analysis of Concrete Gravity Dams Including Dam-Water-Foundation Interaction.* Arnkjell Løkke and Anil K. Chopra. July 2013.
- PEER 2013/16** *Effect of hoop reinforcement spacing on the cyclic response of large reinforced concrete special moment frame beams.* Marios Panagiotou, Tea Visnjic, Grigorios Antonellis, Panagiotis Galanis, and Jack P. Moehle. June 2013.
- PEER 2013/15** *A Probabilistic Framework to Include the Effects of Near-Fault Directivity in Seismic Hazard Assessment.* Shrey Kumar Shahi, Jack W. Baker. October 2013.
- PEER 2013/14** *Hanging-Wall Scaling using Finite-Fault Simulations.* Jennifer L. Donahue and Norman A. Abrahamson. September 2013.
- PEER 2013/13** *publication pending*
- PEER 2013/12** *Nonlinear Horizontal Site Response for the NGA-West2 Project.* Ronnie Kamai, Norman A. Abramson, Walter J. Silva. May 2013.
- PEER 2013/11** *Epistemic Uncertainty for NGA-West2 Models.* Linda Al Atik and Robert R. Youngs. May 2013.
- PEER 2013/10** *NGA-West 2 Models for Ground-Motion Directionality.* Shrey K. Shahi and Jack W. Baker. May 2013.
- PEER 2013/09** *Final Report of the NGA-West2 Directivity Working Group.* Paul Spudich, Jeffrey R. Bayless, Jack W. Baker, Brian S.J. Chiou, Badie Rowshandel, Shrey Shahi, and Paul Somerville. May 2013.
- PEER 2013/08** *NGA-West2 Model for Estimating Average Horizontal Values of Pseudo-Absolute Spectral Accelerations Generated by Crustal Earthquakes.* I. M. Idriss. May 2013.
- PEER 2013/07** *Update of the Chiou and Youngs NGA Ground Motion Model for Average Horizontal Component of Peak Ground Motion and Response Spectra.* Brian Chiou and Robert Youngs. May 2013.
- PEER 2013/06** *NGA-West2 Campbell-Bozorgnia Ground Motion Model for the Horizontal Components of PGA, PGV, and 5%-Damped Elastic Pseudo-Acceleration Response Spectra for Periods Ranging from 0.01 to 10 sec.* Kenneth W. Campbell and Yousef Bozorgnia. May 2013.
- PEER 2013/05** *NGA-West 2 Equations for Predicting Response Spectral Accelerations for Shallow Crustal Earthquakes.* David M. Boore, Jonathan P. Stewart, Emel Seyhan, Gail M. Atkinson. May 2013.
- PEER 2013/04** *Update of the AS08 Ground-Motion Prediction Equations Based on the NGA-West2 Data Set.* Norman Abrahamson, Walter Silva, and Ronnie Kamai. May 2013.
- PEER 2013/03** *PEER NGA-West2 Database.* Timothy D. Ancheta, Robert B. Darragh, Jonathan P. Stewart, Emel Seyhan, Walter J. Silva, Brian S.J. Chiou, Katie E. Wooddell, Robert W. Graves, Albert R. Kottke, David M. Boore, Tadahiro Kishida, and Jennifer L. Donahue. May 2013.
- PEER 2013/02** *Hybrid Simulation of the Seismic Response of Squat Reinforced Concrete Shear Walls.* Catherine A. Whyte and Bozidar Stojadinovic. May 2013.
- PEER 2013/01** *Housing Recovery in Chile: A Qualitative Mid-program Review.* Mary C. Comerio. February 2013.

- PEER 2012/08** *Guidelines for Estimation of Shear Wave Velocity.* Bernard R. Wair, Jason T. DeJong, and Thomas Shantz. December 2012.
- PEER 2012/07** *Earthquake Engineering for Resilient Communities: 2012 PEER Internship Program Research Report Collection.* Heidi Tremayne (Editor), Stephen A. Mahin (Editor), Collin Anderson, Dustin Cook, Michael Erceg, Carlos Esparza, Jose Jimenez, Dorian Krausz, Andrew Lo, Stephanie Lopez, Nicole McCurdy, Paul Shipman, Alexander Strum, Eduardo Vega. December 2012.
- PEER 2012/06** *Fragilities for Precarious Rocks at Yucca Mountain.* Matthew D. Purvance, Rasool Anooshehpour, and James N. Brune. December 2012.
- PEER 2012/05** *Development of Simplified Analysis Procedure for Piles in Laterally Spreading Layered Soils.* Christopher R. McGann, Pedro Arduino, and Peter Mackenzie-Helnwein. December 2012.
- PEER 2012/04** *Unbonded Pre-Tensioned Columns for Bridges in Seismic Regions.* Phillip M. Davis, Todd M. Janes, Marc O. Eberhard, and John F. Stanton. December 2012.
- PEER 2012/03** *Experimental and Analytical Studies on Reinforced Concrete Buildings with Seismically Vulnerable Beam-Column Joints.* Sangjoon Park and Khalid M. Mosalam. October 2012.
- PEER 2012/02** *Seismic Performance of Reinforced Concrete Bridges Allowed to Uplift during Multi-Directional Excitation.* Andres Oscar Espinoza and Stephen A. Mahin. July 2012.
- PEER 2012/01** *Spectral Damping Scaling Factors for Shallow Crustal Earthquakes in Active Tectonic Regions.* Sanaz Rezaeian, Yousef Bozorgnia, I. M. Idriss, Kenneth Campbell, Norman Abrahamson, and Walter Silva. July 2012.
- PEER 2011/10** *Earthquake Engineering for Resilient Communities: 2011 PEER Internship Program Research Report Collection.* Eds. Heidi Faison and Stephen A. Mahin. December 2011.
- PEER 2011/09** *Calibration of Semi-Stochastic Procedure for Simulating High-Frequency Ground Motions.* Jonathan P. Stewart, Emel Seyhan, and Robert W. Graves. December 2011.
- PEER 2011/08** *Water Supply in regard to Fire Following Earthquake.* Charles Scawthorn. November 2011.
- PEER 2011/07** *Seismic Risk Management in Urban Areas. Proceedings of a U.S.-Iran-Turkey Seismic Workshop.* September 2011.
- PEER 2011/06** *The Use of Base Isolation Systems to Achieve Complex Seismic Performance Objectives.* Troy A. Morgan and Stephen A. Mahin. July 2011.
- PEER 2011/05** *Case Studies of the Seismic Performance of Tall Buildings Designed by Alternative Means.* Task 12 Report for the Tall Buildings Initiative. Jack Moehle, Yousef Bozorgnia, Nirmal Jayaram, Pierson Jones, Mohsen Rahnama, Nilesh Shome, Zeynep Tuna, John Wallace, Tony Yang, and Farzin Zareian. July 2011.
- PEER 2011/04** *Recommended Design Practice for Pile Foundations in Laterally Spreading Ground.* Scott A. Ashford, Ross W. Boulanger, and Scott J. Brandenburg. June 2011.
- PEER 2011/03** *New Ground Motion Selection Procedures and Selected Motions for the PEER Transportation Research Program.* Jack W. Baker, Ting Lin, Shrey K. Shahi, and Nirmal Jayaram. March 2011.
- PEER 2011/02** *A Bayesian Network Methodology for Infrastructure Seismic Risk Assessment and Decision Support.* Michelle T. Bensi, Armen Der Kiureghian, and Daniel Straub. March 2011.
- PEER 2011/01** *Demand Fragility Surfaces for Bridges in Liquefied and Laterally Spreading Ground.* Scott J. Brandenburg, Jian Zhang, Pirooz Kashighandi, Yili Huo, and Minxing Zhao. March 2011.
- PEER 2010/05** *Guidelines for Performance-Based Seismic Design of Tall Buildings.* Developed by the Tall Buildings Initiative. November 2010.
- PEER 2010/04** *Application Guide for the Design of Flexible and Rigid Bus Connections between Substation Equipment Subjected to Earthquakes.* Jean-Bernard Dastous and Armen Der Kiureghian. September 2010.
- PEER 2010/03** *Shear Wave Velocity as a Statistical Function of Standard Penetration Test Resistance and Vertical Effective Stress at Caltrans Bridge Sites.* Scott J. Brandenburg, Naresh Bellana, and Thomas Shantz. June 2010.
- PEER 2010/02** *Stochastic Modeling and Simulation of Ground Motions for Performance-Based Earthquake Engineering.* Sanaz Rezaeian and Armen Der Kiureghian. June 2010.
- PEER 2010/01** *Structural Response and Cost Characterization of Bridge Construction Using Seismic Performance Enhancement Strategies.* Ady Aviram, Božidar Stojadinović, Gustavo J. Parra-Montesinos, and Kevin R. Mackie. March 2010.
- PEER 2009/03** *The Integration of Experimental and Simulation Data in the Study of Reinforced Concrete Bridge Systems Including Soil-Foundation-Structure Interaction.* Matthew Dryden and Gregory L. Fenves. November 2009.
- PEER 2009/02** *Improving Earthquake Mitigation through Innovations and Applications in Seismic Science, Engineering, Communication, and Response. Proceedings of a U.S.-Iran Seismic Workshop.* October 2009.

- PEER 2009/01** *Evaluation of Ground Motion Selection and Modification Methods: Predicting Median Interstory Drift Response of Buildings.* Curt B. Haselton, Ed. June 2009.
- PEER 2008/10** *Technical Manual for Strata.* Albert R. Kottke and Ellen M. Rathje. February 2009.
- PEER 2008/09** *NGA Model for Average Horizontal Component of Peak Ground Motion and Response Spectra.* Brian S.-J. Chiou and Robert R. Youngs. November 2008.
- PEER 2008/08** *Toward Earthquake-Resistant Design of Concentrically Braced Steel Structures.* Patxi Uriz and Stephen A. Mahin. November 2008.
- PEER 2008/07** *Using OpenSees for Performance-Based Evaluation of Bridges on Liquefiable Soils.* Stephen L. Kramer, Pedro Arduino, and HyungSuk Shin. November 2008.
- PEER 2008/06** *Shaking Table Tests and Numerical Investigation of Self-Centering Reinforced Concrete Bridge Columns.* Hyung IL Jeong, Junichi Sakai, and Stephen A. Mahin. September 2008.
- PEER 2008/05** *Performance-Based Earthquake Engineering Design Evaluation Procedure for Bridge Foundations Undergoing Liquefaction-Induced Lateral Ground Displacement.* Christian A. Ledezma and Jonathan D. Bray. August 2008.
- PEER 2008/04** *Benchmarking of Nonlinear Geotechnical Ground Response Analysis Procedures.* Jonathan P. Stewart, Annie On-Lei Kwok, Youssef M. A. Hashash, Neven Matasovic, Robert Pyke, Zhiliang Wang, and Zhaohui Yang. August 2008.
- PEER 2008/03** *Guidelines for Nonlinear Analysis of Bridge Structures in California.* Ady Aviram, Kevin R. Mackie, and Božidar Stojadinović. August 2008.
- PEER 2008/02** *Treatment of Uncertainties in Seismic-Risk Analysis of Transportation Systems.* Evangelos Stergiou and Anne S. Kiremidjian. July 2008.
- PEER 2008/01** *Seismic Performance Objectives for Tall Buildings.* William T. Holmes, Charles Kircher, William Petak, and Nabih Youssef. August 2008.
- PEER 2007/12** *An Assessment to Benchmark the Seismic Performance of a Code-Conforming Reinforced Concrete Moment-Frame Building.* Curt Haselton, Christine A. Goulet, Judith Mitrani-Reiser, James L. Beck, Gregory G. Deierlein, Keith A. Porter, Jonathan P. Stewart, and Ertugrul Taciroglu. August 2008.
- PEER 2007/11** *Bar Buckling in Reinforced Concrete Bridge Columns.* Wayne A. Brown, Dawn E. Lehman, and John F. Stanton. February 2008.
- PEER 2007/10** *Computational Modeling of Progressive Collapse in Reinforced Concrete Frame Structures.* Mohamed M. Talaat and Khalid M. Mosalam. May 2008.
- PEER 2007/09** *Integrated Probabilistic Performance-Based Evaluation of Benchmark Reinforced Concrete Bridges.* Kevin R. Mackie, John-Michael Wong, and Božidar Stojadinović. January 2008.
- PEER 2007/08** *Assessing Seismic Collapse Safety of Modern Reinforced Concrete Moment-Frame Buildings.* Curt B. Haselton and Gregory G. Deierlein. February 2008.
- PEER 2007/07** *Performance Modeling Strategies for Modern Reinforced Concrete Bridge Columns.* Michael P. Berry and Marc O. Eberhard. April 2008.
- PEER 2007/06** *Development of Improved Procedures for Seismic Design of Buried and Partially Buried Structures.* Linda Al Atik and Nicholas Sitar. June 2007.
- PEER 2007/05** *Uncertainty and Correlation in Seismic Risk Assessment of Transportation Systems.* Renee G. Lee and Anne S. Kiremidjian. July 2007.
- PEER 2007/04** *Numerical Models for Analysis and Performance-Based Design of Shallow Foundations Subjected to Seismic Loading.* Sivapalan Gajan, Tara C. Hutchinson, Bruce L. Kutter, Prishati Raychowdhury, José A. Ugalde, and Jonathan P. Stewart. May 2008.
- PEER 2007/03** *Beam-Column Element Model Calibrated for Predicting Flexural Response Leading to Global Collapse of RC Frame Buildings.* Curt B. Haselton, Abbie B. Liel, Sarah Taylor Lange, and Gregory G. Deierlein. May 2008.
- PEER 2007/02** *Campbell-Bozorgnia NGA Ground Motion Relations for the Geometric Mean Horizontal Component of Peak and Spectral Ground Motion Parameters.* Kenneth W. Campbell and Yousef Bozorgnia. May 2007.
- PEER 2007/01** *Boore-Atkinson NGA Ground Motion Relations for the Geometric Mean Horizontal Component of Peak and Spectral Ground Motion Parameters.* David M. Boore and Gail M. Atkinson. May 2007.
- PEER 2006/12** *Societal Implications of Performance-Based Earthquake Engineering.* Peter J. May. May 2007.
- PEER 2006/11** *Probabilistic Seismic Demand Analysis Using Advanced Ground Motion Intensity Measures, Attenuation Relationships, and Near-Fault Effects.* Polsak Tothong and C. Allin Cornell. March 2007.

- PEER 2006/10** *Application of the PEER PBEE Methodology to the I-880 Viaduct.* Sashi Kunnath. February 2007.
- PEER 2006/09** *Quantifying Economic Losses from Travel Forgone Following a Large Metropolitan Earthquake.* James Moore, Sungbin Cho, Yue Yue Fan, and Stuart Werner. November 2006.
- PEER 2006/08** *Vector-Valued Ground Motion Intensity Measures for Probabilistic Seismic Demand Analysis.* Jack W. Baker and C. Allin Cornell. October 2006.
- PEER 2006/07** *Analytical Modeling of Reinforced Concrete Walls for Predicting Flexural and Coupled–Shear-Flexural Responses.* Kutay Orakcal, Leonardo M. Massone, and John W. Wallace. October 2006.
- PEER 2006/06** *Nonlinear Analysis of a Soil-Drilled Pier System under Static and Dynamic Axial Loading.* Gang Wang and Nicholas Sitar. November 2006.
- PEER 2006/05** *Advanced Seismic Assessment Guidelines.* Paolo Bazzurro, C. Allin Cornell, Charles Menun, Maziar Motahari, and Nicolas Luco. September 2006.
- PEER 2006/04** *Probabilistic Seismic Evaluation of Reinforced Concrete Structural Components and Systems.* Tae Hyung Lee and Khalid M. Mosalam. August 2006.
- PEER 2006/03** *Performance of Lifelines Subjected to Lateral Spreading.* Scott A. Ashford and Teerawat Juirnarongrit. July 2006.
- PEER 2006/02** *Pacific Earthquake Engineering Research Center Highway Demonstration Project.* Anne Kiremidjian, James Moore, Yue Yue Fan, Nesrin Basoz, Ozgur Yazali, and Meredith Williams. April 2006.
- PEER 2006/01** *Bracing Berkeley. A Guide to Seismic Safety on the UC Berkeley Campus.* Mary C. Comerio, Stephen Tobriner, and Ariane Fehrenkamp. January 2006.
- PEER 2005/16** *Seismic Response and Reliability of Electrical Substation Equipment and Systems.* Junho Song, Armen Der Kiureghian, and Jerome L. Sackman. April 2006.
- PEER 2005/15** *CPT-Based Probabilistic Assessment of Seismic Soil Liquefaction Initiation.* R. E. S. Moss, R. B. Seed, R. E. Kayen, J. P. Stewart, and A. Der Kiureghian. April 2006.
- PEER 2005/14** *Workshop on Modeling of Nonlinear Cyclic Load-Deformation Behavior of Shallow Foundations.* Bruce L. Kutter, Geoffrey Martin, Tara Hutchinson, Chad Harden, Sivapalan Gajan, and Justin Phalen. March 2006.
- PEER 2005/13** *Stochastic Characterization and Decision Bases under Time-Dependent Aftershock Risk in Performance-Based Earthquake Engineering.* Gee Liek Yeo and C. Allin Cornell. July 2005.
- PEER 2005/12** *PEER Testbed Study on a Laboratory Building: Exercising Seismic Performance Assessment.* Mary C. Comerio, editor. November 2005.
- PEER 2005/11** *Van Nuys Hotel Building Testbed Report: Exercising Seismic Performance Assessment.* Helmut Krawinkler, editor. October 2005.
- PEER 2005/10** *First NEES/E-Defense Workshop on Collapse Simulation of Reinforced Concrete Building Structures.* September 2005.
- PEER 2005/09** *Test Applications of Advanced Seismic Assessment Guidelines.* Joe Maffei, Karl Telleen, Danya Mohr, William Holmes, and Yuki Nakayama. August 2006.
- PEER 2005/08** *Damage Accumulation in Lightly Confined Reinforced Concrete Bridge Columns.* R. Tyler Ranf, Jared M. Nelson, Zach Price, Marc O. Eberhard, and John F. Stanton. April 2006.
- PEER 2005/07** *Experimental and Analytical Studies on the Seismic Response of Freestanding and Anchored Laboratory Equipment.* Dimitrios Konstantinidis and Nicos Makris. January 2005.
- PEER 2005/06** *Global Collapse of Frame Structures under Seismic Excitations.* Luis F. Ibarra and Helmut Krawinkler. September 2005.
- PEER 2005/05** *Performance Characterization of Bench- and Shelf-Mounted Equipment.* Samit Ray Chaudhuri and Tara C. Hutchinson. May 2006.
- PEER 2005/04** *Numerical Modeling of the Nonlinear Cyclic Response of Shallow Foundations.* Chad Harden, Tara Hutchinson, Geoffrey R. Martin, and Bruce L. Kutter. August 2005.
- PEER 2005/03** *A Taxonomy of Building Components for Performance-Based Earthquake Engineering.* Keith A. Porter. September 2005.
- PEER 2005/02** *Fragility Basis for California Highway Overpass Bridge Seismic Decision Making.* Kevin R. Mackie and Božidar Stojadinović. June 2005.
- PEER 2005/01** *Empirical Characterization of Site Conditions on Strong Ground Motion.* Jonathan P. Stewart, Yoojoong Choi, and Robert W. Graves. June 2005.

- PEER 2004/09** *Electrical Substation Equipment Interaction: Experimental Rigid Conductor Studies.* Christopher Stearns and André Filiatrault. February 2005.
- PEER 2004/08** *Seismic Qualification and Fragility Testing of Line Break 550-kV Disconnect Switches.* Shakhzod M. Takhirov, Gregory L. Fenves, and Eric Fujisaki. January 2005.
- PEER 2004/07** *Ground Motions for Earthquake Simulator Qualification of Electrical Substation Equipment.* Shakhzod M. Takhirov, Gregory L. Fenves, Eric Fujisaki, and Don Clyde. January 2005.
- PEER 2004/06** *Performance-Based Regulation and Regulatory Regimes.* Peter J. May and Chris Koski. September 2004.
- PEER 2004/05** *Performance-Based Seismic Design Concepts and Implementation: Proceedings of an International Workshop.* Peter Fajfar and Helmut Krawinkler, editors. September 2004.
- PEER 2004/04** *Seismic Performance of an Instrumented Tilt-up Wall Building.* James C. Anderson and Vitelmo V. Bertero. July 2004.
- PEER 2004/03** *Evaluation and Application of Concrete Tilt-up Assessment Methodologies.* Timothy Graf and James O. Malley. October 2004.
- PEER 2004/02** *Analytical Investigations of New Methods for Reducing Residual Displacements of Reinforced Concrete Bridge Columns.* Junichi Sakai and Stephen A. Mahin. August 2004.
- PEER 2004/01** *Seismic Performance of Masonry Buildings and Design Implications.* Kerri Anne Taeko Tokoro, James C. Anderson, and Vitelmo V. Bertero. February 2004.
- PEER 2003/18** *Performance Models for Flexural Damage in Reinforced Concrete Columns.* Michael Berry and Marc Eberhard. August 2003.
- PEER 2003/17** *Predicting Earthquake Damage in Older Reinforced Concrete Beam-Column Joints.* Catherine Pagni and Laura Lowes. October 2004.
- PEER 2003/16** *Seismic Demands for Performance-Based Design of Bridges.* Kevin Mackie and Božidar Stojadinović. August 2003.
- PEER 2003/15** *Seismic Demands for Nondeteriorating Frame Structures and Their Dependence on Ground Motions.* Ricardo Antonio Medina and Helmut Krawinkler. May 2004.
- PEER 2003/14** *Finite Element Reliability and Sensitivity Methods for Performance-Based Earthquake Engineering.* Terje Haukaas and Armen Der Kiureghian. April 2004.
- PEER 2003/13** *Effects of Connection Hysteretic Degradation on the Seismic Behavior of Steel Moment-Resisting Frames.* Janise E. Rodgers and Stephen A. Mahin. March 2004.
- PEER 2003/12** *Implementation Manual for the Seismic Protection of Laboratory Contents: Format and Case Studies.* William T. Holmes and Mary C. Comerio. October 2003.
- PEER 2003/11** *Fifth U.S.-Japan Workshop on Performance-Based Earthquake Engineering Methodology for Reinforced Concrete Building Structures.* February 2004.
- PEER 2003/10** *A Beam-Column Joint Model for Simulating the Earthquake Response of Reinforced Concrete Frames.* Laura N. Lowes, Nilanjan Mitra, and Arash Altoontash. February 2004.
- PEER 2003/09** *Sequencing Repairs after an Earthquake: An Economic Approach.* Marco Casari and Simon J. Wilkie. April 2004.
- PEER 2003/08** *A Technical Framework for Probability-Based Demand and Capacity Factor Design (DCFD) Seismic Formats.* Fatemeh Jalayer and C. Allin Cornell. November 2003.
- PEER 2003/07** *Uncertainty Specification and Propagation for Loss Estimation Using FOSM Methods.* Jack W. Baker and C. Allin Cornell. September 2003.
- PEER 2003/06** *Performance of Circular Reinforced Concrete Bridge Columns under Bidirectional Earthquake Loading.* Mahmoud M. Hachem, Stephen A. Mahin, and Jack P. Moehle. February 2003.
- PEER 2003/05** *Response Assessment for Building-Specific Loss Estimation.* Eduardo Miranda and Shahram Taghavi. September 2003.
- PEER 2003/04** *Experimental Assessment of Columns with Short Lap Splices Subjected to Cyclic Loads.* Murat Melek, John W. Wallace, and Joel Conte. April 2003.
- PEER 2003/03** *Probabilistic Response Assessment for Building-Specific Loss Estimation.* Eduardo Miranda and Hesameddin Aslani. September 2003.
- PEER 2003/02** *Software Framework for Collaborative Development of Nonlinear Dynamic Analysis Program.* Jun Peng and Kincho H. Law. September 2003.

- PEER 2003/01** *Shake Table Tests and Analytical Studies on the Gravity Load Collapse of Reinforced Concrete Frames.* Kenneth John Elwood and Jack P. Moehle. November 2003.
- PEER 2002/24** *Performance of Beam to Column Bridge Joints Subjected to a Large Velocity Pulse.* Natalie Gibson, André Filiatrault, and Scott A. Ashford. April 2002.
- PEER 2002/23** *Effects of Large Velocity Pulses on Reinforced Concrete Bridge Columns.* Greg L. Orozco and Scott A. Ashford. April 2002.
- PEER 2002/22** *Characterization of Large Velocity Pulses for Laboratory Testing.* Kenneth E. Cox and Scott A. Ashford. April 2002.
- PEER 2002/21** *Fourth U.S.-Japan Workshop on Performance-Based Earthquake Engineering Methodology for Reinforced Concrete Building Structures.* December 2002.
- PEER 2002/20** *Barriers to Adoption and Implementation of PBEE Innovations.* Peter J. May. August 2002.
- PEER 2002/19** *Economic-Engineered Integrated Models for Earthquakes: Socioeconomic Impacts.* Peter Gordon, James E. Moore II, and Harry W. Richardson. July 2002.
- PEER 2002/18** *Assessment of Reinforced Concrete Building Exterior Joints with Substandard Details.* Chris P. Pantelides, Jon Hansen, Justin Nadauld, and Lawrence D. Reaveley. May 2002.
- PEER 2002/17** *Structural Characterization and Seismic Response Analysis of a Highway Overcrossing Equipped with Elastomeric Bearings and Fluid Dampers: A Case Study.* Nicos Makris and Jian Zhang. November 2002.
- PEER 2002/16** *Estimation of Uncertainty in Geotechnical Properties for Performance-Based Earthquake Engineering.* Allen L. Jones, Steven L. Kramer, and Pedro Arduino. December 2002.
- PEER 2002/15** *Seismic Behavior of Bridge Columns Subjected to Various Loading Patterns.* Asadollah Esmaeily-Gh. and Yan Xiao. December 2002.
- PEER 2002/14** *Inelastic Seismic Response of Extended Pile Shaft Supported Bridge Structures.* T.C. Hutchinson, R.W. Boulanger, Y.H. Chai, and I.M. Idriss. December 2002.
- PEER 2002/13** *Probabilistic Models and Fragility Estimates for Bridge Components and Systems.* Paolo Gardoni, Armen Der Kiureghian, and Khalid M. Mosalam. June 2002.
- PEER 2002/12** *Effects of Fault Dip and Slip Rake on Near-Source Ground Motions: Why Chi-Chi Was a Relatively Mild M7.6 Earthquake.* Brad T. Aagaard, John F. Hall, and Thomas H. Heaton. December 2002.
- PEER 2002/11** *Analytical and Experimental Study of Fiber-Reinforced Strip Isolators.* James M. Kelly and Shakhzod M. Takhirov. September 2002.
- PEER 2002/10** *Centrifuge Modeling of Settlement and Lateral Spreading with Comparisons to Numerical Analyses.* Sivapalan Gajan and Bruce L. Kutter. January 2003.
- PEER 2002/09** *Documentation and Analysis of Field Case Histories of Seismic Compression during the 1994 Northridge, California, Earthquake.* Jonathan P. Stewart, Patrick M. Smith, Daniel H. Whang, and Jonathan D. Bray. October 2002.
- PEER 2002/08** *Component Testing, Stability Analysis and Characterization of Buckling-Restrained Unbonded Braces™.* Cameron Black, Nicos Makris, and Ian Aiken. September 2002.
- PEER 2002/07** *Seismic Performance of Pile-Wharf Connections.* Charles W. Roeder, Robert Graff, Jennifer Soderstrom, and Jun Han Yoo. December 2001.
- PEER 2002/06** *The Use of Benefit-Cost Analysis for Evaluation of Performance-Based Earthquake Engineering Decisions.* Richard O. Zerbe and Anthony Falit-Baiamonte. September 2001.
- PEER 2002/05** *Guidelines, Specifications, and Seismic Performance Characterization of Nonstructural Building Components and Equipment.* André Filiatrault, Constantin Christopoulos, and Christopher Stearns. September 2001.
- PEER 2002/04** *Consortium of Organizations for Strong-Motion Observation Systems and the Pacific Earthquake Engineering Research Center Lifelines Program: Invited Workshop on Archiving and Web Dissemination of Geotechnical Data, 4–5 October 2001.* September 2002.
- PEER 2002/03** *Investigation of Sensitivity of Building Loss Estimates to Major Uncertain Variables for the Van Nuys Testbed.* Keith A. Porter, James L. Beck, and Rustem V. Shaikhutdinov. August 2002.
- PEER 2002/02** *The Third U.S.-Japan Workshop on Performance-Based Earthquake Engineering Methodology for Reinforced Concrete Building Structures.* July 2002.
- PEER 2002/01** *Nonstructural Loss Estimation: The UC Berkeley Case Study.* Mary C. Comerio and John C. Stallmeyer. December 2001.

- PEER 2001/16** *Statistics of SDF-System Estimate of Roof Displacement for Pushover Analysis of Buildings.* Anil K. Chopra, Rakesh K. Goel, and Chatpan Chintanapakdee. December 2001.
- PEER 2001/15** *Damage to Bridges during the 2001 Nisqually Earthquake.* R. Tyler Ranf, Marc O. Eberhard, and Michael P. Berry. November 2001.
- PEER 2001/14** *Rocking Response of Equipment Anchored to a Base Foundation.* Nicos Makris and Cameron J. Black. September 2001.
- PEER 2001/13** *Modeling Soil Liquefaction Hazards for Performance-Based Earthquake Engineering.* Steven L. Kramer and Ahmed-W. Elgamal. February 2001.
- PEER 2001/12** *Development of Geotechnical Capabilities in OpenSees.* Boris Jeremić. September 2001.
- PEER 2001/11** *Analytical and Experimental Study of Fiber-Reinforced Elastomeric Isolators.* James M. Kelly and Shakhzod M. Takhirov. September 2001.
- PEER 2001/10** *Amplification Factors for Spectral Acceleration in Active Regions.* Jonathan P. Stewart, Andrew H. Liu, Yoojoong Choi, and Mehmet B. Baturay. December 2001.
- PEER 2001/09** *Ground Motion Evaluation Procedures for Performance-Based Design.* Jonathan P. Stewart, Shyh-Jeng Chiou, Jonathan D. Bray, Robert W. Graves, Paul G. Somerville, and Norman A. Abrahamson. September 2001.
- PEER 2001/08** *Experimental and Computational Evaluation of Reinforced Concrete Bridge Beam-Column Connections for Seismic Performance.* Clay J. Naito, Jack P. Moehle, and Khalid M. Mosalam. November 2001.
- PEER 2001/07** *The Rocking Spectrum and the Shortcomings of Design Guidelines.* Nicos Makris and Dimitrios Konstantinidis. August 2001.
- PEER 2001/06** *Development of an Electrical Substation Equipment Performance Database for Evaluation of Equipment Fragilities.* Thalia Agnanos. April 1999.
- PEER 2001/05** *Stiffness Analysis of Fiber-Reinforced Elastomeric Isolators.* Hsiang-Chuan Tsai and James M. Kelly. May 2001.
- PEER 2001/04** *Organizational and Societal Considerations for Performance-Based Earthquake Engineering.* Peter J. May. April 2001.
- PEER 2001/03** *A Modal Pushover Analysis Procedure to Estimate Seismic Demands for Buildings: Theory and Preliminary Evaluation.* Anil K. Chopra and Rakesh K. Goel. January 2001.
- PEER 2001/02** *Seismic Response Analysis of Highway Overcrossings Including Soil-Structure Interaction.* Jian Zhang and Nicos Makris. March 2001.
- PEER 2001/01** *Experimental Study of Large Seismic Steel Beam-to-Column Connections.* Egor P. Popov and Shakhzod M. Takhirov. November 2000.
- PEER 2000/10** *The Second U.S.-Japan Workshop on Performance-Based Earthquake Engineering Methodology for Reinforced Concrete Building Structures.* March 2000.
- PEER 2000/09** *Structural Engineering Reconnaissance of the August 17, 1999 Earthquake: Kocaeli (Izmit), Turkey.* Halil Sezen, Kenneth J. Elwood, Andrew S. Whittaker, Khalid Mosalam, John J. Wallace, and John F. Stanton. December 2000.
- PEER 2000/08** *Behavior of Reinforced Concrete Bridge Columns Having Varying Aspect Ratios and Varying Lengths of Confinement.* Anthony J. Calderone, Dawn E. Lehman, and Jack P. Moehle. January 2001.
- PEER 2000/07** *Cover-Plate and Flange-Plate Reinforced Steel Moment-Resisting Connections.* Taejin Kim, Andrew S. Whittaker, Amir S. Gilani, Vitelmo V. Bertero, and Shakhzod M. Takhirov. September 2000.
- PEER 2000/06** *Seismic Evaluation and Analysis of 230-kV Disconnect Switches.* Amir S. J. Gilani, Andrew S. Whittaker, Gregory L. Fenves, Chun-Hao Chen, Henry Ho, and Eric Fujisaki. July 2000.
- PEER 2000/05** *Performance-Based Evaluation of Exterior Reinforced Concrete Building Joints for Seismic Excitation.* Chandra Clyde, Chris P. Pantelides, and Lawrence D. Reaveley. July 2000.
- PEER 2000/04** *An Evaluation of Seismic Energy Demand: An Attenuation Approach.* Chung-Che Chou and Chia-Ming Uang. July 1999.
- PEER 2000/03** *Framing Earthquake Retrofitting Decisions: The Case of Hillside Homes in Los Angeles.* Detlof von Winterfeldt, Nels Roselund, and Alicia Kitsuse. March 2000.
- PEER 2000/02** *U.S.-Japan Workshop on the Effects of Near-Field Earthquake Shaking.* Andrew Whittaker, ed. July 2000.
- PEER 2000/01** *Further Studies on Seismic Interaction in Interconnected Electrical Substation Equipment.* Armen Der Kiureghian, Kee-Jeung Hong, and Jerome L. Sackman. November 1999.

- PEER 1999/14** *Seismic Evaluation and Retrofit of 230-kV Porcelain Transformer Bushings.* Amir S. Gilani, Andrew S. Whittaker, Gregory L. Fenves, and Eric Fujisaki. December 1999.
- PEER 1999/13** *Building Vulnerability Studies: Modeling and Evaluation of Tilt-up and Steel Reinforced Concrete Buildings.* John W. Wallace, Jonathan P. Stewart, and Andrew S. Whittaker, editors. December 1999.
- PEER 1999/12** *Rehabilitation of Nonductile RC Frame Building Using Encasement Plates and Energy-Dissipating Devices.* Mehrdad Sasani, Vitelmo V. Bertero, James C. Anderson. December 1999.
- PEER 1999/11** *Performance Evaluation Database for Concrete Bridge Components and Systems under Simulated Seismic Loads.* Yael D. Hose and Frieder Seible. November 1999.
- PEER 1999/10** *U.S.-Japan Workshop on Performance-Based Earthquake Engineering Methodology for Reinforced Concrete Building Structures.* December 1999.
- PEER 1999/09** *Performance Improvement of Long Period Building Structures Subjected to Severe Pulse-Type Ground Motions.* James C. Anderson, Vitelmo V. Bertero, and Raul Bertero. October 1999.
- PEER 1999/08** *Envelopes for Seismic Response Vectors.* Charles Menun and Armen Der Kiureghian. July 1999.
- PEER 1999/07** *Documentation of Strengths and Weaknesses of Current Computer Analysis Methods for Seismic Performance of Reinforced Concrete Members.* William F. Cofer. November 1999.
- PEER 1999/06** *Rocking Response and Overturning of Anchored Equipment under Seismic Excitations.* Nicos Makris and Jian Zhang. November 1999.
- PEER 1999/05** *Seismic Evaluation of 550 kV Porcelain Transformer Bushings.* Amir S. Gilani, Andrew S. Whittaker, Gregory L. Fenves, and Eric Fujisaki. October 1999.
- PEER 1999/04** *Adoption and Enforcement of Earthquake Risk-Reduction Measures.* Peter J. May, Raymond J. Burby, T. Jens Feeley, and Robert Wood.
- PEER 1999/03** *Task 3 Characterization of Site Response General Site Categories.* Adrian Rodriguez-Marek, Jonathan D. Bray, and Norman Abrahamson. February 1999.
- PEER 1999/02** *Capacity-Demand-Diagram Methods for Estimating Seismic Deformation of Inelastic Structures: SDF Systems.* Anil K. Chopra and Rakesh Goel. April 1999.
- PEER 1999/01** *Interaction in Interconnected Electrical Substation Equipment Subjected to Earthquake Ground Motions.* Armen Der Kiureghian, Jerome L. Sackman, and Kee-Jeung Hong. February 1999.
- PEER 1998/08** *Behavior and Failure Analysis of a Multiple-Frame Highway Bridge in the 1994 Northridge Earthquake.* Gregory L. Fenves and Michael Ellery. December 1998.
- PEER 1998/07** *Empirical Evaluation of Inertial Soil-Structure Interaction Effects.* Jonathan P. Stewart, Raymond B. Seed, and Gregory L. Fenves. November 1998.
- PEER 1998/06** *Effect of Damping Mechanisms on the Response of Seismic Isolated Structures.* Nicos Makris and Shih-Po Chang. November 1998.
- PEER 1998/05** *Rocking Response and Overturning of Equipment under Horizontal Pulse-Type Motions.* Nicos Makris and Yiannis Roussos. October 1998.
- PEER 1998/04** *Pacific Earthquake Engineering Research Invitational Workshop Proceedings, May 14–15, 1998: Defining the Links between Planning, Policy Analysis, Economics and Earthquake Engineering.* Mary Comerio and Peter Gordon. September 1998.
- PEER 1998/03** *Repair/Upgrade Procedures for Welded Beam to Column Connections.* James C. Anderson and Xiaojing Duan. May 1998.
- PEER 1998/02** *Seismic Evaluation of 196 kV Porcelain Transformer Bushings.* Amir S. Gilani, Juan W. Chavez, Gregory L. Fenves, and Andrew S. Whittaker. May 1998.
- PEER 1998/01** *Seismic Performance of Well-Confined Concrete Bridge Columns.* Dawn E. Lehman and Jack P. Moehle. December 2000.

ONLINE PEER REPORTS

The following PEER reports are available by Internet only at http://peer.berkeley.edu/publications/peer_reports_complete.html.

- PEER 2012/103** *Performance-Based Seismic Demand Assessment of Concentrically Braced Steel Frame Buildings*. Chui-Hsin Chen and Stephen A. Mahin. December 2012.
- PEER 2012/102** *Procedure to Restart an Interrupted Hybrid Simulation: Addendum to PEER Report 2010/103*. Vesna Terzic and Božidar Stojadinovic. October 2012.
- PEER 2012/101** *Mechanics of Fiber Reinforced Bearings*. James M. Kelly and Andrea Calabrese. February 2012.
- PEER 2011/107** *Nonlinear Site Response and Seismic Compression at Vertical Array Strongly Shaken by 2007 Niigata-ken Chuetsu-oki Earthquake*. Eric Yee, Jonathan P. Stewart, and Kohji Tokimatsu. December 2011.
- PEER 2011/106** *Self Compacting Hybrid Fiber Reinforced Concrete Composites for Bridge Columns*. Pardeep Kumar, Gabriel Jen, William Trono, Marios Panagiotou, and Claudia Ostertag. September 2011.
- PEER 2011/105** *Stochastic Dynamic Analysis of Bridges Subjected to Spatially Varying Ground Motions*. Katerina Konakli and Armen Der Kiureghian. August 2011.
- PEER 2011/104** *Design and Instrumentation of the 2010 E-Defense Four-Story Reinforced Concrete and Post-Tensioned Concrete Buildings*. Takuya Nagae, Kenichi Tahara, Taizo Matsumori, Hitoshi Shiohara, Toshimi Kabeyasawa, Susumu Kono, Minehiro Nishiyama (Japanese Research Team) and John Wallace, Wassim Ghannoum, Jack Moehle, Richard Sause, Wesley Keller, Zeynep Tuna (U.S. Research Team). June 2011.
- PEER 2011/103** *In-Situ Monitoring of the Force Output of Fluid Dampers: Experimental Investigation*. Dimitrios Konstantinidis, James M. Kelly, and Nicos Makris. April 2011.
- PEER 2011/102** *Ground-motion prediction equations 1964 - 2010*. John Douglas. April 2011.
- PEER 2011/101** *Report of the Eighth Planning Meeting of NEES/E-Defense Collaborative Research on Earthquake Engineering*. Convened by the Hyogo Earthquake Engineering Research Center (NIED), NEES Consortium, Inc. February 2011.
- PEER 2010/111** *Modeling and Acceptance Criteria for Seismic Design and Analysis of Tall Buildings*. Task 7 Report for the Tall Buildings Initiative - Published jointly by the Applied Technology Council. October 2010.
- PEER 2010/110** *Seismic Performance Assessment and Probabilistic Repair Cost Analysis of Precast Concrete Cladding Systems for Multistory Buildings*. Jeffrey P. Hunt and Božidar Stojadinovic. November 2010.
- PEER 2010/109** *Report of the Seventh Joint Planning Meeting of NEES/E-Defense Collaboration on Earthquake Engineering. Held at the E-Defense, Miki, and Shin-Kobe, Japan, September 18–19, 2009*. August 2010.
- PEER 2010/108** *Probabilistic Tsunami Hazard in California*. Hong Kie Thio, Paul Somerville, and Jascha Polet, preparers. October 2010.
- PEER 2010/107** *Performance and Reliability of Exposed Column Base Plate Connections for Steel Moment-Resisting Frames*. Ady Aviram, Božidar Stojadinovic, and Armen Der Kiureghian. August 2010.
- PEER 2010/106** *Verification of Probabilistic Seismic Hazard Analysis Computer Programs*. Patricia Thomas, Ivan Wong, and Norman Abrahamson. May 2010.
- PEER 2010/105** *Structural Engineering Reconnaissance of the April 6, 2009, Abruzzo, Italy, Earthquake, and Lessons Learned*. M. Selim Günay and Khalid M. Mosalam. April 2010.
- PEER 2010/104** *Simulating the Inelastic Seismic Behavior of Steel Braced Frames, Including the Effects of Low-Cycle Fatigue*. Yuli Huang and Stephen A. Mahin. April 2010.
- PEER 2010/103** *Post-Earthquake Traffic Capacity of Modern Bridges in California*. Vesna Terzic and Božidar Stojadinović. March 2010.
- PEER 2010/102** *Analysis of Cumulative Absolute Velocity (CAV) and JMA Instrumental Seismic Intensity (I_{JMA}) Using the PEER-NGA Strong Motion Database*. Kenneth W. Campbell and Yousef Bozorgnia. February 2010.
- PEER 2010/101** *Rocking Response of Bridges on Shallow Foundations*. Jose A. Ugalde, Bruce L. Kutter, and Boris Jeremic. April 2010.
- PEER 2009/109** *Simulation and Performance-Based Earthquake Engineering Assessment of Self-Centering Post-Tensioned Concrete Bridge Systems*. Won K. Lee and Sarah L. Billington. December 2009.
- PEER 2009/108** *PEER Lifelines Geotechnical Virtual Data Center*. J. Carl Stepp, Daniel J. Ponti, Loren L. Turner, Jennifer N. Swift, Sean Devlin, Yang Zhu, Jean Benoit, and John Bobbitt. September 2009.
- PEER 2009/107** *Experimental and Computational Evaluation of Current and Innovative In-Span Hinge Details in Reinforced Concrete Box-Girder Bridges: Part 2: Post-Test Analysis and Design Recommendations*. Matias A. Hube and Khalid M. Mosalam. December 2009.

- PEER 2009/106** *Shear Strength Models of Exterior Beam-Column Joints without Transverse Reinforcement.* Sangjoon Park and Khalid M. Mosalam. November 2009.
- PEER 2009/105** *Reduced Uncertainty of Ground Motion Prediction Equations through Bayesian Variance Analysis.* Robb Eric S. Moss. November 2009.
- PEER 2009/104** *Advanced Implementation of Hybrid Simulation.* Andreas H. Schellenberg, Stephen A. Mahin, Gregory L. Fenves. November 2009.
- PEER 2009/103** *Performance Evaluation of Innovative Steel Braced Frames.* T. Y. Yang, Jack P. Moehle, and Božidar Stojadinovic. August 2009.
- PEER 2009/102** *Reinvestigation of Liquefaction and Nonliquefaction Case Histories from the 1976 Tangshan Earthquake.* Robb Eric Moss, Robert E. Kayen, Liyuan Tong, Songyu Liu, Guojun Cai, and Jiaer Wu. August 2009.
- PEER 2009/101** *Report of the First Joint Planning Meeting for the Second Phase of NEES/E-Defense Collaborative Research on Earthquake Engineering.* Stephen A. Mahin et al. July 2009.
- PEER 2008/104** *Experimental and Analytical Study of the Seismic Performance of Retaining Structures.* Linda Al Atik and Nicholas Sitar. January 2009.
- PEER 2008/103** *Experimental and Computational Evaluation of Current and Innovative In-Span Hinge Details in Reinforced Concrete Box-Girder Bridges. Part 1: Experimental Findings and Pre-Test Analysis.* Matias A. Hube and Khalid M. Mosalam. January 2009.
- PEER 2008/102** *Modeling of Unreinforced Masonry Infill Walls Considering In-Plane and Out-of-Plane Interaction.* Stephen Kadysiewski and Khalid M. Mosalam. January 2009.
- PEER 2008/101** *Seismic Performance Objectives for Tall Buildings.* William T. Holmes, Charles Kircher, William Petak, and Nabih Youssef. August 2008.
- PEER 2007/101** *Generalized Hybrid Simulation Framework for Structural Systems Subjected to Seismic Loading.* Tarek Elkhoraibi and Khalid M. Mosalam. July 2007.
- PEER 2007/100** *Seismic Evaluation of Reinforced Concrete Buildings Including Effects of Masonry Infill Walls.* Alidad Hashemi and Khalid M. Mosalam. July 2007.

The Pacific Earthquake Engineering Research Center (PEER) is a multi-institutional research and education center with headquarters at the University of California, Berkeley. Investigators from over 20 universities, several consulting companies, and researchers at various state and federal government agencies contribute to research programs focused on performance-based earthquake engineering.

These research programs aim to identify and reduce the risks from major earthquakes to life safety and to the economy by including research in a wide variety of disciplines including structural and geotechnical engineering, geology/seismology, lifelines, transportation, architecture, economics, risk management, and public policy.

PEER is supported by federal, state, local, and regional agencies, together with industry partners.



PEER Core Institutions:
University of California, Berkeley (Lead Institution)
California Institute of Technology
Oregon State University
Stanford University
University of California, Davis
University of California, Irvine
University of California, Los Angeles
University of California, San Diego
University of Southern California
University of Washington

PEER reports can be ordered at http://peer.berkeley.edu/publications/peer_reports.html or by contacting

Pacific Earthquake Engineering Research Center
University of California, Berkeley
325 Davis Hall, mail code 1792
Berkeley, CA 94720-1792
Tel: 510-642-3437
Fax: 510-642-1655
Email: peer_editor@berkeley.edu

ISSN 1547-0587X